NEW OPTICAL WAVEGUIDE DEVICES USING PERIODIC AND CHIRPED SURFACE CORRUGATIONS

and

OPTICAL WAVES IN PERIODIC LAYERED STRUCTURES

Thesis by

Chi-Shain Hong

In Partial Fulfillment of the Requirements

for the Degree of

Doctor of Philosophy

California Institute of Technology

Pasadena, California

1979

(Submitted October 17, 1978)

To my parents

ACKNOWLEDGMENTS

I would like to express my sincere gratitude to my advisor, Professor Amnon Yariv, for his support and excellent guidance during the course of this work. The last four years in his group have been a most educational and fruitful experience for me.

I would like to thank Drs. Huan-Wun Yen and Alexis Livanos for introducing me to laboratory work as well as interesting experiments, and Dr. Bor-Uei Chen of Hughes Research Laboratories for his technical advice and cooperation. Stimulating discussions with Chun-Ching Shih, Pochi Yeh, and Willie Ng have also been most helpful. It is also a pleasure to acknowledge the skillful assistance of Desmond Armstrong with the experimental apparatus.

My special thanks go to Richard Moyer for his diligent and careful assistance with English usage in the writing of my thesis, and Mrs. Ruth Stratton for doing such a wonderful job of typing the manuscript.

The financial support received from the Air Force Office of Scientific Research, the National Science Foundation, and the California Institute of Technology is greatly appreciated.

Finally, I wish to thank my wife, Sui-Shin, and our parents for their encouragement and moral support over the past five years.

ABSTRACT

The first part of this work describes theoretical and experimental studies of some corrugated waveguide devices for use in optical communications and integrated optics. These devices include wavelength demultiplexers and broad-band optical filters using chirped corrugations, and optical scanners using the electrooptic effect in the corrugations.

The theory of corrugated waveguides is well described by the coupled mode formalism. The problem is also treated phenomenologically by picturing the incident waveguide mode as a zig-zag ray which is diffracted by the grating surface at every bounce. Principles of the devices are given, and the parameters which characterize the devices are derived.

Experimental results on fabrication and evaluation of the devices are presented and compared with the design theory. Various techniques which have been developed during the course of this investigation are described in some detail.

The second part of this work describes the propagation of electromagnetic waves in periodic layered structures.

A diagonalization of the unit cell translation operator of a periodic medium is used to obtain exact solutions for the Bloch waves, the dispersion relations, and the band structure of the medium. The general formalism is then applied to deal with such problems as Bragg reflectors, periodic multichannel waveguides, and electromagnetic surface waves.

TABLE OF CONTENTS

Part 1

NEW OPTICAL WAVEGUIDE DEVICES USING PERIODIC AND CHIRPED SURFACE CORRUGATIONS

Part II

OPTICAL WAVES IN PERIODIC LAYERED STRUCTURES

Part I

NEW OPTICAL WAVEGUIDE DEVICES USING PERIODIC AND CHIRPED SURFACE CORRUGATIONS

Chapter 1

INTRODUCTION

1.1 Optical Communications and Integrated Optics

The invention of the laser as an optical oscillator almost twenty years ago introduced the possibility of optical communications. Optical communications, however, did not, initially, receive serious attention, since the transmission of light in the atmosphere suffered from high attenuation, and low loss optical waveguides were not available then. It was not until a few years ago with the advent of very low loss fiber waveguides that the interest in optical communications was stimulated once again.

There are a number of potential advantages in an envisioned optical communications system. The first is its huge capability for carrying information by optical waves. In addition, the decrease in the carrier wavelength allows a reduction in the size of the transmission system. For example, optical waves are transmitted in small waveguides such as glass fibers, instead of the bulky copper cables used for radio waves. Besides their small size and light weight, fiber waveguides have a large bandwidth and are free from any electromagnetic interference. Low loss fibers with transmission losses of 1 dB/km in the spectral range of 0.8 - 1.6 μm are currently available [1]. Fiber waveguides will become more promising for high data density and long distance communication as less dispersive, less lossy, and much stronger fibers are made.

A fiber optic communications link consists, basically, of a light source, an optical fiber, and a detector. A block diagram of such a link is shown in Fig. 1.1a. At the transmitting terminals, light is generated and modulated into signals for transmitting. In repeaters, the attenuated signals are detected and regenerated (i.e., amplified) for the next leg of the journey. At the receiving terminals the signals are detected and demodulated for processing. It is essential that all these terminals and stations be reliable and have dimensions comparable to those of fibers. However, most of the conventional optical systems in use today consist of components which are bulky and heavy, and require careful alignment and protection. In an effort to reduce the size of each optical component, there has evolved a new field called "thin-film guided wave optics" [2].

The structures of fiber and thin-film waveguides are shown in Fig. 1.1b and c. In a thin-film waveguide, light is transversely confined by total internal reflection in the thin film, and is easily affected from the surface. Thus, optical components which are used with such waveguides can be fabricated directly on top of the waveguides. It is conceivable that a large number of components, interconnected by thin-film waveguides, could be fabricated on a common substrate. These planar optical "circuits" would be similar to conventional electronic integrated circuits. This defines the eventual goal of a growing technology called "integrated optics" [3,4,5,6,7]. The resulting integrated optical circuits, which will be compact, rigid, reliable, and free of the problems of vibration and alignment, will accelerate the coming of a new era in optical communications.

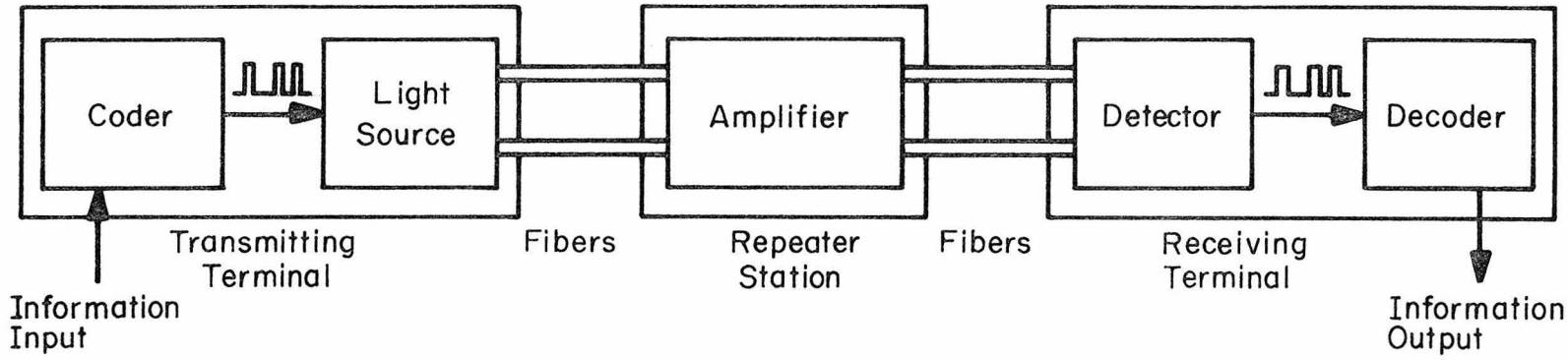

(a)

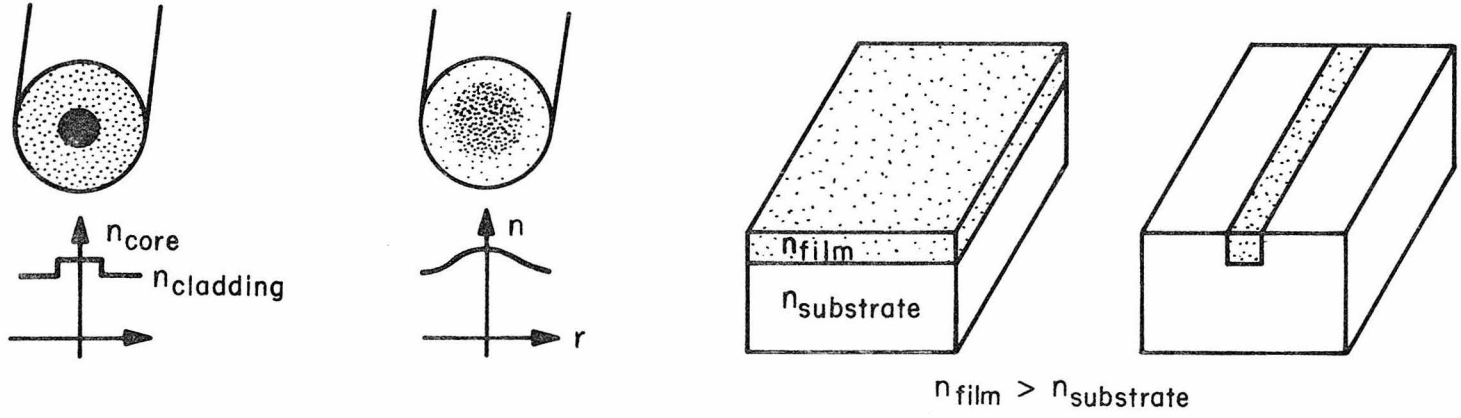

(b) (c)

Fig. 1.1 (a) Block diagram of an optical fiber communications link. (b) Structures of fiber waveguides. (c) Structures of thin-film waveguides.

1.2 Periodic Structures in Optical Waveguides

The development of integrated optics started with the study of thin-film dielectric waveguides and individual components made using such waveguides. Many different materials with good optical quality have been used as bases for fabricating waveguide components. Each particular component requires the optimization of certain parameters which dictates the choice of material. Among these materials, glass or glass-like waveguides are frequently used to demonstrate the fabrication of various passive components such as couplers, lenses, prisms, polarizers, beam-splitters, reflectors, and filters, while Nd^{+3} doped glass may act as an amplification medium [8]. $LiNbO_3$ or $LiTaO_3$ crystals have long been recognized as the best electrooptic and photoelastic material to be used for light modulation, switching, and scanning. GaAs or other III-V compounds with direct bandgaps are believed to be the top candidates for thin-film lasers and detectors.

The design of a waveguide component or the understanding of its operation requires the knowledge of electromagnetic propagation in plain waveguides. This will be addressed in the beginning of Chapter 2. There may exist several different approaches in design which will give a similar function. But there is an approach which is able to perform many functions, namely, the approach using periodic structures [9].

We shall use the term "periodic waveguide" to refer to a waveguide with parameters which are periodically perturbed along the surface of the waveguide. These parameters can be the film index

or the film thickness. For example, a spatially periodic modulation of the film index can be produced photoelastically by a surface acoustic wave as shown in Fig. 1.2a. The film index can also be modulated electrooptically by a pattern of interdigital electrodes deposited on top of the waveguide (Fig. 1.2b). A surface corrugation which modulates the film thickness as shown in Fig. 1.2c is another example of a periodic waveguide. If a waveguide mode can be viewed as a wave which propagates in an equivalent medium of index n_{eff}, which will be defined in Chapter 2, then the periodic waveguide has an effect of modulating this n_{eff} along the periodicity. Much as x-rays are scattered by atomic planes in a crystal, incident light is scattered by dielectric discontinuities. Constructive interference then takes place in a direction where the Bragg condition is satisfied. The use of periodic waveguides thus has the inherent merits of wavelength or directional sensitivity and high efficiency as a result of Bragg diffraction. Figure 1.3 shows three possible applications using periodic waveguides, namely retroreflection, in-plane deflection, and output coupling. The analysis of these problems will comprise the main body of Chapter 2.

Surface acoustic waves and interdigital electrodes have been used extensively for light-beam deflection [10,11] in which the efficiency depends on the electric driving power. Thus, they work as a switch or modulator. Moreover, the deflection of light from a tunable wavelength acoustic wave can be used for scanning the light beam [12]. Due to the feasibility of fabricating submicron periods, corrugated waveguides have found unique applications in such cases as backward

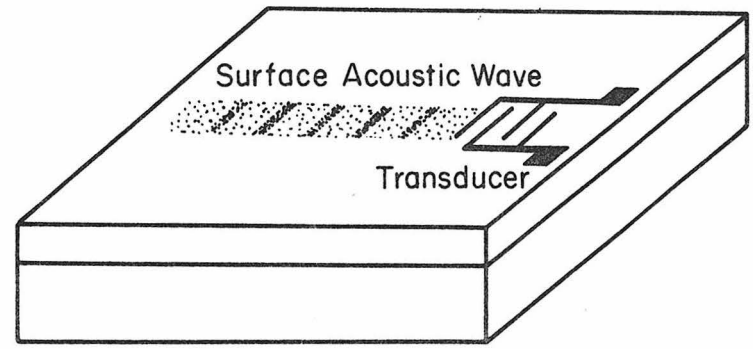

(a)

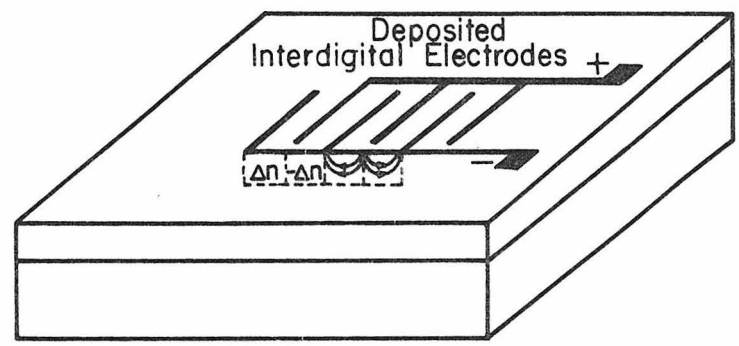

(b)

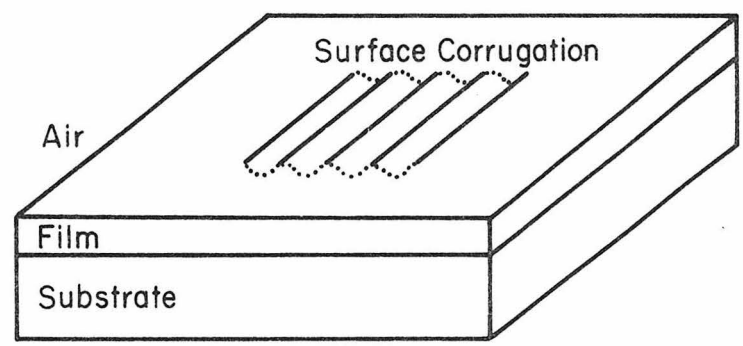

(c)

Fig. 1.2 Structures of periodic waveguides using (a) surface acoustic waves (b) deposited interdigital electrodes (c) surface corrugations.

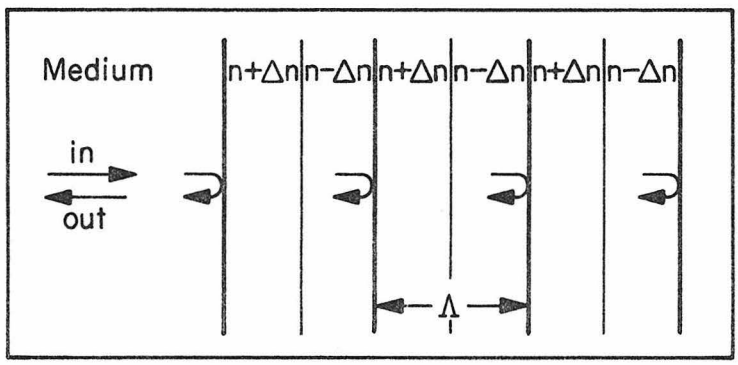

$2\Lambda = \frac{\lambda}{n}$

(a)

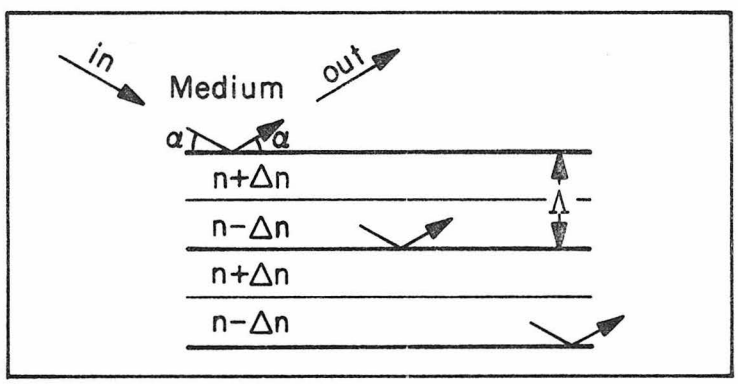

$2\Lambda \sin\alpha = \frac{\lambda}{n}$

(b)

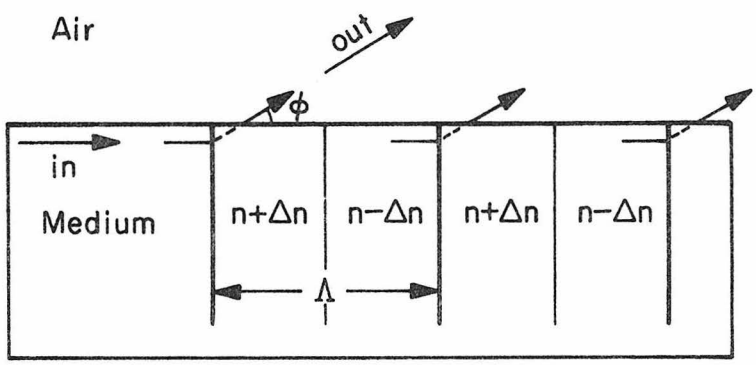

$n\Lambda - \Lambda\cos\phi = \lambda$

(c)

Fig. 1.3 (a) Retroreflection (b) in-plane deflection (c) output coupling in periodic waveguides.

reflection, large-angle deflection, and broadside coupling. In the former case, the distributed feedback (DFB) [13,14] or Bragg reflector (BR) [15,16] GaAs lasers and narrow band filters [17] are important applications of these waveguides. Such lasers eliminate the need for terminating the laser cavity at one of the cleavage planes of the GaAs substrate, and thus they become the only laser structures which can be incorporated with other optical components into thin-film waveguides. The corrugations (or gratings) also provide wavelength selectivity and stability for such lasers.

As can be seen from the above survey, periodic waveguides play an important role in a number of applications of guided wave optics. It is the purpose of part of this work to explore the possibility of using the electrooptic effect in corrugated waveguides and thus make their valuable operations electrically controllable. The new optical devices using the above idea are air-side scanners, large-angle switches, and tunable filters as sketched in Fig. 1.4. Large-angle switches have been studied by Kotani and coworkers [18]. A switch between two optical channels which have an angular separation up to 10° has been achieved in their work. In tunable filters, the spectral tunability is proportional to the electro-optic index change. The tuning range of these filters is considerably smaller than that which can be obtained from another electrooptic device [19] which uses a directional coupler. We will concentrate on air-side scanners and present the result in Chapter 3.

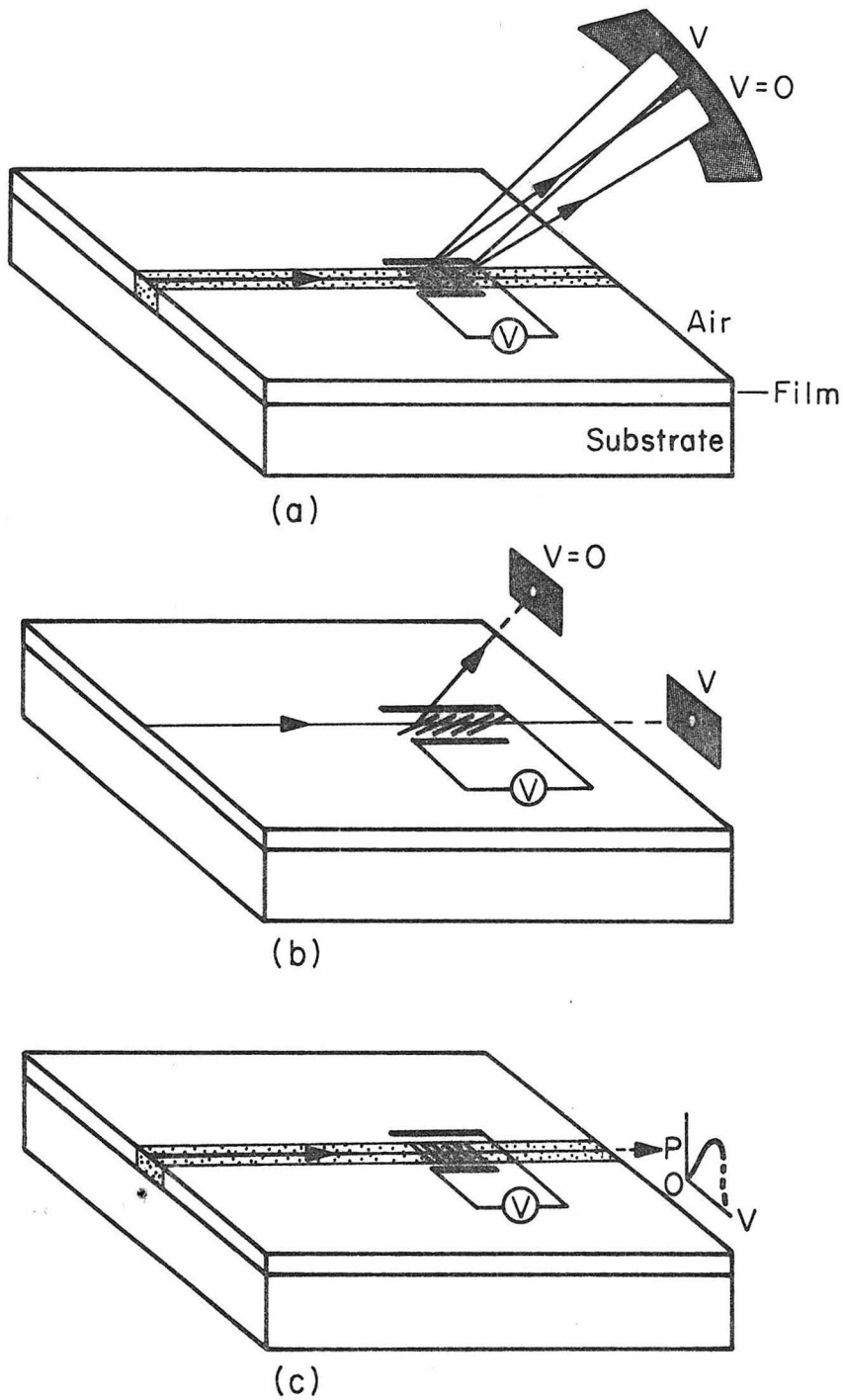

Fig. 1.4 Schematic diagram of (a) a beam scanner (b) a large-angle switch (c) a modulator / tunable filter.

1.3 Applications of Chirped Gratings

In a fiber communications system it is likely that optical carriers of several wavelengths will be multiplexed into a single fiber to increase its information carrying capability. Optical devices which are compatible with such a wide-band operation as wavelength multiplexing, demultiplexing, or broad-band filtering are thus necessary. These can be accomplished by a "chirped" grating. A chirped grating has a monotonic variation in period along the grating length so that each portion of the length responds to one wavelength. Before describing this aspect of applications, let us review some of the previous uses of chirped gratings.

A chirped grating zone plate can be used to compress a laser pulse [20]. In Fig. 1.5a a rapidly rotating plane mirror scans the incoming pulse across the whole plate. The diffracted waves which have a tendency to focus can be made to arrive at the focal point at approximately the same time by matching the rotational motion of the mirror with the traveling times of various portions of the pulse. Thus, the pulse is compressed. A chirped grating corrugation has also been used to reflect surface acoustic waves in which the round-trip traveling distance or delay of a wave is proportional to its wavelength [21]. Such a dispersive delay line (Fig. 1.5b) can be used to compress a frequency modulated (FM) pulse signal which is applied to the input transducer. In the optical regime, a similar delay line to Fig. 1.5b is no longer practical for compressing an FM optical pulse due to the extremely small amount of delay which can be obtained by light in a 1 cm length of waveguide. However, several other interesting applications which use

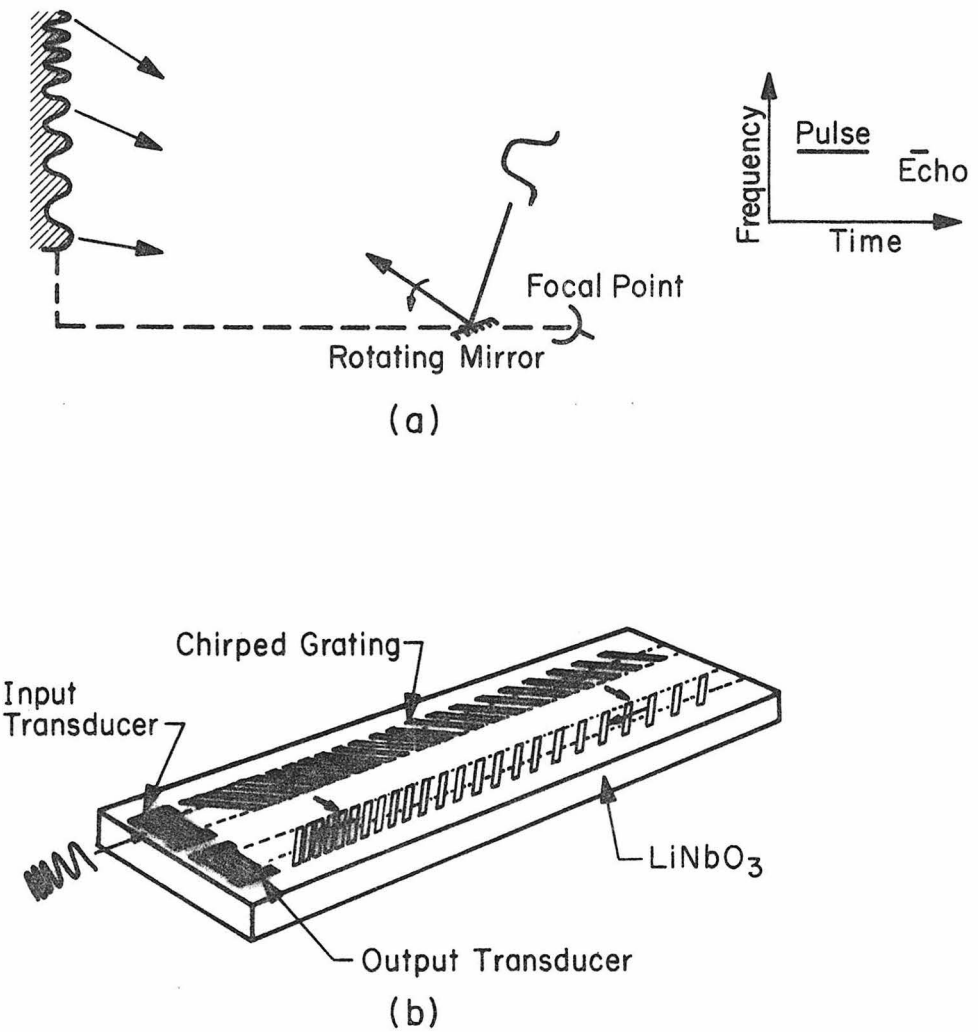

Fig. 1.5 Schematic diagram of (a) a laser pulse compressor (After [20]) (b) an acoustic wave pulse compressor (After [21]).

chirped gratings on top of the waveguides have been proposed and developed. For example, some possible structures for light focusing are shown in Fig. 1.6. Assume we can divide the length of our chirped grating into N subgratings which have uniform periods of $\Lambda_1, \Lambda_2, \cdots, \Lambda_N$. Then the prediction of focusing simply follows the Bragg diffraction, since each subgrating diffracts along a different direction. Both processes have been demonstrated in glass waveguides [22,23]. Their practical applications are illustrated in Fig. 1.7a and b which are a diode laser-waveguide coupler and a radio-frequency spectrum analyzer [24], respectively. In the latter case we present a chirped-grating lens in comparison with Luneburg [25], geodesic [26], and Fresnel [27] lenses.

As mentioned earlier, the main purpose of this investigation on chirped gratings is to demonstrate optical broad-band devices. Bearing this in mind, we propose a couple of ideas as sketched in Fig. 1.8a and b. They are broad-band optical filters and wavelength demultiplexers, respectively. The principles of these devices can easily be seen from the illustrations. Details of these devices will be given in Chapter 4. A possible application of the wavelength demultiplexer is depicted in Fig. 1.8c.

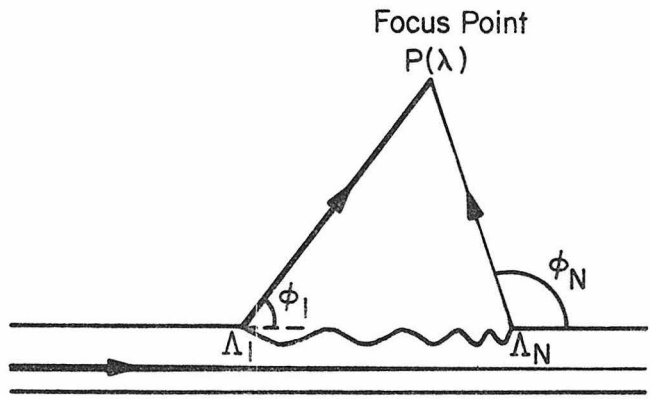

$$\cos \phi_i = n_{eff} - \frac{\lambda}{\Lambda_i}, \quad i = 1, \cdots, N$$

(a)

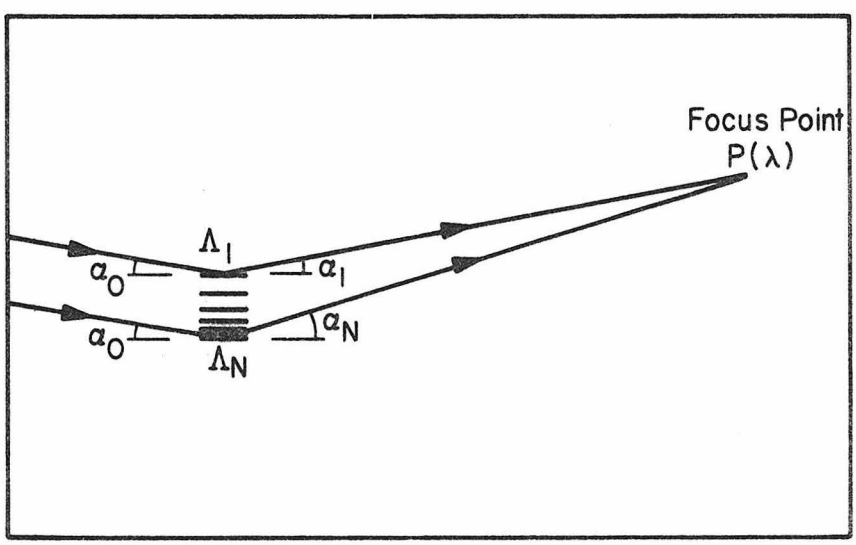

$$\sin \alpha_0 + \sin \alpha_i = \frac{\lambda}{n_{eff}\, \Lambda_i}, \quad i = 1, \cdots, N$$

(b)

Fig. 1.6 Schematic diagram of (a) a focusing grating coupler (b) a grating lens.

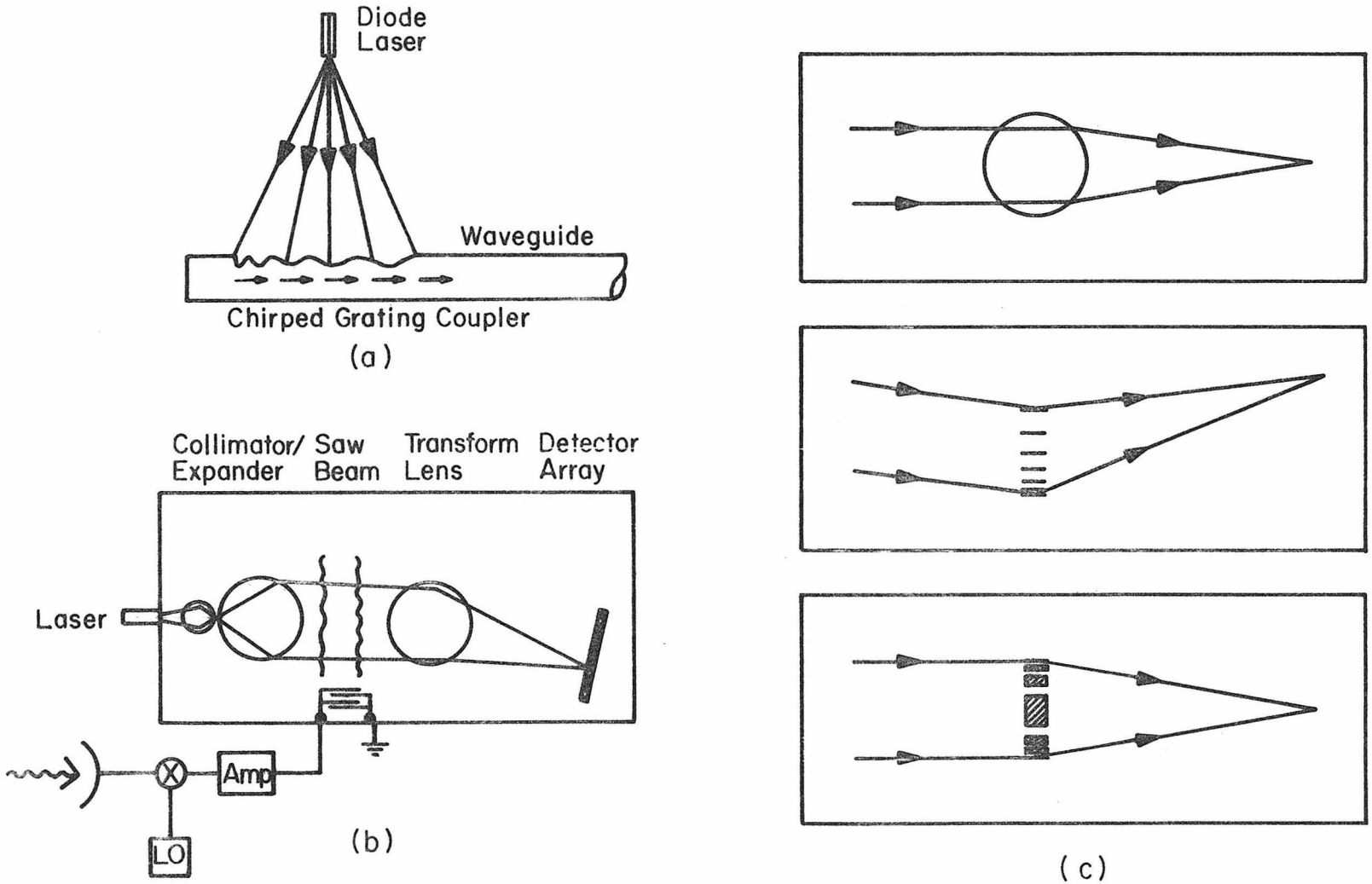

Fig. 1.7 Schematic diagram of (a) a diode laser - waveguide coupler (b) a radio-frequency spectrum analyzer (After [24]) (c) different lens structures used in (b).

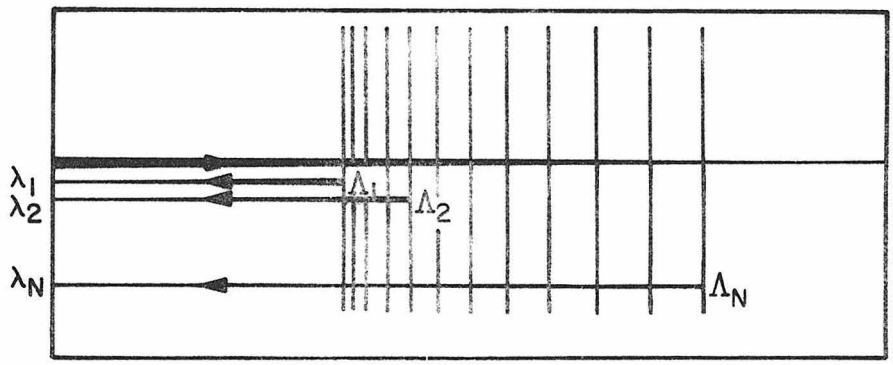

(a) $\lambda_i = 2n_{eff}\Lambda_i, i=1,2,\cdots N$

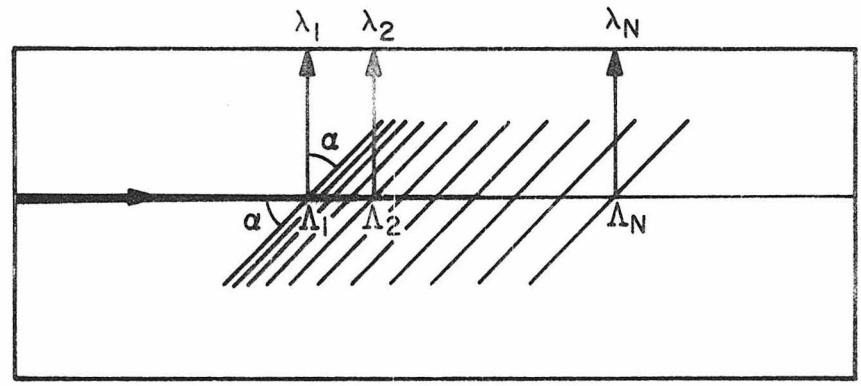

(b) $\lambda_i = 2n_{eff}\Lambda_i \sin\alpha,\ i=1,2,\cdots N$

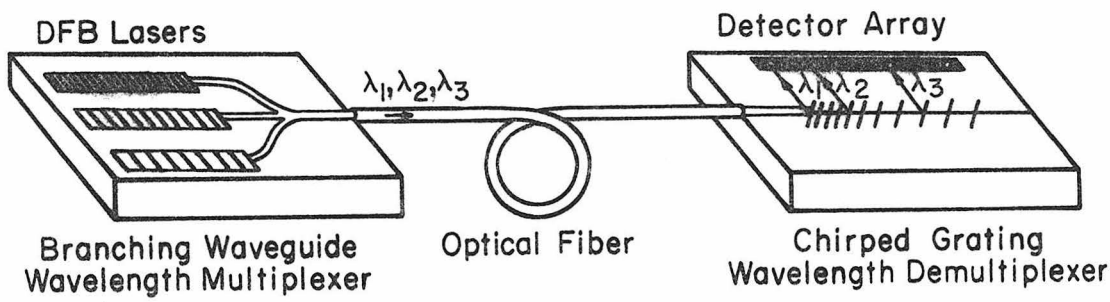

(c)

Fig. 1.8 Schematic diagram of (a) a broad-band optical filter (b) a wavelength demultiplexer (c) a wavelength multiplexing and demultiplexing structure.

Chapter 1 - References

1. N. Niizeki, "Single mode fiber at zero-dispersion wavelength," Topical Meeting on Integrated and Guided Wave Optics, Paper MB1, Salt Lake City, Utah, 1978.
2. See, for example, A. Yariv, Quantum Electronics, 2nd ed. (Wiley, New York, 1975), Chapter 19.
3. S. E. Miller, "Integrated optics: an introduction," Bell Syst. Tech. J. 48, 2059 (1969).
4. A. Yariv, "Active integrated optics," in the Esfahan Symposium on Fundamental and Applied Laser Physics, Esfahan, Iran, 1971 (published by MIT Press).
5. P. K. Tien, "Light waves in thin films and integrated optics," Appl. Optics 10, 2395 (1971).
6. A. Yariv, "Components for integrated optics," Laser Focus 8, 40 (1972).
7. P. K. Tien, "Integrated optics and new wave phenomena," Rev. Mod. Phys. 49, 361 (1977).
8. H. Yajima, S. Kawase, and Y. Sekimoto, "Amplification at 1.06 μm using a Nd:glass thin-film waveguide," Appl. Phys. Lett. 21, 407 (1972).
9. A. Yariv and M. Nakamura, "Periodic structures for integrated optics," IEEE J. Quant. Electron. QE-13, 233 (1977).
10. L. Kuhn, M. L. Dakss, P. F. Heidrich, and B. A. Scott, "Deflection of an optical guided wave by a surface acoustic wave," Appl. Phys. Lett. 17, 265 (1970).

11. J. M. Hammer, D. J. Channin, and M. T. Duffy, "Fast electro-optic waveguide deflector modulator," Appl. Phys. Lett. 23, 176 (1973).

12. F. R. Gfeller and C. W. Pitt, "Collinear acousto-optic deflection in thin films," Electron. Lett. 8, 549 (1972).

13. M. Nakamura, H. W. Yen, A. Yariv, E. Garmire, S. Somekh, and H. L. Garvin, "Laser oscillation in epitaxial GaAs waveguides with corrugation feedback," Appl. Phys. Lett. 23, 224 (1973).

14. M. Nakamura, K. Aiki, J. Umeda, and A. Yariv, "CW operation of distributed feedback GaAs-GaAlAs diode lasers at temperatures up to 300°K," Appl. Phys. Lett. 27, 403 (1975).

15. F. K. Reinhart, R. A. Logan, and C. V. Shank, "GaAs-$Al_xGa_{1-x}As$ injection lasers with distributed Bragg reflectors," Appl. Phys. Lett. 27, 45 (1975).

16. W. Ng and A. Yariv, "Highly collimated broadside emission from room-temperature GaAs distributed Bragg reflector lasers," Appl. Phys. Lett. 31, 613 (1977).

17. D. C. Flanders, H. Kogelnik, R. V. Schmidt, and C. V. Shank, "Grating filters for thin-film optical waveguides," Appl. Phys. Lett. 24, 194 (1974).

18. H. Kotani, M. Kubota, M. Kawabe, S. Namba, and K. Masuda, "Bragg-deflection modulators in corrugated $LiNbO_3$ waveguides," 1977 International Conference on Integrated Optics and Optical Fiber Communication, Paper A11-1, Tokyo, Japan, 1977.

19. R. C. Alferness and R. V. Schmidt, "Tunable optical waveguide directional coupler filter," Topical Meeting on Integrated and Guided Wave Optics, Paper TuA3, Salt Lake City, Utah, 1978.

20. W. E. Kock, "Pulse compression with periodic gratings and zone plate gratings," Proc. IEEE (Lett.) 58, 1395 (1970).

21. R. C. Williamson and H. I. Smith, "The use of surface-elastic-wave reflection gratings in large time-bandwidth pulse-compression filters," IEEE Trans. Microwave Theory Tech. MTT-21, 195 (1973).

22. A. Katzir, A. C. Livanos, and A. Yariv, "Chirped-grating output couplers in dielectric waveguides," Appl. Phys. Lett. 30, 225 (1977).

23. S. K. Yao, private communication; G. Hatakoshi and S. Tanaka, "Grating lenses for integrated optics," Opt. Lett. 2, 142 (1978).

24. M. C. Hamilton, D. A. Wille, and W. J. Miceli, "An integrated optical RF spectrum analyzer," 1976 IEEE Ultrasonics Symposium, Paper BB-3, Annapolis, Maryland, 1976.

25. F. Zernike, "Luneburg lens for optical waveguide use," Opt. Commun. 12, 379 (1974).

26. E. Spiller and J. S. Harper, "High resolution lenses for optical waveguides," Appl. Opt. 13, 2105 (1974).

27. P. R. Ashley and W.S.C. Chang, "Fresnel lens in thin film waveguides," Topical Meeting on Integrated and Guided Wave Optics, Paper MA3, Salt Lake City, Utah, 1978.

Chapter 2

THEORY OF CORRUGATED WAVEGUIDES

2.1 Introduction

The phenomenon of wave propagation in periodic structures is of long standing research interest in many branches of physics and technology. In integrated optics, periodic structures such as corrugated waveguides have been used in a variety of applications (see Fig. 2.1). Some of the devices making use of these corrugated waveguides include reflectors, filters, distributed feedback (DFB) lasers, Bragg reflector (BR) lasers, and input and output waveguide couplers.

This chapter attempts to describe the theory and principle of those corrugated waveguide devices with an effort devoted to bringing out the underlying concepts and introducing the theoretical background for my experimental work. Both a coupled-mode formalism and a zig-zag ray picture are used to analyze problems such as reflection and output coupling. The parameters which are used to characterize the processes are derived.

2.2 Optical Waveguide Modes

Before giving an analysis of corrugated waveguide devices, it is important to understand the basic modes which can be supported in an uncorrugated waveguide [1]. A planar thin-film waveguide is sketched in Fig. 2.2a. It consists of a film of thickness t and index of refraction n_2 sandwiched between two media with indices n_1 and n_3. We are interested in finding the electromagnetic modes which propagate along the waveguide axis.

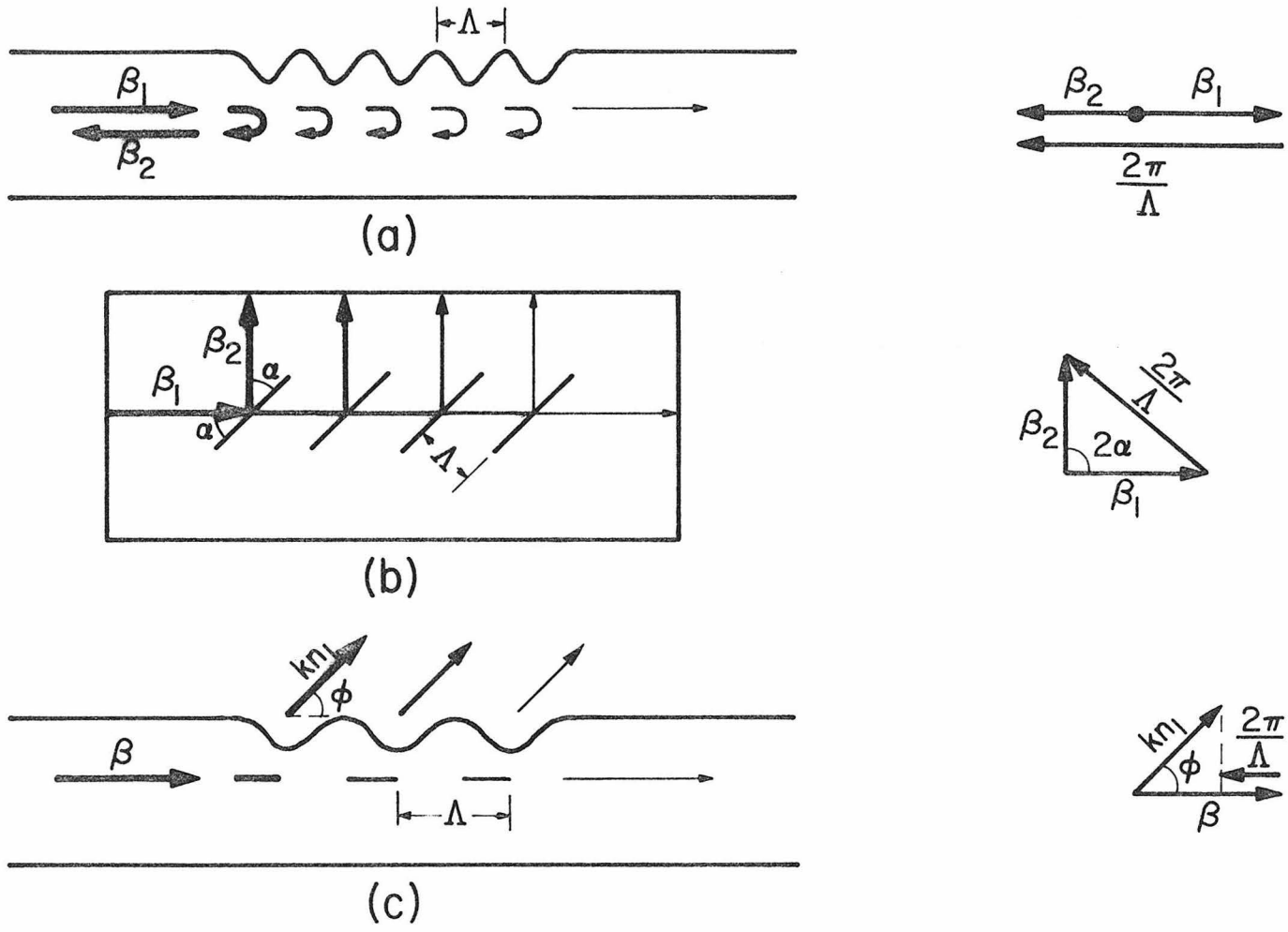

Fig. 2.1 Uses of corrugated waveguides for (a) reflection (b) deflection (c) coupling.

The structure has the transverse index profile

$$n(x) = \begin{cases} n_1 & x > 0 \\ n_2 & -t < x < 0 \\ n_3 & x < -t \end{cases} \tag{2.1}$$

with $n_2 > n_3 \geq n_1$ and $\partial/\partial y = 0$. Using a plane wave analysis, the electric and magnetic fields in each medium obey the equations (see Appendix A)

$$(\nabla^2 + k^2 n_i^2)\, \vec{E}(\vec{r}) = 0 \tag{2.2}$$

$$(\nabla^2 + k^2 n_i^2)\, \vec{H}(\vec{r}) = 0 \ , \quad i=1,2, \text{ or } 3 \tag{2.3}$$

where $k = 2\pi/\lambda$ and λ is the vacuum wavelength. The solutions are subject to the continuity of the tangential components of $\vec{E}$ and $\vec{H}$ at the dielectric interfaces. By matching these boundary conditions, there exist two independent sets of solutions : TE modes with field components E_y, H_z, and H_x, and TM modes with components H_y, E_z, and E_x.

(a) TE modes

Putting $\partial/\partial y = 0$ in (2.2), and taking the form of the field E_y as

$$E_y(\vec{r}) = f(x)\, e^{i\beta z} \tag{2.4}$$

we obtain

$$\left[\frac{d^2}{dx^2} + k^2 n_i^2 - \beta^2\right] f(x) = 0 \tag{2.5}$$

H_z and H_x can be expressed in terms of E_y:

$$H_z = \frac{-i}{\omega\mu_o} \frac{\partial E_y}{\partial x} \propto \frac{df}{dx}$$

and

$$H_x = \frac{i}{\omega\mu_o} \frac{\partial E_y}{\partial z} = \frac{-\beta}{\omega\mu_o} E_y$$

The boundary conditions require that f and df/dx be continuous.

Before embarking on a formal solution of (2.5), it is useful to consider some of physical nature of the solutions by simple arguments. Let us consider the character of the solutions as a function of the propagation constant β at a fixed wavelength λ. For $\beta > kn_2$, it follows directly from (2.5) that f(x) is exponential in all three regions of the waveguide. Because of the need to match both f(x) and its derivative at the two interfaces, the resulting field increases without bound in region 3 if it is evanescent in region 1, and vice versa. Such a mode cannot exist. For $kn_3 < \beta < kn_2$, f(x) is sinusoidal in region 2, but is exponential in regions 1 and 3. This makes it possible to have a solution that satisfies the boundary conditions while being evanescent in both regions 1 and 3. The energy carried by these modes is thus confined to the vicinity of the thin film; consequently, we will refer to them as confined or guided modes. Solutions for $kn_1 < \beta < kn_3$ correspond to evanescent behavior in region 1 and to sinusoidal behavior in regions 2 and 3. We will refer to these modes as substrate radiation modes. For $0 < \beta < kn_1$, the solution becomes sinusoidal in all three regions. These are the radiation modes of the waveguide. The guided modes have discrete β values while the β values of the radiation modes form a continuum. The guided and radiation modes comprise a complete set of solutions.

We are now ready to derive the formal solutions for the waveguide

structure shown in Fig. 2.2a. We limit our derivation to the confined modes, namely the modes which have propagation constants β satisfying $kn_3 < \beta < kn_2$. In this case $f(x)$ is taken as

$$f(x) = \begin{cases} A\, e^{-qx} & x > 0 \\ A(\cos hx - \frac{q}{h} \sin hx) & -t < x < 0 \\ A(\cos ht + \frac{q}{h} \sin ht)\, e^{p(x+t)} & x < -t \end{cases} \tag{2.6}$$

where

$$h = \sqrt{k^2 n_2^2 - \beta^2}$$

$$p = \sqrt{\beta^2 - k^2 n_3^2} \tag{2.7}$$

$$q = \sqrt{\beta^2 - k^2 n_1^2}$$

The continuity conditions lead to the eigenvalue equation

$$\tan ht = \frac{h(p+q)}{h^2 - pq} \tag{2.8}$$

or

$$ht - \psi - \phi = m\pi \quad , \qquad m=0,1,2,\cdots \tag{2.9}$$

where

$$\psi = \tan^{-1} \frac{p}{h}$$

and (2.10)

$$\phi = \tan^{-1} \frac{q}{h}$$

The last equation, in conjunction with (2.7), is used to determine the eigenvalues β which are discrete: β_m. Typical field distributions for the lower order modes are shown in Fig. 2.2b.

Because of the use of plane waves and the assumption of $\partial/\partial y = 0$, a mode power is defined as an energy flow per unit time through an area

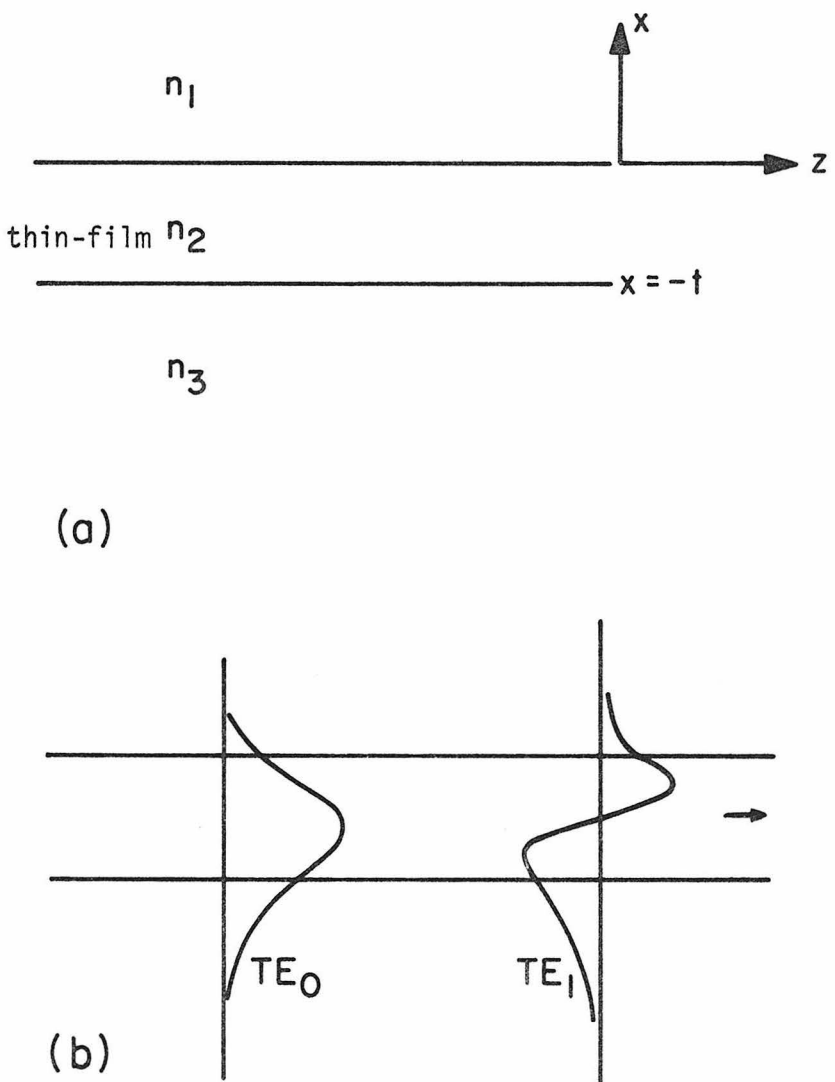

Fig. 2.2 (a) Structure of a planar ($\frac{\partial}{\partial y} = 0$) thin-film waveguide. $n_2 > n_3 \geq n_1$.
(b) Typical field distributions for the first two order confined modes.

with a unit length in the y direction, i.e.,

$$\text{Power flow} = -\frac{1}{2}\int \text{Re}(E_y H_x^*)\, dx$$

$$= \frac{\beta}{2\omega\mu_o}\int |E_y|^2\, dx$$

$$= \frac{\beta}{2\omega\mu_o}\int [f(x)]^2\, dx, \text{ assuming } f(x) \text{ is real} \qquad (2.11)$$

The above integration can be simplified by using a convenient representation for f(x). Using (2.10), (2.6) is rewritten as

$$f(x) = \begin{cases} C\cos\phi\, e^{-qx} & x > 0 \\ C\cos(hx+\phi) & -t < x < 0 \\ C(-1)^m \cos\psi\, e^{p(x+t)} & x < -t \end{cases} \qquad (2.12)$$

After a straightforward calculation,

$$\int_{-\infty}^{\infty} [f(x)]^2\, dx = \frac{C^2}{2}\left(t + \frac{1}{p} + \frac{1}{q}\right) \qquad (2.13)$$

If we define

$$\beta \equiv k n_{eff} \qquad (2.14)$$

where n_{eff} is referred to as the effective index of refraction of the waveguide, then

$$\text{Power flow} = \frac{\varepsilon_o n_{eff} c}{2}\,\frac{C^2}{2}\left(t + \frac{1}{p} + \frac{1}{q}\right)$$

$$= \left(\frac{\varepsilon_o n_{eff}^2}{2}\,\frac{C^2}{2}\right)\left(\frac{c}{n_{eff}}\right)(t_{eff}) \qquad (2.15)$$

= (average energy density)(velocity)(effective cross section)

According to the above interpretation, we define the effective thickness of the waveguide by

$$t_{eff} \equiv t + \frac{1}{p} + \frac{1}{q} \tag{2.16}$$

which is the geometrical film thickness plus the evanescent distances in both cladding media.

The constant C can be normalized in a manner so that Power flow = 1 unit, or

$$\frac{\beta}{2\omega\mu_o} \int_{-\infty}^{\infty} [f(x)]^2 \, dx = 1 \tag{2.17}$$

$$C = 2\sqrt{\frac{\omega\mu_o}{\beta t_{eff}}} \tag{2.18}$$

The orthogonality can be derived directly form (2.5). The result is

$$(\beta_m^2 - \beta_{m'}^2) \int_{-\infty}^{\infty} f_{m'} f_m dx = 0$$

i.e.,

$$\int_{-\infty}^{\infty} f_{m'} f_m dx = 0 \qquad m' \neq m \tag{2.19}$$

Combining with (2.17) we obtain

$$\int_{-\infty}^{\infty} f_{m'} f_m dx = \frac{2\omega\mu_o}{\beta_m} \delta_{m'm} \tag{2.20}$$

(b) TM modes

The field components are

$$H_y = g(x)\, e^{i\beta z}$$

$$E_z = \frac{i}{\omega\varepsilon_o}\,\frac{1}{n^2(x)}\,\frac{\partial H_y}{\partial x} \propto \frac{1}{n^2(x)}\,\frac{dg}{dx} \tag{2.21}$$

$$E_x = \frac{-i}{\omega\varepsilon_o}\,\frac{1}{n^2(x)}\,\frac{\partial H_y}{\partial t} = \frac{\beta}{\omega\varepsilon_o}\,\frac{H_y}{n^2(x)}$$

For confined modes g(x) is taken as

$$g(x) = \begin{cases} A\, e^{-qx} & x > 0 \\ A\left(\cos hx - \dfrac{q}{h}\,\dfrac{n_2^2}{n_1^2}\sin hx\right) & -t < x < 0 \\ A\left(\cos ht + \dfrac{q}{h}\,\dfrac{n_2^2}{n_1^2}\sin ht\right) e^{p(x+t)} & x < -t \end{cases} \tag{2.22}$$

where h, p, and q have the same expressions as in (2.7). Similarly, the continuity requirement gives an eigenvalue equation which can be reduced to the same form as (2.8) by defining

$$\bar{p} \equiv \frac{n_2^2}{n_3^2}\,p \qquad \text{and} \qquad \bar{q} \equiv \frac{n_2^2}{n_1^2}\,q \tag{2.23}$$

and has the form

$$\tan ht = \frac{h(\bar{p} + \bar{q})}{h^2 - \bar{p}\,\bar{q}} \tag{2.24}$$

The expressions of ψ and ϕ for TM modes are obtained by replacing p and q by $\bar{p}$ and $\bar{q}$; (2.9) and (2.12) are still formally true for TM modes.

$$\text{Power flow} = \frac{1}{2}\int \mathrm{Re}(E_x H_y^*)\, dx$$

$$= \frac{\beta}{2\omega\varepsilon_o}\int \frac{|H_y|^2}{n^2(x)}\, dx$$

$$= \frac{\beta}{2\omega\varepsilon_o}\int \frac{[g(x)]^2}{n^2(x)}\, dx, \quad \text{assuming } g(x) \text{ is real} \tag{2.25}$$

and

$$\int_{-\infty}^{\infty} \frac{[g(x)]^2}{n^2(x)}\, dx = \frac{C^2}{2}\left[\frac{t}{n_2^2} + \frac{1}{n_{3p}^2}\,\frac{1+\frac{p^2}{h^2}}{1+\frac{\bar{p}^2}{h^2}} + \frac{1}{n_{1q}^2}\,\frac{1+\frac{q^2}{h^2}}{1+\frac{\bar{q}^2}{h^2}}\right] \tag{2.26}$$

The corresponding formula to (2.15) is

$$\text{Power flow} = \frac{\mu_o n_{eff} c}{2}\,\frac{C^2}{2}\,[\cdots]$$

$$= \left(\frac{\mu_o}{2}\,\frac{C^2}{2}\right)\left(\frac{c}{n_{eff}}\right)(t_{eff}) \tag{2.27}$$

which leads to

$$t_{eff} \equiv n_{eff}^2\,[\cdots] \tag{2.28}$$

We can also establish the orthonormality for TM modes:

$$\int_{-\infty}^{\infty} \frac{g_{m'} g_m}{n^2}\, dx = \frac{2\omega\varepsilon_o}{\beta_m}\,\delta_{m'm} \tag{2.29}$$

A plot of the waveguide dispersion (β/k vs t) for TE and TM modes is shown in Fig. 2.3.

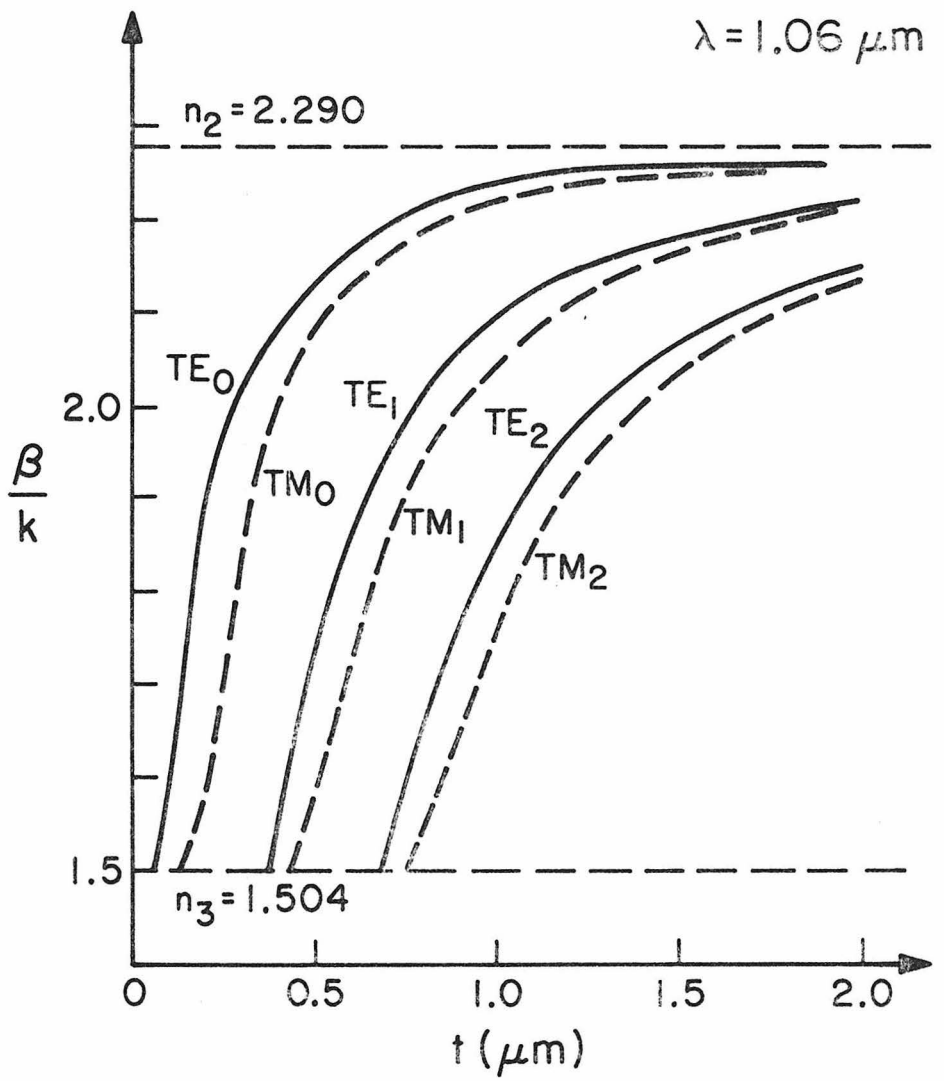

Fig. 2.3 Dispersion curves (β/k vs t) for the confined modes in a dielectric waveguide. $n_1 = 1$.

2.3 Coupled-Mode Formalism for Corrugated Waveguides

Electromagnetic wave propagation in periodic structures has been studied in a variety of applications [2]. One of the most common methods used in solving these problems is the coupled-mode formalism [3]. In this section we shall outline the procedures used in obtaining the coupled-mode equations and the coupling coefficient for a corrugated waveguide [4].

(a) Derivation of coupled-mode equations

For TE modes, E_y obeys the equation (see Appendix A)

$$\left[\frac{\partial^2}{\partial z^2} + \frac{\partial^2}{\partial x^2} + k^2 n^2(z,x)\right] E_y = 0 \tag{2.30}$$

In a corrugated waveguide as shown in Fig.2.4a, $n^2(z,x)$ can be expressed as

$$n^2(z,x) = n^2(x) + \Delta n^2(z,x) \tag{2.31}$$

with

$$n^2(x) = \begin{cases} n_1^2 & x > 0 \\ n_2^2 & -t < x < 0 \\ n_3^2 & x < -t \end{cases} \tag{2.32}$$

as the squared index function of the uncorrugated waveguide, and

$$\Delta n^2(z,x) = \begin{cases} n_1^2 - n_2^2 & \text{in the corrugation} \\ 0 & \text{elsewhere} \end{cases} \tag{2.33}$$

In general, the corrugation has a profile $x = p(z)$. We will use, instead, the width function $z = w(x)$, which is the inverse of the profile

function, and define the single-valued function $w_1(x)$ and $w_2(x)$ as shown in Fig. 2.4a. Since the corrugation is periodic in z, we can expand $\Delta n^2(z,x)$ as a Fourier series

$$\Delta n^2(z,x) = \begin{cases} (n_1^2 - n_2^2) \sum_{\ell} a_\ell(x)\, e^{-i\ell \frac{2\pi}{\Lambda} z} & -d < x < 0 \\ 0 & \text{elsewhere} \end{cases} \tag{2.34}$$

(In this expression, a positive ℓ indicates that the grating will retard the +z wave vector by an amount of $\ell \frac{2\pi}{\Lambda}$; Λ is the period of the grating) where the Fourier coefficient $a_\ell(x)$ is

$$a_\ell(x) = \frac{1}{\Lambda} \int_{w_1(x)}^{w_2(x)} e^{i\ell \frac{2\pi}{\Lambda} z}\, dz \tag{2.35}$$

Hence

$$a_0(x) = \frac{w_2(x) - w_1(x)}{\Lambda}$$

and

$$a_{\ell\neq 0}(x) = \frac{e^{i\ell \frac{2\pi}{\Lambda} w_2(x)} - e^{i\ell \frac{2\pi}{\Lambda} w_1(x)}}{2i\, \ell\pi} \tag{2.36}$$

After replacing $n^2(z,x)$ in (2.30) by (2.31), (2.30) becomes

$$\left[\frac{\partial^2}{\partial z^2} + \frac{\partial^2}{\partial x^2} + k^2 n^2(x)\right] E_y = -k^2\, \Delta n^2(z,x)\, E_y \tag{2.37}$$

The field of the corrugated waveguide can be expanded in terms of the modes of the uncorrugated smooth waveguide

$$E_y = \frac{1}{2} \sum_m A_m(z)\, e^{i\beta_m z}\, f_m(x) + \text{complex conjugate} \tag{2.38}$$

For simplicity we limit ourselves to the case of coupling between the positive and negative going modes with the same propagation constant

$$E_y = \frac{1}{2}\underbrace{[A(z)e^{i\beta z} + B(z)e^{-i\beta z}]}_{E(z)} f(x) + c.c. \tag{2.39}$$

with f(x) satisfying (2.5). Substituting (2.34) and (2.39) into (2.37) and using the slow-varying approximations

$$\left|\frac{d^2A}{dz^2}\right| << \beta\left|\frac{dA}{dz}\right| \qquad \text{and} \qquad \left|\frac{d^2B}{dz^2}\right| << \beta\left|\frac{dB}{dz}\right|$$

we obtain

$$\begin{cases} \dfrac{dB}{dz} = K\,A\,e^{i2\Delta\beta z} \\ \dfrac{dA}{dz} = K^*B\,e^{-i2\Delta\beta z} \end{cases} \tag{2.40}$$

They are the coupled-mode equations, where

$$\Delta\beta = \beta - \ell\frac{\pi}{\Lambda} \tag{2.41}$$

which is a phase mismatch factor, and

$$K = \frac{ik^2}{2\beta}\frac{(n_2^2 - n_1^2)\langle f|a_\ell(x)|f\rangle}{\langle f|f\rangle} \tag{2.42}$$

which is the coupling coefficient. The Dirac bracket in (2.42) means an integral over all x.

It can easily be proved from (2.40) that $\frac{d}{dz}(|A(z)|^2 - |B(z)|^2) = 0$ which describes the conservation of energy in this contradirectional coupling process.

For TM modes, the results are presented in Appendix B.

(b) Calculation of the coupling coefficient

The coupling coefficient, which is defined in (2.42), is an important parameter in estimating the strength of coupling. The expressions for some interesting special corrugation profiles are calculated directly.

For a rectangular profile, $w_1(x) = -w/2$, $w_2(x) = w/2$, and

$$a_{\ell\neq 0}(x) = \frac{\sin(\ell\pi w/\Lambda)}{\ell\pi}$$

$$K = \frac{ik^2}{2\beta} \frac{\sin \frac{\ell\pi w}{\Lambda}}{\ell\pi} \frac{(n_2^2 - n_1^2) \int_{-d}^{0} [f(x)]^2 \, dx}{\int_{-\infty}^{\infty} [f(x)]^2 \, dx}$$

$$= \frac{i \sin \frac{\ell\pi w}{\Lambda}}{\ell\pi} \frac{h^2 d}{\beta t_{eff}} [1 + qd - \tfrac{1}{3}(h^2 - q^2) d^2 - \cdots] \qquad (2.43)$$

where t_{eff}, h, and q were defined previously in (2.16) and (2. 7). Note that K = 0 for $\ell w/\Lambda$ = integer.

For a square profile, which is a special case of $w = \Lambda/2$,

$$K = 0 \quad \text{for} \quad \ell = \text{even}$$

$$K = \frac{(-1)^{\frac{\ell-1}{2}} i}{\ell\pi} \frac{h^2 d}{\beta t_{eff}} [1 + qd - \tfrac{1}{3}(h^2 - q^2) d^2 - \cdots], \quad \ell = 1, 3, \cdots \qquad (2.44)$$

For a sinusoidal profile, $w_2(x) = \frac{\Lambda}{2\pi} \cos^{-1}(-1 - \frac{2x}{d})$, $w_1(x) = -w_2(x)$, and

$$a_{\ell\neq 0}(x) = \frac{\sin[\ell \cos^{-1}(-1 - \frac{2x}{d})]}{\ell\pi}$$

$$K = \frac{ik^2}{2\beta}\frac{1}{\ell\pi}\,\frac{(n_2^2 - n_1^2)\int_{-d}^{0} \sin[\ell \cos^{-1}(-1 - \frac{2x}{d})][f(x)]^2\,dx}{\int_{-\infty}^{\infty}[f(x)]^2\,dx}$$

$$= i\,\frac{h^2 d}{4\beta t_{eff}}\,[1 + \cdots], \qquad \text{for } \ell = 1 \tag{2.45}$$

In the above calculation, the full guide thickness was employed to compute the unperturbed mode field f(x), but, as shown in [5], this could lead to overestimates of the coupling coefficient. The optimal unperturbed mode is that of a relevant four-layer structure. However, Streifer et al. [6] found that one could obtain adequate accuracy without excessive complexity by judiciously choosing the unperturbed guide boundary. They chose t' such that the volume of n_1 material extending into region 2 just equalled the volume of n_2 material extending into region 1, as shown in Fig. 2.4b, i.e.,

$$\Delta n^2(z,x) = \begin{cases} n_1^2 - n_2^2 & \text{in area A} \\ n_2^2 - n_1^2 & \text{in area B, area A = area B} \end{cases} \tag{2.46}$$

In this modification the single-valued width functions are $w_1(x)$, $w_2(x)$, $w_3(x)$, and $w_4(x)$. The Fourier expansion of $\Delta n^2(z,x)$ is

$$\Delta n^2(z,x) = \begin{cases} (n_2^2 - n_1^2)\sum_{\ell} a_\ell(x)\, e^{-i\ell\frac{2\pi}{\Lambda}z} & -d_2 < x < d_1 \\ 0 & \text{elsewhere} \end{cases} \tag{2.47}$$

with $$a_0(x) = -\frac{w_2(x) - w_1(x)}{\Lambda}$$

$$a_{\ell\neq 0}(x) = -\frac{e^{i\ell\frac{2\pi}{\Lambda}w_2(x)} - e^{i\ell\frac{2\pi}{\Lambda}w_1(x)}}{2i\ell\pi} \qquad -d_2 < x < 0$$

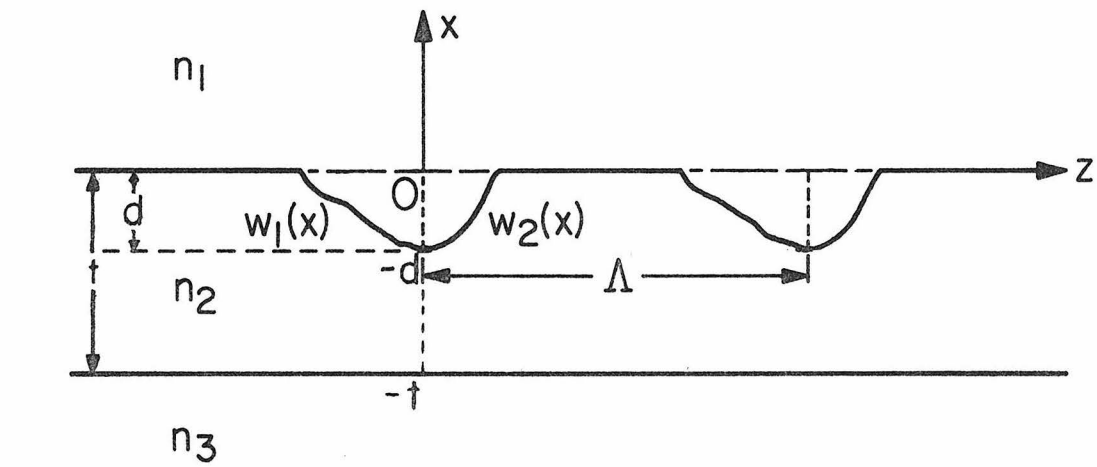

(a)

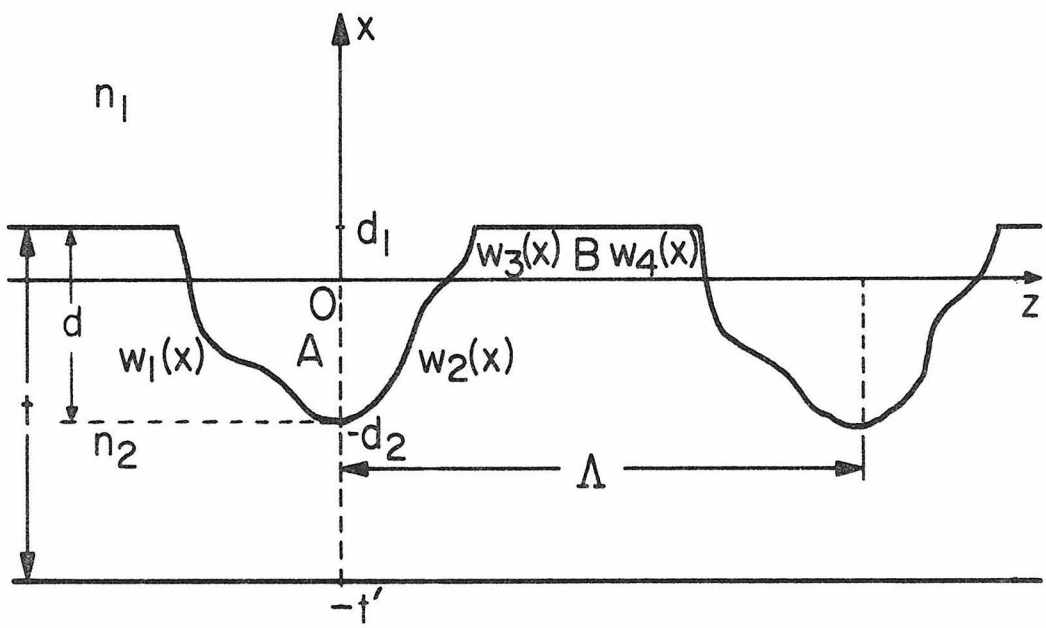

n3

(b)

Fig. 2.4 Definition of single-valued width functions $w_i(x)$ which describe the corrugation profile. In (b), x=0 is determined by equalizing areas A and B.

and $$a_0(x) = \frac{w_4(x) - w_3(x)}{\Lambda} \tag{2.48}$$

$$a_{\ell\neq 0}(x) = \frac{e^{i\ell\frac{2\pi}{\Lambda}w_4(x)} - e^{i\ell\frac{2\pi}{\Lambda}w_3(x)}}{2i\ell\pi} \qquad 0 < x < d_1$$

The corresponding coupling coefficient is

$$K = \frac{-ik^2}{2\beta}\frac{(n_2^2 - n_1^2)\ \langle f|a_\ell(x)|f\rangle}{\langle f|f\rangle} \tag{2.49}$$

For a rectangular profile, $w_1(x) = -w/2$, $w_2(x) = w/2$, $w_3(x) = w/2$, $w_4(x) = \Lambda - w/2$, $d_1 = (w/\Lambda)d$, $d_2 = d - d_1 = (1 - w/\Lambda)d$, and

$$a_{\ell\neq 0}(x) = -\frac{\sin\frac{\ell\pi w}{\Lambda}}{\ell\pi}$$

$$K = \frac{ik^2}{2\beta}\ \frac{\sin\frac{\ell\pi w}{\Lambda}}{\ell\pi}\ \frac{(n_2^2 - n_1^2)\int_{-d_2}^{d_1}[f(x)]^2\,dx}{\int_{-\infty}^{\infty}[f(x)]^2\,dx}$$

$$= \frac{i\sin\frac{\ell\pi w}{\Lambda}}{\ell\pi}\ \frac{h^2 d}{\beta t_{eff}}\left[1 + (1 - \frac{2w}{\Lambda})qd - \frac{1}{3}(1 - \frac{w}{\Lambda})^3(h^2 - q^2)d^2 + \frac{2}{3}(\frac{w}{\Lambda})^3 q^2 d^2 - \cdots\right] \tag{2.50}$$

where β, h, q, and t_{eff} are quantities corresponding to the waveguide with a thickness $t - \frac{w}{\Lambda}d$. Note that $K = 0$ when $\ell w/\Lambda$ = integer. For a square profile, which is a special case of $w = \Lambda/2$

$$K = 0 \qquad \text{for} \qquad \ell = \text{even}$$

$$K = \frac{(-1)^{\frac{\ell-1}{2}}}{\ell\pi}\ i\ \frac{h^2 d}{\beta t_{eff}}\left[1 - \frac{1}{6}(h^2 - 3q^2)(\frac{d}{2})^2 - \cdots\right],\ \ell = 1,3,\cdots \tag{2.51}$$

For a sinusoidal profile, $w_2(x) = \frac{\Lambda}{2\pi} \cos^{-1}(-\frac{2x}{d})$, $w_1 = -w_2(x)$, $w_3(x) = \frac{\Lambda}{2\pi} \cos^{-1}(-\frac{2x}{d})$, $w_4(x) = \Lambda - w_3(x)$, $d_1 = d_2 = d/2$, and

$$a_{\ell\neq 0}(x) = -\frac{\sin[\ell \cos^{-1}(-2x/d)]}{\ell\pi}$$

$$K = \frac{ik^2}{2\beta} \frac{1}{\ell\pi} \frac{(n_2^2 - n_1^2) \int_{-d/2}^{d/2} \sin[\ell \cos^{-1}(-\frac{2x}{d})][f(x)]^2 \, dx}{\int_{-\infty}^{\infty} [f(x)]^2 \, dx}$$

$$= i \frac{h^2 d}{4\beta t_{eff}} [1 + \ldots] \qquad \text{for } \ell = 1 \qquad (2.52)$$

As can be seen, the improved analysis corrects second and higher order terms only.

The derivation of the coupling coefficient for a sinusoidal corrugation is easier by the method of a zig-zag ray picture which will be introduced in Section 2.6.

Alternatively, the coupling coefficients can be derived by a different approach which will help us better understand the origin of the coupling. From the coupled-mode equation (2.40), if we set $\Delta\beta = 0$, then

$$|K| = \left|\frac{1}{A} \frac{dB}{dz}\right| \qquad (2.53)$$

so physically $|K|$ is the fractional reflection of the incident amplitude per unit length in the corrugation. Let us apply this simple idea to the estimation of $|K|$ in a square corrugation. Because of waveguide dispersion (2.8), the propagation constant of the mode is β in the uncorrugated portion and is β-$\delta\beta$ in the corrugated portion of the waveguide.

Each propagation discontinuity will cause a partial reflection (i.e., coupling). Within each period we have two reflections. Although these two reflection coefficients have opposite sign, the propagation phase delay between these two reflected waves is exactly $\ell\pi$ at the Bragg wavelength ($\Delta\beta = 0$), hence they add up in phase, i.e.,

$$|K| = \frac{2|r|}{\Lambda} \tag{2.54}$$

where, to a first-order approximation,

$$|r| = \frac{\delta\beta}{2\beta}$$

Since $\Lambda = \ell\pi/\beta$, we obtain

$$|K| = \frac{\delta\beta}{\ell\pi} \tag{2.55}$$

The next step is to find a relation between $\delta\beta$ and d. From (2.8),

$$\frac{\partial\beta}{\partial t} = \frac{h^2}{\beta t_{eff}}$$

$$\delta\beta = \frac{\partial\beta}{\partial t}\, d = \frac{h^2 d}{\beta t_{eff}} \tag{2.56}$$

thus

$$|K| = \frac{h^2 d}{\ell\pi\beta t_{eff}}$$

which is exactly the same as (2.44) to the first order in d.

In some applications, a corrugated waveguide is used in the in-plane deflection of the guided beam. The magnitude of the coupling coefficient can also be estimated for this case by this simple concept.

The coupled-mode equations for this case are formally similar to those in (2.40) when a coordinate ζ (see Fig. 2.5) is used. Hence

$$|K| = \left|\frac{1}{\Lambda}\frac{dB}{d\zeta}\right| = \frac{2|r|}{\Lambda} \tag{2.57}$$

where $|r|$ is given by the Fresnel formula

$$|r| = \frac{\beta \sin\alpha - (\beta-\delta\beta)\sin(\alpha-\delta\alpha)}{\beta \sin\alpha + (\beta-\delta\beta)\sin(\alpha-\delta\alpha)}$$

To a first-order approximation,

$$|r| = \frac{\beta \cos\alpha\, \delta\alpha + \delta\beta \sin\alpha}{2\beta \sin\alpha} \tag{2.58}$$

The relation between $\delta\alpha$ and $\delta\beta$ can be derived from Snell's law: $\beta\cos\alpha = (\beta-\delta\beta)\cos(\alpha-\delta\alpha)$, and is

$$\delta\alpha = \frac{\delta\beta \cos\alpha}{\beta \sin\alpha}$$

Then (2.58) becomes

$$|r| = \frac{\delta\beta}{2\beta \sin^2\alpha} \tag{2.59}$$

The Bragg condition for this case is

$$\Lambda = \frac{\ell\pi}{\beta \sin\alpha} \tag{2.60}$$

After substituting (2.59) and (2.60) in (2.57), we obtain

$$|K| = \frac{\delta\beta}{\ell\pi \sin\alpha}$$

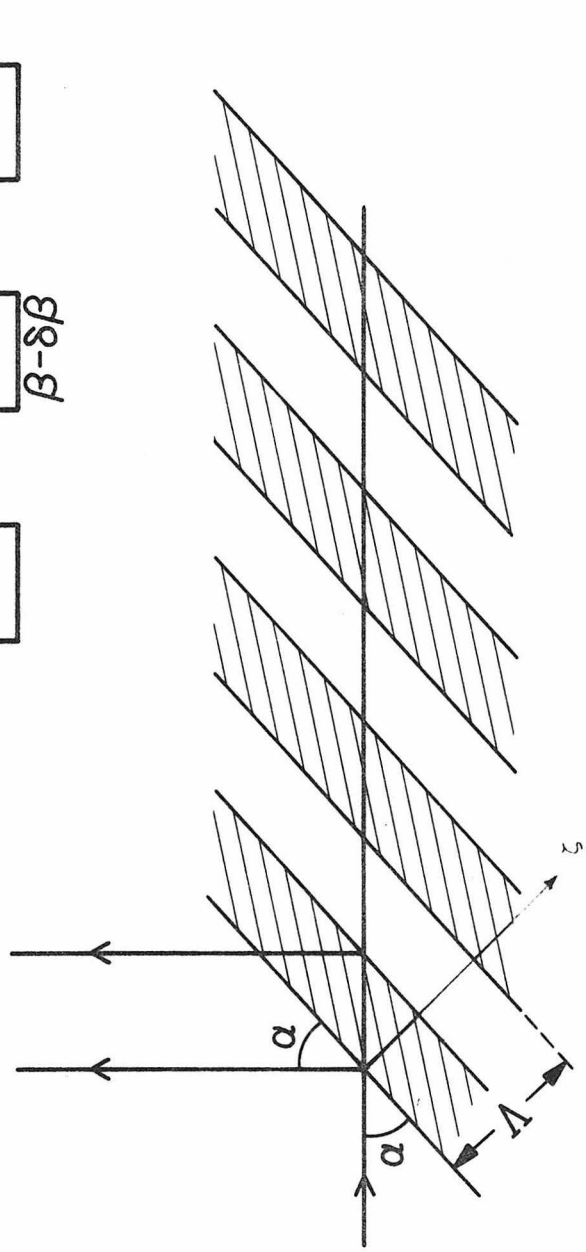

Fig. 2.5 Bragg deflection of light in a corrugated waveguide.

2.4 Solutions of the Coupled-Mode Equations

The coupled-mode equations can be solved once the boundary conditions are specified. In this derivation, the boundary values are given in a coordinate system as shown in Fig. 2.6a for a square corrugation. Compared with that used to calculate K in the last section, this coordinate is shifted by $\Lambda/2$ in the z-direction. Although the phase of K is not important (because the physically measured quantities are all related to the absolute value of K), we still prefer a mathematically proper K in our new coordinate. Hence, in what follows, K is (-1) times that obtained in the last section. For clarity, setting $\ell = 1$, and to a first-order approximation

$$K = \frac{-i}{\pi} \frac{h^2 d}{\beta t_{eff}}$$

After making the following substitutions

$$\begin{aligned} K &= -i\kappa \quad , \qquad \kappa \equiv |K| \\ A(z) &= a(z)\, e^{-i\Delta\beta z} \\ B(z) &= b(z)\, e^{i\Delta\beta z} \end{aligned} \tag{2.61}$$

the E(z) in (2.39) becomes

$$E(z) = \underbrace{a(z)\, e^{i\beta_0 z}}_{E_+(z)} + \underbrace{b(z)\, e^{-i\beta_0 z}}_{E_-(z)} \quad , \qquad \beta_0 \equiv \pi/\Lambda \tag{2.62}$$

and the coupled-mode equations in (2.40) become

$$\begin{cases} \dfrac{db}{dz} + i\Delta\beta \;\; b = -i\kappa a \\ \dfrac{da}{dz} - i\Delta\beta \;\; a = i\kappa b \end{cases} \tag{2.63}$$

Equations in (2.63) can be combined to give second-order differential equations for the incident wave a and the reflected wave b.

$$\frac{d^2b}{dz^2} - \gamma^2 b = 0 \quad , \qquad \gamma = \sqrt{\kappa^2 - (\Delta\beta)^2} \tag{2.64}$$

Boundary conditions are $b(L) = 0$ and $a(0) = 1$. Under phase-matching conditions $\Delta\beta = 0$, we obtain

$$b(z) = i\,\frac{\sinh \kappa(L-z)}{\cosh \kappa L}$$

$$a(z) = \frac{\cosh \kappa(L-z)}{\cosh \kappa L}$$

A plot of the behavior of $|a(z)|^2$ and $|b(z)|^2$ for this case is shown in Fig. 2.6b.

If $\Delta\beta \neq 0$, then

$$b(z) = \frac{i\kappa \sinh \gamma(L-z)}{\gamma \cosh \gamma L - i\Delta\beta \sinh \gamma L}$$

$$a(z) = \frac{\gamma \cosh \gamma(L-z) - i\Delta\beta \sinh \gamma(L-z)}{\gamma \cosh \gamma L - i\Delta\beta \sinh \gamma L} \tag{2.65}$$

The reflection and transmission coefficients are

$$r = \frac{E_-(0)}{E_+(0)} = b(0) = \frac{i\kappa \sinh \gamma L}{\gamma \cosh \gamma L - i\Delta\beta \sinh \gamma L}$$

and

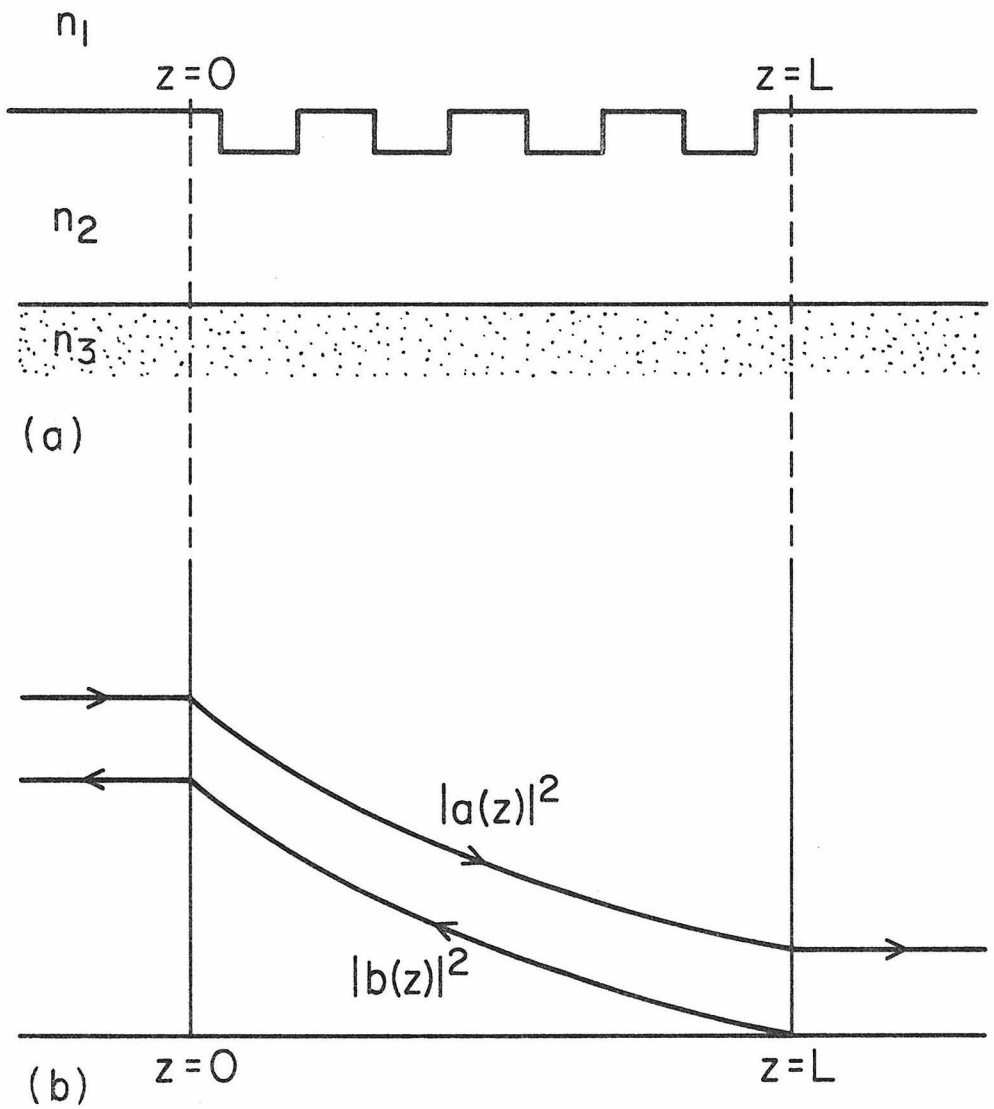

Fig. 2.6 (a) Corrugated section of a dielectric waveguide.
(b) Transfer of power from an incident to a reflected wave at the Bragg frequency.

$$t = \frac{E_+(L)}{E_+(0)} = a(L)\, e^{i\beta_o L} = \frac{\gamma\, e^{i\beta_o L}}{\gamma \cosh \gamma L - i\Delta\beta \sinh \gamma L} \tag{2.66}$$

Both r and t can be written as

$$r = |r|\, e^{i\phi_r}$$

and

$$t = |t|\, e^{i\phi_t} \tag{2.67}$$

By straightforward calculation, one can show that

$$R = |r|^2 = \frac{\kappa^2 \sinh^2 \gamma L}{\gamma^2 + \kappa^2 \sinh^2 \gamma L}$$

$$\phi_r = \frac{\pi}{2} + \tan^{-1}\left(\frac{\Delta\beta}{\gamma} \tanh \gamma L\right) + n\pi \tag{2.68}$$

and

$$T = |t|^2 = \frac{\gamma^2}{\gamma^2 + \kappa^2 \sinh^2 \gamma L}$$

$$\phi_t = \beta_o L + \tan^{-1}\left(\frac{\Delta\beta}{\gamma} \tanh \gamma L\right) + n\pi \tag{2.69}$$

where n is an integer. Note $R + T = 1$ which is a statement of the conservation of energy.

(a) Reflection characteristics

Using κ as a parameter, R is a symmetric function, and $\phi_r - \frac{\pi}{2}$ is an antisymmetric function of $\Delta\beta$. For clarity, we discuss the characteristics of R and ϕ_r only in the domain $\Delta\beta > 0$.

In $\Delta\beta < \kappa$, the effective propagation constant is a complex number which corresponds to the forbidden gap of propagation in the corrugated

waveguide. The expressions for R and ϕ_r are given by (2.68). In the band edge, $\Delta\beta = \kappa$, $\gamma = 0$

$$R = \frac{(\kappa L)^2}{1 + (\kappa L)^2}$$

and (2.70)

$$\phi_r = \frac{\pi}{2} + \tan^{-1}(\kappa L) + n\pi$$

In the allowed band, $\Delta\beta > \kappa$, $\gamma = i\bar{\gamma}$, where

$$\bar{\gamma} = \sqrt{(\Delta\beta)^2 - \kappa^2}$$

$$R = \frac{\kappa^2 \sin^2 \bar{\gamma} L}{\bar{\gamma}^2 + \kappa^2 \sin^2 \bar{\gamma} L}$$

and

$$\phi_r = \frac{\pi}{2} + \tan^{-1}\left(\frac{\Delta\beta}{\bar{\gamma}} \tan \bar{\gamma} L\right) + n\pi \qquad (2.71)$$

To express ϕ_r as a continuous function of $\Delta\beta L$, we set

$$n = 0 \quad \text{when} \quad \Delta\beta L < \sqrt{\left(\frac{\pi}{2}\right)^2 + (\kappa L)^2}$$

and

$$n \quad \text{when} \quad \sqrt{\left[\frac{(2n-1)\pi}{2}\right]^2 + (\kappa L)^2} < \Delta\beta L < \sqrt{\left[\frac{(2n+1)\pi}{2}\right]^2 + (\kappa L)^2}$$

$$\text{with} \quad n=1,2,\cdots$$

Typical plots of $R(\Delta\beta L)$ and $\phi_r(\Delta\beta L)$ are shown in Fig. 2.7

The maximum reflectivity R_o is at $\Delta\beta L = 0$.

$$R_o = \tanh^2 \kappa L \qquad (2.72)$$

The zeros of reflectivity $R = 0$ are at $\bar{\gamma} L = n\pi$ or $\Delta\beta L = \pm\pi \sqrt{n^2 + \left(\frac{\kappa L}{\pi}\right)^2}$, $n=1,2,\cdots$. The locations of secondary maxima of reflectivity are determined by finding the local minima of $\left(\frac{\bar{\gamma} L}{\sin \bar{\gamma} L}\right)^2$. The first few roots are

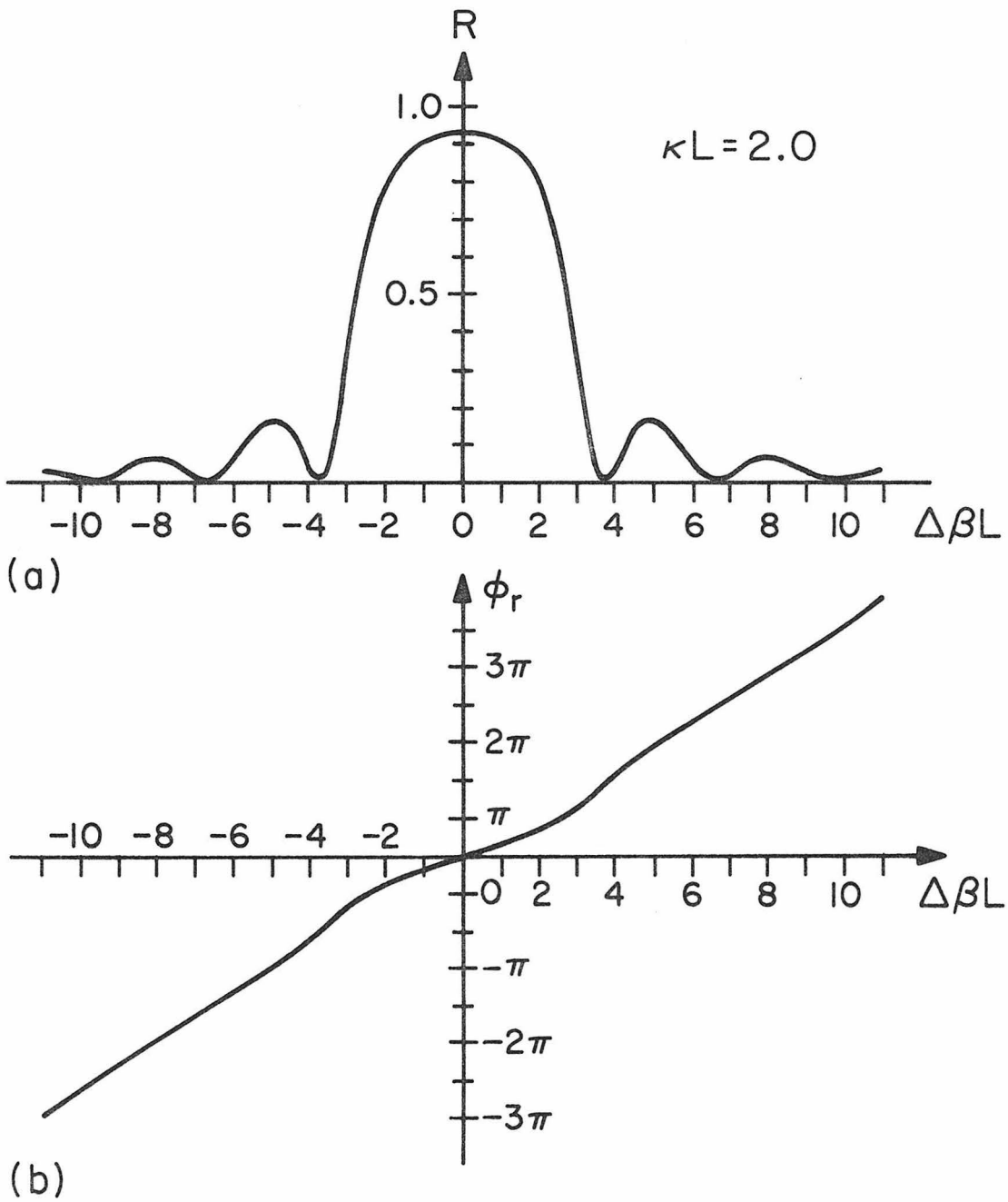

Fig. 2.7 Plot of (a) reflectivity (b) phase delay of a grating reflector as a function of the detuning $\Delta\beta L$.

$\bar{\gamma}L$ = 4.493, 7.725, 10.904, etc. For example, the first side lobe has the maximum reflectivity of

$$R_1 = \frac{1}{1 + \frac{21.191}{(\kappa L)^2}} \qquad \text{at} \quad \Delta\beta L \simeq \pm\sqrt{20.187 + (\kappa L)^2}$$

To estimate the bandwidth of the reflectivity spectrum, we use the relation

$$\frac{\Delta\lambda}{\lambda} \simeq \frac{\Delta(\Delta\beta L)}{\pi N} \tag{2.73}$$

where N is the number of the participating grating period. The bandwidth between the first two reflection zero points is

$$\Delta\lambda_{0\text{-}0} = 2\sqrt{1 + \left(\frac{\kappa L}{\pi}\right)^2}\ \left(\frac{\lambda}{N}\right)$$

The 3-db bandwidth is

$$\Delta\lambda_{FWHM} = \frac{\Delta(\Delta\beta L)_{1/2\text{-}1/2}}{\pi}\left(\frac{\lambda}{N}\right)$$

For example, in terms of (λ/N),

κL		$\Delta\lambda_{0\text{-}0}$	$\Delta\lambda_{FWHM}$
π	,	2.828,	2.486
$\pi/2$	,	2.236,	1.519
$\pi/4$	,	2.062,	1.076

At first glance, it seems that $\phi_r = \pi/2$ at the Bragg frequency ($\Delta\beta = 0$) is a peculiar result [7]. However, after a careful inspection we find it depends on the location of the coordinate origin used in calculating the coefficient K. Corrugations have been used extensively in distributed feedback (DFB) lasers. Using the above analysis, we will give a simple explanation of an interesting fact regarding DFB lasers which

states that the oscillation of a DFB laser does not start at the Bragg frequency where the corrugation provides the maximum feedback [8]. First, we arbitrarily choose a reference plane in the corrugation as in Fig. 2.8 . Using a self-consistent method, the oscillation threshold will depend on the phase of $r_1 r_2$. The frequency at which this phase is $2m\pi$ has the low threshold. At the Bragg frequency, if $r_1 \propto e^{i\phi}$, then it can be proved that $r_2 \propto e^{i(\pi-\phi)}$. Thus $r_1 r_2 \propto e^{i\pi} = -1$ (destructive interference) which may exclude the possibility of oscillation at the Bragg frequency in a DFB laser.

If the waveguide medium has a gain or loss constant α we simply replace β in the solutions by $\beta + i\frac{\alpha}{2}$, where α is positive for loss and negative for gain.

(b) Normal-mode solutions

Although the solutions $E_+(z)$ and $E_-(z)$ in (2.62) are complete solutions of the wave equation, they are not expressed in terms of the normal modes, or Floquet modes, of a periodic structure. A Floquet mode should be a superposition of the fundamental wave function and its spatial harmonics in the structure. In the following, we will prove that E(z) can be rewritten in the Floquet modes, thus demonstrating the equivalence of the coupled-mode solution to the normal-mode solution in a corrugated waveguide.

From (2.62),

$$E(z) = E_+(z) + E_-(z)$$

$$= a(z)\, e^{i\beta_0 z} + b(z)\, e^{-i\beta_0 z} \quad , \qquad \beta_0 = \pi/\Lambda$$

a(z) and b(z) satisfy the equations

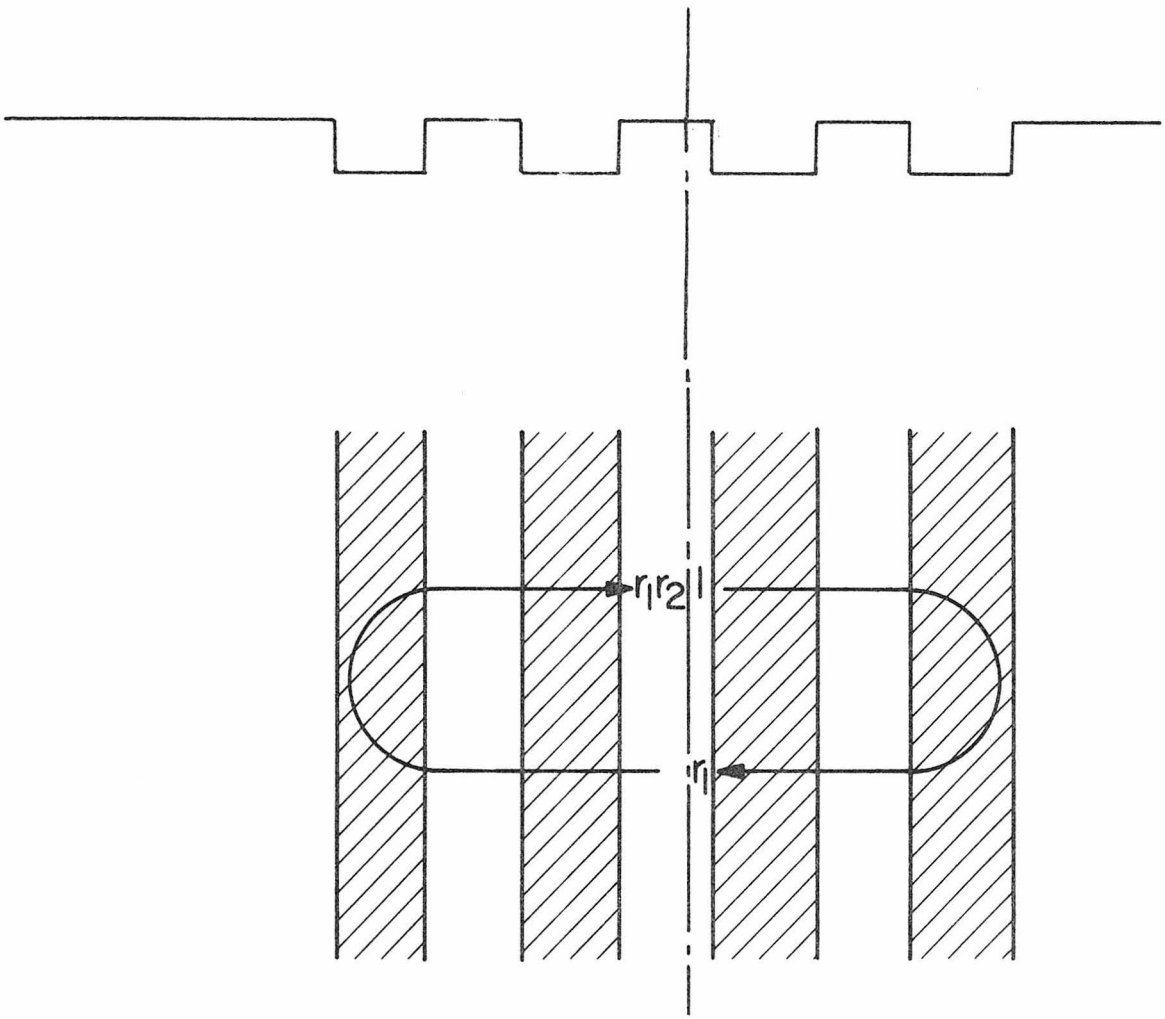

Fig. 2.8 Illustration of a round-trip phase lag in the "cavity" of a distributed feedback (DFB) laser.

$$\left(\frac{d^2}{dz^2} + \bar{\gamma}^2\right) \begin{matrix} a \\ b \end{matrix} \} = 0 \quad , \qquad \bar{\gamma} = \sqrt{(\Delta\beta)^2 - \kappa^2}$$

The general solutions are

$$b(z) = b_1 e^{i\bar{\gamma}z} + b_2 e^{-i\bar{\gamma}z}$$

$$a(z) = a_1 e^{i\bar{\gamma}z} + a_2 e^{-i\bar{\gamma}z}$$

If we choose two independent constants as a_1 and b_2, then, from (2.63), $b_1 = \sigma a_1$ and $a_2 = \sigma b_2$, where $\sigma = (\bar{\gamma}-\Delta\beta)/\kappa$. Hence

$$E_-(z) = b_2 e^{-i(\bar{\gamma}+\beta_0)z} + \sigma a_1 e^{i[(\bar{\gamma}+\beta_0)z - 2\beta_0 z]}$$

$$E_+(z) = a_1 e^{i(\bar{\gamma}+\beta_0)z} + \sigma b_2 e^{-i[(\bar{\gamma}+\beta_0)z - 2\beta_0 z]}$$

a_1 and b_2 are determined by the boundary conditions. If we combine the first term in $\begin{matrix} E_+(z) \\ E_-(z) \end{matrix} \}$ and the second term in $\begin{matrix} E_-(z) \\ E_+(z) \end{matrix} \}$ as $\begin{matrix} F_+(z) \\ F_-(z) \end{matrix} \}$, i.e.,

$$\begin{aligned} F_+(z) &= a_1 e^{i(\bar{\gamma}+\beta_0)z} + \sigma a_1 e^{i[(\bar{\gamma}+\beta_0)z - 2\beta_0 z]} \\ F_-(z) &= b_2 e^{-i(\bar{\gamma}+\beta_0)z} + \sigma b_2 e^{-i[(\bar{\gamma}+\beta_0)z - 2\beta_0 z]} \end{aligned} \tag{2.74}$$

then

$$E(z) = F_+(z) + F_-(z) \tag{2.75}$$

and $F_\pm(z)$ are the Floquet modes ($2\beta_0 = 2\pi/\Lambda$ in this case) which represent the forward and backward waves, respectively.

Several interesting characteristics have to be mentioned. First, the forward and backward waves contain identical amounts of the harmonic due to the translational symmetry of the corrugated waveguide in

the z direction. Second, the group velocities $\pm\ d\omega/d(\bar{\gamma}+\beta_o)$ of the fundamental and $\pm\ d\omega/d(\bar{\gamma}-\beta_o)$ of the harmonic in $F_{\pm}(z)$ are the same, and they depend on the parameter $\bar{\gamma}$. Thus, in the normal-mode formalism, waves of similar group velocity are grouped together, while in the coupled-mode formalism, waves are grouped according to their phase velocity.

2.5 Radiation Coupled from a Corrugated Waveguide

Surface corrugations in a waveguide not only couple the forward going guided modes to the backward going guided modes, but also couple the guided modes to the radiation modes. Our theoretical approach for the latter case still uses the coupled-mode formalism. We express the total field in terms of the Floquet modes of the corrugated structure. A perturbation method will be described to solve the coupled-mode equations. The attenuation constant for the guided mode due to the coupled-radiation loss will be derived.

Consider TE modes. E_y satisfies

$$\frac{\partial^2 E_y}{\partial z^2} + \frac{\partial^2 E_y}{\partial x^2} + k^2 n^2(z,x)\, E_y = 0 \tag{2.76}$$

Now we express E_y as a summation of partial waves in a form dictated by the Floquet theorem.

$$E_y = \sum_m E_m(x)\, e^{i\beta_m z} \tag{2.77}$$

with

$$\beta_m = \beta_o - \frac{2\pi m}{\Lambda} \tag{2.78}$$

If no corrugation were present, then all $E_m(x)$ with $m \neq 0$ would be zero, so that $E_o(x)$ would be the only mode--the incoming guided mode in the waveguide. In addition, $n^2(z,x)$ is expressed as

$$n^2(z,x) = n'^2(x) + (n_1^2 - n_2^2) \sum_{\ell \neq 0} a_\ell(x)\, e^{-i\ell \frac{2\pi}{\Lambda} z} \tag{2.79}$$

Compared with (2.31) and (2.34),

$$n'^2(x) \equiv n^2(x) + (n_1^2 - n_2^2)\, a_o(x)$$

which describes a four-layer structure. Substituting (2.77) and (2.79) in (2.76), we obtain

$$\frac{d^2E_m}{dx^2} + [k^2 n'^2(x) - \beta_m^2]\, E_m = k^2(n_2^2 - n_1^2) \sum_{\ell \neq m} a_{m-\ell}(x)\, E_\ell, \quad \forall m \tag{2.80}$$

The coupled-mode equations given in (2.80) can be solved by the perturbation method [9]. We first assume that all the partial waves $E_m(x)$ with $m \neq 0$ are small. Consequently $E_o(x)$ can be approximately solved by

$$\frac{d^2E_o}{dx^2} + [k^2 n'^2(x) - \beta_o^2]\, E_o = 0 \tag{2.81}$$

which, subject to the continuity conditions at x = 0, -d, and -t, determines β_o and $E_o(x)$. Then the resulting $E_o(x)$ is used on the right hand side of (2.80) to drive the other partial waves $E_m(x)$ for $m \neq 0$:

$$\frac{d^2E_m}{dx^2} + [k^2 n'^2(x) - \beta_m^2]\, E_m = k^2(n_2^2 - n_1^2)\, a_m(x)\, E_o \tag{2.82}$$

Thus we obtain a first-order perturbation solution for E_m. An iterative procedure may be taken to obtain more accurate solutions. For details of this analysis, interested readers are referred to Ref. 9.

The value of β_o determined by (2.81) is a real number which does not reveal the fact that the incident mode E_o is attenuated. This attenuation can be evaluated by calculating the power carried by the partial waves E_m whose $|\beta_m| < kn_3$ (radiation modes). The time-averaged Poynting vector is $\vec{P} = \frac{1}{2} \mathrm{Re}(\vec{E} \times \vec{H}^*)$. It can be shown that the power radiated per unit waveguide length by a TE wave is

$$P' = P_x = \frac{1}{2} \mathrm{Re}(E_y H_z^*), \qquad \text{where} \quad H_z = \frac{-i}{\omega \mu_o} \frac{\partial E_y}{\partial x} \tag{2.83}$$

For a partial wave, $E_y = E_m(x)\, e^{i\beta_m z}$ and $E_m(x)$ is taken as

$$E_m(x) = \begin{cases} E_m(0)\, e^{i\sqrt{k^2 n_1^2 - \beta_m^2}\, x} & x > 0 \\ E_m(-t)\, e^{-i\sqrt{k^2 n_3^2 - \beta_m^2}\, x} & x < -t \end{cases}$$

Thus the power radiated per unit waveguide length by a partial wave is

$$P'_m = \frac{1}{2\omega\mu_o} \mathrm{Re}\left(\sqrt{k^2 n_1^2 - \beta_m^2}\, |E_m(0)|^2 + \sqrt{k^2 n_3^2 - \beta_m^2}\, |E_m(-t)|^2 \right) \tag{2.84}$$

Usually, an output coupler uses only one part of the radiated power expressed above. If β_m^2 exceeds $k^2 n_{1,3}^2$, imaginary terms occur in (2.84); there will be no radiation contribution from such a partial wave. From (2.78) and $kn_3 < \beta_o < kn_2$, $P'_m = 0$ for $m < 0$ and for

large positive m (this, of course, will depend on the magnitude of the grating period Λ). Since the radiated power is proportional to the guided power, then

$$\sum_m P'_m = -\frac{dP_o}{dz} = \alpha P_o \qquad \text{with} \quad P_o = \frac{\beta_o}{2\omega\mu_o} \int |E_o|^2 dx$$

The attenuation constant α is thus given by

$$\alpha = \frac{2\omega\mu_o}{\beta_o} \frac{\sum_m P'_m}{\int |E_o|^2 dx} \tag{2.85}$$

We are also concerned with the direction at which a partial wave will be coupled out. This is given by

$$\phi_i = \cos^{-1}\left(\frac{\beta_m}{kn_i}\right), \qquad i = 1,3 \tag{2.86}$$

which is an angle measured from the waveguide axis.

2.6 Zig-Zag Ray Analysis for Corrugated Waveguides

Coupling parameters for reflection and output coupling in corrugated waveguide devices can also be calculated using a zig-zag ray picture [10]. Its first-order results are in good agreement with those from coupled-mode theory. This approach is especially useful in the case where the coupled-mode analysis is hindered by excessive computation, for example, in sinusoidal corrugations.

In a thin-film dielectric waveguide, light is guided by total

internal reflections at both interfaces between the film and the cladding media; thus a guided mode can be described by a zig-zag ray bouncing back and forth as shown in Fig. 2.9 a. We divide the incident power on the corrugated interface into sections whose widths are equal to the mode bounce distance (see Fig. 2.9 a). Then, in output coupling, the normalized measure of radiated power, α (cm^{-1}) in (2.85), can be expressed as

$$\alpha = N\eta \tag{2.87}$$

where N is the number of sections in a unit length (1 cm) and η is the diffraction efficiency of the surface grating (corrugation). We add up the efficiency (or more correctly, the diffracted power) of each section because the coupled waves from different sections do not overlap or interfere with each other (Fig. 2.9b). However, we should take into account the interference in the case of reflection of the guided mode. The magnitude of the coupling coefficient, κ (cm^{-1}), is defined as

$$\kappa = N\sqrt{\eta} \tag{2.88}$$

This is the optimum estimation, since we add up the diffracted amplitude coherently from different sections of incident wave (Fig. 2.9 c). This may not be exactly true.

The whole problem can be separated into two independent subproblems: one is the calculation of the diffraction efficiency η of the surface grating, and the other is the estimate of N (cm^{-1}) which is the bounce rate of the incident mode.

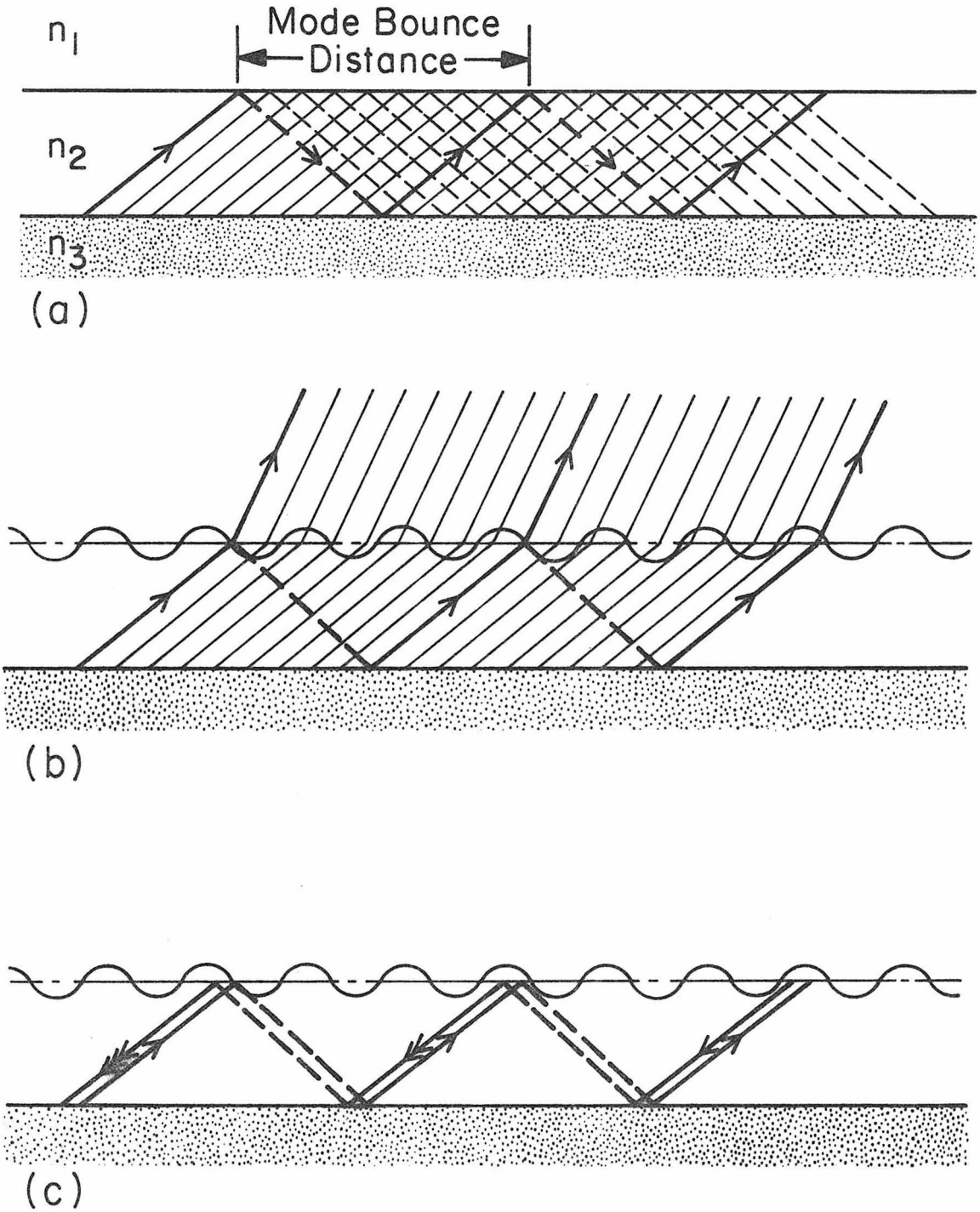

Fig. 2.9 Zig-zag ray picture illustrating (a) mode bounce distance (b) process of output coupling (c) process of reflection (feedback) in a corrugated waveguide.

(a) Diffraction efficiency η

The phenomenon of diffraction at a corrugated interface between two dielectric media has been a subject of interest for many years. The geometry is sketched in Fig. 2.10. In electromagnetic theory, the field amplitudes of different diffraction orders can be solved, in principle, by matching the boundary conditions on the corrugated interface. In the case of a small sinusoidal corrugation, we can derive, to some order of approximation, the diffraction efficiency of a given order in closed form.

For TE waves (see Fig. 2.10),

$$E_y = \begin{cases} A\, e^{i(\sigma_o x + \beta_o z)} + \sum_\ell b_\ell\, e^{i(-\rho_\ell x + \beta_\ell z)} & \text{in } n_2 \text{ medium} \\ \sum_\ell c_\ell\, e^{i(\tau_\ell x + \beta_\ell z)} & \text{in } n_1 \text{ medium} \end{cases} \tag{2.89}$$

where $\beta_\ell = \beta_o + \ell K, \qquad K \equiv \frac{2\pi}{\Lambda}$

$$\sigma_o = \sqrt{k^2 n_2^2 - \beta_o^2}\ , \quad \rho_\ell = \sqrt{k^2 n_2^2 - \beta_\ell^2}\ , \quad \rho_o = \sigma_o$$

and $$\tau_\ell = \sqrt{k^2 n_1^2 - \beta_\ell^2}$$

The boundary conditions are that E_y and H_t are continuous on the corrugated surface described by $x = f(z)$. The tangential magnetic field is

$$H_t = \frac{1}{\sqrt{1 + f'^2}} H_z + \frac{f'}{\sqrt{1 + f'^2}} H_x \tag{2.90}$$

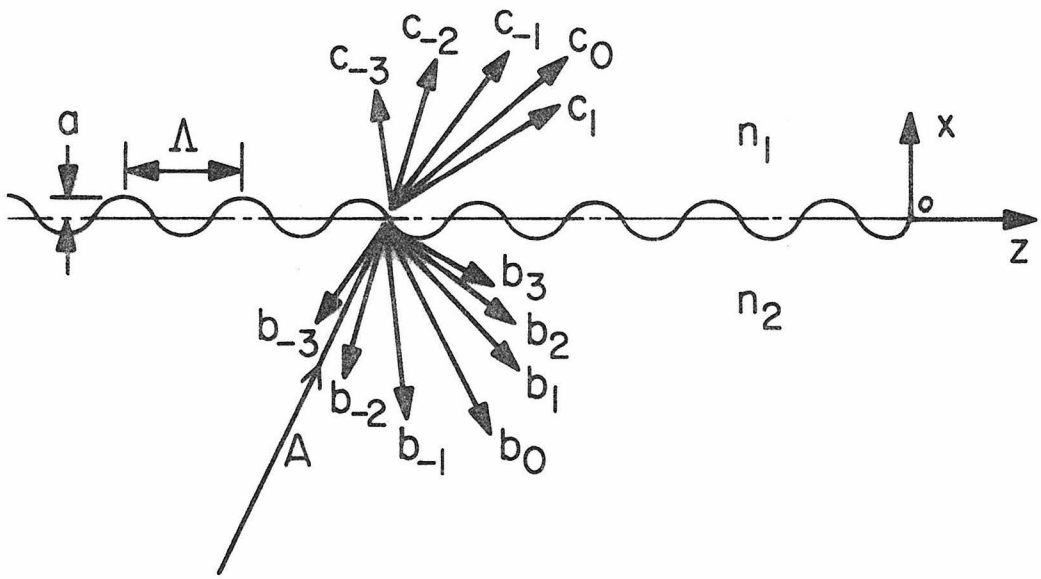

Fig. 2.10 Incident and diffracted waves at both sides of a surface grating. The coordinate and grating parameters used in the analysis are also shown.

where $f' \equiv df/dz$,

$$H_z = \frac{-i}{\omega\mu_o}\frac{\partial E_y}{\partial x} \qquad \text{and} \qquad H_x = \frac{i}{\omega\mu_o}\frac{\partial E_y}{\partial z}$$

If $f(z) = a \sin Kz$, where a is the grating amplitude and thus half of the corrugation depth d, namely, $a = d/2$, then imposing the continuity requirement leads to a pair of equations [11]

$$\sum_\nu [-b_{\mu+\nu}J_\nu(\rho_{\mu+\nu}a) + c_{\mu-\nu}J_\nu(\tau_{\mu-\nu}a)] = AJ_\mu(\sigma_o a)$$

and

$$\sum_\nu \left[\frac{\rho_\mu^2 - \nu K\beta_\mu}{\rho_{\mu+\nu}} b_{\mu+\nu}J_\nu(\rho_{\mu+\nu}a) + \frac{\tau_\mu^2 + \nu K\beta_\mu}{\tau_{\mu-\nu}} c_{\mu-\nu}J_\nu(\tau_{\mu-\nu}a)\right] = \frac{\sigma_o^2 - \mu K\beta_o}{\sigma_o} AJ_\mu(\sigma_o a) \tag{2.91}$$

where J_ν are Bessel functions.

Assume a small perturbation $ka << 1$. Then for a zero-order approximation, $\mu = 0$, we obtain

$$b_o = \frac{\sigma_o - \tau_o}{\sigma_o + \tau_o} A$$

$$c_o = \frac{2\sigma_o}{\sigma_o + \tau_o} A \tag{2.92}$$

For a first-order approximation, $\mu = -1$ (as mentioned previously, we are interested only in the negative order of the diffraction), we have equations which involve both b_{-1}, c_{-1} and b_o, c_o. After using the result (2.92), we obtain

$$c_{-1} = b_{-1}$$

$$\frac{b_{-1}}{A} = -a\,\frac{\sigma_o(\sigma_o - \tau_o)}{\rho_{-1} + \tau_{-1}} \tag{2.93}$$

It is apparent that each order of approximation follows from the preceding orders. Each time we need to solve only two unknowns from two equations in (2.91). For a second-order approximation $\mu = -2$, we obtain

$$\frac{b_{-2}}{A} = \frac{a^2}{4}\,\frac{\sigma_o(\sigma_o-\tau_o)}{\rho_{-2}+\tau_{-2}}\,[\tau_o + \tau_{-2} + 2(\rho_{-1} - \tau_{-1})]$$

$$\frac{c_{-2}}{A} = \frac{a^2}{4}\,\frac{\sigma_o(\sigma_o - \tau_o)}{\rho_{-2}+\tau_{-2}}\,[\tau_o - \rho_{-2} + 2(\rho_{-1} - \tau_{-1})] \tag{2.94}$$

For a third-order approximation $\mu = -3$, we obtain

$$\frac{b_{-3}}{A} = -\frac{a^3}{8}\,\frac{\sigma_o(\sigma_o-\tau_o)}{\rho_{-3}+\tau_{-3}}\,[\tfrac{1}{3}(\sigma_o^2 + \tau_o^2) - (\rho_{-1}^2 - \rho_{-1}\tau_{-1} + \tau_{-1}^2) + \rho_{-2}\tau_{-2}$$

$$+ (\rho_{-2}-\tau_{-2})(\tau_o + 2\rho_{-1} - 2\tau_{-1}) + \tau_{-3}(\tfrac{2}{3}\tau_o + \rho_{-1} - \tau_{-1})] \tag{2.95}$$

$$\frac{c_{-3}}{A} = -\frac{a^3}{8}\,\frac{\sigma_o(\sigma_o-\tau_o)}{\rho_{-3}+\tau_{-3}}\,[\tfrac{1}{3}(\sigma_o^2 + \tau_o^2) - (\rho_{-1}^2 - \rho_{-1}\tau_{-1} + \tau_{-1}^2) + \rho_{-2}\tau_{-2}$$

$$+ (\rho_{-2} - \tau_{-2})(\tau_o + 2\rho_{-1} - 2\tau_{-1}) - \rho_{-3}(\tfrac{2}{3}\tau_o + \rho_{-1} - \tau_{-1})]$$

The diffraction efficiencies are defined by

$$\eta_\ell = \mathrm{Re}\left(\frac{\rho_\ell}{\sigma_o}\left|\frac{b_\ell}{A}\right|^2 + \frac{\tau_\ell}{\sigma_o}\left|\frac{c_\ell}{A}\right|^2\right) \tag{2.96}$$

where ℓ indicates a diffraction order. Note, $\beta_o = \beta$, $\sigma_o = h$, and $\tau_o = iq$ for the incident condition equivalent to a guided mode, where h and q are defined in (2.7).

(b) Bounce rate N

The bounce rate N is the number of bounces per unit length. At first glance, it would seem that $N = 1/(2t \cot \theta)$, where t is the waveguide thickness and θ is the incident angle of the mode whose $\beta = kn_2 \cos \theta$. However, to treat the problem accurately, the Goos-Hänchen shift [12] at the interfaces (or dielectric discontinuities) should be taken into account. The Goos-Hänchen shift is a phenomenon associated with the total internal reflection of a ray (which can be the axis of a finite uniform beam or a Gaussian beam, for example). It is a lateral displacement between the incident and reflected rays at the interfaces, as illustrated in Fig. 2.11, so the distance between two consecutive bounces at the same interface is

$$L_B = 2(t \cot \theta + s_1 + s_3)$$

It can be proved that

$$s_1 = \frac{\cot \theta}{q} \qquad \text{and} \qquad s_3 = \frac{\cot \theta}{p}$$

where q and p are defined in (2.7). The bounce distance is then expressed as

$$L_B = 2t_{eff} \cot \theta \tag{2.97}$$

where t_{eff} is exactly the effective thickness of the waveguide as defined in (2.16). The bounce rate is then

$$N = \frac{1}{L_B} = \frac{1}{2t_{eff} \cot \theta} = \frac{h}{2\beta t_{eff}} \tag{2.98}$$

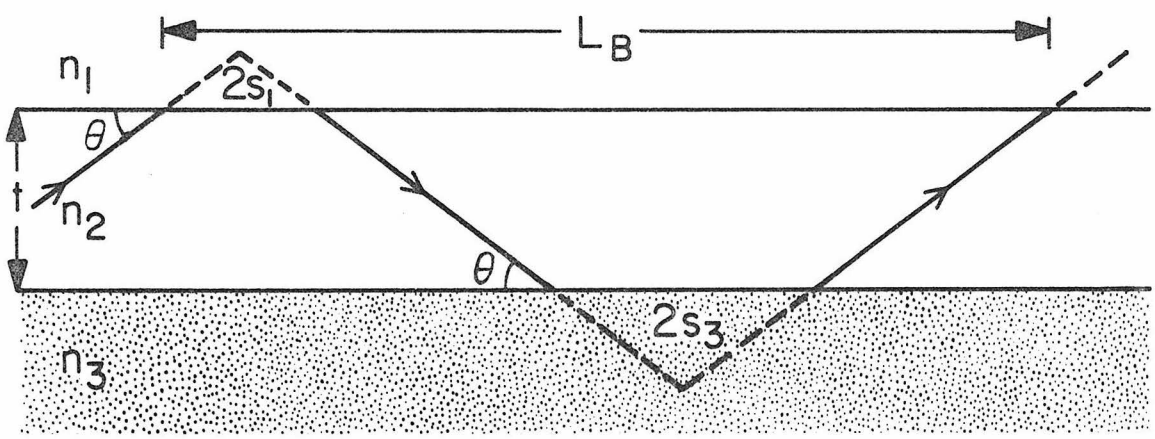

Fig. 2.11 Goos-Hänchen shifts and resulting bounce distance of a zig-zag ray which is totally reflected at both interfaces in a waveguide structure.

(c) Derivation of the coupling parameters

Now we are ready to derive the coupling parameters using the above-described zig-zag ray theory. The results should provide direct evidence of the equivalence between this ray formalism and coupled-mode or other first-order perturbation theories.

As a first example, consider the coupling coefficient (2.88). In this case, $-\ell K = 2\beta$, $\beta_\ell = -\beta$, $\rho_\ell = \sigma_o = h$, and $\tau_\ell = \tau_o = iq$. Thus, $\eta_\ell = |b_\ell/A|^2$, and

$$\kappa_\ell = \frac{h}{2\beta t_{eff}} \left|\frac{b_\ell}{A}\right| \tag{2.99}$$

For $\ell = -1$ (Fig. 2.12a), it can be shown from (2.93) that $|b_{-1}/A| = ha$. Thus

$$\kappa_{-1} = \frac{h^2 a}{2\beta t_{eff}} \tag{2.100}$$

which is exactly the same as (2.52) derived from coupled-mode theory. Similarly, for $\ell=-2$ (Fig. 2.12b),

$$\kappa_{-2} = \frac{h^2 a^2}{4\beta t_{eff}} \sqrt{k^2(n_2-n_1)^2 + q^2} \tag{2.101}$$

and for $\ell = -3$ (Fig. 2.12c),

$$\kappa_{-3} = \frac{h^2 a^3}{8\beta t_{eff}} \sqrt{\left[\frac{2}{3}h^2 + \left(k^2 n_1^2 - \frac{\beta^2}{9}\right) - \sqrt{k^2 n_2^2 - \frac{\beta^2}{9}}\sqrt{k^2 n_1^2 - \frac{\beta^2}{9}}\right]^2 + q^2\left(\sqrt{k^2 n_2^2 - \frac{\beta^2}{9}} - \sqrt{k^2 n_1^2 - \frac{\beta^2}{9}}\right)^2} \tag{2.102}$$

Fig. 2.13 is a plot of coupling coefficients κ_ℓ versus corrugation depth $d = 2a$ using (2.100), (2.101) and (2.102). Also shown in the

figure are the results in Ref. 6 which uses coupled-mode theory. They are in good agreement with each other when ka < 1.

Next, consider (2.87)- a measure of radiated power in output coupling. After substituting (2.96) and (2.98) in (2.87), we obtain

$$\alpha_\ell = \frac{1}{2\beta t_{eff}} \mathrm{Re}\left(\rho_\ell \left|\frac{b_\ell}{A}\right|^2 + \tau_\ell \left|\frac{c_\ell}{A}\right|^2\right) \tag{2.103}$$

As usual, this result of ray optics can be interpreted in terms of electromagnetic plane waves. The guided power in the waveguide is

$$P_o = \frac{\beta}{2\omega\mu_o} 2|A|^2 t_{eff}$$

and the radiated power per unit waveguide length is

$$P'_\ell = \frac{1}{2\omega\mu_o} \mathrm{Re}\left(\rho_\ell |b_\ell|^2 + \tau_\ell |c_\ell|^2\right)$$

Thus expression (2.103) can be rewritten as

$$\alpha_\ell = \frac{P'_\ell}{P_o}$$

which is similar to the definition of attenuation constant in (2.85). More importantly, our ray-picture approximation is able to give analytic expressions for α_ℓ. For example, consider second-order feedback (Fig. 2.12b), in which the first-order diffracted waves are coupled out normal to the surface. It can be calculated immediately that

$$\alpha_{-1} = \frac{h^2 a^2}{2\beta t_{eff}} k(n_2 - n_1) \tag{2.104}$$

Similarly, for the third-order feedback case (Fig. 2.12c), the first- and

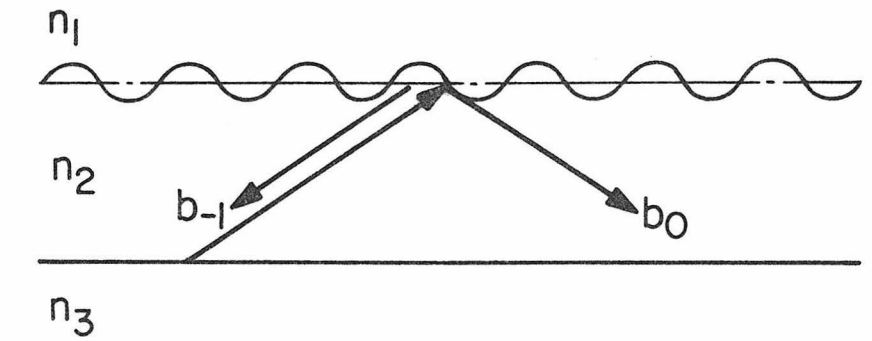

(a)

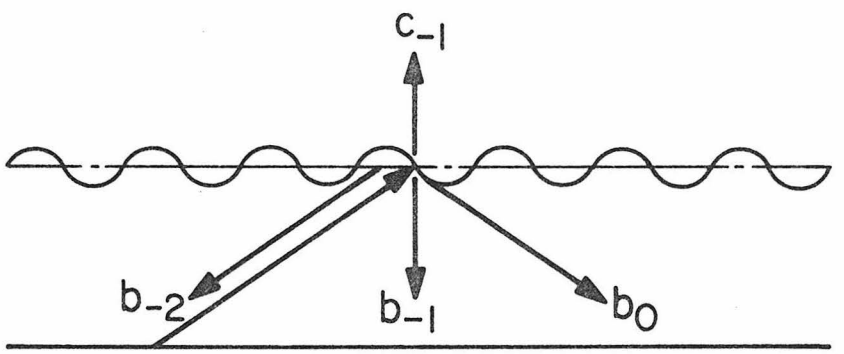

(b)

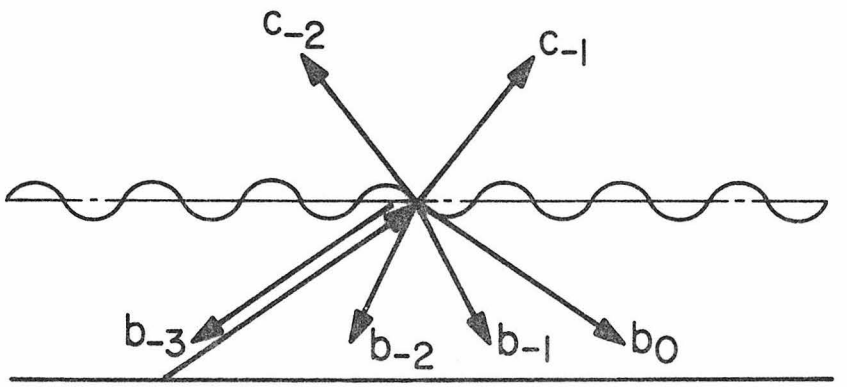

(c)

Fig. 2.12 Schematic diagram showing the related diffraction components in (a) 1st-order (b) 2nd-order (c) 3rd-order feedback configurations. The evanescent components are not shown.

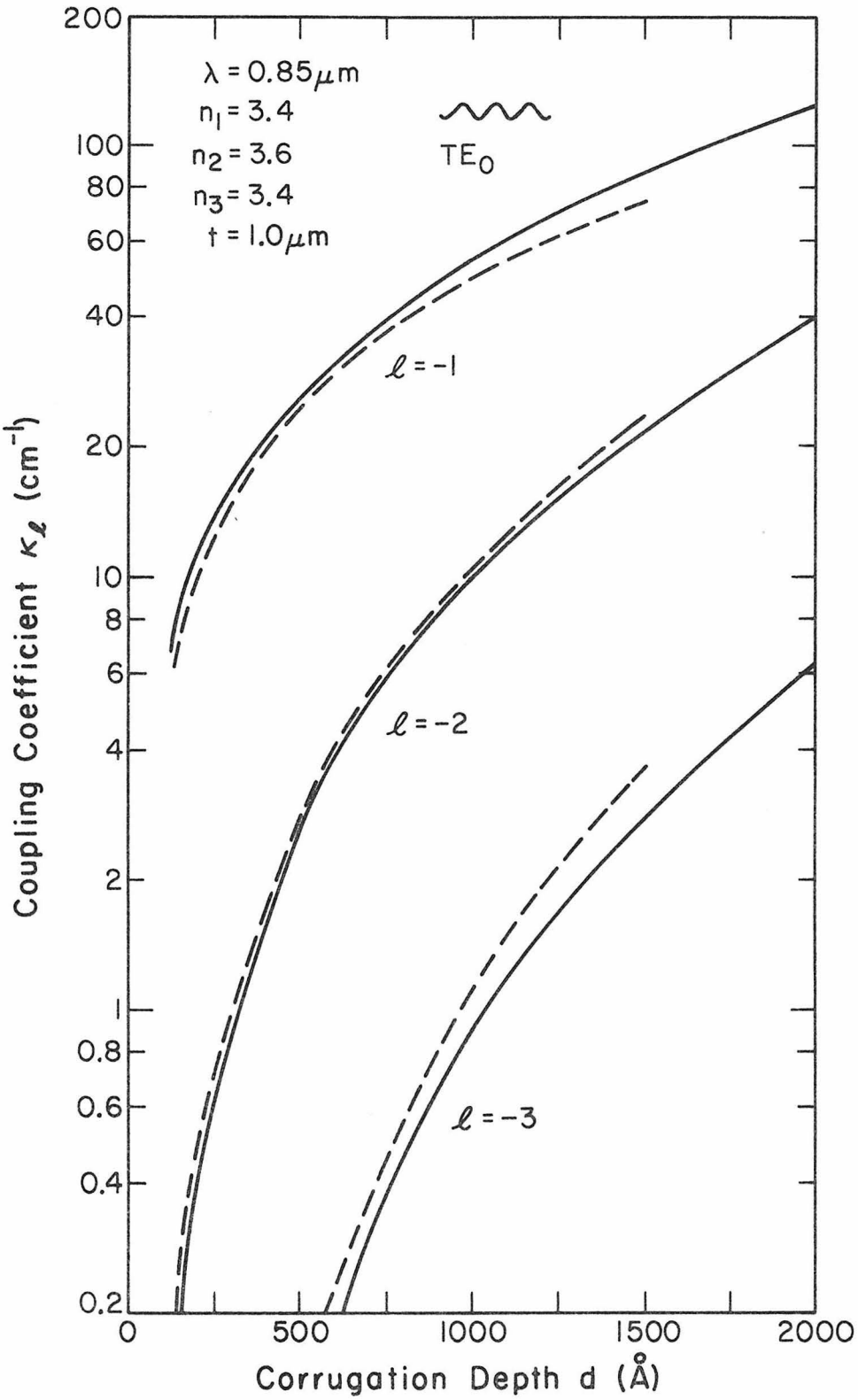

Fig. 2.13 Coupling coefficient versus corrugation depth for 1st-, 2nd-, and 3rd-order feedbacks. Dashed lines are results of ray-picture approximation. Solid lines are results of coupled-mode analysis (After [6]).

second-order diffracted waves are radiated out of the waveguide, which results in attenuation constants

$$\alpha_{-1} = \frac{h^2 a^2}{2\beta t_{eff}} \frac{k^2(n_2^2 - n_1^2)}{\sqrt{k^2 n_2^2 - \frac{\beta^2}{9}} + \sqrt{k^2 n_1^2 - \frac{\beta^2}{9}}}$$

and (2.105)

$$\alpha_{-2} = \frac{h^2 a^4}{32\beta t_{eff}} \frac{k^2(n_2^2 - n_1^2)}{\sqrt{k^2 n_2^2 - \frac{\beta^2}{9}} + \sqrt{k^2 n_1^2 - \frac{\beta^2}{9}}} \left[4\left(k^2 n_2^2 - \frac{\beta^2}{9}\right)\right.$$

$$\left. + 4\left(k^2 n_1^2 - \frac{\beta^2}{9}\right) + q^2 - 7\sqrt{k^2 n_2^2 - \frac{\beta^2}{9}}\sqrt{k^2 n_1^2 - \frac{\beta^2}{9}}\right]$$

Fig. 2.14 is a plot of (2.104) versus corrugation depth, d. Compared with the result from coupled-mode analysis, the agreement is good only for small d such that ka < 1. Fig. 2.15 is a plot of (2.103) versus corrugation period for two partial waves ℓ = -1 and -2, given d = 500Å (ka < 1). Also shown in the figure are results from coupled-mode analysis [9]. As can be seen, they are in good agreement and $\alpha_{-1} >> \alpha_{-2}$, since ka < 1 is fulfilled. To summarize, the ray-picture approximation is simple and gives the analytic results which are good when the corrugation depths are small.

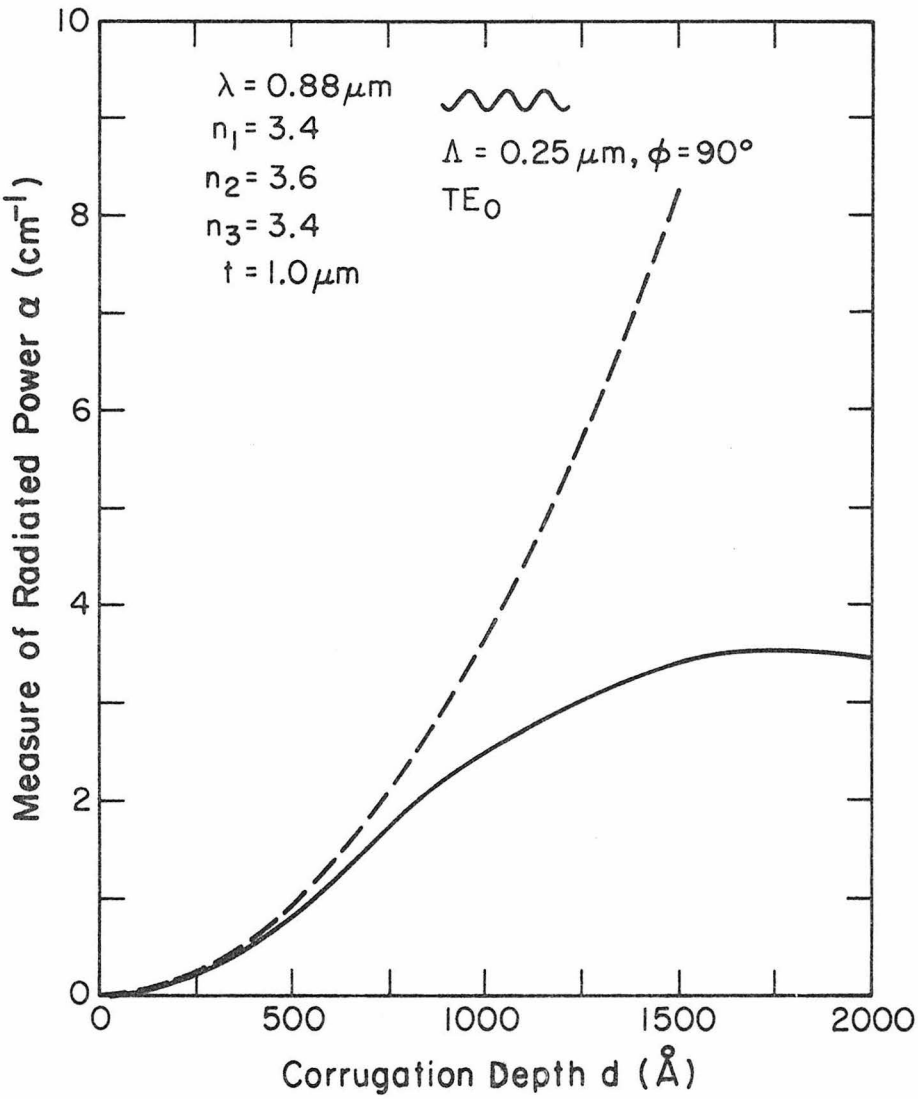

Fig. 2.14 Radiated power versus corrugation depth. Dashed line is obtained from ray-picture approximation. Solid line is obtained from coupled-mode analysis (After [9]). They are in good agreement only for small corrugation depths.

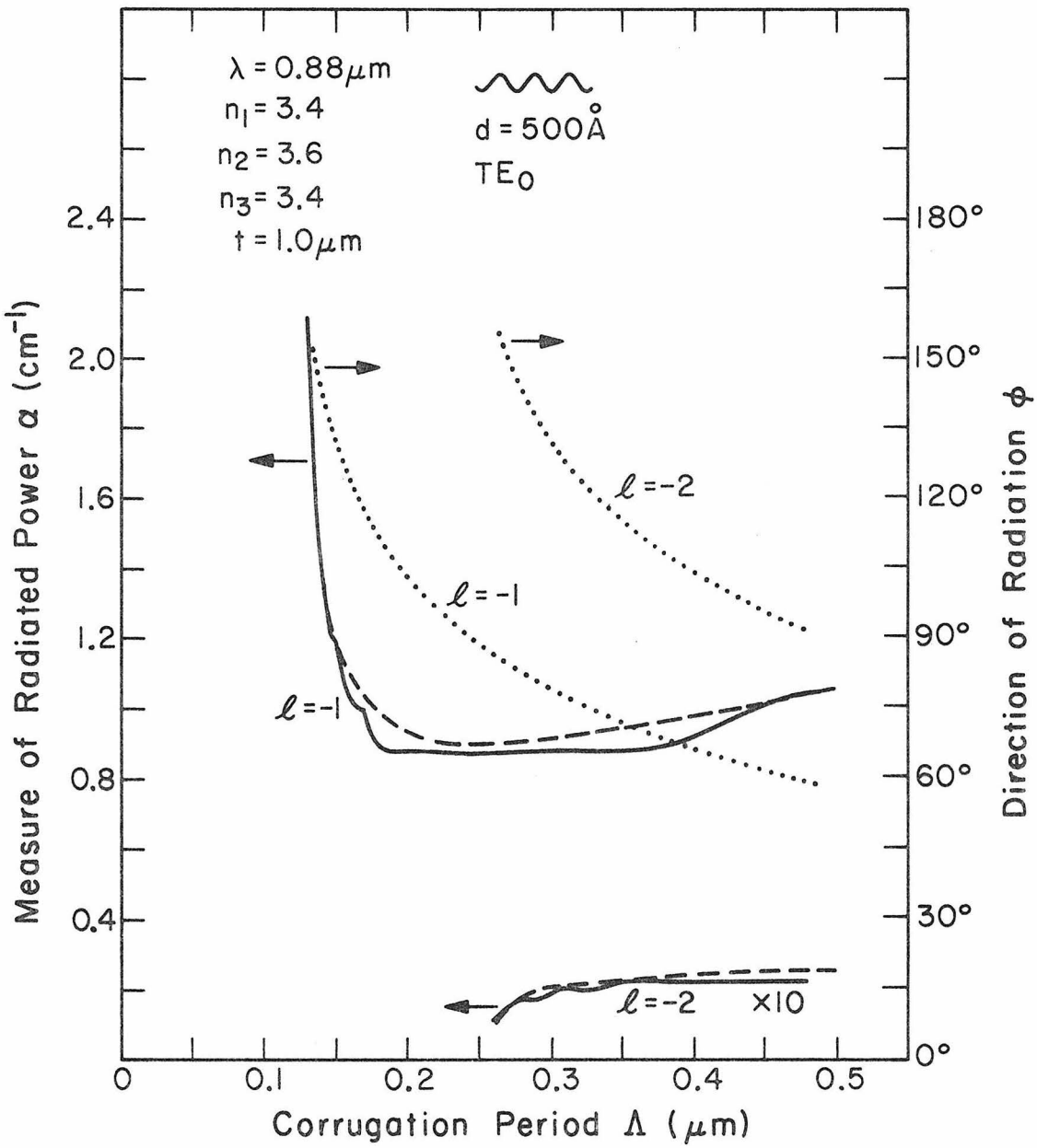

Fig. 2.15 Radiated power versus corrugation period for two partial waves ℓ=-1 and ℓ=-2. Results of ray-picture approximation (dashed lines) and coupled-mode analysis (solid lines, after [9]) are compared. Dotted lines are the corresponding direction of radiation.

Chapter 2 - References

1. See, for example, D. Marcuse, Theory of Dielectric Optical Waveguides (Academic Press, New York, 1974), Chap. 1.
2. See, for example, C. Elachi, "Waves in active and passive periodic structures: a review", Proc. IEEE 64, 1666 (1976).
3. J. R. Pierce, "Coupling of modes of propagation", J. Appl. Phys. 25, 179 (1954).
4. A. Yariv, "Coupled-mode theory for guided-wave optics", IEEE J. Quantum Electron. QE-9, 919 (1973).
5. K. Handa, S. T. Peng, and T. Tamir, "Improved perturbation analysis of dielectric gratings", Appl. Phys. 5, 325 (1975).
6. W. Streifer, D. R. Scifres, and R. D. Burnham, "Coupling coefficients for distributed feedback single- and double-heterostructure diode lasers", IEEE J. Quantum Electron. QE-11, 867 (1975).
7. P. K. Tien, "Integrated optics and new wave phenomena", Rev. Mod. Phys. 49, 391 (1977).
8. H. Kogelnik and C. V. Shank, "Coupled-wave theory of distributed feedback lasers", J. Appl. Phys. 43, 2327 (1972).
9. W. Streifer, D. R. Scifres, and R. D. Burnham, "Analysis of grating-coupled radiation in GaAs:GaAlAs lasers and waveguides", IEEE J. Quantum Electron. QE-12, 422, 494 (1976); W. H. Lee, private commun.
10. P. Zory, "Corrugated grating coupled devices and coupling coefficients", Topical Meeting on Integrated Optics, Paper WB1, Salt Lake City, Utah, 1976.

11. D. Marcuse, "Higher-order scattering losses in dielectric waveguides", Bell Syst. Tech. J. 51, 1801 (1972).

12. F. Goos and H. Hänchen, "Ein neuer und fundamentaler Versuch zur Totalreflexion ", Ann. Physik (6) 1, 333 (1947);
J. J. Burke, "Lateral shifts of light beams on total reflection", Opt. Sci. Newsletter (Univ. Arizona, Tucson) 5, 31 (1971).

Chapter 3

ELECTROOPTIC SCANNING OF LIGHT COUPLED FROM A CORRUGATED $LiNbO_3$ WAVEGUIDE

3.1 Introduction

In this chapter, we describe a method of beam scanning in which the direction of light radiated from a grating output coupler in a dielectric waveguide is controlled, via the electrooptic effect, by an applied electric field. Bragg diffraction (either output coupling [1] or in-plane deflection [2]) from a variable wavelength acoustic wave has been used for optical scanning. The advantages of our proposed method over the above technique will be the capabilities of (1) high speed scanning (or switching), and (2) broadside coupling to air.

Details of some experimental techniques will be presented in Chapter 5. The principle and theory of the device are given. Experimental results are compared with theory. The prospect and further considerations of the device are discussed.

3.2 Device Theory

The principle of the device can be described using a $LiNbO_3$ waveguide in the manner sketched in Fig. 3.1 where x, y, and z are the crystal axes. Consider a guided mode with a propagation constant β along the x-axis, incident upon a grating coupler with a period Λ . The wave will be diffracted into air (radiated) with an angle ϕ with respect to the x-axis. The angle ϕ is determined by (2.86) or the phase-matching diagram in Fig. 3.1,

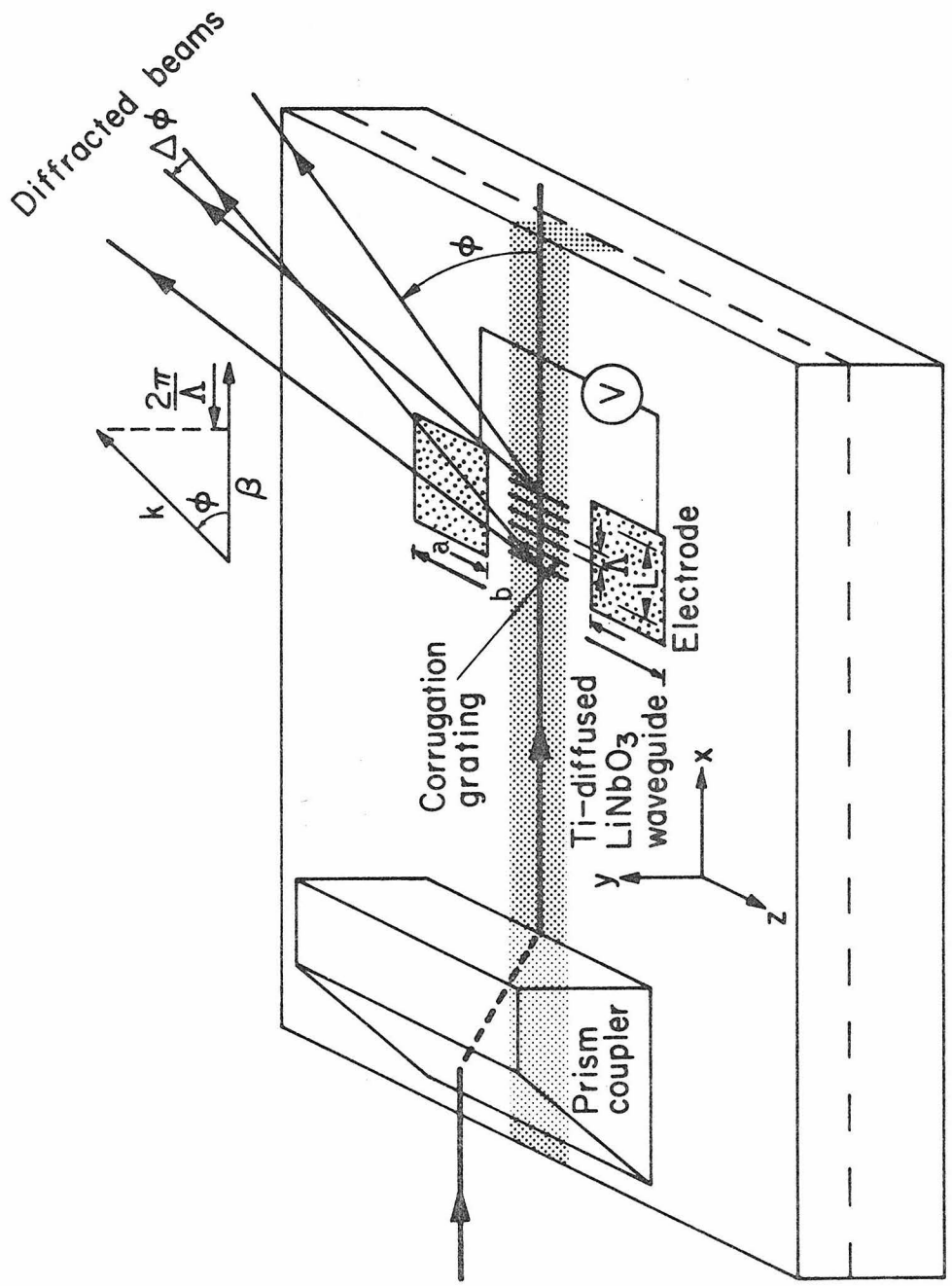

Fig. 3.1 Schematic diagram of the electrooptic beam scanner.

$$\beta - \frac{2\pi}{\Lambda} = k \cos \phi \tag{3.1}$$

where $k = 2\pi/\lambda$ and λ is the vacuum wavelength. If we replace β by kn_{eff} as in (2.14), then (3.1) becomes

$$n_{eff} - \frac{\lambda}{\Lambda} = \cos \phi \tag{3.2}$$

For a given λ and Λ, the angle ϕ depends on the index n_{eff}. The angle of deflection (scanning) corresponding to a small change of index is then

$$\Delta\phi = - \frac{\Delta n_{eff}}{\sin \phi} \tag{3.3}$$

The number of resolvable spots N in the angle of deflection is obtained by dividing the magnitude of $\Delta\phi$ by the angular divergence $\delta\phi$ of the coupled wave.

This angular divergence is determined by several factors. The first is nonuniformity of the film thickness in the coupling region. As a matter of fact, we have local variations of n_{eff} due to waveguide dispersion. By differentiating (3.1), this factor is

$$\delta\phi = - \frac{\delta\beta}{k \sin \phi} = \frac{- \frac{\partial n_{eff}}{\partial t} \delta t}{\sin \phi} \tag{3.4}$$

The angular divergence is also diffraction limited by the finite coupling length L, and is

$$\delta\phi = \frac{\lambda}{L \sin \phi} \tag{3.5}$$

where L is the shorter of the grating lengths or the 1/e folding

distance for the guided mode intensity along the grating. Note, an optimum coupling length is reached when (3.5) is equal to (3.4), and no improvement in resolution will be gained by further increasing the coupling length: $L_{optimum} = \lambda/\delta n_{eff}$. In a structure with uniform waveguide and grating parameters, (3.5) is the main term to be considered.

From (3.3) and (3.5), we obtain

$$N = \frac{|\Delta n_{eff}| L}{\lambda} \tag{3.6}$$

The number of resolvable spots is thus independent of the choice of ϕ or Λ. To estimate Δn_{eff}, we choose both the direction of the applied electric field and that of the mode polarization as parallel to the z (optic) axis of $LiNbO_3$. Strictly speaking, to evaluate Δn_{eff} we have to know the applied electric field distribution first, and then calculate the electrooptically induced index change to obtain the new index profile of the waveguide and new n_{eff}. However, if the optical field of the guided mode is well confined so that the applied electric field is almost uniform across it, then we can approximate Δn_{eff} by the electrooptic index change at the waveguide axis. This change is given by [3]

$$\Delta n_e = -\frac{1}{2} n_e^3 r_{33} E_z \tag{3.7}$$

with E_z given by [4]

$$E_z = \frac{2}{\pi} \frac{V}{a} \tag{3.8}$$

where V and a are the applied voltage and separation between the two electrodes, respectively.

3.3 Holographic Gratings

An important step in the fabrication of corrugated waveguide devices is that of corrugating a waveguide surface. Since the period of the corrugations required in this application is of the order of a micron or less, classical ruling and conventional photolithographic techniques cannot be used for writing the grating lines. Instead, the grating masks have to be generated either by electron-beam lithography or holographic interference techniques. The latter, which records the interference fringes of two collimated intersecting laser beams, will be used in our work.

In the holographic interference technique, the surface to be corrugated is spin-coated with a layer of photoresist. Two plane waves of the same wavelength λ are incident upon the photoresist surface at an angle 2θ as shown in Fig. 3.2a. The total field on the surface is

$$E|_{x=0} = A\, e^{ikz\, \sin\theta} + \rho A\, e^{-ikz\, \sin\theta + i\phi}$$

where ρ and ϕ are the amplitude ratio and the phase difference between the two beams, respectively. The corresponding intensity distribution is

$$|E|^2_{x=0} = |A|^2 \left[1 + \rho^2 + 2\rho \cos(2kz \sin\theta - \phi)\right] \qquad (3.9)$$

which is modulated in the z direction with a period $\Lambda = \lambda/(2\sin\theta)$. When $\rho = 1$, we have the extremes of 0 and $4|A|^2$ in (3.9); so the intensity contrast is maximum if the intensity of the two beams is equal over the surface. In addition, as long as ϕ is constant in time, the interference pattern will remain stationary in space. Fig. 3.2b shows a resulting photoresist pattern after development.

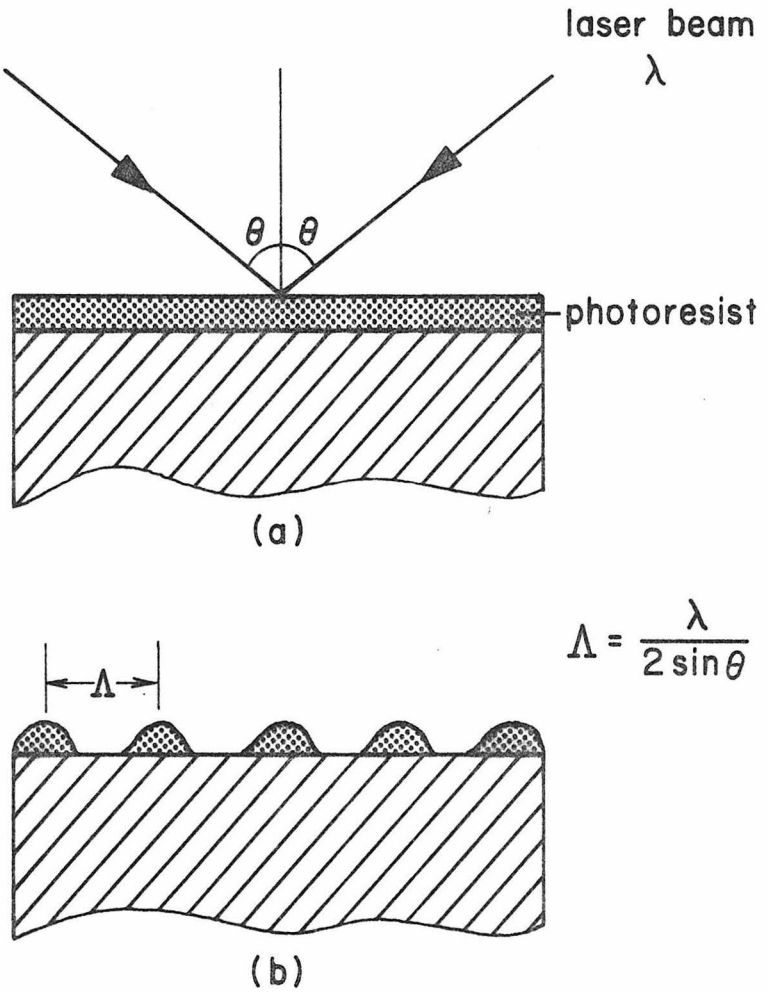

Fig. 3.2 (a) Exposure of photoresist by two interfering laser beams.
(b) Photoresist pattern after development.

3.4 Experimental Results

In our first experiment, we used a planar Ti-diffused $LiNbO_3$ waveguide. The waveguide was formed by diffusing a 200 Å Ti metal film into a Y-cut $LiNbO_3$ substrate at 975°C for 5 hours [5]. The resulting waveguide supported a TE_0 mode with an index $n_{eff} = 2.212$ at $\lambda = 6328$ Å. The surface corrugation was then fabricated by ion-beam etching through a photoresist mask generated by a holographic interference technique. The period of the corrugation was determined to be 5180 Å. We chose a shallow corrugation to ensure that the coupling length L was the geometrical length of the grating.

A TE_0 mode at $\lambda = 6328$ Å was excited in the waveguide by a rutile prism coupler and diffracted out to air by the corrugation grating. The diffraction angle ϕ was calculated and measured to be 8°. A typical far-field diffraction pattern for the coupled wave is shown in Fig. 3.3. Also shown in this figure is a plot of the measured angular divergence $\delta\phi$ versus the grating length L. For L = 2.5 mm, $\delta\phi \sim 0.15°$, which was larger than the calculated value $\delta\phi_{ideal} = 0.10°$.

The electrooptically induced index change was produced by applying a voltage to a pair of parallel Al electrodes deposited photolithographically on top of the waveguide. The separation between the two electrodes was a = 33 μm. The scanning of the coupled beam is shown in Fig. 3.4. This double exposure shows two states: without an applied voltage and with an applied voltage of 500 volts, which corresponds to a field of 10 volts/μm. The measured number of resolvable spots was 3, while the number predicted by (3.6) was 6.

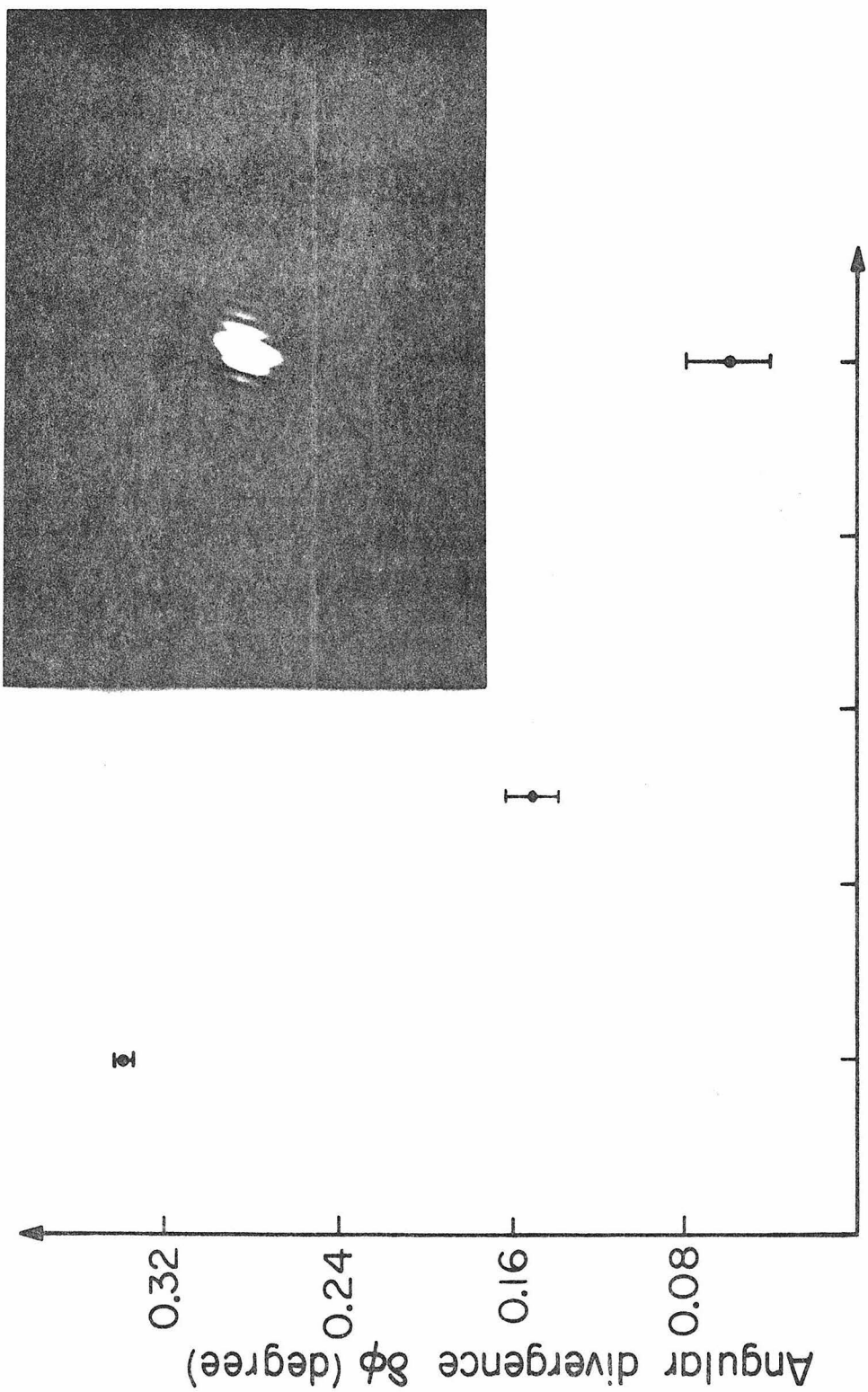

Fig. 3.3 Measured angular divergence versus the grating length. Inset is a typical far-field diffraction pattern of the coupled wave from a planar waveguide.

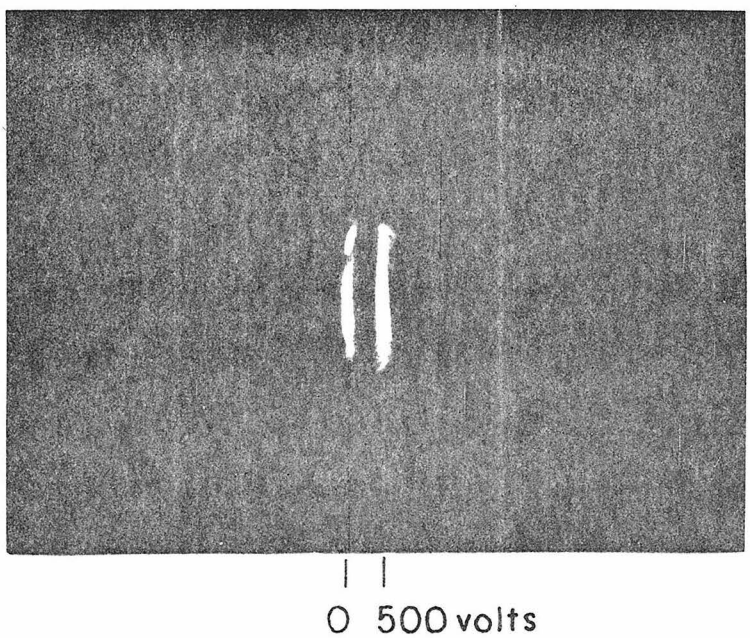

Fig. 3.4 Photograph of the resolved spots corresponding to the applied voltages as indicated. The device has L=2.5mm and a=33μm.

The discrepancies between the measured and the calculated values were partly due to an overestimate of Δn_{eff}, and partly due to imperfections in the structure.

To achieve a better electrooptic interaction, we performed the second experiment on a channel waveguide. A channel waveguide on a $LiNbO_3$ substrate was formed by the oxidation of a 4 μm wide, 200 Å thick Ti film at 600°C for 4 hours, and then the diffusion of the resulting oxide at 950°C for 5 hours [6]. It supported a single mode (n_{eff} = 2.210) with a loss constant of 1 db/cm. The grating parameters were Λ = 4200Å and L = 2.5 mm, so $\phi \sim 45°$ and $\delta\phi_{ideal} \sim 0.02°$. A typical far-field diffraction pattern of the coupled wave from the channel waveguide is shown in Fig. 3.5a. Fig. 3.5b shows the scanning of the coupled beam. The voltage of 150 volts is applied to electrodes with a spacing of 10 μm ($E_z \simeq 10$ volts/μm). The photograph in Fig. 3.5c shows three well resolved spots corresponding to voltages of 0, 100, and 200 volts, respectively. From the measurement, N ≃ 5 when V = 200 volts. The theoretical number is 8.

In this application we have used an electrooptically induced index change $\Delta n_e = (1\text{-}2) \times 10^{-3}$. A further reduction of the voltages required can be made by decreasing the separation between the two electrodes. The resolution can be improved by increasing the coupling length in the grating with a corresponding penalty in the switching speed. This will be discussed in a later section.

To summarize, we have demonstrated angular scanning of a beam coupled from a corrugated $LiNbO_3$ waveguide. This was done by using

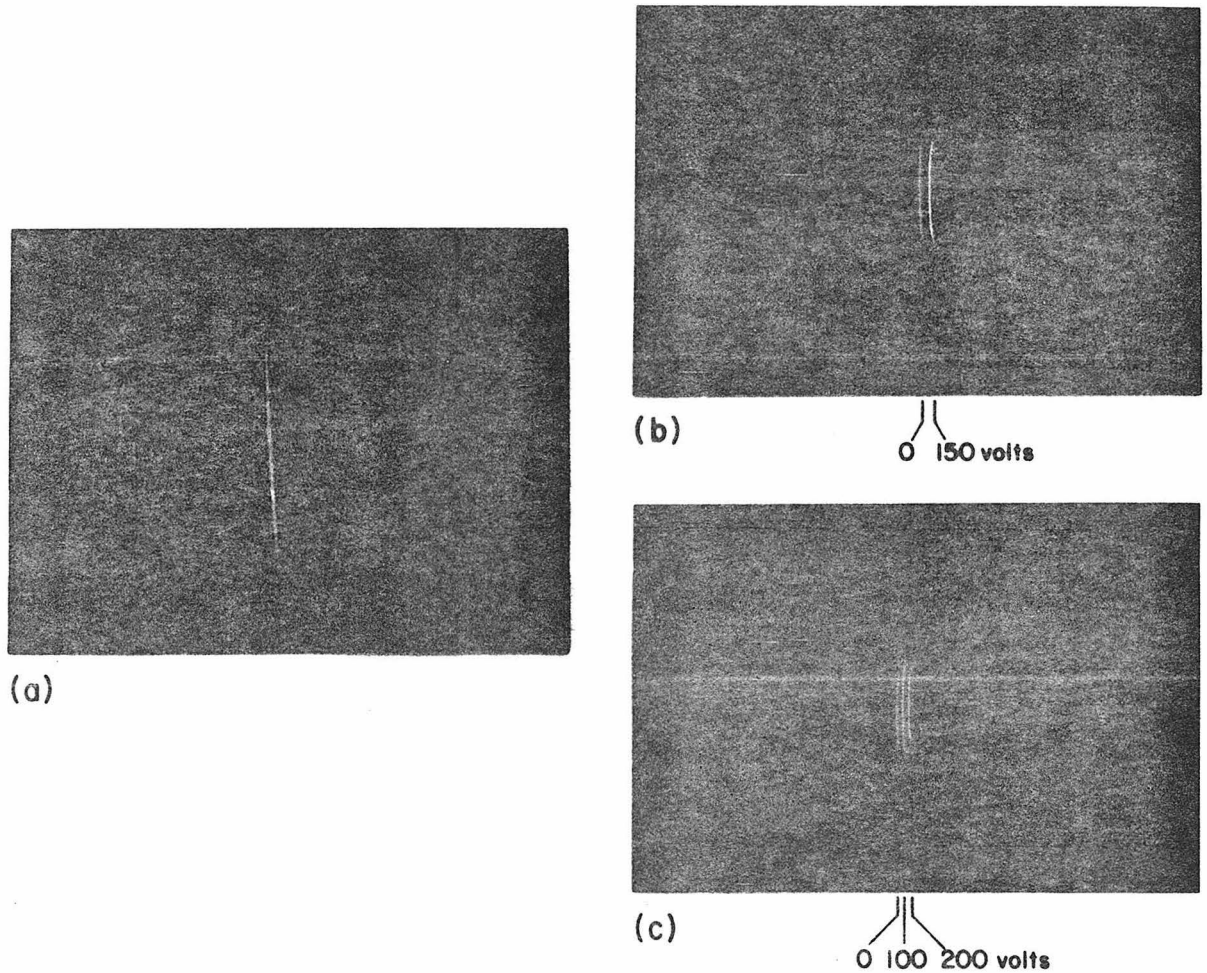

Fig. 3.5 (a) Typical far-field diffraction pattern of the coupled wave from a 4μm channel waveguide. (b) and (c) are photographs of the well-resolved spots corresponding to the applied voltages as indicated. The device has L=2.5mm and a=10μm.

the electrooptic effect to modulate the index of refraction in the corrugated section of the waveguide. The number of resolution elements is limited by the dielectric breakdown of the waveguide material. We have demonstrated the capability of producing one resolved spot per 3 volts/μm applied field. In principle, by using a grating of 1 cm length and an applied field of 40 volts/μm in the system of Fig. 3.1, the number of resolution elements should be ∿100.

3.5 Coupling Efficiency

In a previous section, we investigated the number of resolvable spots obtainable from the described electrooptic scanner. It is also important to consider other pertinent device parameters such as coupling efficiency and switching speed. The efficiency of a grating coupler in a diffused waveguide can be calculated using the method of a zig-zag ray approximation described in Section 2.6. The characteristics of guided modes in such waveguides are, of course, prerequisite in this consideration.

(a) Modes in a diffused waveguide

The diffused waveguide used in our experiment has a graded index of refraction in the film. According to Ref. 5, the small increase of index in the substrate has a Gaussian distribution. Thus the index profile for this waveguide structure (Fig. 3.6a) is

$$n(x) = \begin{cases} n_1 & x < 0 \\ n_3 + \Delta n\, e^{-x^2/\sigma^2}, \quad \Delta n \ll n_3 & x > 0 \end{cases} \tag{3.10}$$

where Δn is the increment at the surface, and σ is the 1/e folding

depth. Consider TE modes, $E_y = f(x)\, e^{i\beta z}$ where $f(x)$ satisfies

$$\frac{d^2f}{dx^2} + [k^2n^2(x) - \beta^2]f = 0 \qquad (3.11)$$

Closed-form solutions of (3.11) with $n(x)$ given by (3.10) do not exist. If we approximate the Gaussian function in (3.10) by a parabola: $\exp(-x^2/\sigma^2) \simeq 1 - x^2/\sigma^2$, (3.11) will become similar to a simple harmonic oscillator (SHO) equation in $x < 0$. We further assume that $f(0) = 0$ which is a good approximation for the large dielectric discontinuity at the waveguide surface. Then, the guided modes of interest have a formal similarity to the odd order modes (which are antisymmetric with respect to $x = 0$) of a SHO. This approximation method has been justified by comparing the measured and calculated β_m values [7].

After the following substitutions:

$$\xi = \alpha x \ , \ \alpha = \sqrt{k(2n_3\Delta n)^{1/2}/\sigma} \ , \text{ and } \mu = \frac{k^2(n_3^2 + 2n_3\Delta n) - \beta^2}{\alpha^2} \ ,$$

(3.11) becomes

$$\frac{d^2f}{d\xi^2} + (\mu - \xi^2)\, f = 0 \quad , f(0) = 0$$

The solutions require

$$\mu = 4m + 3$$

or
$$\beta^2 = \beta_m^2 = k^2(n_3^2 + 2n_3\Delta n) - (4m + 3)\, k\, (2n_3\Delta n)^{1/2}/\sigma \qquad (3.12)$$

with $m = 0,1,2,\ldots$(mode index). The corresponding eigenfunctions are

given by

$$f_m(\xi) \propto H_{2m+1}(\xi)\, e^{-\xi^2/2} \tag{3.13}$$

where H_{2m+1} are the Hermite polynomials. Typical field distributions for the first few modes are shown in Fig. 3.6b. Putting m = 0 in (3.12), we obtain the expression for n_{eff} of TE_0 mode.

$$n_{eff}^2 = n_3^2 + 2n_3\Delta n - 3(2n_3\Delta n)^{1/2}\ \frac{\lambda}{2\pi\sigma} \tag{3.14}$$

The waveguide used in the experiment has the following data:

$\lambda = 0.6328\ \mu m$, $\sigma = 2\ \mu m$, $n_3 = 2.2$, and $\Delta n = 0.02$

Hence $n_{eff} = 2.210$. Compare this to the observed value of 2.212.

To improve the above approximation, we can include a quartic term with an adjustable coefficient in the approach to a true Gaussian function and use this term as a first-order perturbation source [8] to the zero-order solutions described above.

(b) Coupling efficiency

For a grating coupler,

$$\text{the coupling efficiency} = \alpha_{-1} L \tag{3.15}$$

where L is the grating length, and $\alpha_{-1} = N\eta_{-1}$ as defined in (2.87). N is the mode bounce rate (cm^{-1}), and η_{-1} is the diffraction efficiency.

In a diffused waveguide, the zig-zag ray model of a guided mode can be described in a manner shown in Fig. 3.6c. The mode bounce rate is thus

$$N = \frac{1}{L_B} \qquad \text{with} \quad L_B = 2(r + s_1) \tag{3.16}$$

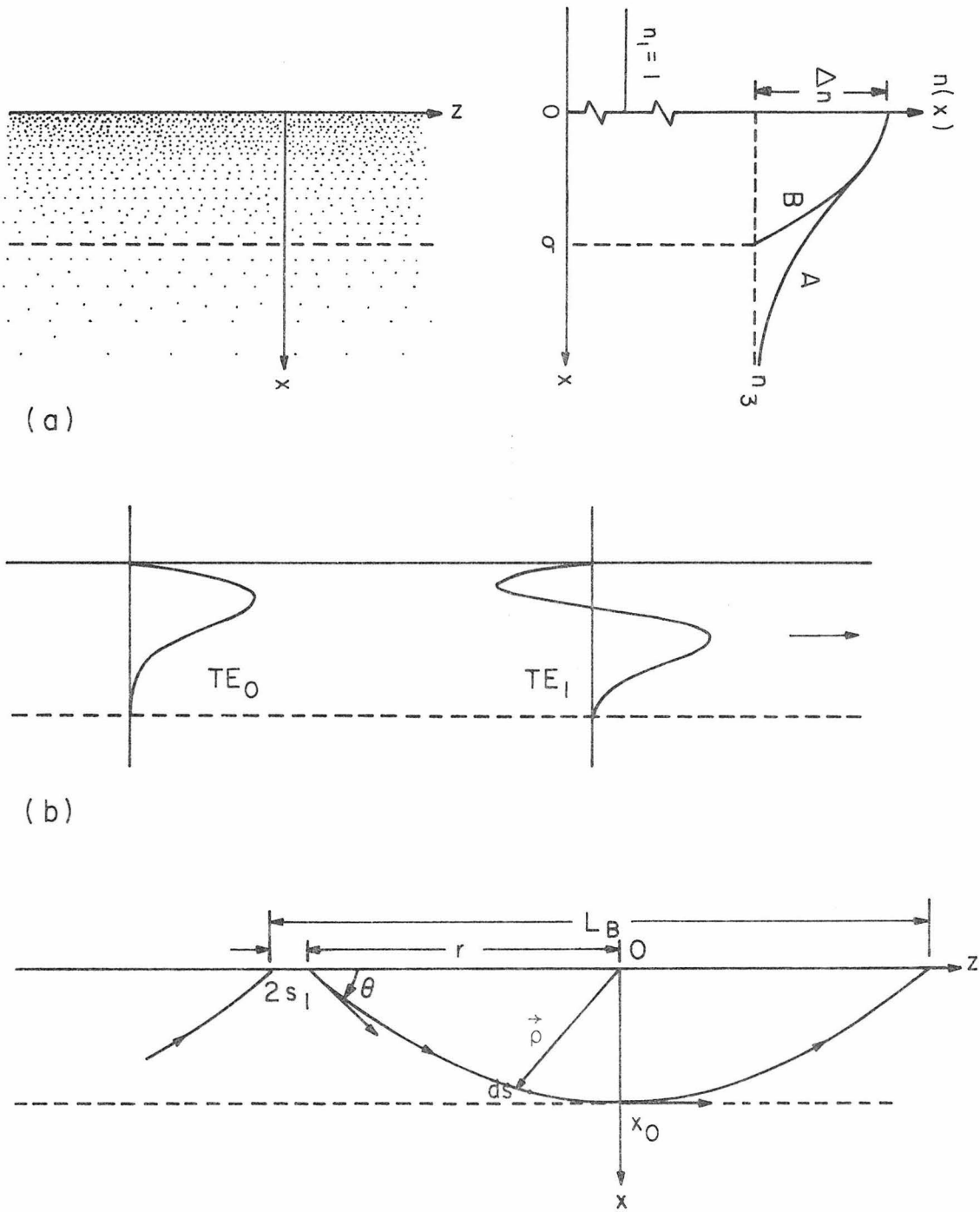

Fig. 3.6 (a) Index profile of a diffused waveguide. Curve A is the true Gaussian function. Parabola curve B is an approximate profile. (b) Approximate field distributions for the first two order TE modes. (c) Zig-zag ray model in a diffused waveguide and the relevant coordinates and parameters.

where the correction for the Goos-Hänchen shift $2s_1$ is necessary only at the dielectric discontinuity at $x = 0$. $2r$ is the distance between the entering and emerging points of the ray at the waveguide surface. It is determined by solving the (eikonal) ray equation. The ray equation [9] is written as (Fig. 3.6c)

$$\frac{d}{ds}\left(n \frac{d\vec{\rho}}{ds}\right) = \vec{\nabla} n \tag{3.17}$$

For a very confined mode, $ds \simeq dz$, and the x-component of (3.17) is reduced to

$$\frac{d^2x}{dz^2} = \frac{1}{n} \frac{dn}{dx} \tag{3.18}$$

Using the approximate $n(x)$

$$n(x) = n_3 + \Delta n - \Delta n \frac{x^2}{\sigma^2} \qquad x > 0$$

Then, to first-order in Δn, (3.18) becomes

$$x'' = - \frac{\Delta n}{n_3} \frac{2x}{\sigma^2}$$

where the prime indicates a derivative with respect to z. The boundary conditions are

$$z = -r \quad , \quad x = 0 \quad , \quad x' = \tan\theta$$

$$z = 0 \quad , \quad x = x_o \quad , \quad x' = 0$$

where $\pm \tan\theta$ is the slope of the trajectory at the surface, $\theta = \cos^{-1}\left(\frac{n_{eff}}{n_3+\Delta n}\right)$, and x_o is the turning point. r in (3.16) is thus

determined as follows:

$$x' = \tan\theta, \quad x = 0 \implies x' = \sqrt{\tan^2\theta - \frac{2\Delta n}{n_3}\frac{x^2}{\sigma^2}}$$

$$x' = 0 \ , \quad x = x_o \quad \text{determines} \quad \frac{x_o}{\sigma} = \frac{\tan\theta}{\sqrt{\frac{2\Delta n}{n_3}}}$$

$$z = 0 \ , \quad x = x_o \implies z = \frac{\sigma}{\sqrt{\frac{2\Delta n}{n_3}}}\left(\sin^{-1}\frac{x}{x_o} - \frac{\pi}{2}\right)$$

$$z = -r, \quad x = 0 \quad \text{determines} \quad r = \frac{\pi\sigma}{2\sqrt{\frac{2\Delta n}{n_3}}} \tag{3.19}$$

Note that r is independent of θ, which is not generally true. This is an artifact of the parabolic approximation used in the above derivation. The Goos-Hänchen shift is given by

$$s_1 = \frac{\cot\theta}{q} \tag{3.20}$$

where

$$q = k\sqrt{n_{eff}^2 - n_1^2}$$

Applying the same data used to calculate n_{eff} in (3.14), we obtain

$$\theta = 5.4^\circ \quad , \quad r = 23.3\ \mu m \ , \quad \text{and} \quad s_1 = 0.5\ \mu m$$

Thus $N = 1/L_B = 210\ cm^{-1}$.

Next, we calculate the diffraction efficiency of the surface grating. We are only interested in the diffraction to the air side. From (2.96)

$$\eta_{-1} = \frac{\tau_{-1}}{\sigma_o} \left|\frac{c_{-1}}{A}\right|^2 \qquad \text{with} \qquad \frac{c_{-1}}{A} = -a\,\frac{\sigma_o(\sigma_o - \tau_o)}{\rho_{-1} + \tau_{-1}} \tag{3.21}$$

where $\sigma_o = k\sqrt{(n_3 + \Delta n)^2 - n_{eff}^2}$, $\tau_o = iq = ik\sqrt{n_{eff}^2 - n_1^2}$

$$\rho_{-1} = k\sqrt{(n_3 + \Delta n)^2 - (n_{eff} - \frac{\lambda}{\Lambda})^2}, \quad \tau_{-1} = k\sqrt{n_1^2 - (n_{eff} - \frac{\lambda}{\Lambda})^2}$$

Using the values $a = 200\text{Å}$ (or $d = 400$ Å), $\Lambda = 4200$ Å, and the previous data, we obtain $\eta_{-1} = 0.29\%$.

Thus $\alpha_{-1} = N\eta_{-1} = 0.61\ \text{cm}^{-1}$, and the coupling efficiency (3.15) is 15% for $L = 2.5$ mm.

The coupling efficiency can be increased by using a blazed grating. A result of such a consideration is shown in Fig. 3.7a [10]. The curve shown is for propagation from left to right. For the opposite direction of propagation the same curve is obtained when the abscissa is replaced with $1 - \frac{\Delta}{\Lambda}$. From Fig. 3.7b it follows that the radiated power exercised by modes traveling in opposite directions is not equal and can differ by a large factor. This is analogous to the blazing effect in conventional spectroscopic gratings. For $\Delta/\Lambda = 0$, the power radiated into region 1 is approximately 10 times that radiated into region 3, and conversely for $\Delta/\Lambda = 1.0$ (or $1 - \frac{\Delta}{\Lambda} = 0$). In the former case, the guide appears to widen as the wave passes under each sawtooth. Thus power is allowed to leak out to the superstrate. In the latter case, a wave traveling in the opposite direction sees a contracting guide under each sawtooth, and power is forced toward the substrate in a manner similar to that of a tapered coupler. Alternatively, this can be explained using a ray

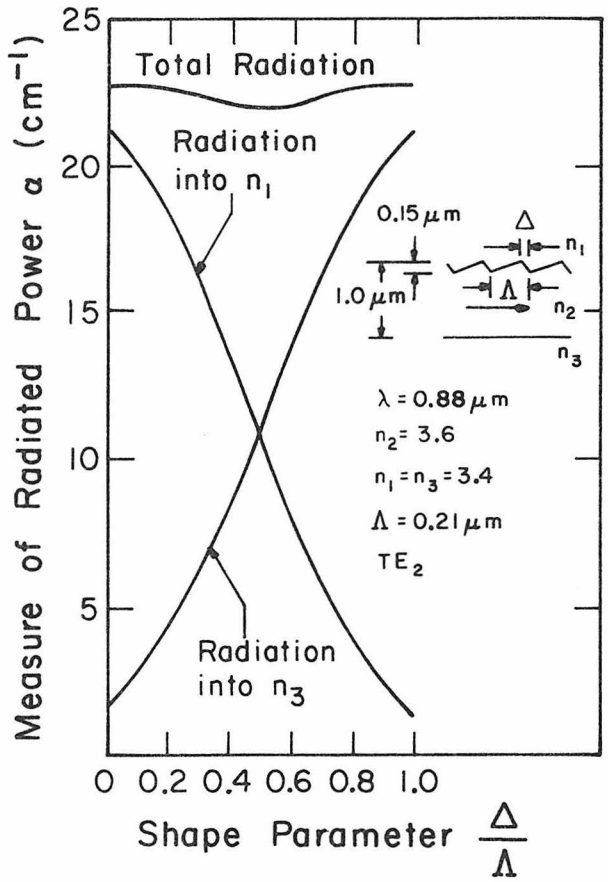

(a)

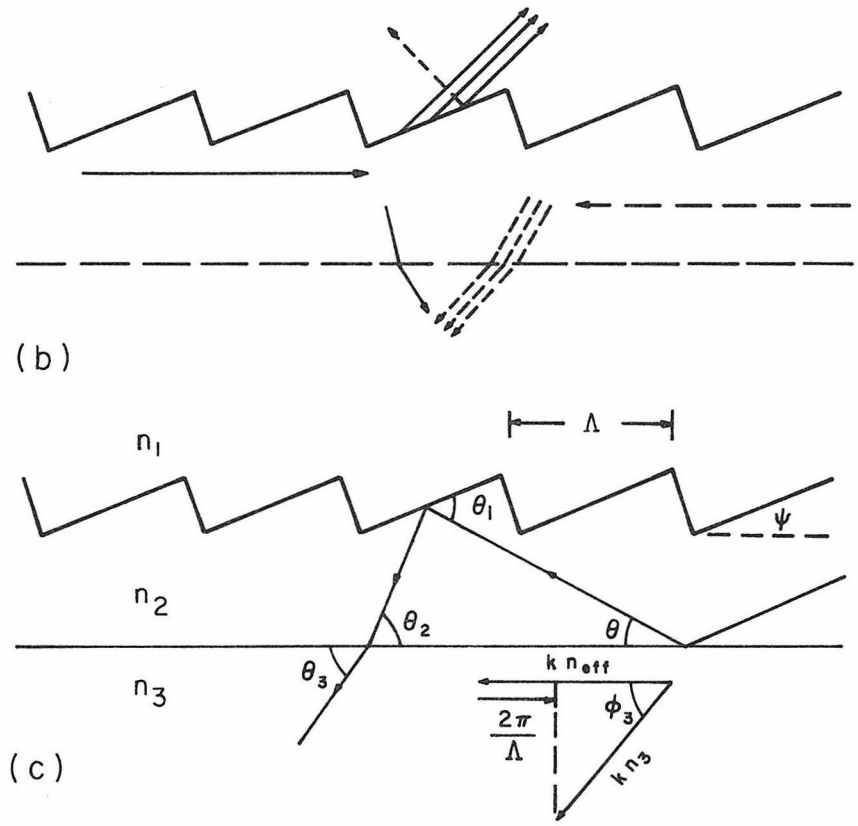

Fig. 3.7 (a) Radiated power versus shape parameter in a triangular grating coupler (After [10]). (b) Blazing effect in a corrugated waveguide. (c) Ray picture of a guided wave in a waveguide with a blazed grating at the surface. The blazing effect is optimized when $\theta_3 = \phi_3$.

picture as in Fig. 3.7c. The direction of the beam coupled into the substrate is determined by the phase-matching condition

$$n_3 \cos \phi_3 = n_{eff} - \frac{\lambda}{\Lambda} \tag{3.22}$$

The radiation that is coupled out will be enhanced if the face of the grating is inclined at such an angle that the guided wave is reflected and then refracted into the direction specified by (3.22). In Fig. 3.7c, this implies $\theta_3 = \phi_3$. θ_3 is related to the n_{eff} of the waveguide and the blazing angle ψ by the following equations from geometric optics considerations:

$$\theta_1 = \theta + \psi \quad , \qquad \theta = \cos^{-1}\left(\frac{n_{eff}}{n_2}\right)$$

$$\theta_2 = \theta_1 + \psi$$

$$n_3 \cos \theta_3 = n_2 \cos \theta_2 \tag{3.23}$$

Experimentally, a high-efficiency blazed grating coupler has been demonstrated[11]. The technique used for fabricating such gratings and some preliminary results will be discussed in Chapter 5.

3.6 Switching Speed and Power Consumption

The switching speed of an acousto-optic device is limited by the finite transit time of the acoustic wave across the optical beam. However, this drawback does not exist in an electrooptic device in which the transit time of light across the device (say, the grating length in our case) is very short compared with the RC time-constant of the device.

The capacitance C for an electrode configuration in Fig. 3.1 is given by [12]

$$C = \frac{K'}{K} \varepsilon L \tag{3.24}$$

where ε is a composite dielectric constant to be discussed later. K and K' are the complete elliptic integrals: K = K(k), K' = K(k'), $k' = \sqrt{1-k^2}$, and k = a/b. Parameters a, b, and L are all shown in Fig. 3.1. Assume b >> a, then (3.24) is reduced to

$$C = \frac{2}{\pi} \ell n(\frac{4b}{a}) \varepsilon L \tag{3.25}$$

For example, if a/b = 1/5, (3.25) gives C = 1.91 ε L. Compare this to the value of 1.90 εL obtained from (3.24) using polynomial expansions of the complete elliptical integrals. The electrodes are deposited on the surface of a $LiNbO_3$ crystal. We can approximate [13] the composite dielectric constant of this structure by

$$\varepsilon = \frac{1}{2} (\varepsilon_o + \sqrt{\varepsilon_y \varepsilon_z}) \tag{3.26}$$

where ε_y and ε_z are the relevant dielectric constants of $LiNbO_3$. $\varepsilon_y = 43\ \varepsilon_o$, $\varepsilon_z = 28\ \varepsilon_o$, and ε_o is the vacuum permittivity. Thus, in the case of a/b = 1/5, the device capacitance is C(pf) = 3.0 L(cm).

If a load resistance R is placed in shunt with C, and the combination is driven by a matched [14] voltage generator, the operational bandwidth is given by

$$B = \frac{1}{\pi RC} \tag{3.27}$$

The power dissipated is

$$P = \frac{V_m^2}{2R} \tag{3.28}$$

where the peak voltage V_m is determined by the desired number of resolvable spots N. In terms of (3.27), we obtain the expression for the power per bandwidth:

$$\frac{P}{B} = \frac{\pi}{2} C V_m^2 \tag{3.29}$$

For example, using a grating length L = 1 cm and a separation between the two electrodes a = 5 μm, it requires π volts to produce a resolvable spot. If we choose N = 5, then V_m = 15 volts, which still can be generated by a high-speed transistor circuitry. The device capacitance is 3.0 pf. The maximum switching speed (or operational bandwidth) could be as high as 2 GHz for R = 50Ω. The power required per unit bandwidth is thus 1 mW/MHz.

Chapter 3 - References

1. F. R. Gfeller and C. W. Pitt, "Collinear acousto-optic deflection in thin films," Electron. Lett. 8, 549 (1972).
2. C. S. Tsai, L. T. Nguyen, S. K. Yao, and M. A. Alhaider, "High-performance acousto-optic guided-light-beam device using two tilting surface acoustic waves," Appl. Phys. Lett. 26, 140 (1975).
3. A. Yariv, Quantum Electronics, 2nd ed. (Wiley, New York, 1975), Chap. 14.
4. D. Marcuse, "Electro-optic coupling between TE and TM modes in anisotropic slabs," IEEE J. Quantum Electron. QE-11, 759 (1975).
5. R. V. Schmidt and I. P. Kaminow, "Metal-diffused optical waveguides in $LiNbO_2$," Appl. Phys. Lett. 25, 458 (1974).
6. B. Chen, G. L. Tangonan, and A. Lee, "Horn structures for integrated optics," Opt. Commun. 20, 250 (1977).
7. R. D. Standley and V. Ramaswamy, "Nb-diffused $LiTaO_3$ optical waveguides: planar and embedded strip guides," Appl. Phys. Lett. 25, 711 (1974).
8. J. F. Lotspeich, "A perturbation analysis of modes in diffused optical waveguides with Gaussian index profile," Opt. Commun. 18, 567 (1976).
9. M. Born and E. Wolf, Principles of Optics, 2nd ed. (Macmillan, New York, 1964), p. 122.
10. W. Streifer, R. D. Burnham, and D. R. Scifres, "Analysis of grating-coupled radiation in GaAs:GaAlAs lasers and waveguides--II: Blazing effects," IEEE J. Quantum Electron. QE-12, 494 (1976).

11. T. Aoyagi, Y. Aoyagi, and S. Namba, "High-efficiency blazed grating couplers," Appl. Phys. Lett. 29, 303 (1976).

12. American Institute of Physics Handbook, 2nd ed., D. E. Gray, ed. (McGraw-Hill, New York, 1963), p. 5-15.

13. H. Engan, "Excitation of elastic surface waves by spatial harmonics of interdigital transducers," IEEE Trans. Electron Devices ED-16, 1014 (1969).

14. I. P. Kaminow and E. H. Turner, "Electro-optic light modulators," Proc. IEEE 54, 1374 (1966).

Chapter 4

WAVELENGTH DEMULTIPLEXERS AND BROAD-BAND OPTICAL FILTERS

4.1 Introduction

In this chapter, we describe the fabrication of multifrequency waveguide devices which include wavelength demultiplexers and broad-band filters. These ideas are illustrated in Fig. 4.1, showing devices in which chirped gratings are used. A chirped grating has a monotonic variation in period along the grating length. In a chirped-grating deflector different wavelengths are deflected from different locations of the grating, and are separated spatially. Similarly, in a chirped-grating reflector, different wavelengths are reflected at different points along the grating. Thus the "chirp" in the grating has the effect of deflecting or reflecting a broad band of wavelengths.

The coupled-mode theory developed in Chapter 2 will be extended to study the characteristics of these two devices. Experimental results are discussed and compared with theory. For details of some experimental techniques, the interested reader is referred to Chapter 5.

4.2 Chirped Gratings

In fabricating a chirped-grating mask, we again use a holographic interference technique. The sample is exposed to the pattern produced by the interference of a collimated beam and a cylindrically focused beam derived from the same laser. In this case, the total field on the surface (Fig. 4.2) is

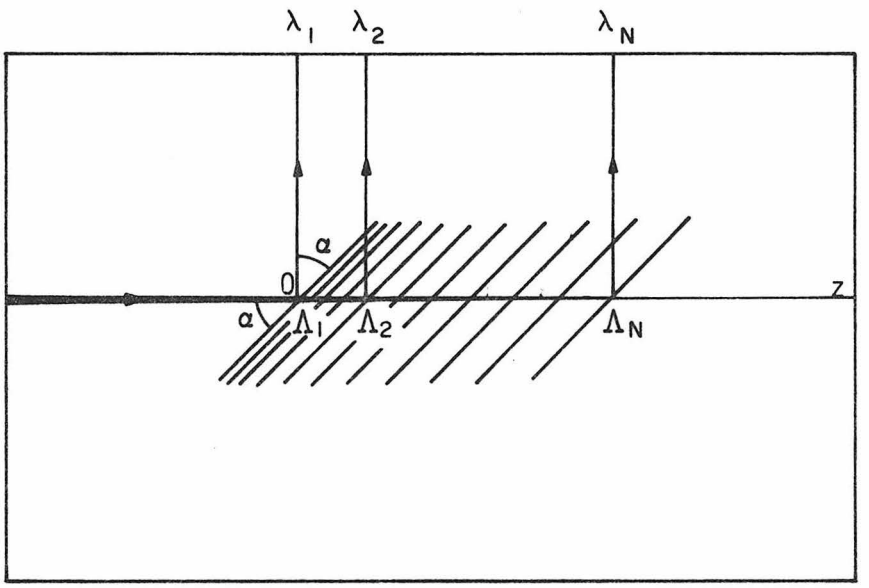

(a) $\lambda_i = 2n_{eff}\Lambda_i \sin\alpha$, $I = 1, 2, \cdots N$

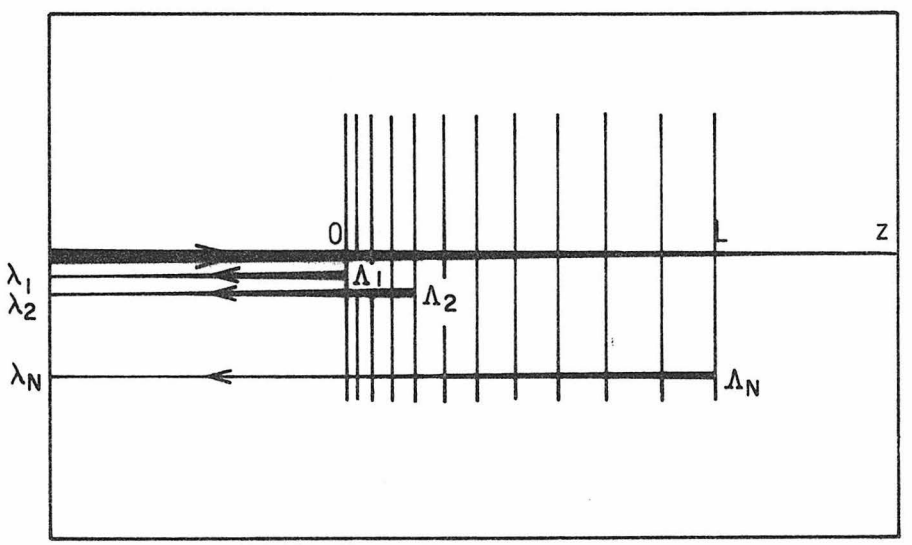

(b) $\lambda_i = 2n_{eff}\Lambda_i$, $i = 1, 2, \cdots N$

Fig. 4.1 Schematic diagram of (a) a wavelength demultiplexer and (b) a broad-band optical filter in which chirped gratings are used.

$$E|_{x=0} = A\, e^{-ikz \sin\theta} + B\, e^{-ik\sqrt{(z-z_f)^2 + x_f^2}}$$

where $k = 2\pi/\lambda$, and λ is the recording wavelength. The resulting interference pattern is

$$|E|^2_{x=0} = 2|A|^2\,[1 + \cos\phi(z)], \quad \text{assuming } A = B,$$

where $\phi(z) = k(z \sin\theta - \sqrt{(z-z_f)^2 + x_f^2})$. The period distribution is thus given by

$$\Lambda(z) = \frac{2\pi}{d\phi/dz} = \frac{\lambda}{\sin\theta + \dfrac{z_f - z}{\sqrt{(z_f-z)^2 + x_f^2}}} \quad , \qquad 0 < z < L \qquad (4.1)$$

For small chirps , $L \ll z_f, x_f$, and (4.1) can be approximated by

$$\Lambda(z) \simeq \Lambda(0) + \frac{\Lambda(0)^2}{\lambda\, r_f} z$$

or

$$\frac{2\pi}{\Lambda(z)} = \frac{2\pi}{\Lambda(0)} - \frac{2\pi}{\lambda}\frac{z}{r_f}$$

These linear functions will be used in our device analysis.

4.3 Theory of Wavelength Demultiplexers

Some interesting parameters in the design of demultiplexers are the deflection efficiency, and the approximate number of resolvable wavelengths. In this analysis, we assume a chirped grating whose period varies linearly with a rate γ in a length L. The period variation in the direction (z) of the incident beam is thus

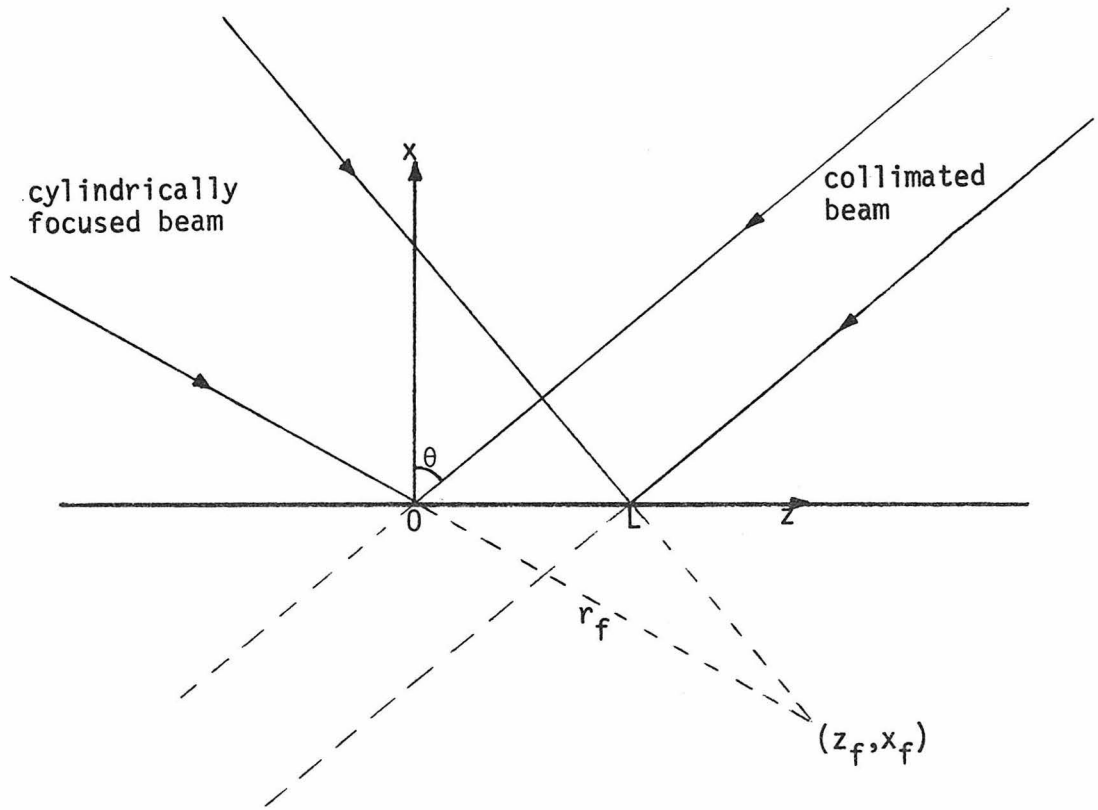

Fig. 4.2 Holographic interference method used for generating fringe patterns of variable period, namely chirped gratings.

$$\Lambda(z) = \Lambda(0) + (\gamma \sin \alpha)z \ , \qquad 0 < z < L/\sin \alpha \tag{4.2}$$

where α is the incident angle with respect to the grating lines (Fig. 4.1a). The equivalent chirping rate is $\gamma \sin \alpha$. The effective corrugated section which will deflect light with a wavelength λ can be derived from coupled-mode theory. As shown in Section 2.4, a grating possesses stop bands of

$$\Delta(\Delta\beta) = 2\kappa_\ell \tag{4.3}$$

in which the propagation is forbidden. $\kappa_\ell(\alpha)$ is the ℓ^{th}-order coupling coefficient, and $\Delta\beta$ is a phase mismatch factor which in this case is $\Delta\beta = \beta \sin \alpha - \ell \pi/\Lambda$. In terms of wavelength, (4.3) becomes

$$(\Delta\lambda)_B = \frac{\kappa_\ell \lambda^2}{\pi n_{eff} \sin \alpha} \tag{4.4}$$

The subscript B indicates that the interval $\Delta\lambda$ has a center wavelength λ which satisfies the Bragg condition

$$\ell\lambda = 2n_{eff} \Lambda \sin \alpha \tag{4.5}$$

Conversely, if we fix the wavelength at (4.5) and vary the grating period, then the period interval which has the effect of deflecting this center wavelength can be derived from (4.4) and (4.5)

$$(\Delta\Lambda)_B = \frac{\kappa_\ell \lambda^2 \ell}{2\pi n_{eff}^2 \sin^2 \alpha} \tag{4.6}$$

In a chirped grating described by (4.2), the effective length along the

z axis, which corresponds to the amount of period variation in (4.6) is $L_{eff}/\sin\phi$ where

$$L_{eff} = \frac{(\Delta\Lambda)_B}{\gamma} = \frac{\kappa_\ell \lambda^2 \ell}{2\pi\gamma n_{eff}^2 \sin^2\alpha} \tag{4.7}$$

Although a plane wave analysis is employed in the above derivation, we always use a finite beam in a practical device. This leads to a consideration of the spatial resolution of the deflected beams. The above expression for L_{eff} is still applicable if the beam width w_{beam} is much larger than $L_{eff}\cos\alpha$. We also assume that $L_{eff}/\sin\alpha >> \lambda$, so the divergence of the deflected beam is negligible. It can be easily shown that the approximate number of resolvable wavelengths in the described demultiplexer is

$$N = \frac{L/\sin\alpha}{L_{eff}/\sin\alpha + w_{beam}} \tag{4.8}$$

where L_{eff} is taken as a wavelength-averaged value. The deflection efficiency is obtained from (2.72) by replacing L by L_{eff}.

$$R = \tanh^2\kappa_\ell L_{eff} = \tanh^2 \frac{\kappa_\ell^2 \lambda^2 \ell}{2\pi\gamma n_{eff}^2 \sin^2\alpha} \tag{4.9}$$

4.4 Experimental Results

An optical demultiplexer such as the one just described was fabricated in a glass waveguide and investigated using a tunable dye laser. The grating period required in this case was $\sim 3000\text{Å}$. In the first experiment, a glass waveguide was fabricated by sputter-depositing [1] a layer of Corning 7059 glass on a glass substrate. The

resulting waveguide supported a TM_0 mode with an index $n_{eff} \simeq 1.5$ at $\lambda = 6000\text{Å}$. A chirped-grating corrugation was then fabricated [1] on top of the waveguide. Its period variation ranged from 2930 to 3210Å over a distance of 6.5 mm. To demonstrate the demultiplexing effect, the output from a tunable dye laser was coupled into the waveguide with a prism coupler. The angle α at which the guided beam was incident upon the grating lines was set at $\sim 42°$. Fig. 4.3a shows the deflection of two different wavelengths from two different locations in the chirped grating. This is shown schematically in Fig. 4.3b. The two wavelengths have a 200Å difference and are separated spatially by 4 mm.

To measure more quantitatively some interesting parameters of the device, we performed a second experiment. A second sample was fabricated. The thickness of the waveguide was measured to be $t = 0.65$ μm. This waveguide supported a single mode (TM_0) of $n_{eff} = 1.54$ at $\lambda = 6000\text{Å}$ Other relevant indices of refraction were determined [1]: $n_3 = 1.51$ and $n_2 = 1.57$. The period variation of the grating was approximately linear over a portion of the total length. This region of interest has a period from 2975 to 3105Å over a distance $L = 3.5$ mm. So the chirping rate was $\gamma = 4 \times 10^{-6}$. The sinusoidal corrugation depth was estimated [1] to be $d = 400\text{Å}$, which corresponded to a coupling coefficient (B.6) of $\kappa_1 \simeq 80\ \text{cm}^{-1}$. The incident conditions were chosen so that the incident angle $\alpha = 40°$, and the beam width $w_{beam} = 500$ μm. Hence the effective length (4.7), the deflection efficiency (4.9), and the number of resolvable wavelengths (4.8) were calculated to be $L_{eff} \simeq 120$ μm, $R \simeq 50\%$, and $N \simeq 8$, respectively. The deflection efficiency was roughly measured by

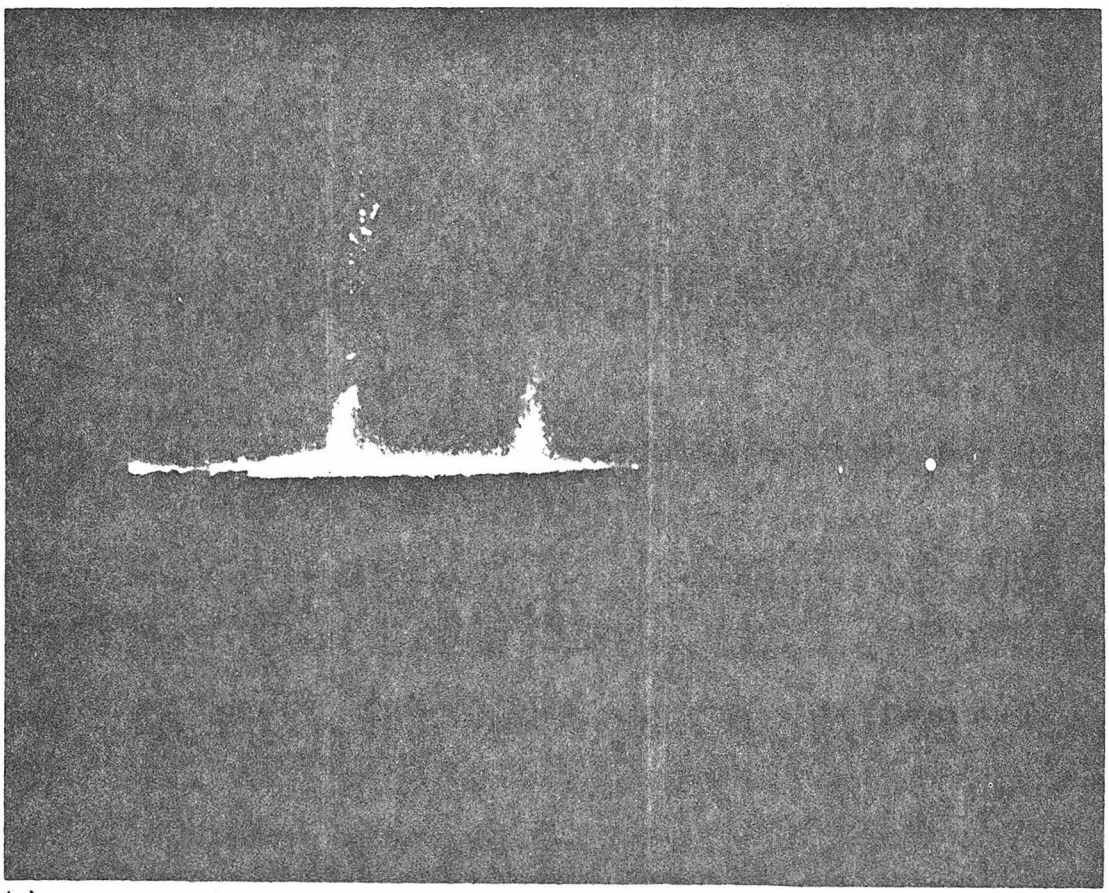

(a)

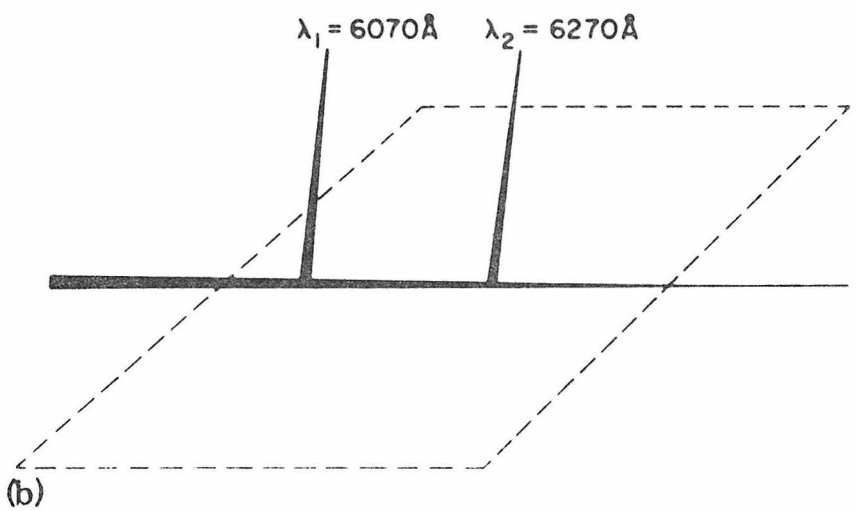

(b)

Fig. 4.3 (a) Photograph showing the deflection of two different wavelengths from two different locations in a chirped grating. (b) Schematic drawing of the experimental result shown in (a). The dashed lines outline the grating region.

using a fiber probe, and was ∿10%. The measured number of resolvable wavelengths was ∿7. Quantitative determination of R was thwarted by excessive scattering loss. The measured and calculated N were in good agreement.

To summarize, we have demonstrated the fabrication of wavelength demultiplexers using chirped gratings on the surface of thin-film glass waveguides. A demultiplexer with 8 resolvable wavelengths and 50% deflection efficiency has been studied. The deflection efficiency can be increased by using a small chirping rate with a corresponding penalty in the number of resolvable wavelengths or the device length. This device can demultiplex, according to wavelength, an optical signal traveling in a fiber, and send each wavelength component to a differeng fiber or detector in an array.

4.5 Theory of Broad-Band Grating Filters

Filter response of nonuniform almost-periodic structures has been the subject of current theoretical interest. The analysis of this problem uses coupled-mode theory. Kogelnik [2] showed that the reflection coefficient satisfied a Riccati equation and reported numerical results for reflection from chirped gratings and tapered gratings. In the case of small variations, it is possible to use perturbation techniques. Streifer et al. [3] used such a technique to obtain simple formulas for the first-order results. For linear chirps, Matsuhara et al. [4] gave an analytical solution which was in the form of the Whittaker function. However, we shall prove that the solution should

be in a form of parabolic cylinder functions. A simple method based on the direct integration of the coupled-mode equations will also be included in our analysis.

The generalized coupled-mode equations (see Appendix C) are

$$\begin{cases} \dfrac{dB}{dz} = K\,A\,e^{i(2\beta z - \phi(z))} \\ \dfrac{dA}{dz} = K^{*}B\,e^{-i(2\beta z - \phi(z))} \end{cases} \tag{4.10}$$

where $\phi(z) = \int_0^z \dfrac{2\pi}{\Lambda(z)}\,dz$

A and B are the complex amplitudes of the incident and reflected modes under consideration. K is the coupling coefficient and β is the propagation constant of the modes. In a chirped grating whose period varies as

$$\frac{2\pi}{\Lambda(z)} = \frac{2\pi}{\Lambda(0)} - 2\gamma z \quad , \qquad 0 < z < L \tag{4.11}$$

the phase $\phi(z)$ becomes

$$\phi(z) = \frac{2\pi}{\Lambda(0)}\,z - \gamma z^2$$

and the equations in (4.10) become

$$\begin{cases} \dfrac{dB}{dz} = i\kappa\,A\,e^{-i2\delta z}\,e^{i\gamma z^2} \\ \dfrac{dA}{dz} = -i\kappa B\,e^{i2\delta z}\,e^{-i\gamma z^2} \end{cases} \tag{4.12}$$

where κ is assumed to be a real and positive number. δ is a phase mismatch factor and is defined by

$$\delta = \frac{\pi}{\Lambda(0)} - \beta \tag{4.13}$$

The point where the Bragg resonance condition $\frac{2\pi}{\Lambda(z)} - 2\beta = 0$ is satisfied shall be referred to as the Bragg point z_B. We find

$$z_B = \delta/\gamma \tag{4.14}$$

which is a function of wavelength ($\beta = \beta(\lambda)$).

To simplify the equations, instead of using the coordinate z as in (4.11), we use z as a local coordinate (i.e., $z = 0$ corresponds to the Bragg point) for a given wavelength (or β). This results in

$$\frac{2\pi}{\Lambda(z)} = 2\beta - 2\gamma z \qquad -z_B < z < L - z_B$$

$$\phi(z) = 2\beta z - \gamma z^2$$

$$\begin{cases} \dfrac{dB}{dz} = i\kappa A\, e^{i\gamma z^2} \\ \dfrac{dA}{dz} = -i\kappa B\, e^{-i\gamma z^2} \end{cases} \tag{4.15}$$

If the condition $\gamma L << \beta$ is satisfied in our gratings, we can make the following substitutions

$$A = u\, e^{-\frac{1}{2} i\gamma z^2}, \qquad B = v\, e^{\frac{1}{2} i\gamma z^2}$$

The equations in (4.15) become

$$\begin{cases} \dfrac{dv}{dz} + i\gamma z v - i\kappa u = 0 \\ \dfrac{du}{dz} - i\gamma z u + i\kappa v = 0 \end{cases} \tag{4.16}$$

Equations (4.16) can be combined to give second-order differential equations for the incident wave u and the reflected wave v

$$\begin{cases} \dfrac{d^2v}{dz^2} + (\gamma^2 z^2 - \kappa^2 + i\gamma)v = 0 \\ \dfrac{d^2u}{dz^2} + (\gamma^2 z^2 - \kappa^2 - i\gamma)u = 0 \end{cases} \tag{4.17}$$

The boundary conditions are $v(L - z_B) = 0$ and $u(-z_B) = 1$. If we use a dimensionless variable ζ defined by

$$\zeta = (2\gamma)^{1/2} z$$

The equations (4.17) become

$$\begin{cases} \dfrac{d^2v}{d\zeta^2} + (\frac{1}{4}\zeta^2 - b)v = 0 \\ \dfrac{d^2u}{d\zeta^2} + (\frac{1}{4}\zeta^2 - a)u = 0 \end{cases} \tag{4.18}$$

where $a = \sigma + i/2$, $b = \sigma - i/2$, and $\sigma = \kappa^2/2\gamma$ (4.19)

These are the standard equations for the parabolic cylinder functions [5,6]. Some important properties of these functions are listed in Appendix D.

From (D.1) and (4.18), we see that the parameter c has different values for incident and reflected modes. These are a and b, and the corresponding functions are denoted by $E_a(\zeta)$ and $E_b(\zeta)$, respectively. Since a and b are complex conjugates, $[E_a(\zeta)]^* = E_b^*(\zeta)$ and $[E_b(\zeta)]^* = E_a^*(\zeta)$. Replacing c with b in the recurrence relation (D.3)

and with a in (D.4), we obtain a pair of equations

$$\begin{cases} \dfrac{dE_b(\zeta)}{d\zeta} + i\,\dfrac{\zeta}{2}\,E_b(\zeta) - i\sigma^{1/2}\,E_a(\zeta) = 0 \\ \dfrac{dE_a(\zeta)}{d\zeta} - i\,\dfrac{\zeta}{2}\,E_a(\zeta) + i\sigma^{1/2}\,E_b(\zeta) = 0 \end{cases} \tag{4.20}$$

which are, in fact, the same coupled-mode equations (4.16) satisfied by v and u, after the variable z is changed to ζ. Thus

$$\begin{pmatrix} u(\zeta) \\ v(\zeta) \end{pmatrix} = \begin{pmatrix} E_a(\zeta) \\ E_b(\zeta) \end{pmatrix}$$

is a pair of solutions for our problem. It can be easily shown that other independent solution-pairs are

$$\begin{pmatrix} E_a^*(\zeta) \\ E_b^*(\zeta) \end{pmatrix}, \quad \begin{pmatrix} E_a(-\zeta) \\ -E_b(-\zeta) \end{pmatrix}, \quad \text{and} \quad \begin{pmatrix} -E_a^*(-\zeta) \\ E_b^*(-\zeta) \end{pmatrix}$$

Consequently, the general solutions for $\begin{pmatrix} u(\zeta) \\ v(\zeta) \end{pmatrix}$ may be written as some linear combination of two of the above four linearly independent solutions. Using the coupled-mode equations (4.20) in the Wronskian (D.2) for the functions $E_a(\zeta)$ and $E_a^*(\zeta)$, we obtain $|E_a|^2 - |E_b|^2 = 2\sigma^{-1/2}$ which is constant for all ζ and describes the energy conservation law in the physical process.

In order to apply the asymptotic properties of the E-functions and thus simplify the solutions, we assume that the boundary coordinates satisfy a certain condition. For $\sigma \gg 1$ (very small chirps), this

condition is $|\zeta_{bdry}| >> \sigma$. For $\sigma << 1$, this condition is $|\zeta_{bdry}| >> 1$ (or $\min(z_B, L-z_B) >> \gamma^{-1/2}$). So the assumption is that the Bragg point or region of maximum coupling cannot be near the grating edges. Hence, the boundary condition $v(z = L-z_B) = 0$, which coincides with the asymptotic behavior of $E_b(\zeta)$ (see (D.8)), gives

$$v(\zeta) = C\, E_b(\zeta)$$

The constant C will be determined by the other boundary condition. In terms of the functions (D.7) of negative arguments

$$v(\zeta) = \frac{C}{2e^{2\pi\sigma} - 1} [-e^{\pi\sigma} E_b(-\zeta) + (e^{2\pi\sigma} - 1)^{1/2} E_b^*(-\zeta)]$$

The corresponding $u(\zeta)$ is

$$u(\zeta) = \frac{C}{2e^{2\pi\sigma} - 1} [e^{\pi\sigma} E_a(-\zeta) - (e^{2\pi\sigma} - 1)^{1/2} E_a^*(-\zeta)]$$

Using the asymptotic expressions (D.8)

$$u(z=-z_B) = \frac{C}{2e^{2\pi\sigma} - 1} e^{\pi\sigma} 2^{1/2} \sigma^{-1/4}$$, neglecting the phase factor

The condition $u(z=-z_B) = 1$ leads to

$$C = 2^{-1/2} \sigma^{1/4} e^{-\pi\sigma}(2e^{2\pi\sigma} - 1)$$

Thus

$$u(\zeta) = 2^{-1/2} \sigma^{1/4} e^{-\pi\sigma}[e^{\pi\sigma} E_a(-\zeta) - (e^{2\pi\sigma} - 1)^{1/2} E_a^*(-\zeta)]$$

$$= 2^{-1/2}\sigma^{1/4}[e^{-\pi\sigma} E_a(\zeta) + 2(e^{2\pi\sigma} - 1)^{1/2} E_a^*(\zeta)] \qquad (4.21)$$

and

$$v(\zeta) = 2^{-1/2}\,\sigma^{1/4}\,e^{-\pi\sigma}(2e^{2\pi\sigma} - 1)\,E_b(\zeta)$$

$$= 2^{-1/2}\,\sigma^{1/4}\,e^{-\pi\sigma}[-e^{\pi\sigma}E_b(-\zeta) + (e^{2\pi\sigma} - 1)^{1/2}\,E_b^*(-\zeta)] \qquad (4.22)$$

Power series expansions about $\zeta = 0$ are possible for numerical evaluation of $v(\zeta)$, but are useful only for $|\zeta| << |b|$. Asymptotic series are also available for $|\zeta| >> |b|$. For $|\zeta|$ comparable to $|b|$, the numerical values are best calculated by direct integration of the coupled-mode equations in (4.16). Typical field intensity distributions for the reflected mode are shown in Fig. 4.4. The reflectivity is thus the steady-state value of the curve at the far-left side of the figure. An analytical expression for the reflectivity R can be derived from the asymptotic behavior of (4.22)

$$R = |v(z=-z_B)|^2 = 1 - e^{-2\pi\sigma} = 1 - e^{-\pi\kappa^2/\gamma} \qquad (4.23)$$

The correctness is checked by the expression for the transmissivity

$$T = |u(z = L-z_B)|^2 = e^{-\pi\kappa^2/\gamma} = 1 - R$$

The expression (4.23) is good to all wavelengths whose Bragg points are not near the grating edges.

Regions of the guide for which $2\pi/\Lambda(z) \leq \beta + kn_3$ will cause the mode to radiate into the substrate of index n_3. If the light is coupled into the larger period end of the guide, most of the light is radiated into the substrate before it reaches the Bragg point z_B and is reflected. If we define z_s by $2\pi/\Lambda(z_s) = \beta + kn_3$, then clearly z_s must be greater than z_B for the right-traveling mode to be reflected efficiently. However,

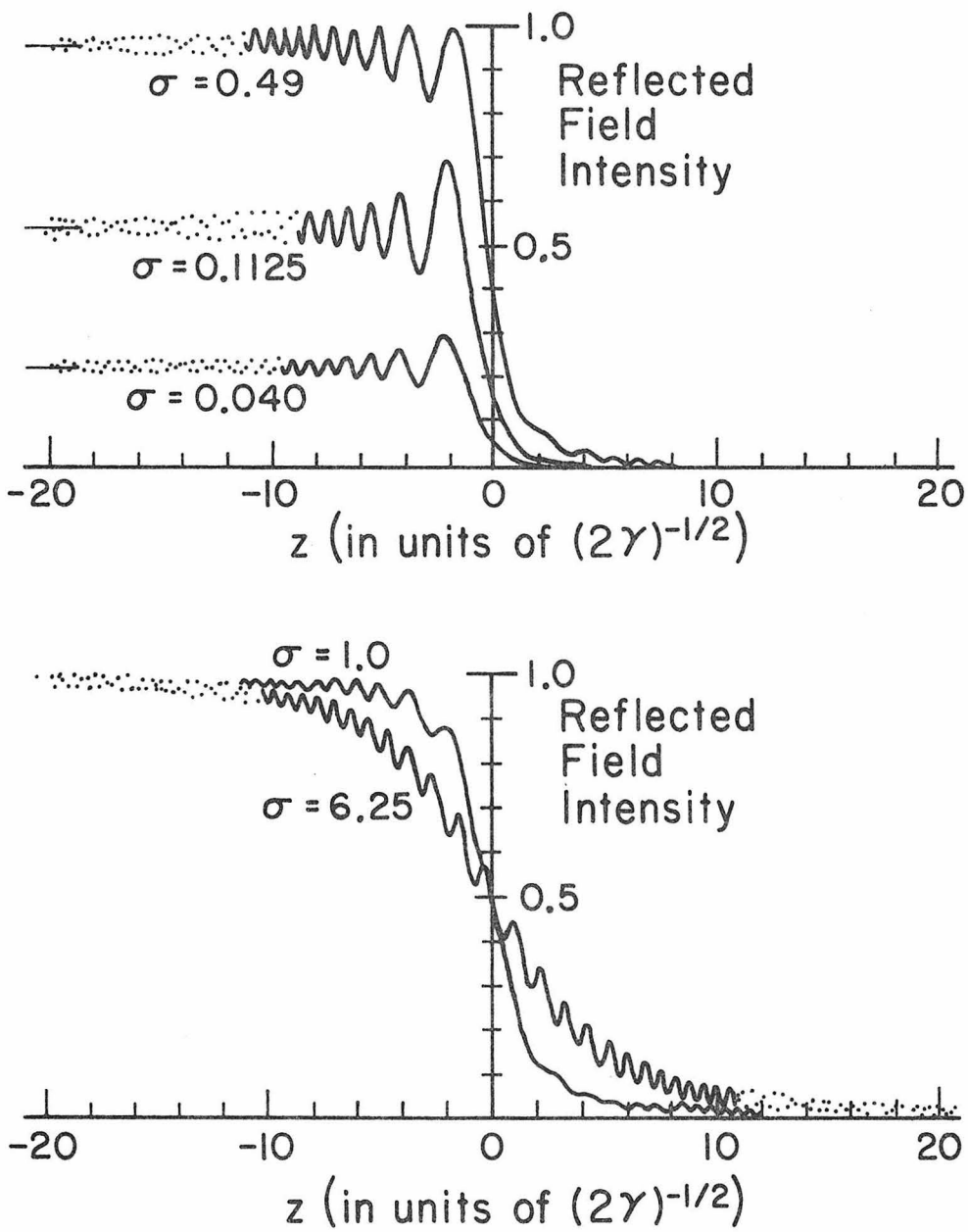

Fig. 4.4 Reflected field intensity as a function of distance from the Bragg point of a chirped grating reflector with various σ (or γ) 's. Note that the scale of distance is different from curve to curve.

if z_s is only slightly larger than z_B, we may not obtain full reflection. If at least 90% of the reflected light intensity is to be reflected before the point z_s, then it can be shown from (4.22) that

$$z_s - z_B > \sqrt{\frac{5}{2\pi}}\,\gamma^{-1/2} \qquad \text{for} \quad \sigma << 1$$

Also, $$2\gamma(z_s - z_B) = \frac{2\pi}{\Lambda(z_B)} - \frac{2\pi}{\Lambda(z_s)} = \beta - kn_3$$

The condition thus becomes

$$\gamma < \frac{\pi}{10}\,(\beta - kn_3)^2 \tag{4.24}$$

For $\sigma << 1$ the incident mode is coupled into the reflected mode only over a portion of the grating length, and the resulting reflection may be small. Under these conditions we may set $A \sim 1$. Imposing the boundary condition $B(L-z_B) = 0$, the reflected amplitude $B(-z_B)$ can be approximately solved by direct integration of (4.15)

$$B(-z_B) = -i \int_{-z_B}^{L-z_B} \kappa\, e^{i\gamma z^2}\, dz \tag{4.25}$$

Most of the contribution will come from a region of width $\sim \gamma^{-1/2}$ centered about the Bragg point. If $\min(z_B, L - z_B) >> \gamma^{-1/2}$, we thus extend the limits of integration from $-\infty$ to $+\infty$, and evaluate the integral by the method of stationary phase. The result is

$$B(-z_B) = -i\kappa\left(\frac{\pi}{\gamma}\right)^{1/2} e^{i\pi/4}$$

and the reflectivity R is

$$R \equiv |B(-z_B)|^2 = \frac{\pi\kappa^2}{\gamma} \tag{4.26}$$

which is the same as (4.23) when $\pi\kappa^2/\gamma << 1$. The bandwidth of the chirped grating filter is proportional to γL. Thus, for a given grating length L, the reflectivity-bandwidth products are constant if the coupling strengths are uniform over the entire length. Note that the above integral method can be applied to the case with more complex period functions.

If we account for residual waveguide losses by replacing β everywhere by $\beta + i\frac{\alpha}{2}$, where $\alpha/2$ is the (amplitude) loss constant, integration of (4.12) becomes

$$B(0) = -i \int_0^L \kappa(z)\, e^{i\gamma z^2}\, e^{-i\, 2(\delta - \frac{\alpha}{2})z}\, dz$$

The method of stationary phase gives

$$R \equiv |B(0)|^2 = \frac{\pi\kappa^2}{\gamma}\, e^{-2\alpha z_B} \qquad (4.27)$$

The κ's in (4.26) and (4.27) are evaluated at the Bragg point. The exponential factor in (4.27) can be interpreted by noting that $2z_B$ is the round trip traveling distance before reflection.

4.6 Experimental Results

We again used a glass waveguide to demonstrate this device. The fabrication of the glass waveguide and chirped grating was similar to that described in Section 4.4. In the first experiment, we used a waveguide with the following parameters: $t = 0.77$ μm, $n_{eff} = 1.524$, $n_3 = 1.515$, and $n_2 = 1.544$ at $\lambda = 5950\text{Å}$. It supported a single TE mode with a propagation loss constant of 3-5 db/cm. The grating period required in this

application was ∿2000Å. The special technique used to obtain such a small period will be described in Chapter 5. The resulting chirped grating had a period from 1905 to 2005Å over a length L = 10 mm. Figure 4.5 consists of SEM photographs of a section of such a structure. The corrugation had a sinusoidal profile and had a depth of 350Å determined from these SEM pictures.

The experimental setup used to examine our chirped grating filter is sketched in Fig. 4.6. The output beam from a tunable dye laser (linewidth ∿ 0.5Å) was coupled into the waveguide by a prism coupler. This prism coupler also served as the output coupler for the reflected mode. The incident and reflected waves were separated by a beam splitter. and their relative power ratio was measured. The light was coupled into the short period end of the guide so as to minimize losses due to radiation into the substrate, as explained in the previous section. As a result, longer wavelengths penetrated further into the grating before reflection and thus experienced a larger attenuation due to the residual waveguide loss (most of which comes from surface scattering). The observed spectral response is shown in Fig. 4.7a. The residual loss α can be determined from Fig. 4.7a-d to be 2.41 cm^{-1}. The observed reflectivity at λ is multiplied by a factor $e^{2\alpha z_B(\lambda)}$, where $2z_B(\lambda)$ is the round trip traveling distance, to obtain the intrinsic filter reflectivity. The loss-corrected spectral response of this filter (Filter 1) is then shown in Fig. 4.8. Its bandwidth is ∿ 300Å.

In the second experiment, a bandwidth of ∿ 150Å was designed and fabricated. A uniform-period grating filter was also

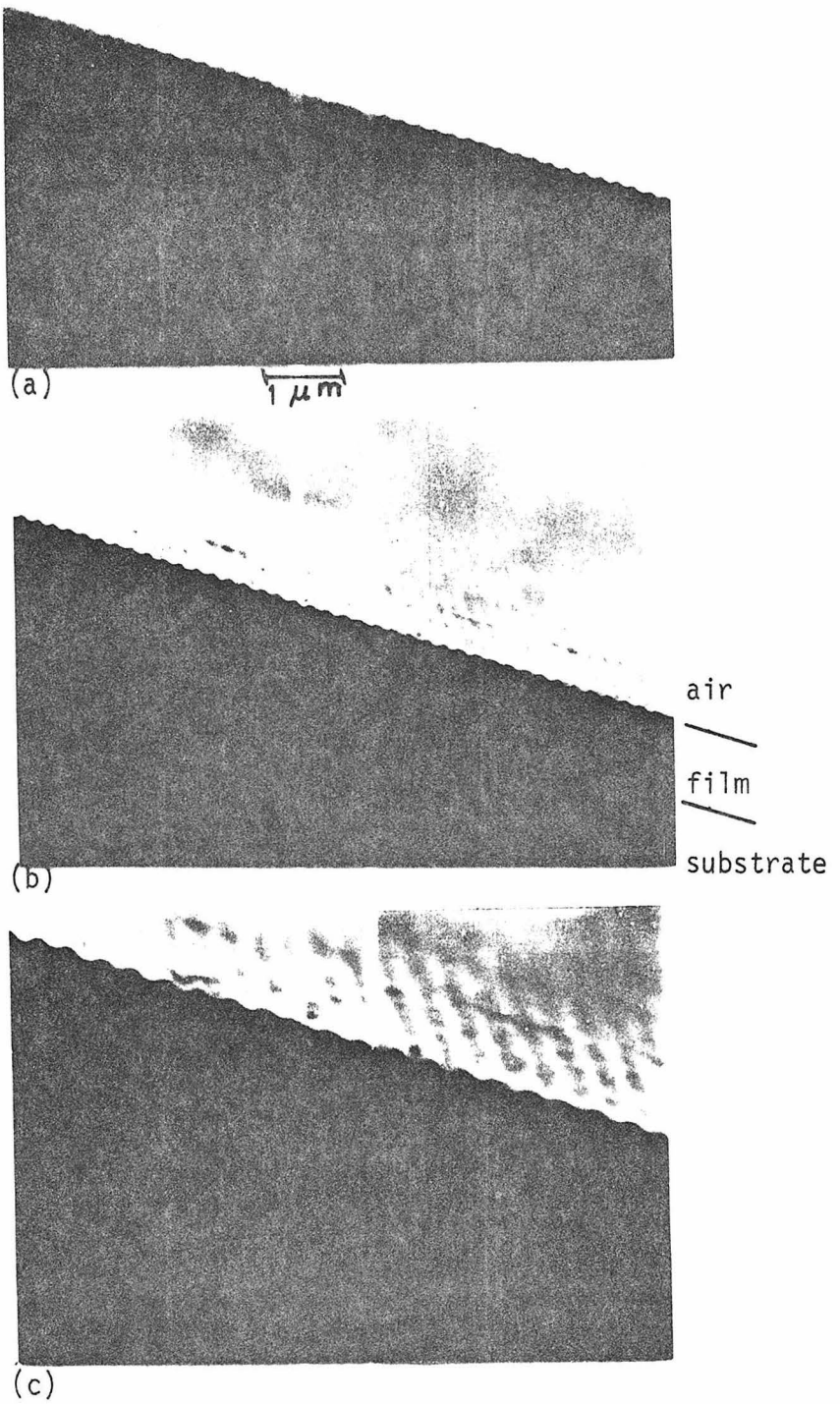

Fig. 4.5 SEM photographs of a section of a glass waveguide and surface corrugation. The structure has a waveguide thickness of 0.77μm and a corrugation depth of 350 Å.

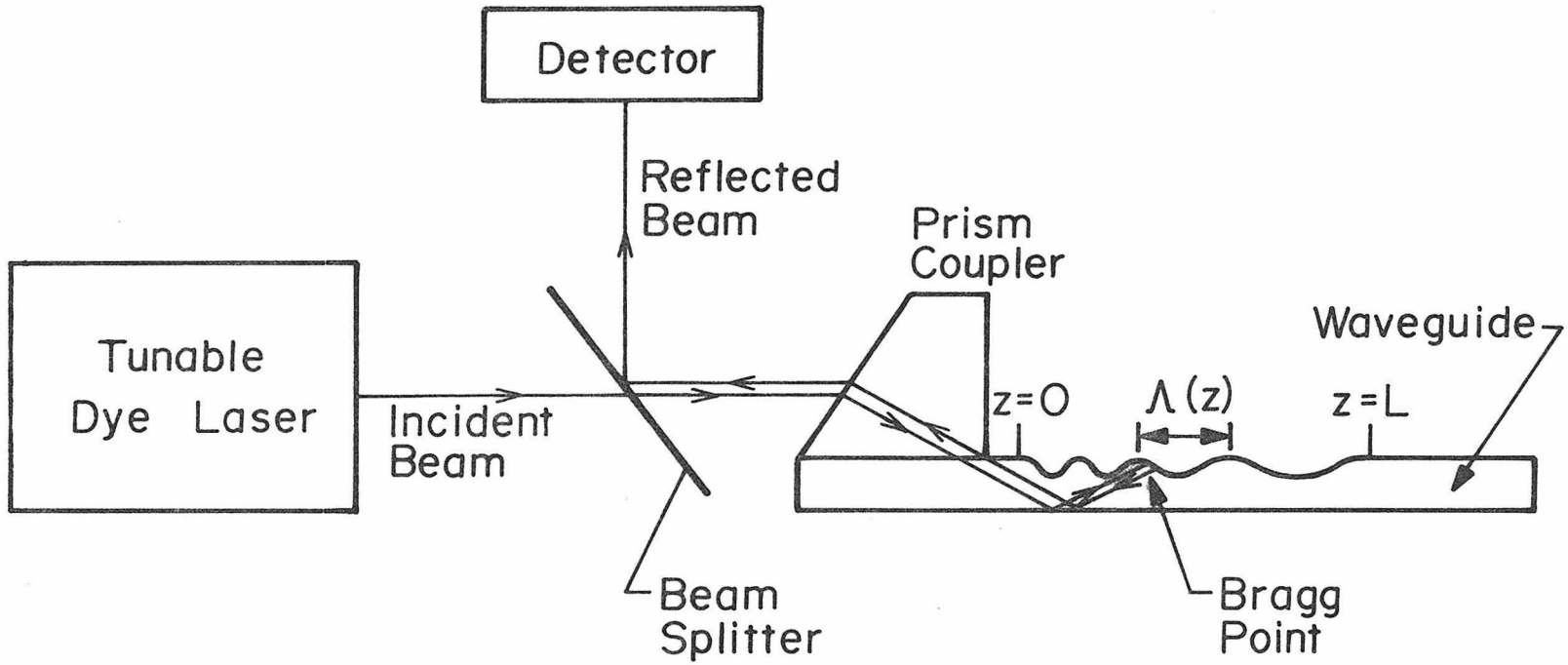

Fig. 4.6 Schematic of grating-filter evaluation setup.

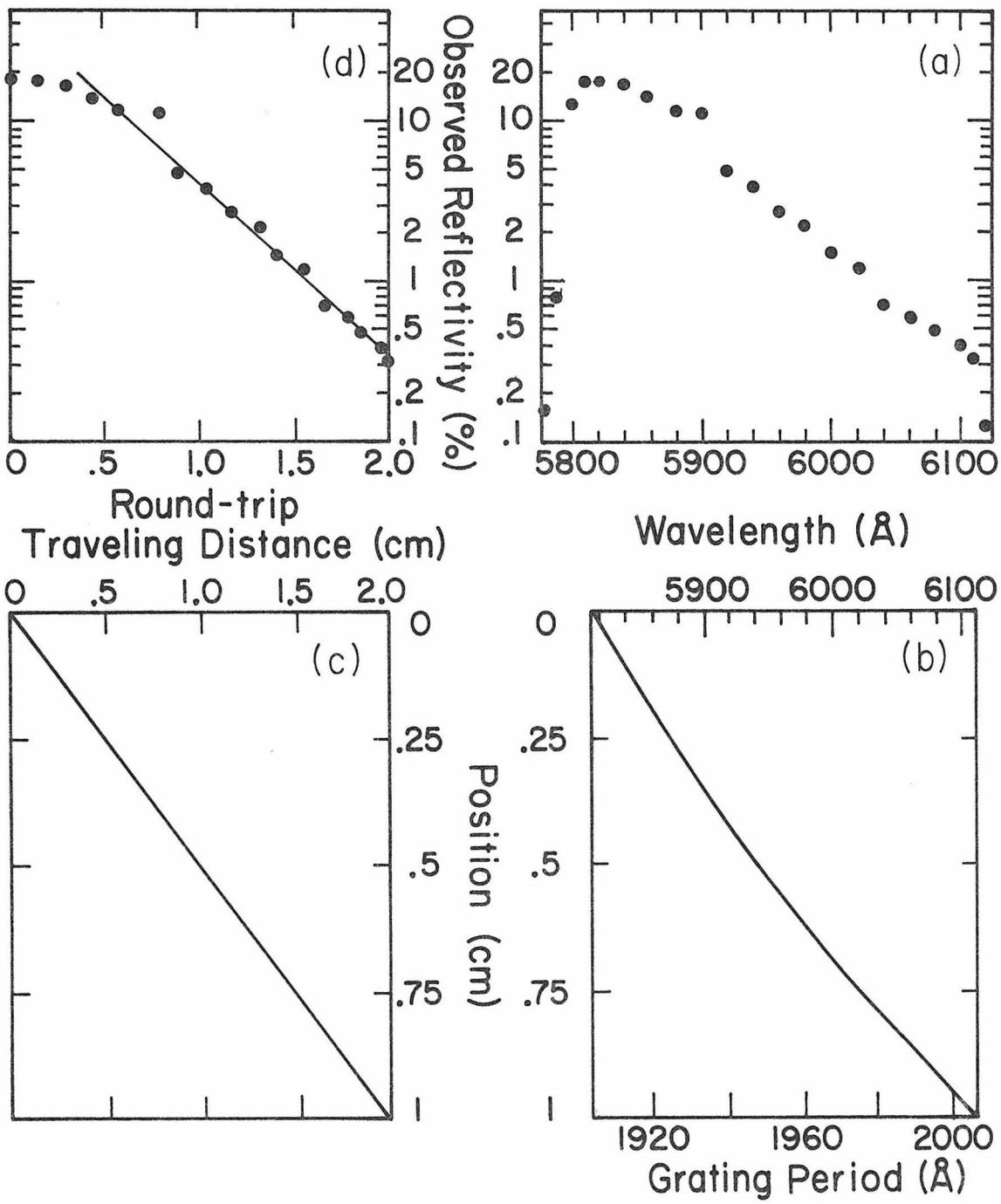

Fig. 4.7 (a) Observed reflectivity versus wavelength for a chirped grating filter. (b) and (c) are then used to obtain the corresponding plot (d) of observed reflectivity versus round-trip traveling distance. The residual loss is thus determined from the slope of this function.

fabricated for comparison.

The device parameters of all these three filters are listed in Table 4.1. The intrinsic filter responses are shown in Fig. 4.8, where the band-limited characteristic of the uniform-period grating filter is detailed in the inset. The ability to tailor-design the bandwidth of an optical filter is thus manifest. The response data are summarized in Table 4.2. The bandwidths are in good agreement with the design values, while the measured and calculated values of reflectivity are within 10% due to the difficulty in the estimation of coupling efficiency of the prism coupler.

To summarize, we have demonstrated the fabrication of broad-band optical filters using chirped gratings on top of thin-film glass waveguides. Grating filters with bandwidths of 300 and 150Å and reflectivities of 18 and 40% respectively, have been demonstrated. The control of the waveguide, corrugation, and chirp parameters will lead to band rejection filters whose response conforms closely to design values.

		Period (Λ)	Length (L)	Corrugation depth (d)	Waveguide thickness (t)	Effective index (n_{eff}) at λ=5950Å[a]
Filter 1	Chirped	1905 Å – 2005 Å	10 mm	350 Å	0.77 μm	1.524
Filter 2	Chirped	1925 Å – 1975 Å	10 mm	400 Å	0.85 μm	1.524
Filter 3	Uniform period	1955 Å	1 mm	250 Å	0.80 μm	1.519

a. $n_3 \simeq 1.515$, $n_2 \simeq 1.54$, $n_1 = 1$

Table 4.1 List of parameters of three grating filters.

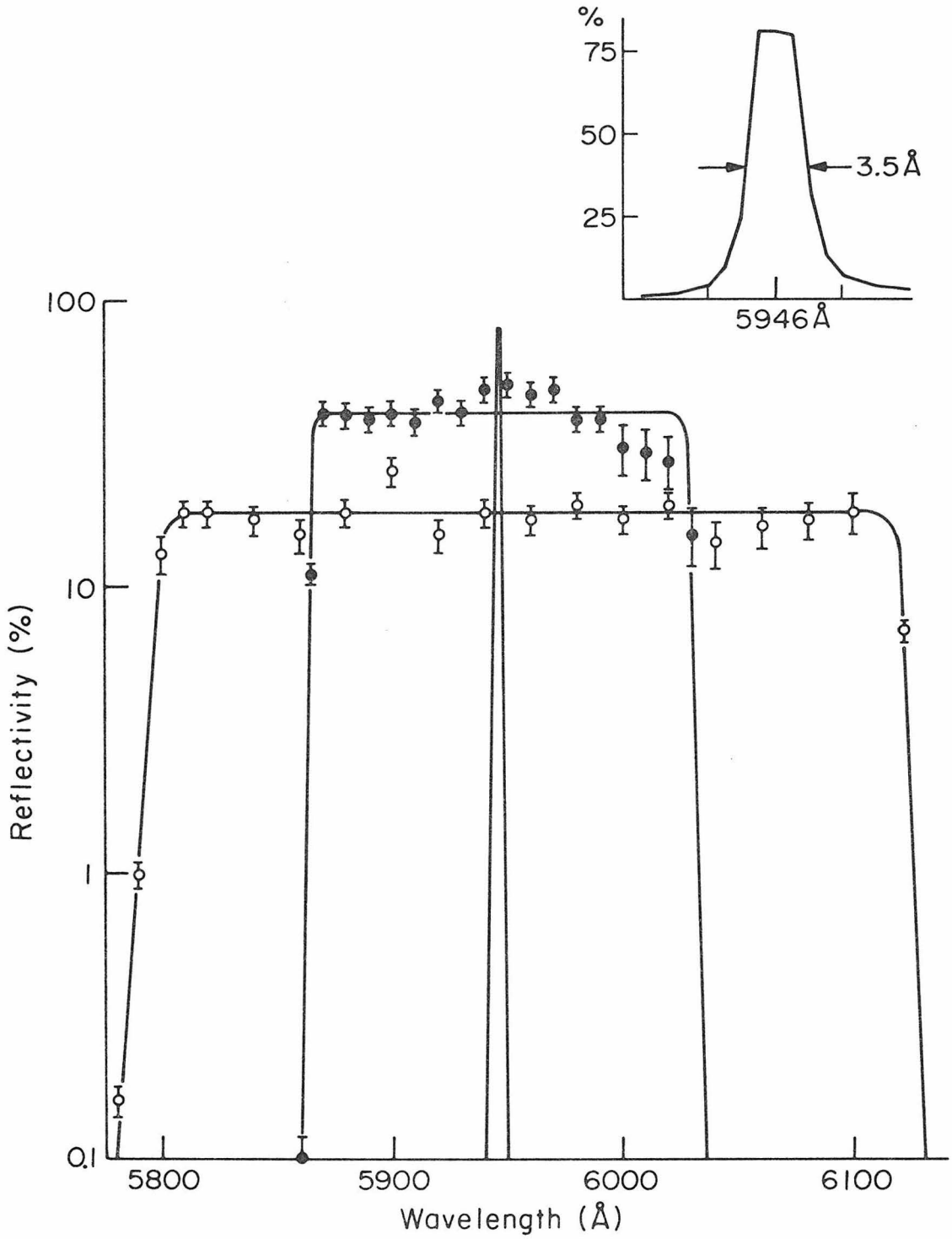

Fig. 4.8 Reflectivity versus wavelength for grating filters. Circle represents Filter 1; dot represents Filter 2. A narrow-band filter (Filter 3) is also shown for comparison and detailed in the inset.

		Wavelength response	Bandwidth (meas)	Bandwidth (calc)	Reflectivity (meas)	Reflectivity (calc)
Filter 1	Chirped	5810 Å - 6110 Å	300 ± 10Å	~305Å	18%	21%
Filter 2	Chirped	5870Å - 6020Å	150 ± 10Å	~150Å	40%	42%
Filter 3	Uniform period	5946 Å	4Å	3 Å	80%	90%

Table 4.2 Summary of response data obtained from three grating filters.

Chapter 4 - References

1. For details of experimental techniques, see Chapter 5.
2. H. Kogelnik, "Filter response of nonuniform almost-periodic structures," Bell Syst. Tech. J. 55, 109 (1976).
3. W. Streifer, D. R. Scifres, and R. D. Burnham, "Perturbation analysis of nonuniform almost-periodic Bragg reflectors," J. Opt. Soc. Am. 66, 1359 (1976).
4. M. Matsuhara, K. O. Hill, and A. Watanabe, "Optical-waveguide filters: Synthesis," J. Opt. Soc. Am. 65, 804 (1975).
5. Handbook of Mathematical Functions, M. Abramowitz and I. A. Stegun, eds. (Dover, New York, 1970), p. 685.
6. R. B. Smith, "Analytic solutions for linearly tapered directional couplers," J. Opt. Soc. Am. 66, 882 (1976).

Chapter 5

EXPERIMENTAL TECHNIQUES

5.1 Introduction

It is the purpose of this chapter to describe some of the important experimental techniques which have been used and developed in connection with the previously mentioned corrugated waveguide devices. These include the fabrication of thin-film waveguides and surface corrugations, and the measurement methods used to characterize them. Of these, the very important holographic interference and ion-beam etching techniques used in fabricating gratings and the useful prism coupler method for determining the waveguide parameters will be discussed in some detail.

5.2 Fabrication of Thin-Film Optical Waveguides

There are two kinds of waveguides which have been used in our experiments: Ti-diffused $LiNbO_3$ waveguides and sputtered glass waveguides. Their fabrication methods are described as follows:

(a) Ti-diffused $LiNbO_3$ waveguides

$LiNbO_3$ waveguides can be fabricated by a variety of methods [1]. Of these, the in-diffusion of titanium metal is simple, and the resulting waveguides have very good optical quality. The diffusion also smooths out the irregularities of the original Ti pattern edge. The channel waveguide fabricated by this method thus has low scattering loss from the side wall. In our work, a film of Ti metal was electron-gun evaporated on a $LiNbO_3$ substrate. Note, in fabricating channel waveguides, we started with a few microns wide strip Ti pattern, which was

cut by the lift-off photolithographic technique. The sample was then placed in a furnace to diffuse the Ti metal. Since the Ti metal was very easily oxidized, we assumed in the process the diffusant was TiO_2. To insure this, we also tried to oxidize the Ti metal completely at a lower temperature (say, 600°C) before diffusion at 950°C. We chose a diffusion time sufficiently long to make the diffusion complete. The maximum change of index and the diffusion depth thus depended on the amount of Ti deposited. In our experiment, we used a 200Å film and a diffusion time of 5 hours. After diffusion, the diffusant (and thus the change of index of refraction) had a Gaussian profile into the substrate with a depth of 2 μm. The fractional increment of index at the surface was (0.5-1)%. The resulting waveguide supported a TE_0 mode with a loss constant of $\sim$ 1 db/cm.

(b) Sputtered glass waveguides

Glass waveguides are typically fabricated by depositing a glass film on a glass substrate. RF sputtering is generally used for depositing such a thin film, the sputtering agent being either pure oxygen [2] or a mixture of argon and oxygen[3]. In this work, we explored the possibility of using ion beam sputtering as a deposition method. The ion beam was directed to bombard the target material, and the ejected particles were deposited onto a substrate.

The original ion beam machine is shown in Fig. 5.1. The chamber was alternatively modified as shown in Fig. 5.2. The target surface is inclined at an angle with respect to the ion beam. The sputtered particles have a specific spatial distribution [4]. The simplest way to

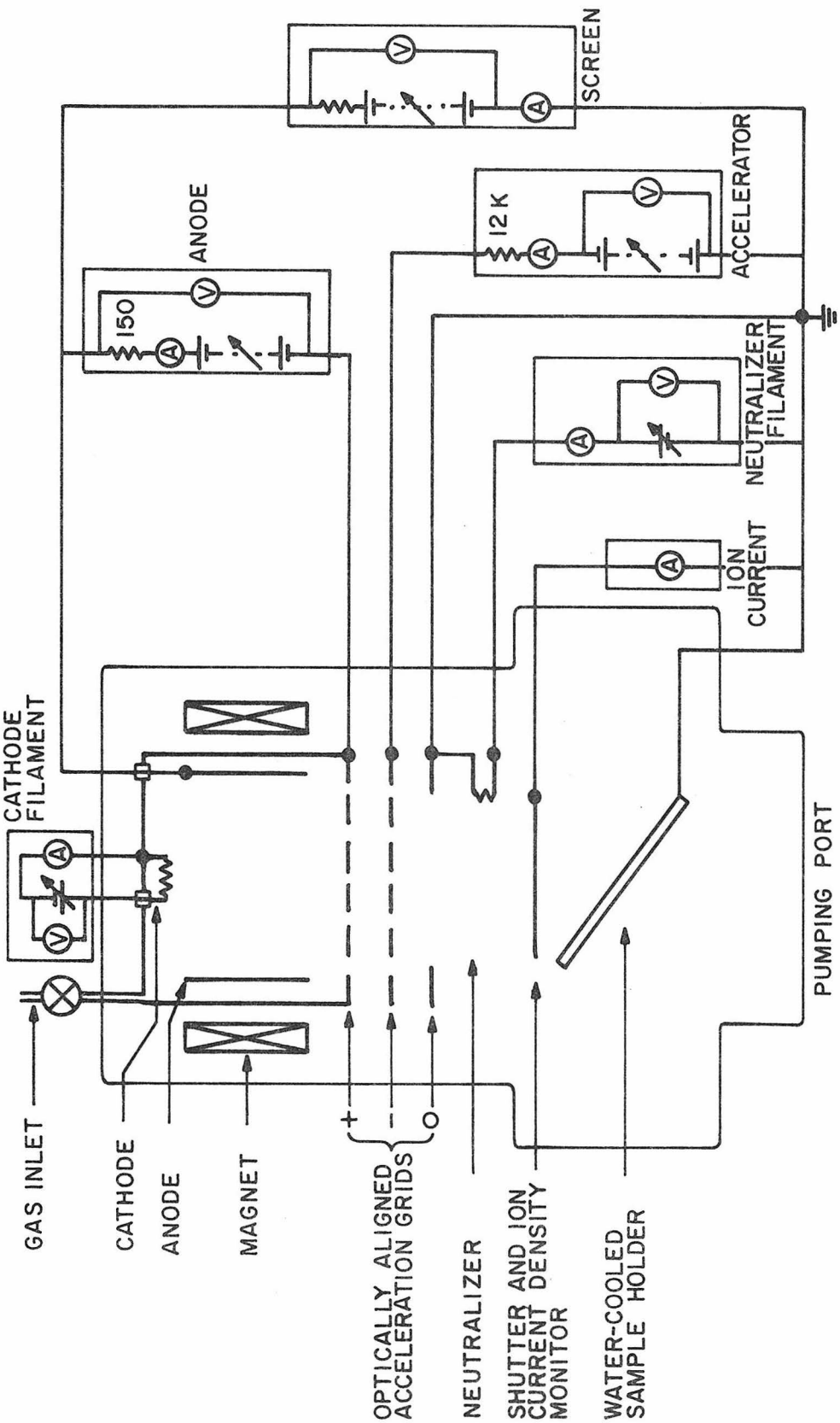

Fig. 5.1 Schematic diagram of an ion beam milling machine (MIM-TLA 5.5 from Technics).

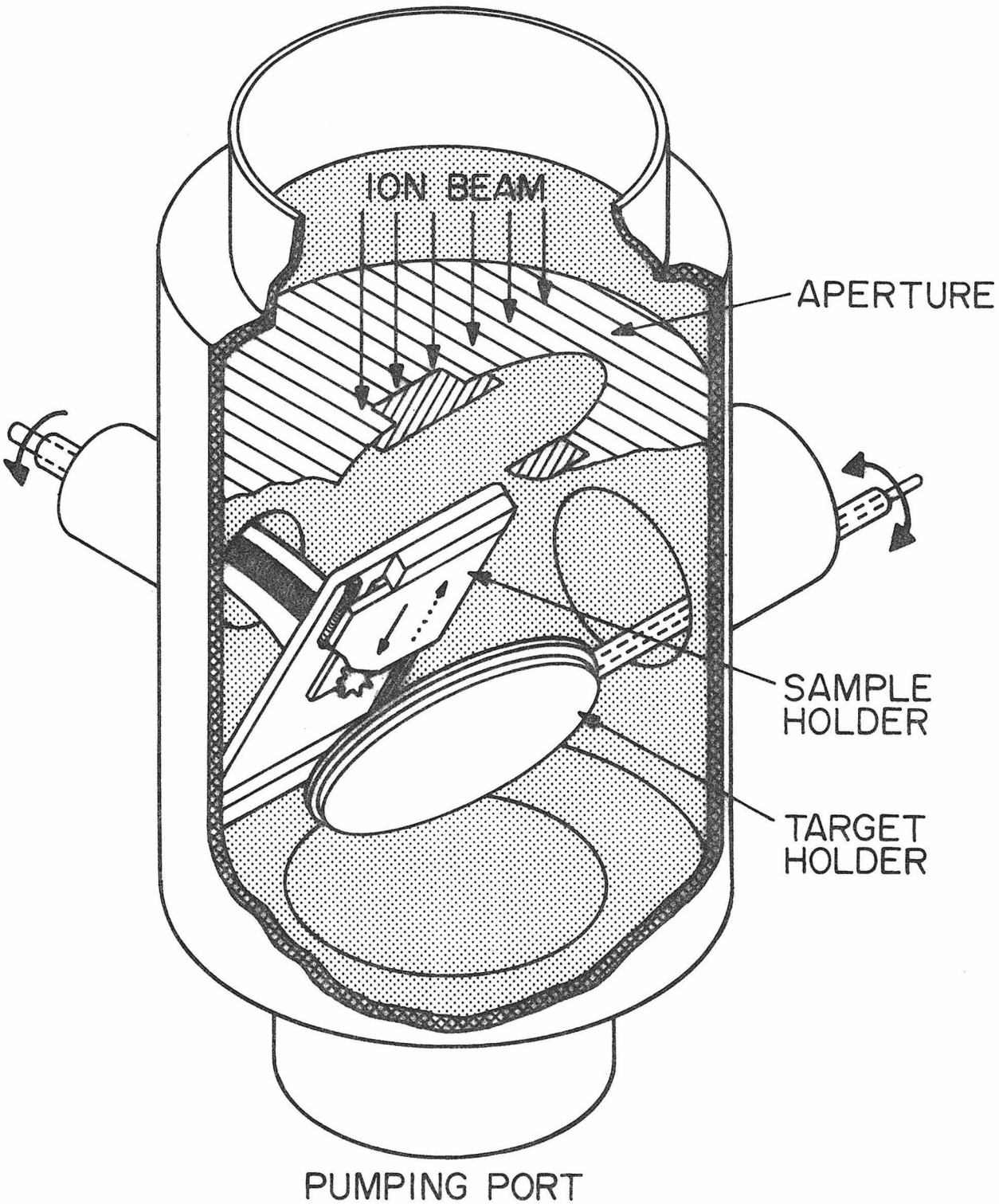

Fig. 5.2 Schematic drawing of the portions of the original ion milling machine modified for sputtering.

even it out is to set the substrate far away from the target and move the substrate back and forth in the manner shown in the figure. Furthermore, another degree of randomness can be generated by slowly rotating the target within a small angle during sputtering. The deposited film will then be uniform to a certain extent along the translational direction. A molybedenum aperture is inserted between the ion source and the target. This limits the beam to the target area and minimizes possible contamination from the beam sputtering other materials within the chamber. To fabricate a glass waveguide, we used a target of Corning 7059 glass (which is an alumino-borosilicate glass) and a substrate of regular microslide (namely, a soda-lime glass). The ion source was from argon, which had a pressure of (2-3) x 10^{-4} torr. The accelerating voltage and the ion current density were 2 kV and 0.3 mA/cm^2, respectively. The target surface was situated at an angle of 30° with respect to the ion beam. The distance between the substrate and the target was 6 cm. Oxygen with a partial pressure of 1:4 to the argon was introduced into the chamber to repair oxygen deficiencies in the sputtering process. The deposition rate was then calibrated to be 0.36 ± 0.01 μm/hr. We used a film thickness of 0.7-1.0 μm, so a typical sputtering time was 2-3 hours. Data in Fig. 5.3 are typical film thickness measurements with a Sloan Dektak. The uniformity was better than 5% across a distance of 1 cm. The resulting film had an index of refraction 2-3 % higher than that of the substrate. The waveguide had a propagation loss of 3-5 db/cm at the wavelength of 6000Å.

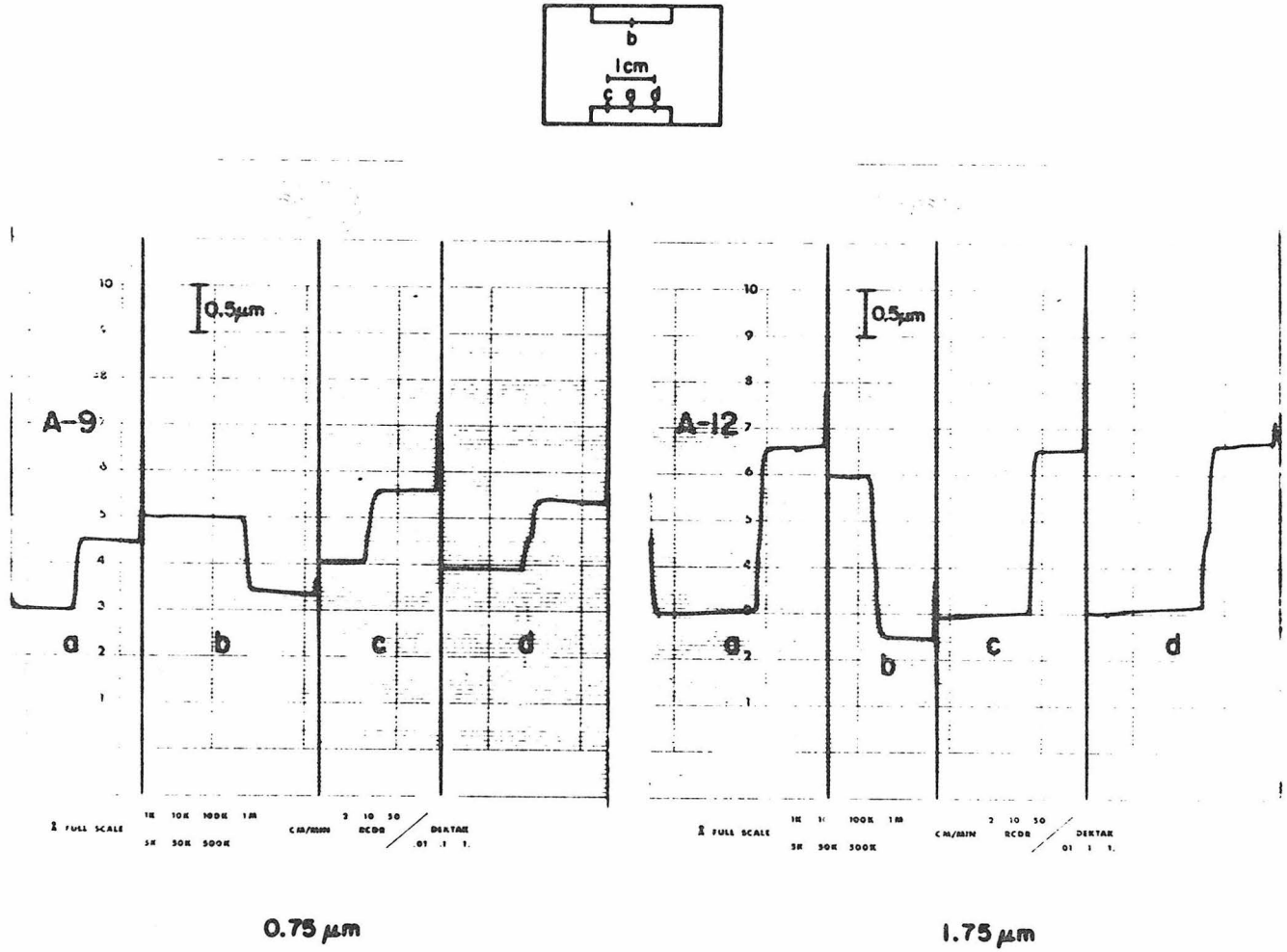

Fig. 5.3 Typical film thickness measurements with a Sloan Dektak. a, b, c, and d are points shown in the inset.

5.3 Measurement of Waveguide Parameters

Prism-film couplers [5] are generally used in the laboratory for coupling a laser beam into thin-film dielectric waveguides. A prism-film coupler can also be used to evaluate waveguide parameters such as the propagation constant β and the attenuation constant α for a guided mode. The principle of this device is an evanescent field coupling. It is the synchronized optical "tunneling" in the air gap existing between the prism and film which makes the coupling possible. In the experiment, we pressed the prism against the waveguide surface to reduce the air gap to the order of magnitude of a wavelength. Then the coupler was rotated with respect to the laser beam to find an angle at which a guided mode was "excited". This was indicated by the presence of a scattered light streak.

(a) Measurement of β or n_{eff}—

Using a prism-film coupler (Fig. 5.4a) it can easily be shown that the n_{eff} of the excited mode can be expressed by

$$n_{eff} = n_p \sin[\alpha - \sin^{-1}(\frac{\sin \phi}{n_p})] \tag{5.1}$$

where the index n_p and angle α are parameters associated with the prism; ϕ is the incident angle. We used a rotating table which could be read to an angular precision of one second of arc. The index n_p can be determined by the method of minimum deviation. However, the dispersion data provided by the manufacturer, especially for glass material, are well established. These optical data are generally acceptable and reproduceable. The accuracy of n_{eff} thus obtained in my experiment was

good to the third decimal place, e.g., 1.524 ± 0.001.

In practice, we prefer small values of ϕ to minimize the Fresnel reflection loss at the incident interface. This dictates the choice of α. We also like to keep the coupling spot almost stationary when the coupler is rotated. This determines the relative positions among the prism, the rotating center, and the laser beam. The offset between the rotating center and the laser beam was shown [6] to be $r_o = \ell_p/n_p$ where ℓ_p is a normal distance from the coupling spot to the incident interface. This offset is small when the prism is small. Rigorously, this offset (see Fig. 5.4b) will depend on the incident angle ϕ and can be expressed as

$$\frac{r - r_o}{r_o} = \frac{\phi}{2} - \frac{\phi^2}{4} + \cdots \qquad (5.2)$$

For small ϕ's this correction factor is small.

(b) Determination of film index n_2

The index of refraction of a thin film can be determined by the Abelès method [7]. In the waveguide experiment, it can also be determined as follows. For a multimode waveguide, if the mode spectrum $(\beta_0, \beta_1, \cdots)$ is obtained, then from the eigenvalue equation (2.9), we have at least two simultaneous equations for solving two unknown parameters n_2 and t. In a single-mode waveguide, if we can determine the film thickness t by other methods, then n_2 can be solved from a single equation of (2.9). The above method depends on the value of n_3 being

previously determined. We found n_3 could be determined by the Brewster angle method. The accuracy depends on the fineness of angular division about the Brewster angle. For example, using our rotating table, n_3 of a soda-lime glass was determined to be 1.515 ± 0.001 at $\lambda = 6000\text{Å}$. In our experiment, a single mode glass waveguide was used. The film thickness t was measured to be 0.75 μm with a Sloan Dektak. The measured effective index was $n_{eff} = 1.524 \pm 0.001$. The best fit gave $n_2 = 1.544$.

(c) Coupling efficiency of a prism coupler

A prism coupler is a very efficient device to couple light into and out of thin-film waveguides. In some experiments, we have to estimate this coupling efficiency. Assume in a coupling length L, the laser illumination is uniform, and the air gap a (which determines the coupling strength) is also uniform. Following a plane wave analysis, the coupling efficiency can be expressed [8] as

$$\eta = 2 \frac{(1 - e^{-\xi})}{\xi} \tag{5.3}$$

where $\xi = \frac{T L}{2L_B}$

L_B is the geometrical bounce distance of the guided mode. T is the characteristic transmissivity of this prism-air-film system, which is proportional to exp(-2qa), where q is the field decay constant in the air film. The maximum efficiency occurs at $\xi = 1.25$, and is $\eta = 81\%$. If we use it as an output coupler, the efficiency can be 100% following the reciprocal theorem. In the experiment, the coupling spot was

chosen near the prism corner; the incident laser beam was typically focused to a size of 100-200 μm. If the prism corner was not exactly 90^{o}, then the reflected beams were separated from the incident beam. We observed two such reflected beams, which indicated that part of the beam was not incident directly on the coupling spot and thus did not contribute to the coupling. Taking this and the Fresnel reflection loss into account, we obtain

$$\eta_i = 1 - \frac{P_1'}{P_i(1 - R)^2 - P_2'} \tag{5.4}$$

The notations are defined in Fig. 5.4c. By measuring P_i, P_1', and P_2', a value of 60% was obtained. The system had a total efficiency of ∿50% for input coupling; 90% for output coupling.

(d) Measurement of waveguide loss

The intrinsic waveguide loss has been roughly estimated [2] by monitoring the intensity of scattered light along the length of the guide. The scattered light was collected, for example, by a fiber optic probe. In principle, the attenuation constant α can be deduced by measuring the transmitted power as a function of propagation distance. Using a pair of prism couplers [9], a guided mode is coupled into and out of the waveguide. The output power is thus expressed

$$P_o(z) = P_i \eta_i e^{-\alpha z}$$

where η_i is the input coupling efficiency; z is the separation between the two prisms. If care is taken to keep the input condition constant

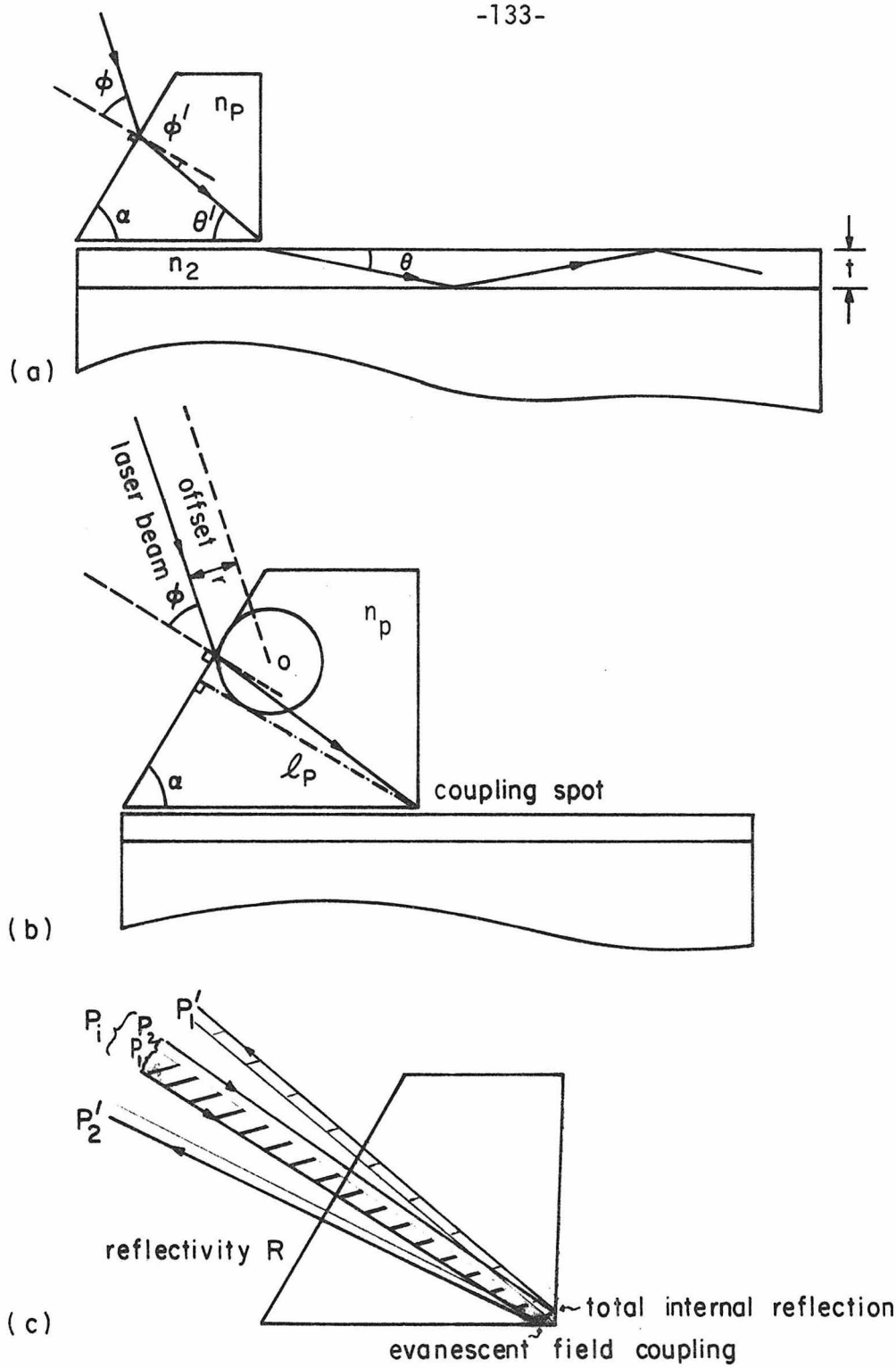

Fig. 5.4 Diagrams of prism couplers showing (a) the phase-matched condition under which the incident beam is coupled into the film (b) the offset of the incident beam so that the beam is kept incident at the prism corner when the coupler is rotated (c) the incident beam P_i which is focused to the prism corner. P_i can be divided into P_1 (shaded) and P_2. P_1 will contribute the coupling, and part of it will be reflected back (P_1'). P_2 cannot contribute to the forward coupling, and is totally reflected(P_2').

when the output prism is moved and reloaded, then it can be shown that

$$\alpha = \frac{\ell n\ P_o(z_1) - \ell n\ P_o(z_2)}{z_2 - z_1} \tag{5.5}$$

Using this method, we found our glass waveguides had a loss constant α = 3-5 db/cm, and $LiNbO_3$ waveguides, $\alpha \simeq 1$ db/cm.

5.4 Fabrication of Holographic Gratings

In previous chapters, we introduced the general theory of optical interference methods used for producing holographic gratings with uniform and variable periods. Here we describe the experimental details.

The optical setup used in the experiment is shown in Fig. 5.5. The light source used most often in our work was an argon laser (4579Å line) or a helium-cadmium laser (4416 or 3250 Å line). A spatial filtering arrangement consisting of a quartz lens and a 12.5 μm pinhole was used as shown. The quality of the expanded beam before and after using a pinhole is shown in Fig. 5.6. The "roughness" of the beam consisted of high spatial Fourier components at the focal plane of lens, and was thus filtered out by the pinhole. The Fourier transform of the fundamental Gaussian mode was centered at the pinhole and was thus unaffected. Sometimes apertures were also placed between the beam splitter and the mirrors to block unwanted reflections from the former. If we take the expanded beams (spherical waves) into account, the interference pattern (or contours of equal intensity) is expressed from Fig. 5.7a as

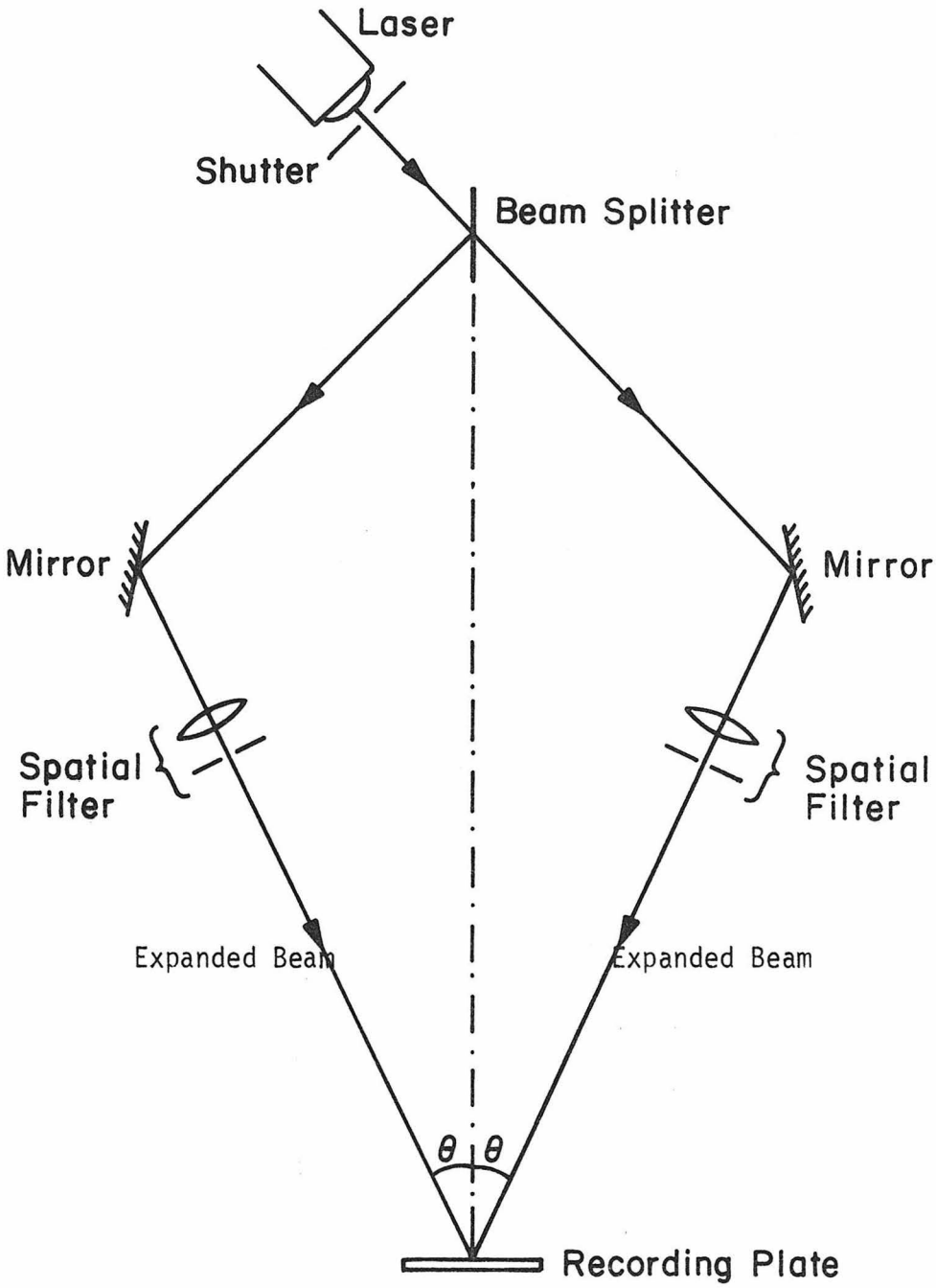

$$\theta = \sin^{-1} \frac{\lambda}{2\Lambda}$$

Fig. 5.5 Experimental setup for fabricating holographic gratings.

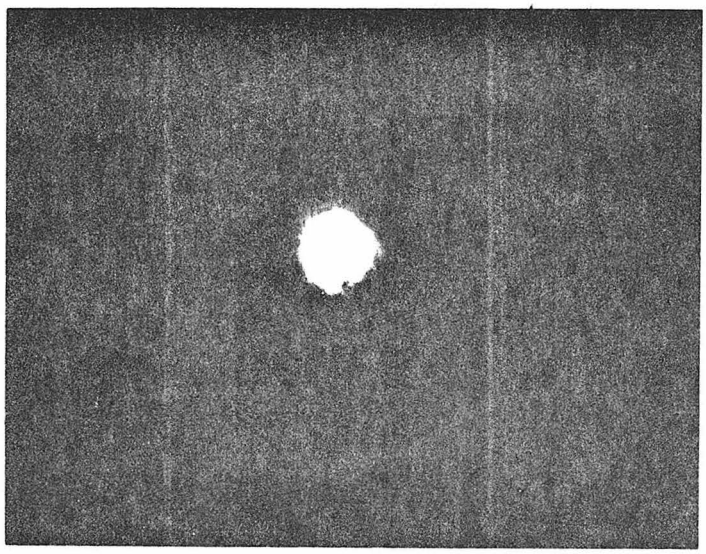

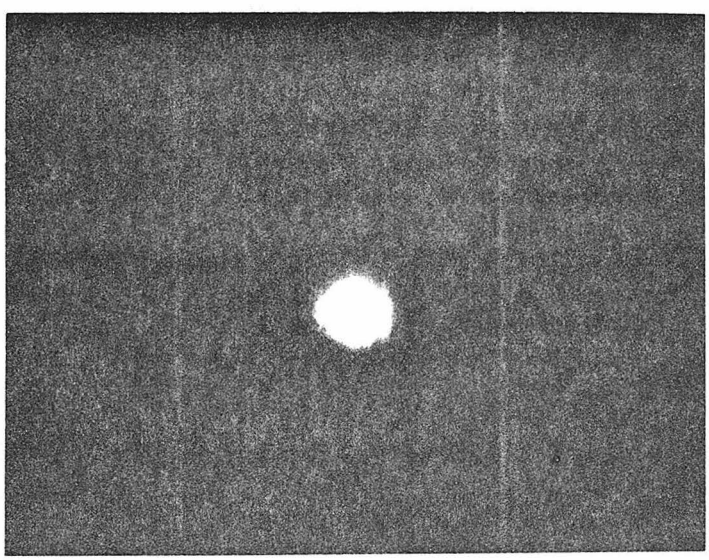

Fig. 5.6 An expanded He-Cd laser beam before and after spatial filtering.

$$y^2 + \left(z - \frac{c_2R_1 - c_1R_2}{R_1 - R_2}\right)^2 = \frac{2R_1R_2m\lambda}{R_1 - R_2} + 2R_1R_2 + \left(\frac{c_2R_1 - c_1R_2}{R_1 - R_2}\right)^2 ,$$

$$y^2 + z^2 \ll R_{1,2}^2$$

which is a set of concentric circles with the integer m as a parameter. The center is at $\frac{c_2R_1 - c_1R_2}{R_1 - R_2}$ on the z axis, and the radii of curvature are

$$\sqrt{\frac{2R_1R_2m\lambda}{R_1 - R_2} + 2R_1R_2 + \left(\frac{c_2R_1 - c_1R_2}{R_1 - R_2}\right)^2}$$

If $R_1 = R_2 = R$, the contours become straight lines with periodicity $\Lambda = \lambda/(\sin\theta_1 + \sin\theta_2)$. The period at the pattern edge Λ_1 and that at the center Λ_0 (see Fig. 5.7b) differ by

$$\frac{\Lambda_1 - \Lambda_0}{\Lambda_0} = \frac{1}{\cos\varepsilon} - 1 \qquad (5.6)$$

where $\varepsilon = \sin^{-1}\frac{\frac{L}{2}\cos\theta}{R}$ to a first-order approximation. A typical order of magnitude is 10^{-5} for L/R = 0.01. This deviation is a very small factor indeed.

The smallest period that can be obtained from the above experimental setup is $\Lambda = \lambda/2$ (when $\theta = 90°$). In order to obtain gratings with a period less than $\lambda/2$, we make the exposure take place inside a liquid bath [10]. The recording wavelength is thus reduced by a factor which is equal to the index of refraction of the liquid. For example, we used xylene liquid to reduce the wavelength of an Ar^+ line (4579Å) to obtain gratings with period ~2000Å in the fabrication of filters.

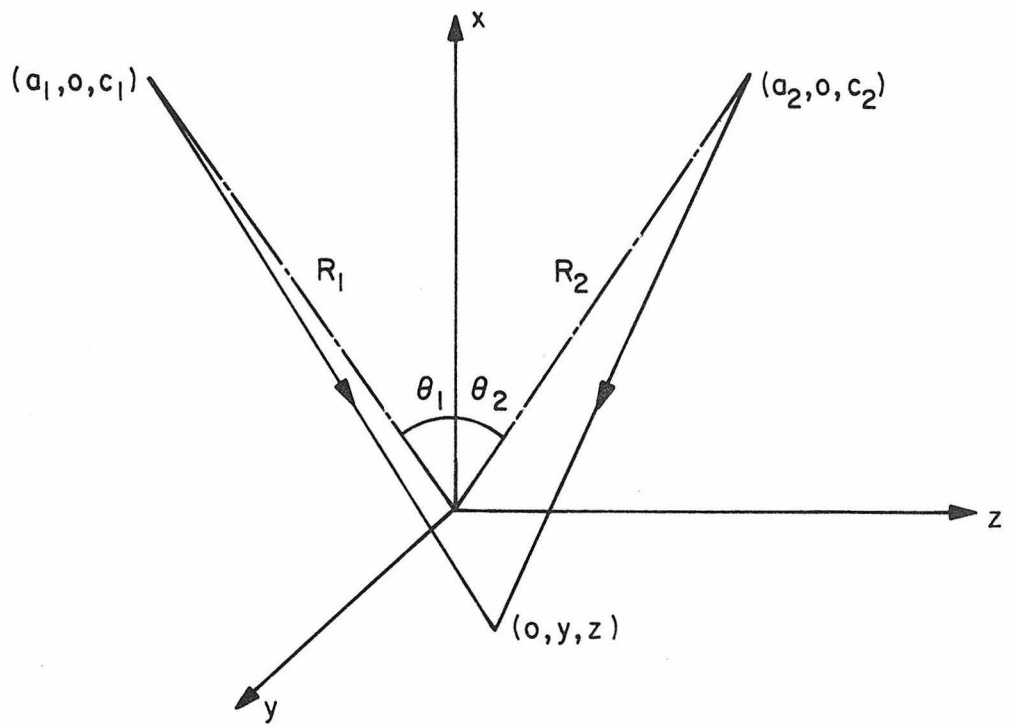

(a)

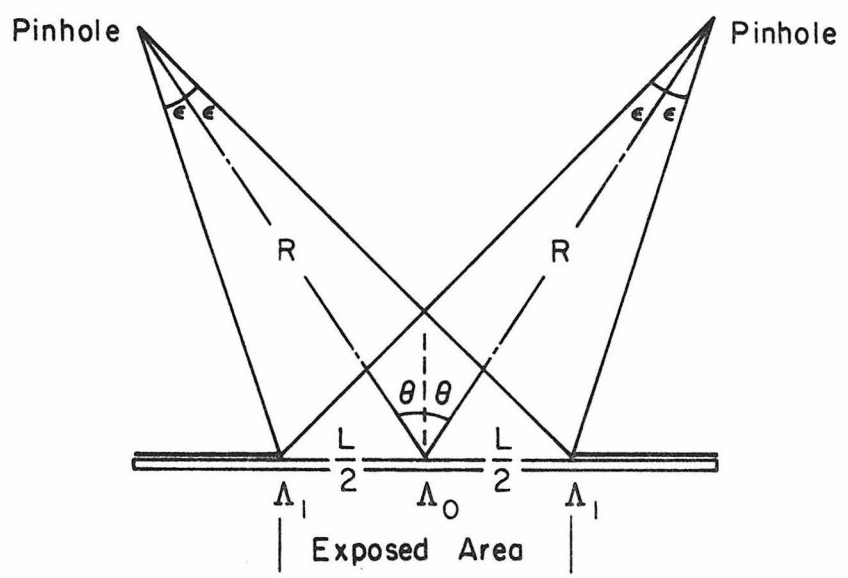

(b)

Fig. 5.7 Interference with spherical waves (expanded beams). (a) Coordinates showing the spherical centers and the recording plane. (b) Symmetric case of (a), which is used to examine the period variation across the exposed area.

The currently available photoresist and developer used in the above-mentioned holographic interference lithography were:

Photoresist	Shipley AZ1350B
Developer	Shipley AZ303A:deionized water = 1:6

Best results were obtained when the spin-coated thickness of the photoresist was less than the grating period to be fabricated and the developing time was fixed at 10 sec. A thin photoresist layer was obtained by diluting the photoresist with the thinner. The etched depth thus depended upon the amount of exposure. This analysis is presented in Appendix E.

The setup used for the fabrication of chirped gratings is shown schematically in Fig. 5.8. The converging beam was generated with a cylindrical lens that was placed after the spatial filter. A neutral density plate was introduced before the cylindrical lens so that the focused beam had the same intensity as the collimated beam on the recording plate. We have shown previously that such an interference pattern has a period distribution (4.1):

$$\Lambda(z) = \frac{\lambda}{\sin\theta + \dfrac{z_f - z}{\sqrt{(z_f - z)^2 + x_f^2}}}, \qquad 0 < z < L \tag{5.7}$$

The focal position (z_f, x_f) can be expressed in terms of θ, L, and the F number ($F \equiv f/w$) of the cylindrical lens as follows (see the inset of Fig. 5.8). We will use the converging angle 2α as a parameter, where

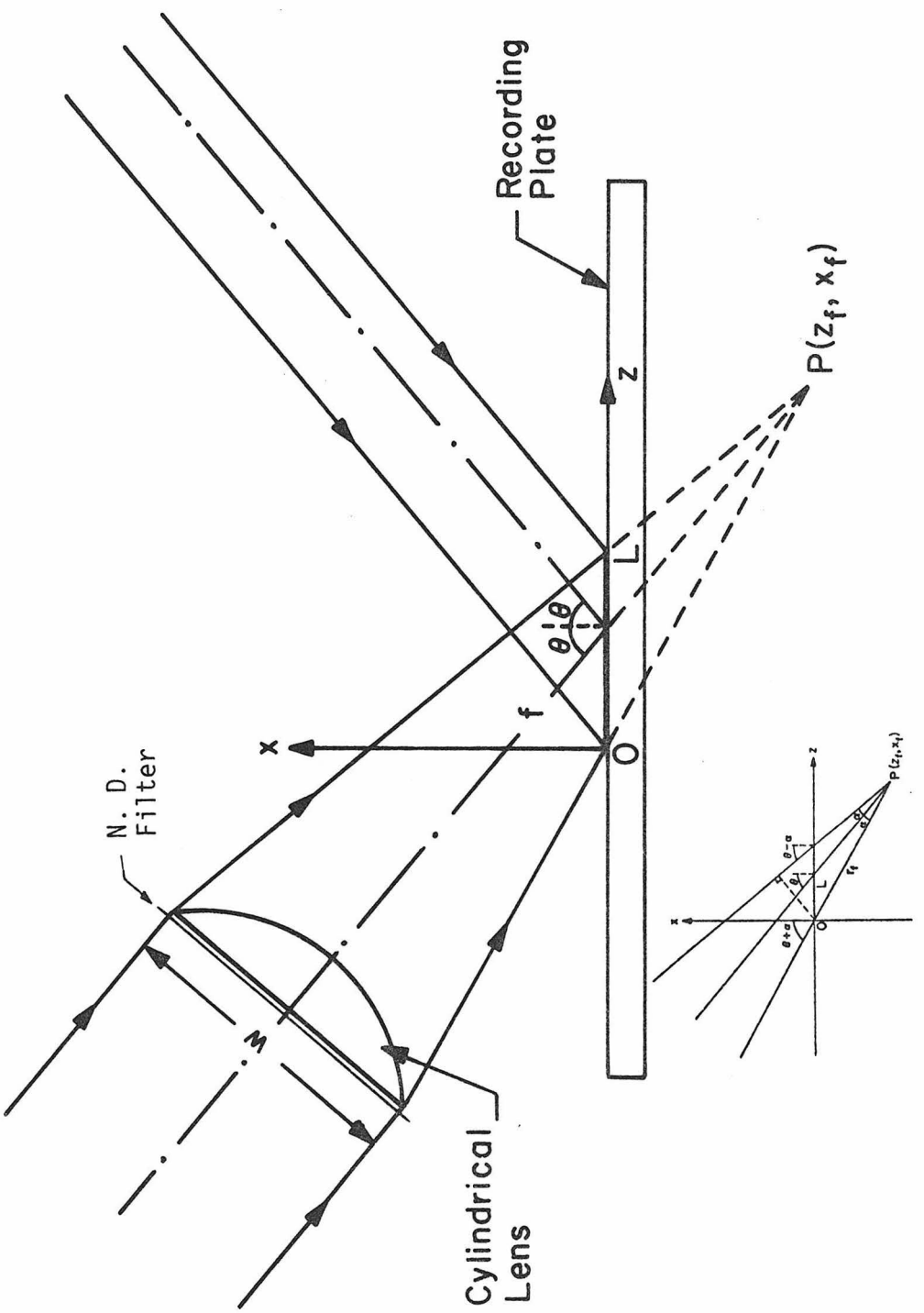

Fig. 5.8 Experimental setup for the fabrication of chirped gratings. Geometrical detail of the focused beam is shown in the inset.

$\alpha = \tan^{-1}(\frac{1}{2F})$. From simple geometry, we obtain

$$r_f = \frac{L \cos(\theta-\alpha)}{\sin 2\alpha}$$

Then

$$z_f = r_f \sin(\theta+\alpha) = \frac{L(\sin 2\theta + \sin 2\alpha)}{2 \sin 2\alpha}$$

$$x_f = -r_f \cos(\theta+\alpha) = -\frac{L(\cos 2\theta + \cos 2\alpha)}{2 \sin 2\alpha} \qquad (5.8)$$

Typical plots of $\Lambda(z)$ are shown in Fig. 5.9. These plots were used in the design of our broad-band filters.

5.5 Surface Corrugation by Ion-Beam Etching

The photoresist grating can be transferred to the waveguide surface by ion beam etching (sputtering) [11]. The term "sputtering" refers to the ejection of atoms from a target surface by bombarding with energetic (keV) particles. The process is nonselective to all materials as long as the ion energy exceeds the binding energy of the target material. Ion beam etching is also characterized by an extremely high resolution (e.g., a 500Å linewidth) capability and an absence of lateral etching or "undercutting". In contrast, most chemical etchants are material selective and possess some etching habit. Chemical etching is extensively used in semiconductor processing. For glass materials, or in case the surface to be etched is not totally exposed, ion beam etching is the method of choice. Compared with plasma etching, the directed ion beam has the advantage that it is able to bombard the target at any desired angle.

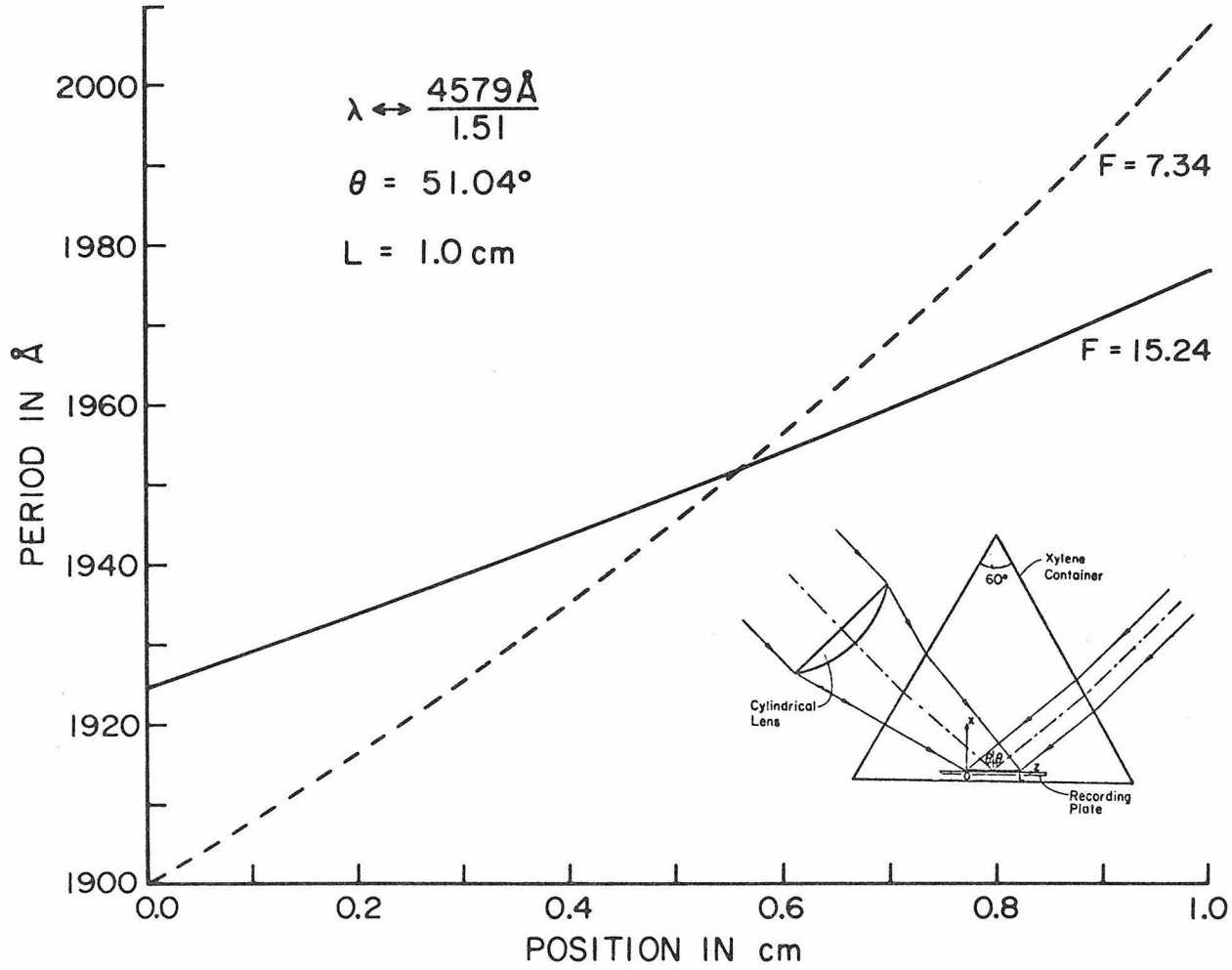

Fig. 5.9 Typical period distribution of chirped gratings. These small period gratings are fabricated in a xylene bath shown in the inset.

The etching conditions used in our experiment were an ion energy of 1-2 keV and an ion current density of 0.1 mA/cm^2. We used such a high ion energy to improve the beam collimation and such a low ion current to better control the etching process. The substrate was inclined at an angle 20-30° relative to the ion beam, the grating lines being oriented parallel to the ion beam. This induced a smoothing of irregularities in the photoresist mask and produced deep grooves in the substrate. Consider a profile erosion under ion bombardment. Since the ion sputtering rate varies with the angle of incidence, facets are formed on the profile of photoresist, and the profile erodes at a rate dominated by the etching rate of these facets. If the substrate is normal to the ion beam, the erosion rate of resist profile will be twice the angular maximum etching rate of resist [12]. The substrate (glass or $LiNbO_3$), however, erodes only at a normal-incidence rate which is smaller than the former. As a result, the groove aspect ratio (depth/period) of the pattern will be degraded. The resist erosion rate is minimized when the substrate is inclined to the angle of maximum etching rate of resist [12]. On the other hand, we also like the inclination to be adjusted to obtain the possibly larger etching rate for the substrate. The determination of our etching conditions was made according to this tradeoff.

Blazed gratings can also be fabricated by ion-beam etching. By inclining the substrate to be corrugated at an angle α to the ion-beam and using photoresist lines to shadow one side of the grooves, gratings with an asymmetric tooth-shape were thus formed. Fig. 5.10 shows the profiles of such gratings for various values of angle α . It can be seen

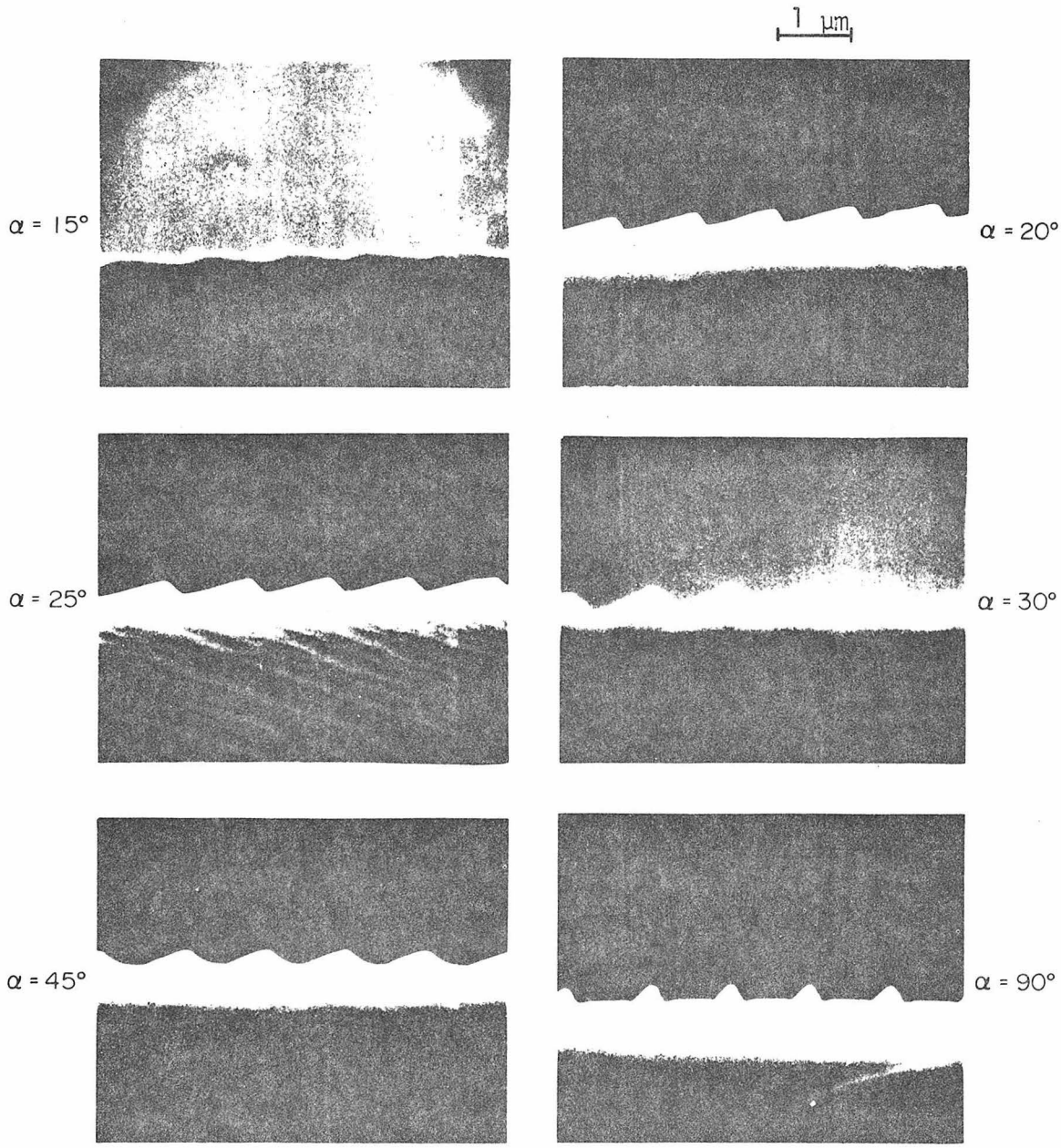

Fig. 5.10 Blazed gratings fabricated at various angles of ion beam etching on the (100) GaAs substrate.

that this method is capable of controlling the blazing angle in 10-20°. The blazing effect was roughly evaluated by measuring the intensities of the +1 and -1 order diffracted beams from a normally incident beam (6328Å He-Ne laser). With the laser polarization perpendicular to the grating grooves, our best results correspond to an absolute diffraction efficiency of 54% and an extinction ratio of 227. The blazed grating has an important application in improving the coupling efficiency of the grating coupler.

5.6 Measurement of Grating Parameters

The grating period and corrugation depth are the two major parameters in a corrugated waveguide device. The grating period determines the filtered wavelength, the deflection angle in the plane of waveguide, and the coupling angle. The corrugation depth determines the optical efficiency of the device. Both the period and depth of the corrugation need to be accurately measured in order to characterize devices. The methods of these measurements are described as follows.

(a) Determination of grating periods

Grating periods can be easily determined with a Littrow configuration. The grating is mounted on a rotary table, and a laser beam is directed to it. The grating is then rotated until the diffracted beam and the incident beam directions coincide (see Fig. 5.11a). This occurs when the condition $2\Lambda \sin\theta = \lambda$ is satisfied. The period Λ is thus determined by measuring this Littrow angle θ. The sensitivity of this measurement is given by $d\Lambda/d\theta = -\Lambda \cot\theta$. For example, in the measurement of a period Λ = 4200Å using an Ar^+ laser λ = 4579Å, we have

$\theta = 33.03^{o}$ and $|d\Lambda/d\theta| = 1.88\text{Å}$/min of arc. Hence, typically, an error of 1 minute in angular reading will result in an error of $\sim 2\text{Å}$ in period measurement.

The measurement of small periods is not as straightforward. For a grating with a period $\Lambda \simeq 0.2$ μm, we cannot observe diffraction in air using $\lambda = 4579\text{Å}$. However, the diffraction will occur in a medium with index of refraction $n > \lambda/2\Lambda$. The arrangement used to make the observation possible is shown in Fig. 5.11b. A grating is attached to one of the prism faces with xylene (an index matching fluid). The prism is then rotated until the diffracted beam from the grating retraces the incident beam path. This incident angle ϕ is measured. The grating period is then given by $\Lambda = \lambda/(2n \cos\theta)$, where $\theta = \alpha - \sin^{-1}(\sin\phi/n)$. The above formulas involve the index n and the angle α of the prism, which have to be determined beforehand.

(b) Determination of corrugation depths

Corrugation depths can be measured from SEM photographs. However, nondestructive methods were also developed in the course of this work. These methods are based on a diffraction efficiency measurement. The grating is coated with a thin layer of metal to become a reflection grating. By measuring the intensity of the diffracted beam from a normally incident laser beam, the corrugated depth d is thus calculated from the formula $\eta_{\ell} = J_{\ell}^{2}(kd)$ assuming $kd << 1$, where $k = 2\pi/\lambda$. The corrugation depth as a function of diffraction efficiency is plotted in Fig. 5.12a. We used this configuration for large period gratings.

For small period gratings, the optical arrangement used to evalu-

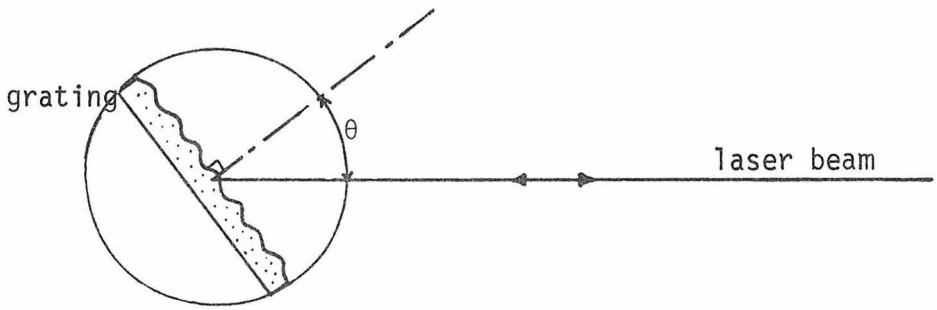

$$\Lambda = \frac{\lambda}{2 \sin\theta}$$

(a)

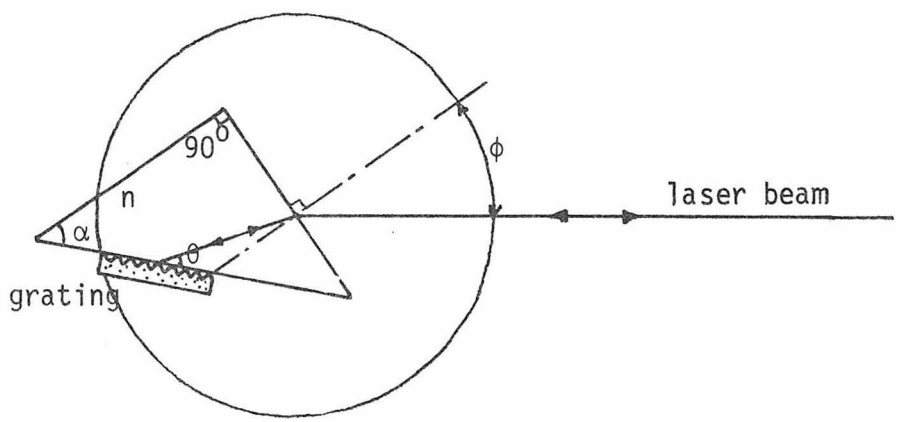

$$\Lambda = \frac{\lambda}{2n \cos\theta}$$

$$\theta = \alpha - \sin^{-1}\left(\frac{\sin\phi}{n}\right)$$

(b)

Fig. 5.11 Littrow reflection configurations for grating period measurements. The prism in (b) allows the measurement of small periods as can be seen by the factor n in the denominator.

ate the corrugation depth is shown in Fig. 5.12b. It is especially useful for transparent substrates. We rotate the stage until a diffracted beam first appears in the transmitted side. The measured diffraction efficiency, corrected by the reflection loss at the exit interface, is then used to calculate the corrugation depth from the formula shown in the figure.

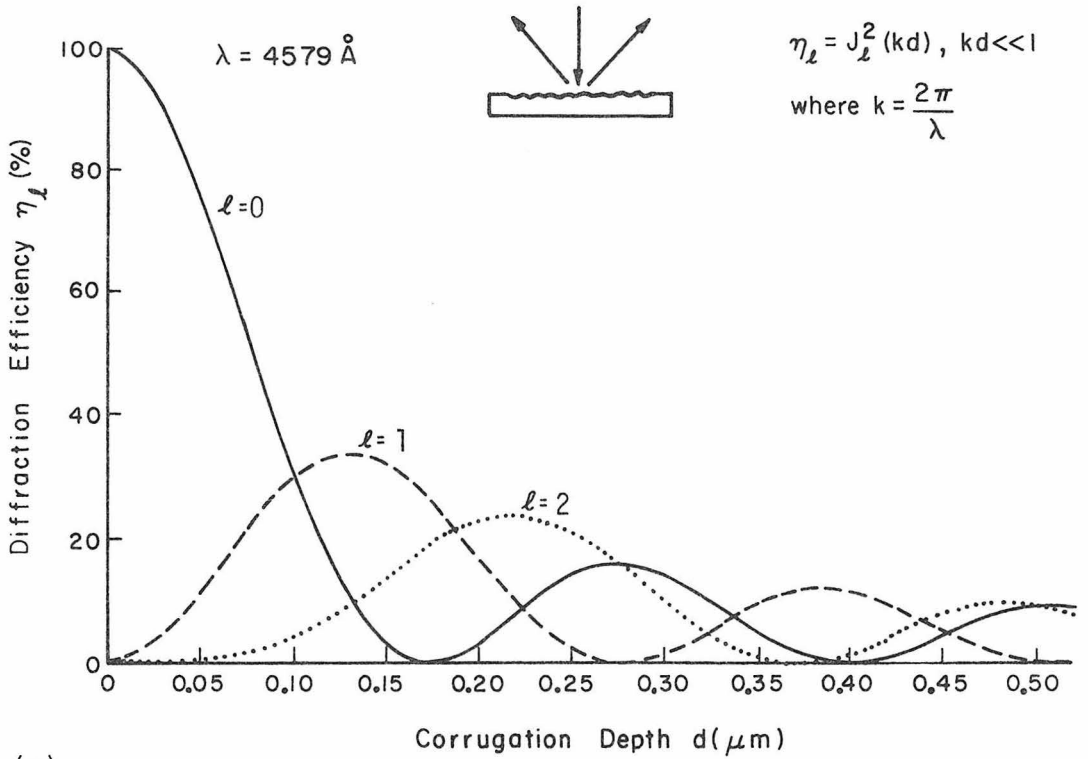

(a)

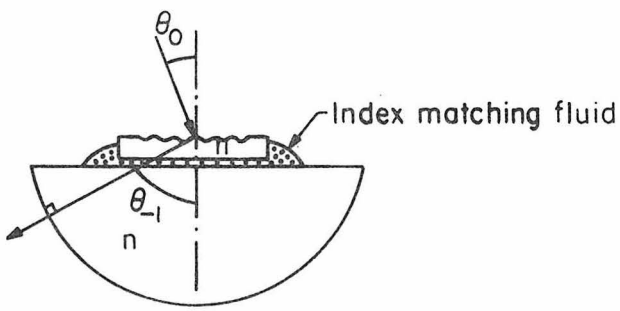

kd<<1

$$\eta_{-1} = \frac{k^2 d^2}{4} \frac{\sqrt{n^2 - (\frac{\lambda}{\Lambda} - \sin\theta_0)^2}\ \cos\theta_0\ (\cos\theta_0 - \sqrt{n^2 - \sin^2\theta_0})^2}{n^2 - 1} \quad \text{for TE waves}$$

(b)

Fig. 5.12 Determination of the corrugation depth through the measurement of diffraction efficiency (a) for reflection gratings and (b) for transmission gratings.

Chapter 5 - References

1. J. Noda and M. Fukuma, "Fabrication of optical waveguides in $LiNbO_3$ and $LiTaO_3$", 1977 International Conference on Integrated Optics and Optical Fiber Communication, Paper 02-1, Tokyo, Japan, 1977.
2. J. E. Goell and R. D. Standley, "Sputtered glass waveguide for integrated optical circuits", Bell Syst. Tech. J. (Briefs) 48, 3445 (1969).
3. C. W. Pitt, "Sputtered-glass optical waveguides", Electron. Lett. 9, 401 (1973).
4. B. M. Gurmin, Yu. A. Ryzhov, and I. I. Shkarban, "Angular distributions of atoms sputtered from polycrystalline targets by inert-gas ions", Bull. Acad. Sci. USSR, Phys. Ser. 33, 752 (1969).
5. P. K. Tien, R. Ulrich, and R. J. Martin, "Modes of propagating light waves in thin deposited semiconductor films", Appl. Phys. Lett. 14, 291 (1969).
6. R. Ulrich and R. Torge, "Measurement of thin film parameters with a prism coupler", Appl. Opt. 12, 2901 (1973).
7. F. Abelès, "La détermination de l'indice et de l'épaisseur des couches minces transparentés", J. Physique Rad. 11, 310 (1950).
8. P. K. Tien and R. Ulrich, "Theory of prism-film coupler and thin-film light guides", J. Opt. Soc. Am. 60, 1325 (1970).
9. F. Zernike, J. W. Douglas, and D. R. Olson, "Transmission measurements in optical waveguides produced by proton irradiation of fused silicon", 1971 Spring Meeting of the Optical Society of America, Paper WC19, Tucson, Arizona, 1971 .

10. H. W. Yen, "GaAs-GaAlAs Distributed Feedback and Distributed Bragg Reflector Lasers," Caltech Ph.D. thesis, 1976, p. 155.

11. H. L. Garvin, "High resolution fabrication by ion beam sputtering", in the Kodak Microelectronics Seminar, San Diego, California, 1972.

12. L. F. Johnson, G. W. Kammlott, and K. A. Ingersoll, "Generation of periodic surface corrugations", Appl. Opt. 17, 1165 (1978).

Appendix A

DERIVATION OF THE HELMHOLTZ EQUATIONS

In a dielectric medium without free charge and current, Maxwell's equations are written

$$\begin{aligned} \vec{\nabla} \cdot \vec{D} &= 0 \\ \vec{\nabla} \cdot \vec{B} &= 0 \\ \vec{\nabla} \times \vec{E} &= -\frac{\partial \vec{B}}{\partial t} \\ \vec{\nabla} \times \vec{H} &= \frac{\partial \vec{D}}{\partial t} \end{aligned} \tag{A.1}$$

where $\vec{B} = \mu_o \vec{H}$, and $\vec{D} = \varepsilon_o \vec{E} + \vec{P} = \varepsilon_o n^2 \vec{E}$. $\vec{E}$ and $\vec{H}$ are the electric and magnetic field, respectively. If a harmonic time dependence of $e^{-i\omega t}$ is assumed, then the last two equations in (A.1) become

$$\vec{\nabla} \times \vec{E} = i\omega\mu_o \vec{H} \tag{A.2}$$

$$\vec{\nabla} \times \vec{H} = -i\omega\varepsilon_o n^2 \vec{E} \tag{A.3}$$

Taking the curl of (A.2) and using (A.3), we obtain the equation for the electric field $\vec{E}$

$$(\nabla^2 + k^2 n^2)\vec{E} = \vec{\nabla}(\vec{\nabla} \cdot \vec{E}) \tag{A.4}$$

where $k^2 = \omega^2 \mu_o \varepsilon_o$ or $k = 2\pi/\lambda$; λ = vacuum wavelength. If $\vec{E}$ is along a direction of translational symmetry of the dielectric constant, or if the medium is homogeneous, (A.4) becomes

$$(\nabla^2 + k^2 n^2)\vec{E} = 0 \tag{A.5}$$

Similarly, the magnetic field H satisfies

$$\vec{\nabla} \times \left(\frac{1}{n^2} \vec{\nabla} \times \vec{H}\right) = k^2 \vec{H} \tag{A.6}$$

In the case of a homogeneous medium, (A.6) becomes

$$(\nabla^2 + k^2 n^2)\vec{H} = 0 \tag{A.7}$$

Appendix B

DERIVATION OF THE TM-MODE COUPLING COEFFICIENT

The magnetic field H obeys (A.6):

$$\vec{\nabla} \times \left(\frac{1}{n^2} \vec{\nabla} \times \vec{H}\right) = k^2 \vec{H} \quad , \qquad k = 2\pi/\lambda \tag{B.1}$$

For a TM waveguide mode, the independent field component $H_y = H_y(z,x)$. From (B.1), H_y satisfies

$$\frac{\partial}{\partial z} \left(\nu \frac{\partial H_y}{\partial z}\right) + \frac{\partial}{\partial x} \left(\nu \frac{\partial H_y}{\partial x}\right) + k^2 H_y = 0 \quad , \quad \nu \equiv \frac{1}{n^2} \tag{B.2}$$

In a structure such as that treated in Section 2.3, the function ν is periodic in z and can be expressed

$$\nu(z,x) = \nu'(x) + \Delta\nu \sum_{\ell \neq 0} a_\ell(x)\, e^{-i\ell \frac{2\pi}{\Lambda} z} \tag{B.3}$$

where $\qquad \nu'(x) \equiv \nu(x) + \Delta\nu\, a_0(x)$

Here $\nu(x)$ describes the inverse squared index distribution for the uncorrugated waveguide; $\Delta\nu \equiv \frac{1}{n_1^2} - \frac{1}{n_2^2}$ is the "perturbed" amplitude; a_ℓ are Fourier coefficients for the corrugated profile. For the contradirectional coupling, assume

$$H_y = [A(z)\, e^{i\beta z} + B(z)\, e^{-i\beta z}]\, g(x) \tag{B.4}$$

where g(x) is the transverse field distribution of the mode in a structure described by $\nu'(x)$. Following the same approximation in deriving (2.40), we again obtain the coupled-mode equations

$$\begin{cases} \dfrac{dB}{dz} = \kappa\, A\, e^{i2\Delta\beta z} \\ \dfrac{dA}{dz} = \kappa^{*} B\, e^{-i2\Delta\beta z} \end{cases} \tag{B.5}$$

where $\Delta\beta = \beta - \beta_o$, $\beta_o \equiv \ell\pi/\Lambda$, and

$$K = \frac{1}{2i\beta} \frac{\langle g|\Delta\nu\,[\frac{d}{dx}(a_\ell \frac{dg}{dx}) + \beta_o^2\, a_\ell g]\rangle}{\langle g|\nu' g\rangle}$$

Integration by parts leads to

$$K = \frac{i}{2\beta} \frac{\Delta\nu\{\int a_\ell(x)[\frac{dg}{dx}]^2\,dx - \beta_o^2 \int a_\ell(x)[g(x)]^2\,dx\}}{\int \nu'(x)[g(x)]^2\,dx} \tag{B.6}$$

which is the coupling coefficient for TM modes.

Appendix C

DERIVATION OF GENERALIZED COUPLED-MODE EQUATIONS

In Chapter 2, only uniform K and Λ over the coupling length have been considered. If the corrugation depth or waveguide thickness varies along the coupling length, then K is no longer constant. However, the equation can be generalized by replacing the constant K by K(z). If the period of corrugation is variable, $\Lambda = \Lambda(z)$, the generalization of the equation can be illustrated with the following example.

Assume

$$n^2(z) = n^2 + \underbrace{\Delta n^2 \cos \phi(z)}_{\text{perturbation term}} \tag{C.1}$$

where

$$\phi(z) = \int_0^z \frac{2\pi}{\Lambda(z)}\, dz$$

This is a one-dimensional problem. E(z) satisfies

$$\left[\frac{d^2}{dz^2} + k^2 n^2(z)\right] E(z) = 0$$

Assuming a solution of the form

$$E(z) = A(z)\, e^{i\beta z} + B(z)\, e^{-i\beta z}, \quad \beta = kn \tag{C.2}$$

and using the slow-varying approximation, we obtain

$$\begin{cases} \dfrac{dB}{dz} = K\, A\, e^{i(2\beta z - \phi(z))} \\ \dfrac{dA}{dz} = K^* B\, e^{-i(2\beta z - \phi(z))} \end{cases} \tag{C.3}$$

where K is interpreted as a coupling coefficient. These are generalized coupled-mode equations.

Appendix D

PARABOLIC CYLINDER FUNCTIONS

Some of the properties of parabolic cylinder functions used in Section 4.5 are listed below.

A complex solution of the equation

$$\frac{d^2w}{d\zeta^2} + (\frac{1}{4}\zeta^2 - c)w = 0 \qquad (D.1)$$

is $E(c,\zeta)$, where c is a complex parameter, and ζ is a real variable. $E(c,\zeta)$ and $E^*(c,\zeta)$ are linearly independent and their Wronskian is

$$W[E(c,\zeta), E^*(c,\zeta)] = -2i \qquad (D.2)$$

Two recurrence relations with c's differing by i are:

$$\frac{dE(c,\zeta)}{d\zeta} + i\frac{\zeta}{2}E(c,\zeta) - i[\pm(c+\frac{i}{2})]^{1/2}E(c+i,\zeta) = 0 \qquad (D.3)$$

and

$$\frac{dE(c,\zeta)}{d\zeta} - i\frac{\zeta}{2}E(c,\zeta) \pm i[\pm(c-\frac{i}{2})]^{1/2}E(c-i,\zeta) = 0 \qquad (D.4)$$

The $\pm$ signs apply in the right- and left-half of the complex c plane, respectively. The linear relation

$$(1+e^{2\pi c})^{1/2}E(c,\zeta) = e^{\pi c}E^*(c,\zeta) + iE^*(c,-\zeta) \qquad (D.5)$$

is useful in writing solutions for negative ζ in terms of the functions of positive ζ. The asymptotic expansion of $E(c,\zeta)$ for $\zeta >> |c|$ is

$$E(c,\zeta) = (\frac{2}{\zeta})^{1/2}[-\frac{\Gamma(\frac{1}{2}+ic)}{\Gamma(\frac{1}{2}-ic)}]^{1/4} e^{i\frac{\zeta^2}{4} - ic\,\ell n\,\zeta} s(c,\zeta) \qquad (D.6)$$

where

$$s(c,\zeta) \sim 1 + \sum_{r=1}^{\infty} (-i)^r \frac{\Gamma(2r+\frac{1}{2}+ic)}{\Gamma(\frac{1}{2}+ic)} \frac{1}{2^r r! \zeta^{2r}}$$

Special Cases for c = a,b

According to (4.19), $\begin{matrix} a \\ b \end{matrix} = \sigma \pm i/2$, and σ is real and positive. The corresponding functions are $E_a(\zeta) \equiv E(a,\zeta)$ and $E_b(\zeta) \equiv E(b,\zeta)$. Note that $[E_a(\zeta)]^* = E_b^*(\zeta)$ and $[E_b(\zeta)]^* = E_a^*(\zeta)$. Using these identities in (D.5), we obtain

$$\begin{aligned} E_a^*(-\zeta) &= (e^{2\pi\sigma} - 1)^{1/2} E_a(\zeta) - e^{\pi\sigma} E_a^*(\zeta) \\ E_b^*(-\zeta) &= (e^{2\pi\sigma} - 1)^{1/2} E_b(\zeta) + e^{\pi\sigma} E_b^*(\zeta) \\ E_a(-\zeta) &= [E_b^*(-\zeta)]^* \\ E_b(-\zeta) &= [E_a^*(-\zeta)]^* \end{aligned} \tag{D.7}$$

The asymptotic expressions of the functions for positive large values of ζ are

$$\begin{aligned} E_a(\zeta) &= 2^{1/2} \sigma^{-1/4} e^{i\theta(\sigma,\zeta)} s_a(\zeta) \\ E_b(\zeta) &= 2^{1/2} \sigma^{1/4} \zeta^{-1} e^{i\theta(\sigma,\zeta)} s_b(\zeta) \\ E_a^*(\zeta) &= [E_b(\zeta)]^* \\ E_b^*(\zeta) &= [E_a(\zeta)]^* \end{aligned} \tag{D.8}$$

where $\theta(\sigma,\zeta) = \zeta^2/4 - \sigma \ln \zeta + \frac{1}{2} \arg \Gamma(i\sigma) - \pi/8$.

Appendix E

ANALYSIS OF EXPOSURE AND DEVELOPMENT OF PHOTORESIST

Positive photoresist plays an important role in fabricating relief structures in microelectronics and thin-film optical circuits. In particular, AZ-1350B photoresists, manufactured by the Shipley Co., exhibit very high resolution and thus are especially useful in the fabrication of gratings with submicron periods.

Positive photoresist materials are composed of two major components: a base resin and a light-sensitive "inhibitor" compound (which inhibits dissolution of the unexposed resist in an alkaline aqueous developer solution). Photodecomposition of the inhibitor molecules during the exposure decreases its concentration and, as a consequence, increases the etching rate of the exposed resist during development. AZ-1350B photoresists are sensitive to ultraviolet and blue light. In use, the photoresist is spin-coated on the surface of a substrate. The film is then exposed and developed. Here we shall derive the relationship between the etched depth Δ and the exposure E (in units of energy per unit area).

The rate at which the inhibitor concentration at a depth x is reduced by exposure can be described by

$$\frac{\partial M(x,t)}{\partial t} = -c\ I(x,t)\ M(x,t) \quad , \qquad c \equiv \frac{\eta\alpha}{h\nu} \tag{E.1}$$

where $M(x,t)$ = local inhibitor concentration, $I(x,t)$ = light intensity, $h\nu$ = photon energy, η = quantum efficiency, and α = absorption cross

section of inhibitor molecules. Assuming $\alpha M_o a << 1$ (M_o is the concentration in an unexposed film; a is the film thickness), the light intensity is almost uniform across the film, $I(x,t) \simeq I$ (const). Then the fractional concentrations of the residual and destroyed inhibitors after an exposure of t seconds are

$$f_2(t) \equiv \frac{M(t)}{M_o} = e^{-cIt}$$

and (E.2)

$$f_1(t) = 1 - f_2(t)$$

respectively. If the developer etching rate of unexposed resist is r_2 and that of fully bleached resist is r_1, then the etching process is expressed

$$\frac{dx}{dt} = r_1 f_1 + r_2 f_2 = r_1 - \Delta r f_2 \tag{E.3}$$

where $\Delta r = r_1 - r_2$.

In this process the photoresist film is exposed for T seconds and then developed for D seconds. The exposure is defined by $E \equiv IT$. From (E.2) we obtain $f_2 = \exp(-cE)$. Equation (E.3) thus becomes

$$\frac{dx}{dt} = r_1 - \Delta r\, e^{-cE}$$

The resulting etched depth between exposed and unexposed resist is

$$\begin{aligned} \Lambda &= (r_1 - \Delta r\, e^{-cE})D - r_2 D \\ &= \Delta r(1 - e^{-cE})D \\ &\sim \Delta r\, cE\, D \qquad \text{if } cE << 1 \end{aligned} \tag{E.4}$$

The above exponential term represents the material nonlinearity which can be neglected if $cE \ll 1$. For a given photoresist, the exposure E can be reduced and the above condition can be satisfied by using an efficient developer. Compared to the AZ developer, AZ-303A developer much enhanced the photoresist sensitivity and speed. We also found a 6:1 solution (one part of developer diluted with six parts of water) had an acceptable etching rate and behaved linearly (E.4) in the range of our interest. This allowed high-efficiency holographic gratings to be made.

Part II

OPTICAL WAVES IN PERIODIC LAYERED STRUCTURES

Chapter 1

INTRODUCTION

1.1 Wave Propagation in Layered Media

Periodic layered structures play a significant role in a number of important optical applications. These include multilayer coatings for both high reflection and antireflection purposes as well as for monochromatic filtering [1]. Other proposals involve the use of these structures for phase matching in nonlinear optical applications [2,3,4] and for obtaining optical birefringence in layered media composed of isotropic materials [5,6].

Recent developments in the crystal growing field, especially in molecular beam epitaxy [7], make it possible to grow multilayers with well controlled periodicities and with layer thicknesses down to 10Å. We may thus consider the periodic optical medium as a new optical medium to take its place among homogeneous isotropic and anisotropic materials. Before proceeding with the many applications envisaged for periodic media, we need to understand precisely and in detail the nature of electromagnetic wave propagation in these media.

These applications in stratified media benefitted largely from the pioneering analysis of Abelès [8] who introduced the matrix method to treat the propagation of waves in layered structures. Electromagnetic propagation in periodic layered media was considered in detail with the direction of propagation normal to the layers by Levin [9]. Rytov [5] investigated the electromagnetic properties of a finely stratified medium. His results are valid for any layer thickness. However, he

considered only some special cases of wave propagation. Weinstein [10] derived general expressions for the reflectivity and transmissivity of multilayer coatings of any number of components. Epstein [11] found that the equivalent index of refraction of a symmetrical period is a pure imaginary number in a stop band, while it is a real number in a pass band of an alternating layered structure. Propagation characteristics of periodic arrays of dielectric slabs were also studied by Lewis and Hessel [12]. They explained those characteristics in terms of stability diagrams and equivalent networks.

Although a number of special cases have been analyzed, a general theory has not been established. This work describes a general theory of electromagnetic propagation in periodic media. Our approach is general, so that many situations considered previously will be shown to be special cases of our formalism. The theory has a strong formal similarity to the quantum theory of electrons in crystals and thus makes heavy use of the concepts of Bloch modes, forbidden gaps, evanescent waves, and even surface levels. In addition to demonstrating the application of the theory to such familiar problems as the reflectivity of multilayer coatings, we also consider guiding phenomena in multilayer structures.

1.2 Multilayer Waveguides

The historical interest in multilayer structures was restricted primarily to the design of reflection coatings. Little attention, however, was paid to the guided waves in these structures. During the last decade, layered structures have been used as waveguides in a variety of

devices such as thin-film passive waveguides and heterojunction semiconductor lasers [13]. Multilayer waveguides are becoming increasingly important in integrated optics. The dual "channel" waveguide has been studied extensively in the theory of branching waveguides [14] and directional couplers [15] which are used as mode selectors and switches in integrated optics. Multichannel waveguides will probably be used in the switching network of a high data rate communications system [16].

In this work, guiding characteristics in periodic multilayer waveguides are investigated. Of particular interest are waves guided by the boundary of a semi-infinite periodic layered structure. These waves were considered in a superficial manner by Arnaud and Saleh [17]. However, for a rigorous treatment, it is necessary to use the results of our general theory presented here.

Chapter 1 - References

1. See, for example, O. S. Heavens, Optical Properties of Thin Solid Films (Dover, New York, 1965), p. 207.
2. A. Ashkin and A. Yariv, Bell Labs. Tech. Memo MM-61-124-46 (November 13, 1961).
3. N. Bloembergen and A. J. Sievers, "Nonlinear optical properties of periodic laminar structures", Appl. Phys. Lett. 17, 483 (1970).
4. C. L. Tang and P. P. Bey, "Phase matching in second-harmonic generation using artificial periodic structures", IEEE J. Quantum Electron. QE-9, 9 (1973).
5. S. M. Rytov, "Electromagnetic properties of a finely stratified medium", Zh. Eksp. Teor. Fiz. 29, 605 (1955).
6. J. P. van der Ziel, M. Ilegems, and R. M. Mikulyak, "Optical birefringence of thin GaAs-AlAs multilayer films", Appl. Phys. Lett. 28, 735 (1976).
7. A. Y. Cho and J. R. Arthur, Progress in Solid State Chemistry (Pergamon, Oxford, 1975), Vol. 10, p. 156.
8. F. Abelès, "Recherches sur la propagation des ondes électromagnétiques sinusoïdales dans les milieux stratifiés. Application aux couches minces", Ann.Physique (12) 5, 596, 706 (1950).
9. M. L. Levin, "Propagation of a plane electromagnetic wave in a periodical layered medium", Zh. Tekh. Fiz. 18, 1399 (1948).
10. W. Weinstein, "The reflectivity and transmissivity of multiple thin coatings", J. Opt. Soc. Am. 37, 576 (1947).

11. L. I. Epstein, "The design of optical filters", J. Opt. Soc. Am. 42, 806 (1952).

12. L. R. Lewis and A. Hessel, "Propagation characteristics of periodic arrays of dielectric slabs", IEEE Trans. Microwave Theory Tech. MTT-19, 276 (1971).

13. M. B. Panish, "Heterostructure Injection Lasers", Proc. IEEE 64, 1512 (1976).

14. H. Yajima, "Dielectric thin-film optical branching waveguide", Appl. Phys. Lett. 22, 647 (1973).

15. A. Ihaya, H. Furuta, and H. Noda, "Thin-film optical directional coupler", Proc. IEEE (Lett.) 60, 470 (1972).

16. H. Ogiwara and H. Yamamoto, "Optical waveguide switch (3 x 3) for an optical switching system", Appl. Opt. 17, 1182 (1978).

17. J. A. Arnaud and A.A.M. Saleh, "Guidance of surface waves by multilayer coatings", Appl. Opt. 13, 2343 (1974).

Chapter 2

BLOCH FORMULATION OF ELECTROMAGNETIC PROPAGATION IN PERIODIC MEDIA

2.1 Introduction

A systematic approach which formulates electromagnetic propagation in periodic media will be presented in this chapter. It is based on the Bloch formalism of periodic structures.

The Bloch wave function was introduced in 1928 to describe electron motion in crystals [1]. The resulting theory of energy bands was a great advancement in solid state physics. Electromagnetic propagation in a periodic layered medium has its formal similarity to electron motion in a one-dimensional periodic square-well potential field [2]. Thus we expect that all the interesting properties of electrons in crystalline solids should have their counterparts in the optics of periodic media. Of these, the analogous band structure of a periodic medium is totally new in optics.

The mathematical derivations can be largely simplified by choosing a convenient representation for the wave function and by using matrix algebra. Thus, before giving our Bloch solution, we will start with the above-mentioned approach in the next section.

2.2 Matrix Method and Translation Operator

For the sake of clarity in introducing the basic concepts, we will consider only the simplest type of periodic medium. The periodic medium treated in what follows consists of alternating layers of different indices of refraction. The index profile is given by

$$n(x) = \begin{cases} n_2 & 0 < x < b \\ n_1 & b < x < \Lambda \end{cases} \tag{2.1}$$

with

$$n(x+\Lambda) = n(x) \tag{2.2}$$

where the x-axis is normal to the interfaces, and Λ is the period. The geometry of the structure is sketched in Fig. 2.1.

The field within each homogeneous layer can be expressed as a sum of an incident plane wave and a reflected plane wave. In the case of TE waves (E-vector normal to the plane of incidence), the electric field in the n_α-layer of the n^{th} unit cell is thus written as

$$E(z,x) = E(x)\, e^{i\beta z} \tag{2.3}$$

with

$$E(x) = a_n^{(\alpha)}\, e^{ik_{\alpha x}(x-n\Lambda)} + b_n^{(\alpha)}\, e^{-ik_{\alpha x}(x-n\Lambda)} \tag{2.4}$$

where

$$k_{\alpha x} = \sqrt{(\frac{\omega}{c} n_\alpha)^2 - \beta^2}\ , \qquad \alpha=1,2 \tag{2.5}$$

The electric field can also be represented by a column vector whose components are the complex amplitudes $a_n^{(\alpha)}$ and $b_n^{(\alpha)}$:

$$\begin{pmatrix} a_n^{(\alpha)} \\ b_n^{(\alpha)} \end{pmatrix}$$

The column vectors are not independent of each other. They are related through the continuity conditions at the interfaces. As a matter of fact, only one vector (or two components of two different vectors) can

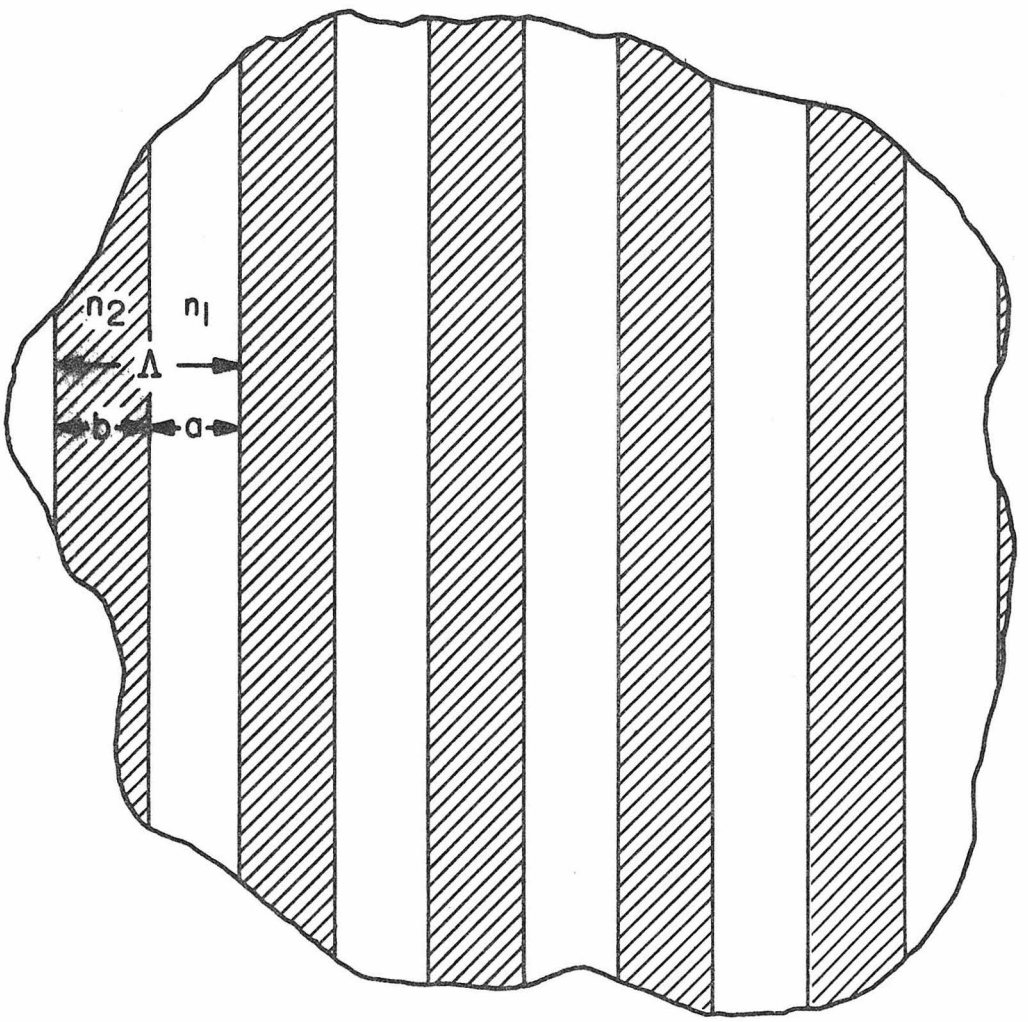

Fig. 2.1 A portion of a typical periodic medium.

be chosen arbitrarily. Imposing continuity of E and dE/dx at $x = (n-1)\Lambda$ (see Fig. 2.2),

$$a_{n-1} + b_{n-1} = c_n e^{-ik_{2x}\Lambda} + d_n e^{ik_{2x}\Lambda} \tag{2.6}$$

$$k_{1x}(a_{n-1} - b_{n-1}) = k_{2x}(c_n e^{-ik_{2x}\Lambda} - d_n e^{ik_{2x}\Lambda}) \tag{2.7}$$

or in terms of a matrix equation for our column vectors,

$$\begin{pmatrix} a_{n-1} \\ b_{n-1} \end{pmatrix} = \frac{1}{2} \begin{pmatrix} (1+\frac{k_{2x}}{k_{1x}})e^{-ik_{2x}\Lambda} & (1-\frac{k_{2x}}{k_{1x}})e^{ik_{2x}\Lambda} \\ (1-\frac{k_{2x}}{k_{1x}})e^{-ik_{2x}\Lambda} & (1+\frac{k_{2x}}{k_{1x}})e^{ik_{2x}\Lambda} \end{pmatrix} \begin{pmatrix} c_n \\ d_n \end{pmatrix} \tag{2.8}$$

Similarly, the boundary conditions at $x = (n-1)\Lambda + b$ lead to

$$c_n e^{-ik_{2x}a} + d_n e^{ik_{2x}a} = a_n e^{-ik_{1x}a} + b_n e^{ik_{1x}a} \tag{2.9}$$

$$k_{2x}(c_n e^{-ik_{2x}a} - d_n e^{ik_{2x}a}) = k_{1x}(a_n e^{-ik_{1x}a} - b_n e^{ik_{1x}a}) \tag{2.10}$$

or

$$\begin{pmatrix} c_n \\ d_n \end{pmatrix} = \frac{1}{2} \begin{pmatrix} (1+\frac{k_{1x}}{k_{2x}})e^{i(k_{2x}-k_{1x})a} & (1-\frac{k_{1x}}{k_{2x}})e^{i(k_{2x}+k_{1x})a} \\ (1-\frac{k_{1x}}{k_{2x}})e^{-i(k_{2x}+k_{1x})a} & (1+\frac{k_{1x}}{k_{2x}})e^{-i(k_{2x}-k_{1x})a} \end{pmatrix} \begin{pmatrix} a_n \\ b_n \end{pmatrix} \tag{2.11}$$

where we have defined $a_n \equiv a_n^{(1)}$, $b_n \equiv b_n^{(1)}$, $c_n \equiv a_n^{(2)}$, and $d_n \equiv b_n^{(2)}$. By eliminating $\binom{c_n}{d_n}$, the matrix equation

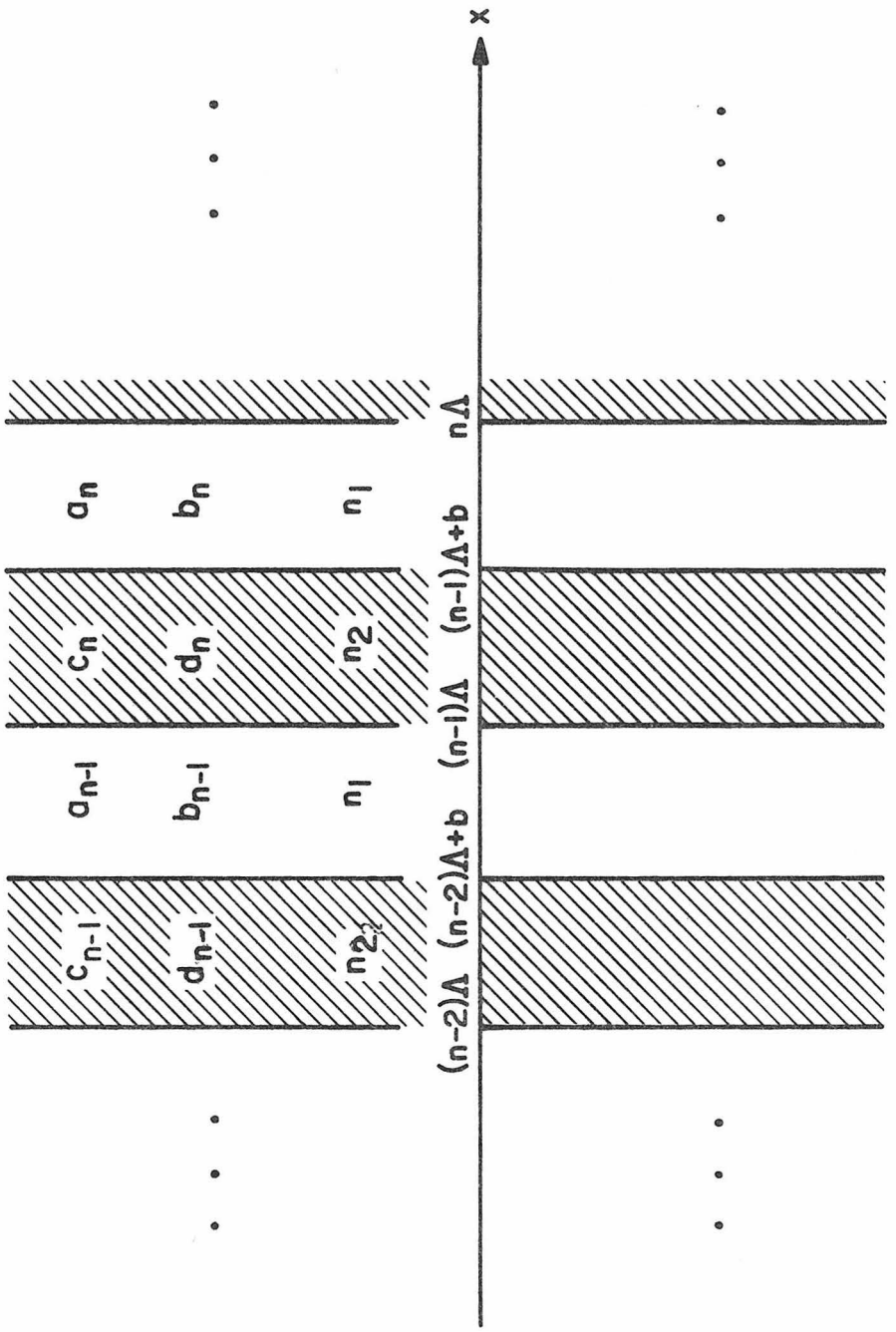

Fig. 2.2 Plane wave amplitudes associated with the n^{th} and $(n-1)^{th}$ unit cells.

$$\begin{pmatrix} a_{n-1} \\ b_{n-1} \end{pmatrix} = \begin{pmatrix} A & B \\ C & D \end{pmatrix} \begin{pmatrix} a_n \\ b_n \end{pmatrix} \tag{2.12}$$

is obtained. The matrix elements are

$$A = e^{-ik_{1x}a}[\cos k_{2x}b - \frac{1}{2} i(\frac{k_{2x}}{k_{1x}} + \frac{k_{1x}}{k_{2x}}) \sin k_{2x}b] \tag{2.13}$$

$$C = e^{-ik_{1x}a}[\frac{1}{2} i(\frac{k_{2x}}{k_{1x}} - \frac{k_{1x}}{k_{2x}}) \sin k_{2x}b] \tag{2.14}$$

$$B = C^* \tag{2.15}$$

$$D = A^* \tag{2.16}$$

and according to (2.5) can be viewed as functions of β. The matrix in (2.12) is the unit cell translation matrix which relates the complex amplitudes of the incident plane wave a_{n-1} and the reflected plane wave b_{n-1} in one layer of a unit cell to those of the equivalent layer in the next unit cell. Because of the fact that this matrix relates the fields of two equivalent layers with the same index of refraction, it is unimodular, i.e.,

$$AD - BC = 1 \tag{2.17}$$

which can be verified using expressions in (2.13)-(2.16). It is important to notice that the matrix which relates $\begin{pmatrix} c_{n-1} \\ d_{n-1} \end{pmatrix}$ to $\begin{pmatrix} c_n \\ d_n \end{pmatrix}$ is different from the matrix in (2.12). These matrices, however, possess the same trace. As will be shown later, the trace of the translation matrix is directly

related to the band structure of the periodic medium.

The matrix elements for TM waves (H-vector normal to the plane of incidence) are slightly different from those of the TE waves. They are given by

$$A_{TM} = e^{-ik_{1x}a}\left[\cos k_{2x}b - \frac{1}{2}\, i\left(\frac{k_{2x}}{k_{1x}}\frac{n_1^2}{n_2^2} + \frac{k_{1x}}{k_{2x}}\frac{n_2^2}{n_1^2}\right)\sin k_{2x}b\right] \tag{2.18}$$

$$C_{TM} = e^{-ik_{1x}a}\left[\frac{1}{2}\, i\left(\frac{k_{2x}}{k_{1x}}\frac{n_1^2}{n_2^2} - \frac{k_{1x}}{k_{2x}}\frac{n_2^2}{n_1^2}\right)\sin k_{2x}b\right] \tag{2.19}$$

$$B_{TM} = C_{TM}^{*} \tag{2.20}$$

$$D_{TM} = A_{TM}^{*} \tag{2.21}$$

As noted above, only one column vector is independent. We can choose it, as an example, as the column vector of the n_1-layer in the zeroth unit cell. The remaining column vectors of the equivalent layers are given as

$$\begin{pmatrix} a_n \\ b_n \end{pmatrix} = \begin{pmatrix} A & B \\ C & D \end{pmatrix}^{-n} \begin{pmatrix} a_o \\ b_o \end{pmatrix} \tag{2.22}$$

By using (2.17), the above equation can be simplified to

$$\begin{pmatrix} a_n \\ b_n \end{pmatrix} = \begin{pmatrix} D & -B \\ -C & A \end{pmatrix}^{n} \begin{pmatrix} a_o \\ b_o \end{pmatrix} \tag{2.23}$$

The column vector for the n_2-layer can always be obtained by using (2.11).

2.3 Bloch Waves and Band Structures

The periodic medium is equivalent to a one-dimensional lattice which is invariant under the lattice translation. The lattice or unit cell translation operator T is defined by

$$Tx = x + \Lambda \tag{2.24}$$

It follows that

$$T\,E(x) = E(T^{-1}x) = E(x-\Lambda) \tag{2.25}$$

The ABCD matrix derived in the previous section is thus a representation of the unit cell translation operator. According to the Floquet theorem, a wave propagating in a periodic medium is of the form [3]

$$E_K(x) = u_K(x)\, e^{iKx} \tag{2.26}$$

where $u_K(x)$ is periodic with a period Λ, i.e.,

$$u_K(x+\Lambda) = u_K(x) \tag{2.27}$$

It follows that

$$E_K(x+\Lambda) = E_K(x)\, e^{iK\Lambda} \tag{2.28}$$

The subscript K indicates that the function $E_K(x)$ depends on K. The parameter K is known as the Bloch wave number. The problem at hand is thus that of determining K and $E_K(x)$.

In terms of our column vector representation, and from (2.4), the periodic condition (2.28) for the Bloch wave is simply

$$\begin{pmatrix} a_n \\ b_n \end{pmatrix} = e^{iK\Lambda} \begin{pmatrix} a_{n-1} \\ b_{n-1} \end{pmatrix} \tag{2.29}$$

It follows from (2.12) and (2.29) that the column vector of the Bloch wave satisfies the following eigenvalue problem

$$\begin{pmatrix} A & B \\ C & D \end{pmatrix} \begin{pmatrix} a_n \\ b_n \end{pmatrix} = e^{-iK\Lambda} \begin{pmatrix} a_n \\ b_n \end{pmatrix} \tag{2.30}$$

The phase factor $\exp(-iK\Lambda)$ is thus the eigenvalue of the translation matrix (A,B,C,D) and is given by

$$e^{-iK\Lambda} = \frac{A+D}{2} \pm \sqrt{\left(\frac{A+D}{2}\right)^2 - 1} \tag{2.31}$$

The two eigenvalues in (2.31) are the inverse of each other, since the translation matrix is unimodular. The eigenvectors corresponding to the eigenvalues (2.31) are obtained from (2.30) and are

$$\begin{pmatrix} B \\ e^{-iK\Lambda} - A \end{pmatrix} \quad \text{times an arbitrary constant} \tag{2.32}$$

If we choose the eigenvector of the zeroth column as an independent vector, the eigenvectors of the remaining columns are then derived from (2.29) as

$$\begin{pmatrix} a_n \\ b_n \end{pmatrix} = e^{inK\Lambda} \begin{pmatrix} a_o \\ b_o \end{pmatrix} \tag{2.33}$$

According to (2.4) and (2.33), the final result for the Bloch wave in the n_1-layer of the n^{th} unit cell is

$$E_K(x) = \{[a_o e^{ik_{1x}(x-n\Lambda)} + b_o e^{-ik_{1x}(x-n\Lambda)}]e^{-iK(x-n\Lambda)}\} e^{iKx} \tag{2.34}$$

where a_o and b_o are given by (2.32). This completes the solution of the Bloch waves.

Equation (2.31) gives the dispersion relation among ω, β, and K. It can be rewritten as

$$K(\beta,\omega) = \frac{1}{\Lambda} \cos^{-1}\left(\frac{A+D}{2}\right) \tag{2.35}$$

Regimes where $\left|\frac{A+D}{2}\right| < 1$ correspond to real K's and thus to propagating Bloch waves. When $\left|\frac{A+D}{2}\right| > 1$, $K = \frac{\ell\pi}{\Lambda} + iK_i$ and has an imaginary part so that the Bloch wave is evanescent. These are the so-called "forbidden" gaps of the periodic medium. The band edges are the regimes where $\left|\frac{A+D}{2}\right| = 1$. The band structure for a typical periodic medium as obtained from (2.35) is shown in Figs. 2.3 and 2.4 for TE and TM waves, respectively. It is interesting to notice that the TM forbidden gaps shrink to zero when $\beta = \frac{\omega}{c} n_2 \sin\theta_{2B}$ with θ_{2B} as the Brewster angle, since at this angle the incident and reflected waves are uncoupled. The dispersion relation ω vs K for the special case $\beta = 0$, i.e., normal incidence, is shown in Fig. 2.5.

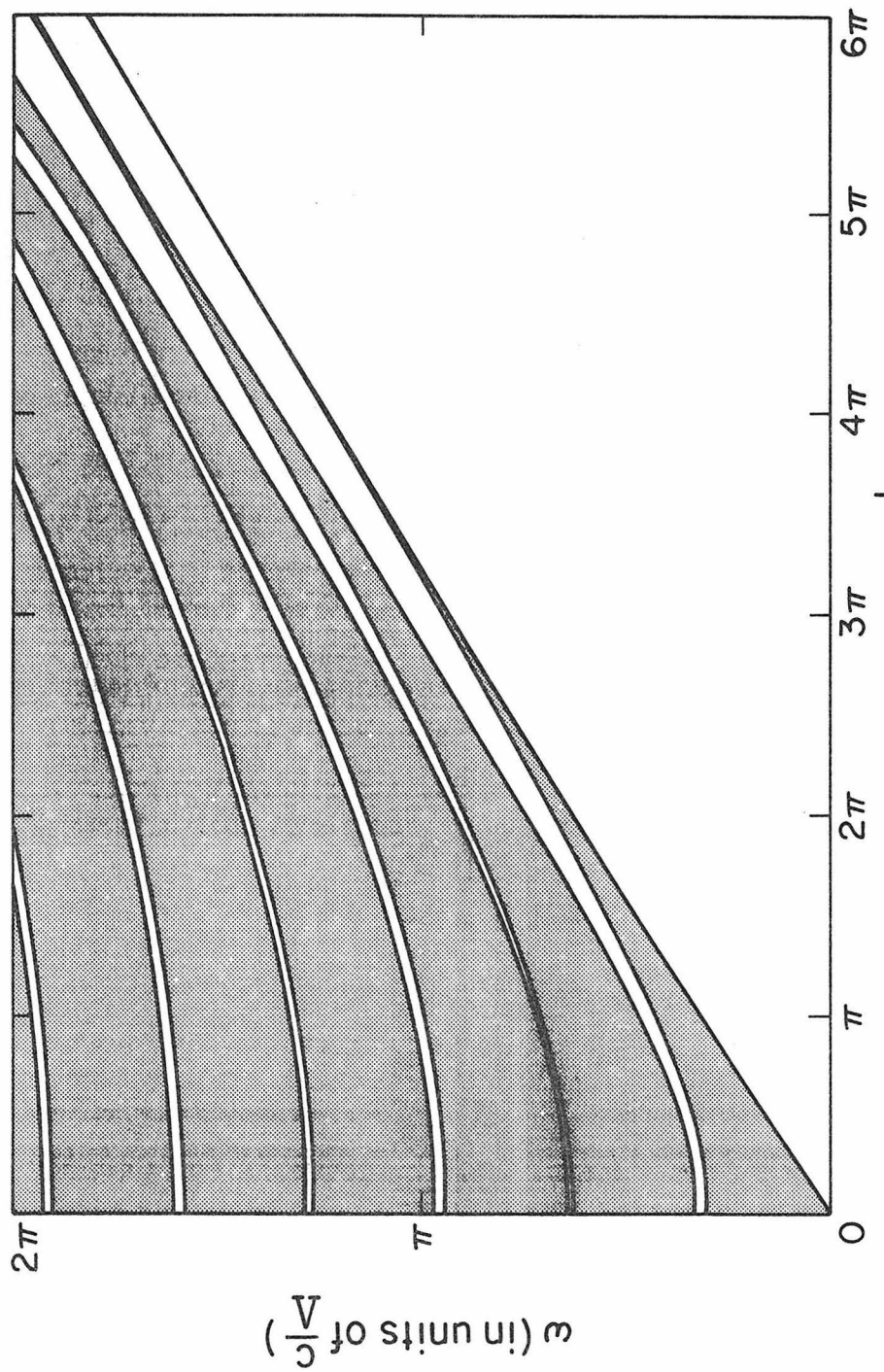

Fig. 2.3 TE wave ($\vec{E}$ normal to the plane of incidence) band structure in the ω-β plane. The dark zones are the allowed bands.

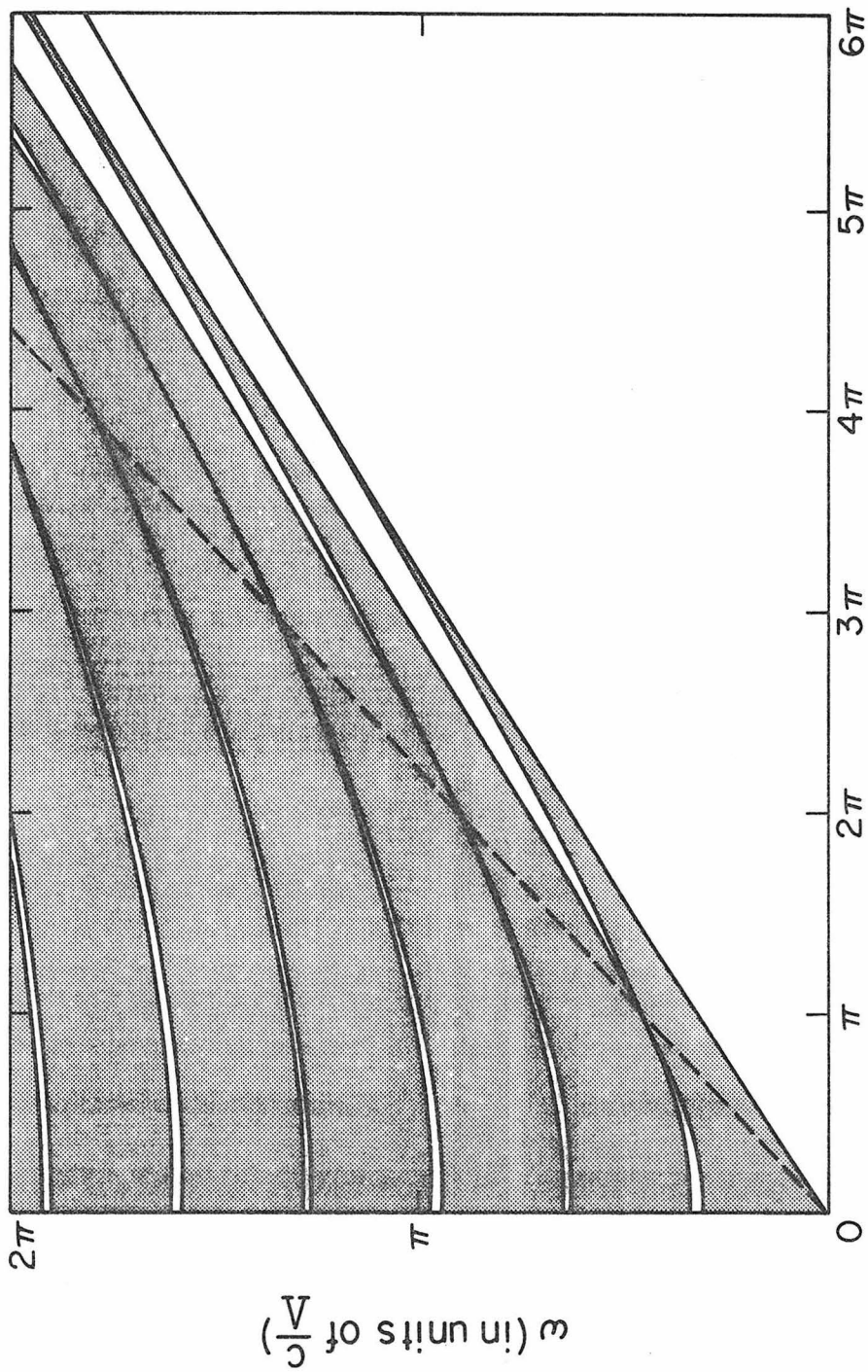

Fig. 2.4 TM wave ($\vec{H}$ normal to the plane of incidence) band structure in the ω-β plane. The dashed line is $\beta = \frac{\omega}{c} n_2 \sin \theta_{2B}$. The dark zones are the allowed bands.

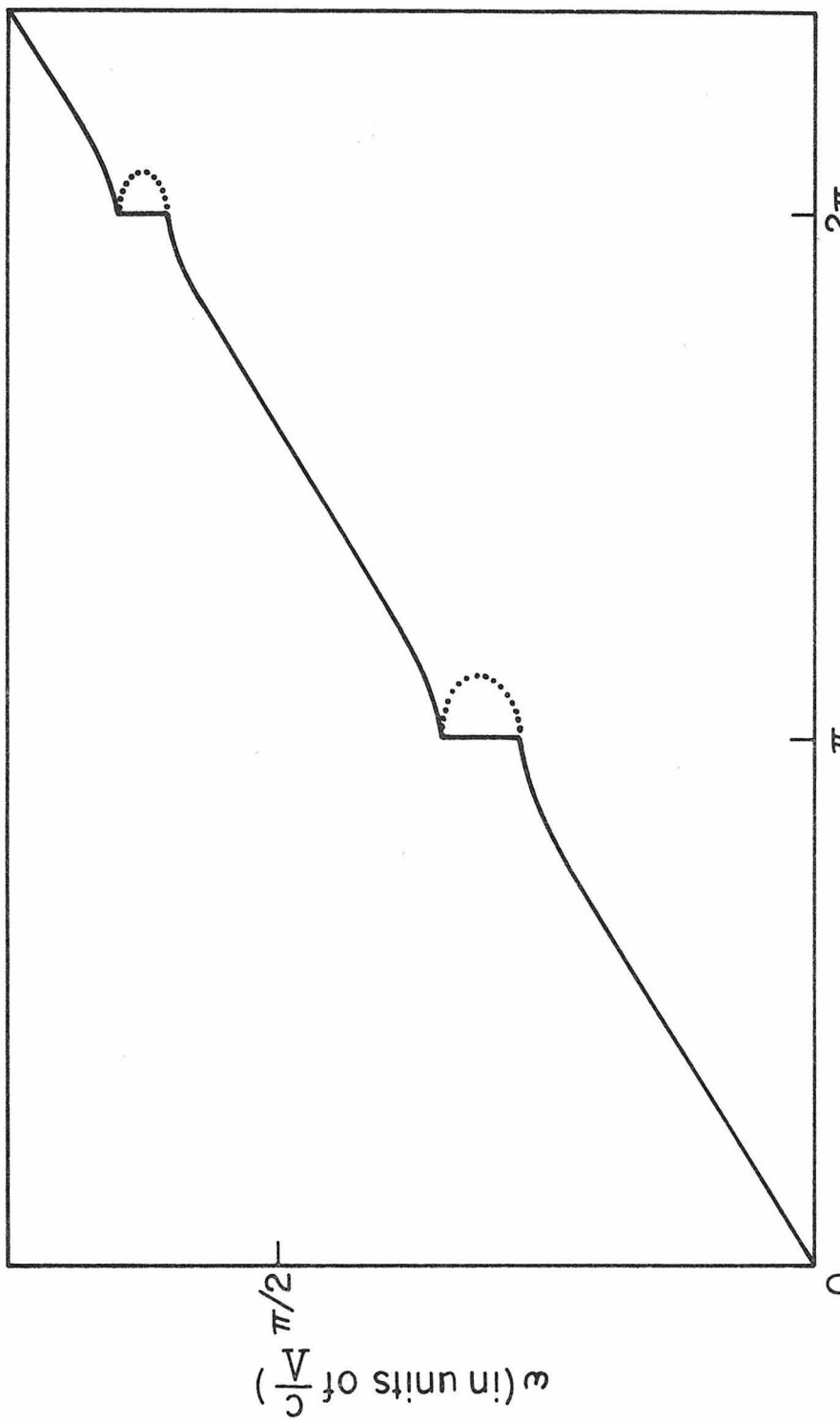

Fig. 2.5 Dispersion relation between ω and K when β = 0 (normal incidence). Dotted curves are the imaginary part of K in arbitrary scales.

Chapter 2 - References

1. F. Bloch, "Über die Quantenmechanik der Elektronen in Kristallgittern," Z. Physik 52, 555 (1928).

2. D. Kossel, "Analogies between thin-film optics and electron-band theory of solids", 1966 Annual Meeting of the Optical Society of America, Paper ThF1, San Francisco, California, 1966.

3. See, for example, C. Kittel, Introduction to Solid State Physics, 5th ed. (Wiley, New York, 1976), p. 190, or
J. Mathews and R. L. Walker, Mathematical Methods of Physics, 2nd ed. (Benjamin, Reading-Massachusetts, 1970), p. 198.

Chapter 3

ANALYSIS OF BRAGG REFLECTORS

3.1 Introduction

As we pointed out previously, the original interest in periodic multilayer structures was in reflection coatings or interference filters [1]. These operations use Bragg diffraction and thus are known as "Bragg" reflectors.

Recent developments in integrated optics have made very heavy use of corrugated waveguides as Bragg reflectors for guided waves [2]. Surface corrugations (or gratings) provide a spatially periodic perturbation on the effective index of refraction of the waveguide. If the corrugation has a rectangular profile, the resulting index variation simulates exactly our periodic medium.

The above two areas of practical interest have given us a great stimulus to study Bragg reflectors as the first application of our new formalism of periodic media. In what follows, we will employ the theory described in the previous chapter to analyze the reflection characteristics of multilayer reflectors. The application to grating reflectors in guided wave optics will also be included.

3.2 Multilayer Reflectors

For simplicity, consider the structure sketched in Fig. 3.1 which consists of a periodic medium of N unit cells as a reflector.

As a result of successive multiplications of the unit cell translation matrix in (2.12), we obtain a matrix equation which relates the

incident, reflected, and transmitted waves by

$$\begin{pmatrix} a_o \\ b_o \end{pmatrix} = \begin{pmatrix} A & B \\ C & D \end{pmatrix}^N \begin{pmatrix} a_N \\ 0 \end{pmatrix} \tag{3.1}$$

The N^{th} power of a unimodular matrix can be simplified by the following matrix identity [3]:

$$\begin{pmatrix} A & B \\ C & D \end{pmatrix}^N = \begin{pmatrix} AU_{N-1} - U_{N-2} & BU_{N-1} \\ CN_{N-1} & DU_{N-1} - U_{N-2} \end{pmatrix} \tag{3.2}$$

where

$$U_N = \frac{\sin(N+1)K\Lambda}{\sin K\Lambda} \tag{3.3}$$

with K given by (2.35). The reflection coefficient is defined by

$$r_N = b_o/a_o \tag{3.4}$$

and is immediately obtained from (3.1) and (3.2) as

$$r_N = \frac{CU_{N-1}}{AU_{N-1} - U_{N-2}} \tag{3.5}$$

The reflectivity is obtained by taking the absolute square of r_N:

$$|r_N|^2 = \frac{|C|^2}{|C|^2 + \left(\frac{\sin K\Lambda}{\sin NK\Lambda}\right)^2} \tag{3.6}$$

We have in (3.6) an analytic expression of the reflectivity of a multilayer reflector. The term $|C|^2$ is directly related to the reflectivity of a single unit cell by

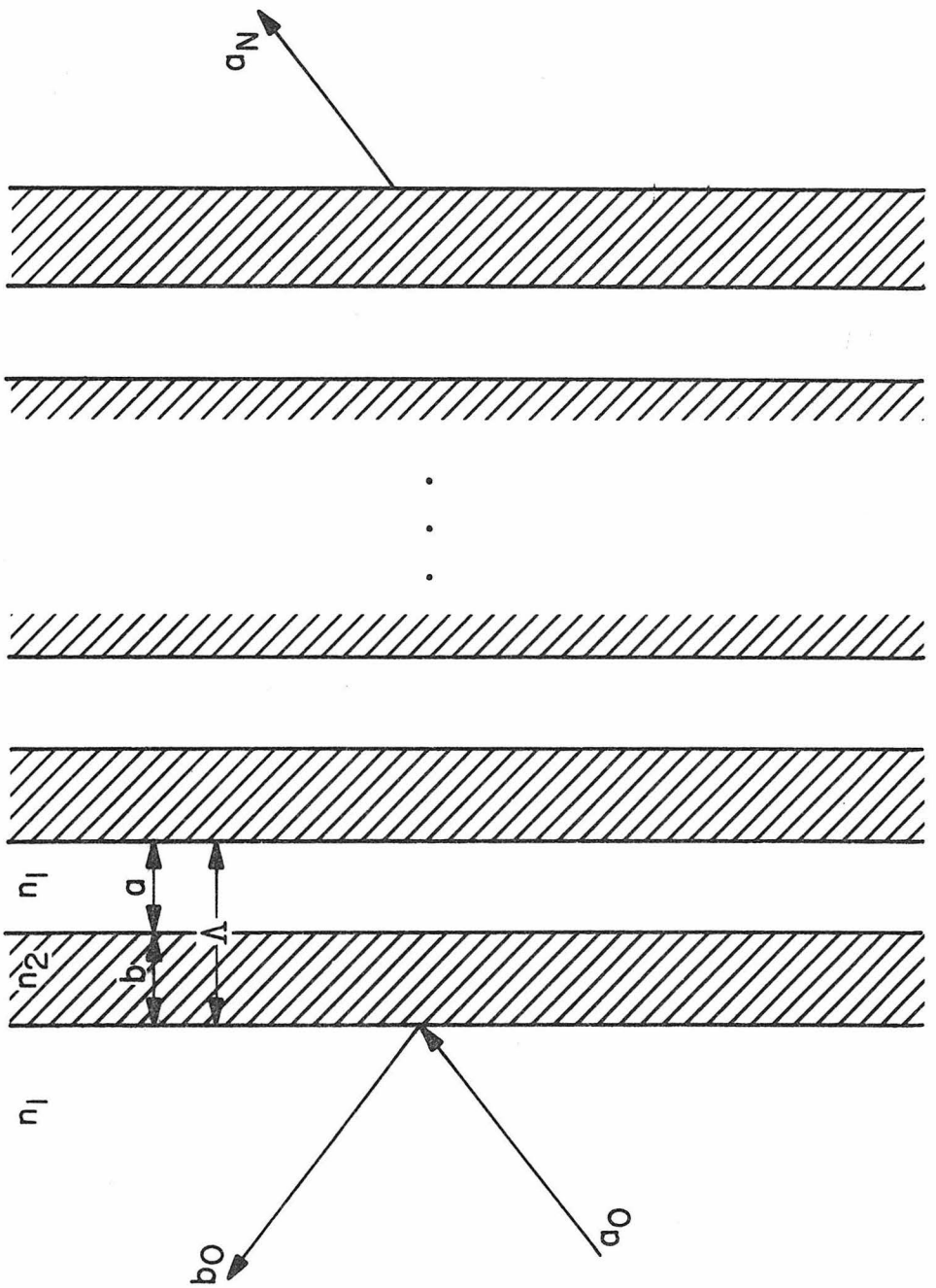

Fig. 3.1 Structure of a simple N-period multilayer reflector.

$$|C|^2 = \frac{|r_1|^2}{1 - |r_1|^2} \tag{3.7}$$

The second term in the denominator of (3.6) is a fast varying function of K, or alternatively, of β and ω. Therefore it dominates the structure of the reflectivity spectrum. Between any two forbidden gaps of the periodic medium there are exactly N-1 nodes where the reflectivity vanishes. The peaks of the reflectivity occur at the centers of the forbidden gaps. There are exactly N-2 side lobes which are all under the envelope $|C|^2 / [|C|^2 + (\sin K\Lambda)^2]$.

At the band edges, $K\Lambda = \ell\pi$ and the reflectivity is given by

$$|r_N|^2 = \frac{|C|^2}{|C|^2 + (\frac{1}{N})^2} \tag{3.8}$$

In the forbidden gap, $K\Lambda = \ell\pi + iK_i\Lambda$ and the reflectivity formula of (3.6) becomes

$$|r_N|^2 = \frac{|C|^2}{|C|^2 + (\frac{\sinh K_i\Lambda}{\sinh NK_i\Lambda})^2} \tag{3.9}$$

For a large N the second term in the denominator approaches zero exponentially as $\exp[-2(N-1)K_i\Lambda]$. It follows that the reflectivity in the forbidden gap is near unity for a Bragg reflector with a substantial number of periods.

TE and TM waves have different band structures and different reflectivities. For TM waves incident at the Brewster angle, there is no reflected wave. Mathematically, this is due to the vanishing of the

dynamical factor $|C|^2$ at that angle. The reflectivity for some typical multilayer reflectors as a function of frequency, using the angle of incidence as a parameter, are shown in Figs. 3.2 and 3.3.

Similarly, the transmission coefficient and transmissivity are obtained as

$$t_N = \frac{a_N}{a_o} = \frac{1}{AU_{N-1} - U_{N-2}} \tag{3.10}$$

and

$$|t_N|^2 = \cdots = 1 - |r_N|^2 \tag{3.11}$$

respectively.

3.3 Grating Reflectors

The analysis of grating reflectors uses the coupled mode theory [4] which is essentially a very good first-order approximation. It also indicates that a grating with a rectangular profile corresponds to the case described above. Here we shall prove that the exact solution (3.9) will reduce to the coupled mode solution when the "perturbation" is small.

Equation (3.9) is rewritten as

$$|r_N|^2 = \frac{|C|^2\left(\frac{\sinh NK_i\Lambda}{\sinh K_i\Lambda}\right)^2}{1 + |C|^2\left(\frac{\sinh NK_i\Lambda}{\sinh K_i\Lambda}\right)^2} \tag{3.12}$$

where

$$K_i\Lambda = \ell n\left(-\frac{A+D}{2} + \sqrt{\left(\frac{A+D}{2}\right)^2 - 1}\right) \tag{3.13}$$

and A, C, and D are given by (2.13), (2.14), and (2.16), respectively. After defining

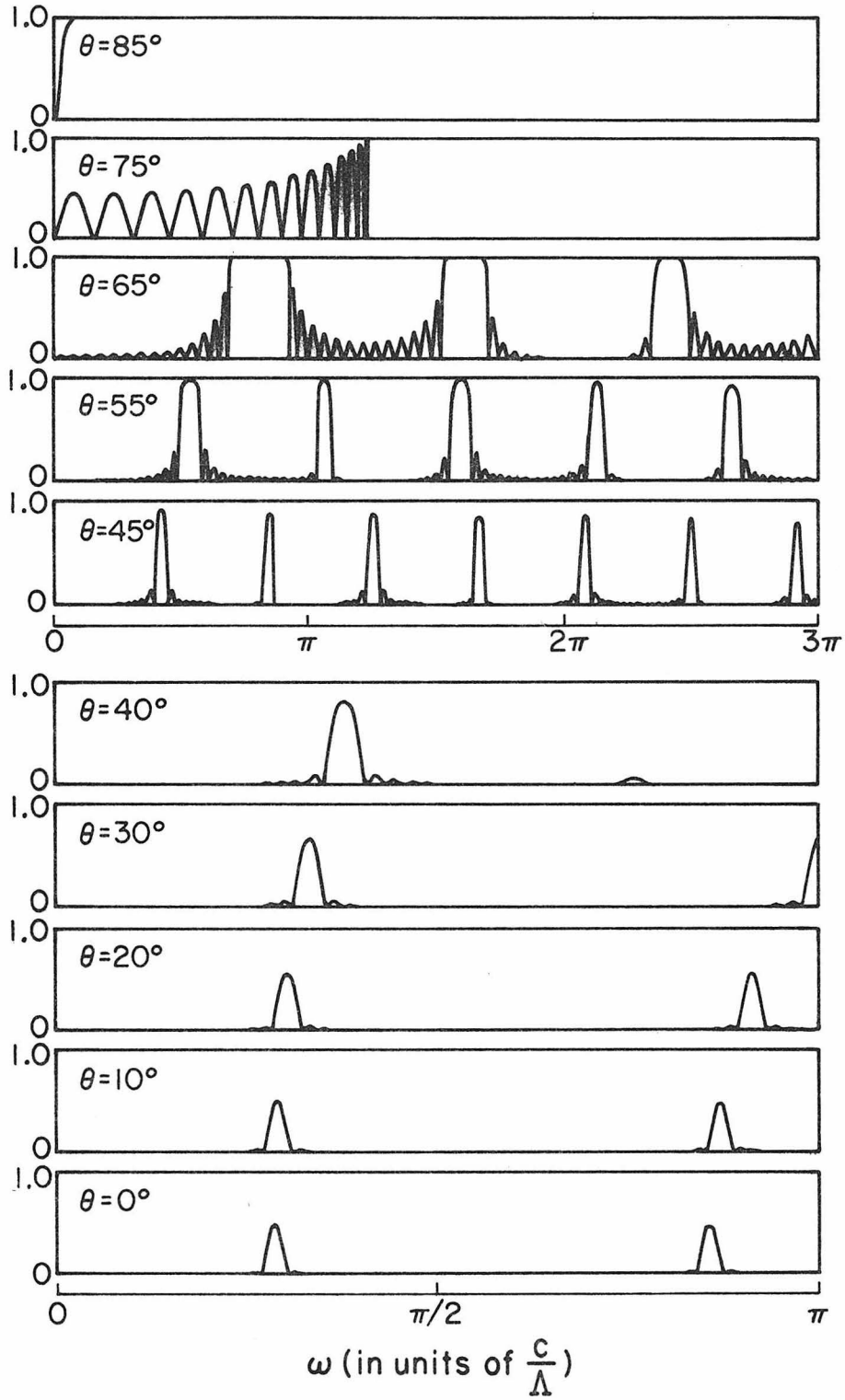

Fig. 3.2 TE wave reflectivity spectra of a 15-period multilayer reflector at various angles of incidence.

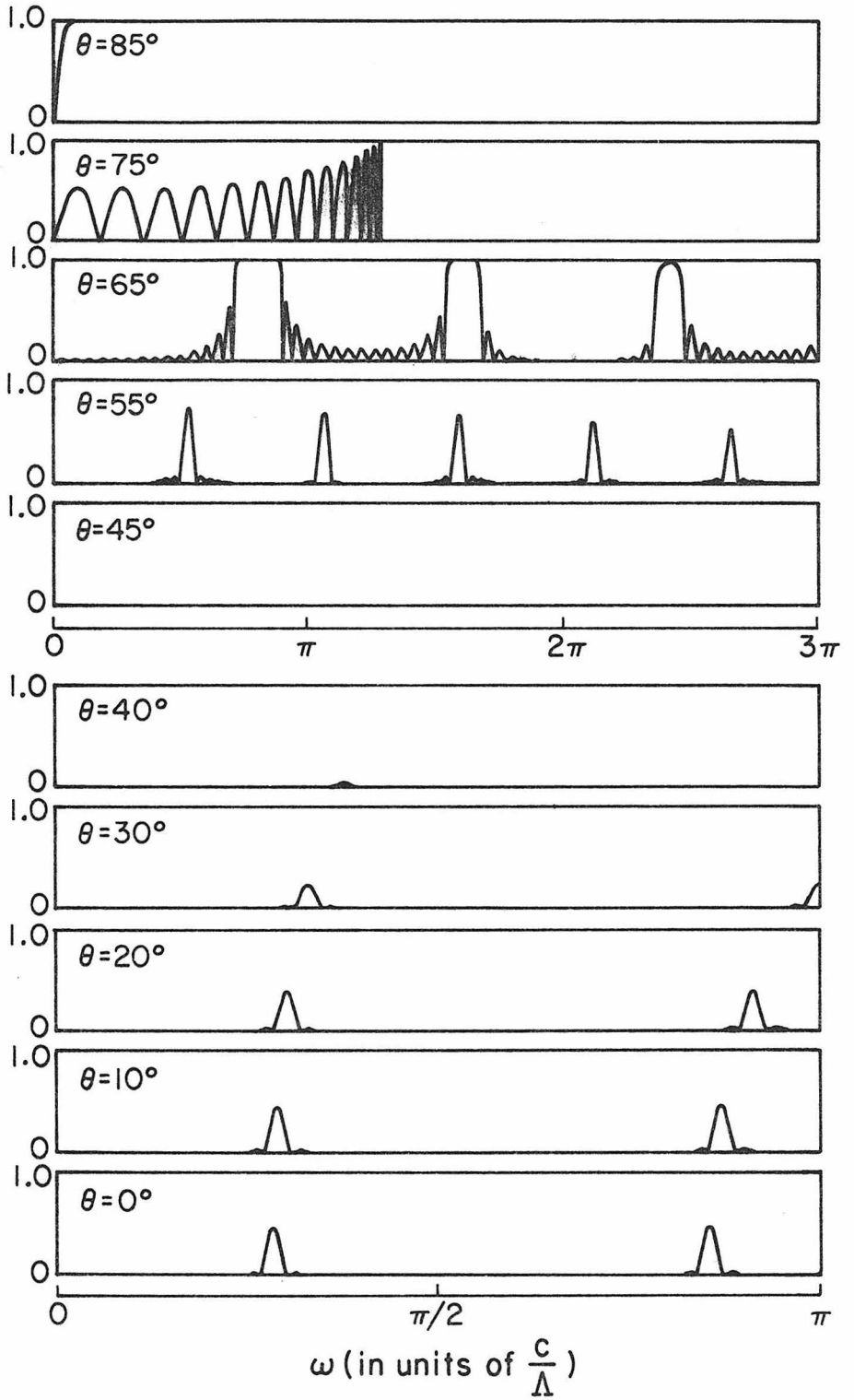

Fig. 3.3 TM wave reflectivity spectra of a 15-period multilayer reflector at various angles of incidence.

$$\sinh x \equiv |C| \frac{\sinh NK_i\Lambda}{\sinh K_i\Lambda} \tag{3.14}$$

we obtain

$$|r_N|^2 = \tanh^2 x \tag{3.15}$$

Assume in the structure

$$a = b = \frac{\Lambda}{2} \quad , \qquad n_1 \simeq n_2 = n \quad , \quad \text{and} \quad n_1 - n_2 = \Delta n << n$$

then it can be shown that, under the Bragg condition,

$$C = -\frac{\Delta n}{n} - \cdots$$

$$-\frac{A+D}{2} = 1 + \frac{1}{2}\left(\frac{\Delta n}{n}\right)^2 + \cdots$$

$$K_i\Lambda = \ell n\left(1 + \frac{\Delta n}{n} + \cdots\right) \simeq \frac{\Delta n}{n}$$

and

$$\sinh x \simeq \frac{\Delta n}{n} N \tag{3.16}$$

The reflectivity (3.15) thus becomes

$$|r_N|^2 \simeq \left(\frac{\Delta n}{n} N\right)^2 \tag{3.17}$$

On the other hand, from the coupled mode analysis [4] the reflectivity at the Bragg resonance is

$$|r_N|^2 = \tanh^2 \kappa L \tag{3.18}$$

where κ, the coupling coefficient, is given by

$$\kappa = \frac{2|r|}{\Lambda} \tag{3.19}$$

with r the reflection coefficient of a single interface, and

$$L = N\Lambda \tag{3.20}$$

Using the same assumptions in the structure as above, we obtain

$$|r| = \frac{\Delta n}{2n}$$

and

$$\kappa = \frac{\Delta n}{n\Lambda} \tag{3.21}$$

Thus the resulting reflectivity is

$$|r_N|^2 = \tanh^2(\frac{\Delta n}{n} N) \simeq (\frac{\Delta n}{n} N)^2 \tag{3.22}$$

which is exactly the same as (3.17). Equations (3.17) and (3.22) are simply results of constructive interference.

Grating reflectors which are characterized by a small Δn need a large number of periods to provide substantial reflectivity. As the number of periods, or more accurately, the effective length of the grating increases, the frequency resolution increases. This explains why a grating filter also works like a very narrow band filter. Typical filter responses are shown in Fig. 3.4, which is a plot of an exact expression of $|r_N|^2$ versus ω.

The coupled mode analysis is able to express the incident and reflected field distributions inside a grating reflector. Our matrix method gives instead a recurrence relationship between plane wave amplitudes of equivalent layers. For example, by setting $a_0 = 1$ in (3.10) and (3.5),

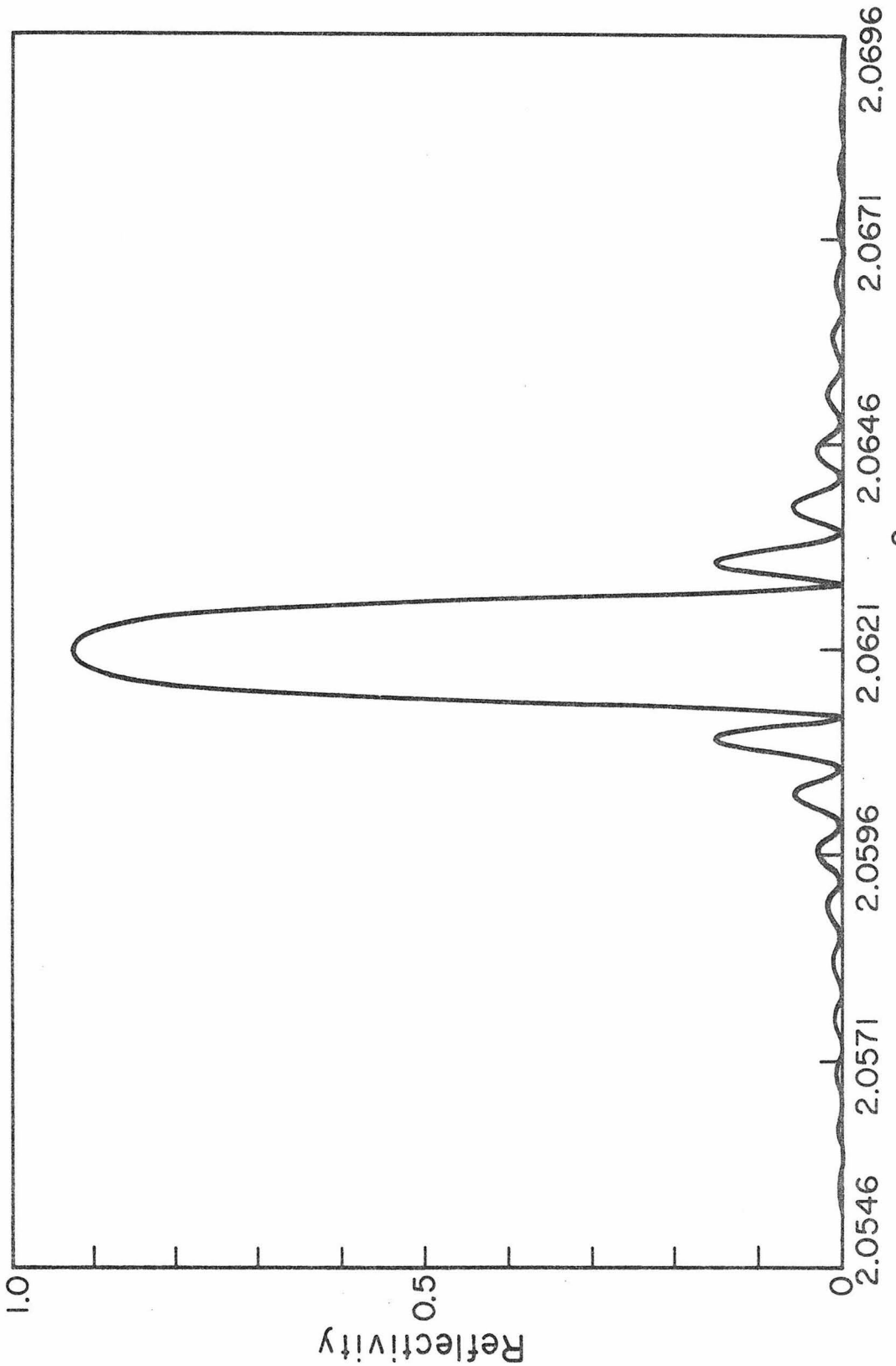

Fig. 3.4 Reflectivity spectrum of a 3000-period grating reflector.

$$a_N = \frac{1}{AU_{N-1} - U_{N-2}} \tag{3.23}$$

$$b_o = \frac{CU_{N-1}}{AU_{N-1} - U_{N-2}} \tag{3.24}$$

These are the boundary conditions. After the relevant translation matrix operation, we obtain

$$a_n = \frac{AU_{N-n-1} - U_{N-n-2}}{AU_{N-1} - U_{N-2}} \tag{3.25}$$

and

$$b_n = \frac{CU_{N-n-1}}{AU_{N-1} - U_{N-2}} \tag{3.26}$$

The amplitudes c_n and d_n at the neighboring layer can be obtained by (2.11). Plots of field intensities versus position (n) using absolute squares of (3.25) and (3.26) are shown in Fig. 3.5.

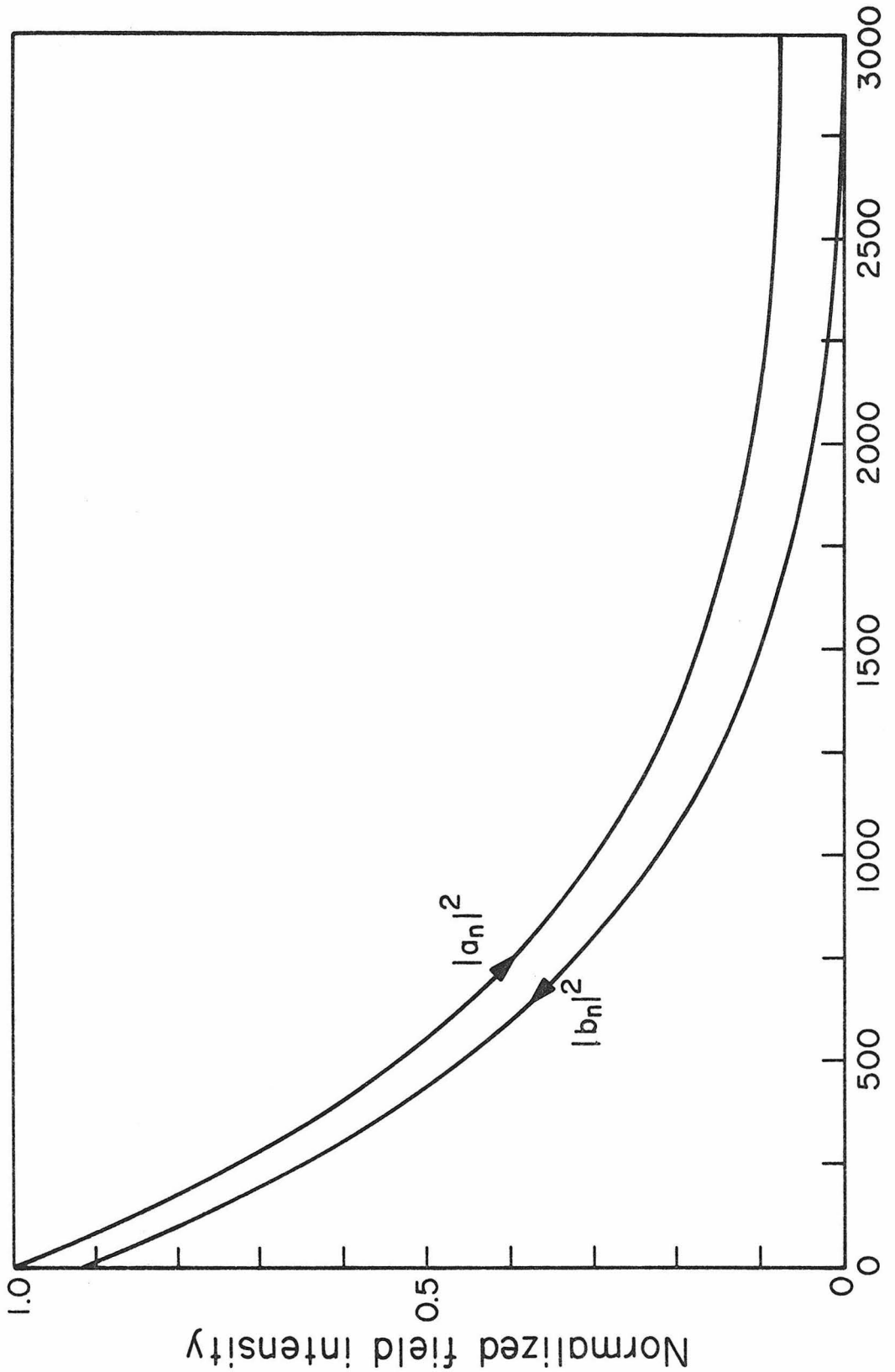

Fig. 3.5 Behavior of incident and reflected field intensities inside a grating reflector.

Chapter 3 - References

1. See, for example, O. S. Heavens, Optical Properties of Thin Solid Films (Dover, New York, 1965), p. 207.

2. See, for example, A. Yariv and M. Nakamura, "Periodic structures for integrated optics", IEEE J. Quantum Electron. QE-13, 233 (1977).

3. M. Born and E. Wolf, Principles of Optics, 2nd ed. (Macmillan, New York, 1964), p. 67.

4. A. Yariv, "Coupled-mode theory for guided-wave optics," IEEE J. Quantum Electron. QE-9, 919 (1973).

Chapter 4

ANALYSIS OF MULTICHANNEL WAVEGUIDES AND OPTICAL SURFACE WAVES

4.1 Introduction

It is the purpose of this chapter to investigate the guided modes in a periodic layered structure. Of particular interest are those modes which have a large degree of lateral field confinement. Although these confined modes cannot exist in an infinite periodic medium, the structures of practical use are expected to have only a finite number of periods. These finite structures, capable of mode confinement, will be referred to as periodic multichannel waveguides.

The analysis of the problem involves matching the boundary conditions at every interface. The conventional method thus suffers from the serious difficulty of solving a large number of linear simultaneous equations. However, the problem can be made much easier by using our new method described in Chapter 2 that involves only the manipulation of 2 x 2 matrices. Besides, many interesting guiding phenomena can be interpreted in terms of our band structures of periodic media. Moreover, the prediction of guiding of confined modes (surface waves) in a structure consisting of a semi-infinite periodic medium is beyond the scope of conventional methods.

In this work, periodic multichannel waveguides and electromagnetic surface waves will be treated. Analytic expressions for the mode dispersion relations and typical field distributions of the modes can easily be obtained by our method.

4.2 Periodic Multichannel Waveguides

In this section we look for the guided modes which propagate parallel to the interfaces of the layers and are laterally confined in a portion of the periodic medium. We will limit our analysis to TE modes only. Two important periodic multichannel waveguides (PMW) will be considered in the following.

(a) Symmetric type

Consider the simplest kind of symmetric PMW structure with the index of refraction given by

$$n(x) = \begin{cases} n_2 & n\Lambda < x < n\Lambda + b \quad (n=0,1,2,\cdots,N-1) \\ n_1 & \text{otherwise} \end{cases} \tag{4.1}$$

with $n_1 < n_2$. The geometry of the waveguide structure is sketched in Fig. 4.1. Since we are interested in confined modes only, the fields must be transversely evanescent in the n_1 medium. The translation matrix which relates the field in one period to that of the next one is given by (2.12):

$$\begin{pmatrix} a_{n-1} \\ b_{n-1} \end{pmatrix} = \begin{pmatrix} A & B \\ C & D \end{pmatrix} \begin{pmatrix} a_n \\ b_n \end{pmatrix} \tag{4.2}$$

where, after defining $k_{1x} = iq$ and $k_{2x} = p$ in (2.13)-(2.16),

$$A = e^{qa}[\cos pb - \frac{1}{2}(\frac{p}{q} - \frac{q}{p}) \sin pb] \tag{4.3}$$

$$B = e^{-qa}[-\frac{1}{2}(\frac{p}{q} + \frac{q}{p}) \sin pb] \tag{4.4}$$

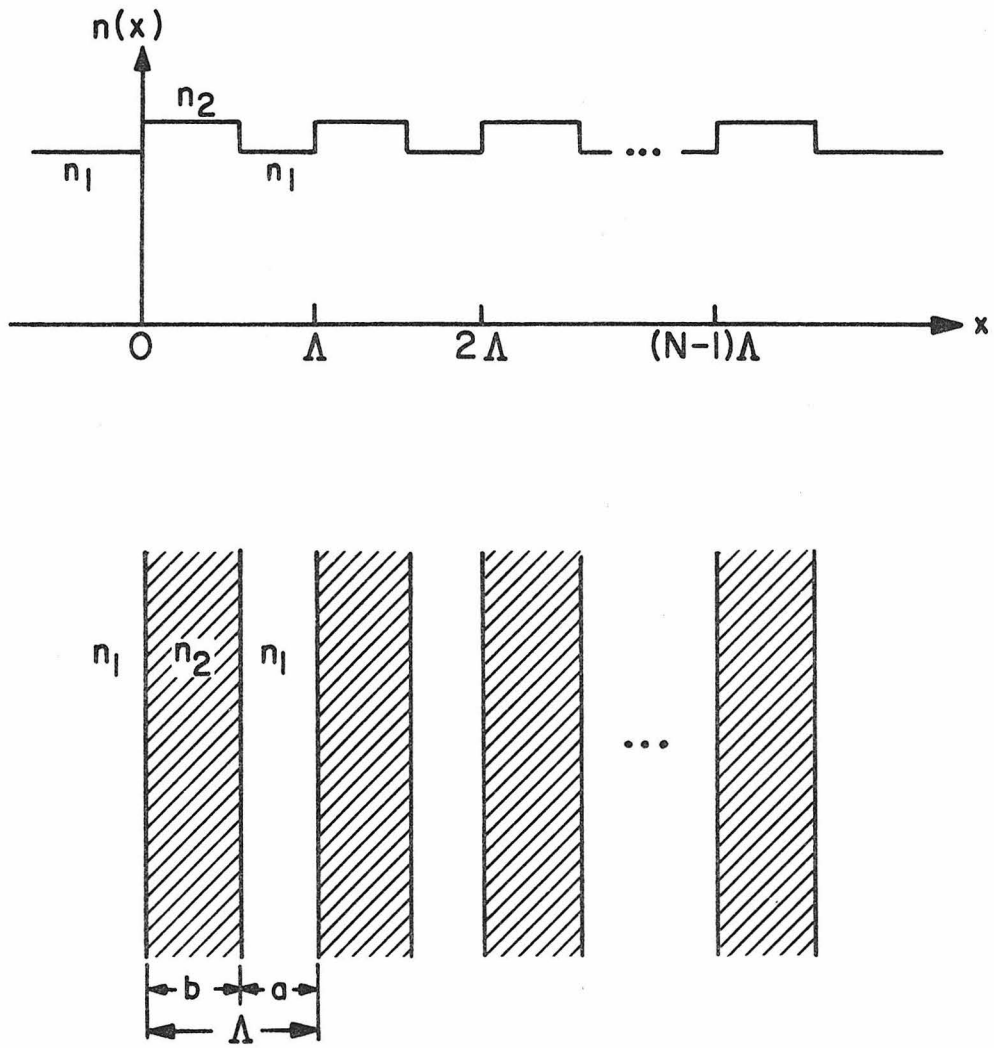

Fig. 4.1 Structure of a symmetric N-channel waveguide.

$$C = e^{qa}\left[\frac{1}{2}\left(\frac{p}{q}+\frac{q}{p}\right) \sin pb\right] \tag{4.5}$$

$$D = e^{-qa}\left[\cos pb + \frac{1}{2}\left(\frac{p}{q}-\frac{q}{p}\right) \sin pb\right] \tag{4.6}$$

with

$$q = \sqrt{\beta^2 - \left(\frac{\omega}{c} n_1\right)^2} \tag{4.7}$$

$$p = \sqrt{\left(\frac{\omega}{c} n_2\right)^2 - \beta^2} \tag{4.8}$$

As a result of successive multiplications of the matrix in (4.2), the matrix equation which relates the fields on both sides of the finite periodic medium is obtained:

$$\begin{pmatrix} 0 \\ b_o \end{pmatrix} = \begin{pmatrix} A & B \\ C & D \end{pmatrix}^N \begin{pmatrix} a_N \\ 0 \end{pmatrix} \tag{4.9}$$

We set $a_o = b_N = 0$ in (4.9), since only outward evanescent fields can be present in the "cladding" media. After using the Chebyshev identity (3.3) for the N^{th} power of the matrix in (4.9) it follows immediately that

$$A \frac{\sin NK\Lambda}{\sin K\Lambda} - \frac{\sin(N-1)K\Lambda}{\sin K\Lambda} = 0 \tag{4.10}$$

which is the mode dispersion relation.

If the left-hand side of (4.10) is plotted as a function of β for a given frequency ω, the β's at which the function becomes zero are the eigenvalues which correspond to the mode propagation constants. It can be shown mathematically that there are exactly N eigenvalues in each allowed band where $K\Lambda$ varies from $\ell\pi$ to $(\ell+1)\pi$ and none elsewhere [1].

Physically our waveguide structure can be considered as a system of N interacting slab waveguides. The N modes are simply due to the "splitting" of an N-fold degenerate mode as the separations between the N identical slab waveguides are reduced from infinity. Each confined mode of the single waveguide thus gives rise to a band with N modes. The dispersion relation (ω vs β) is shown in Fig. 4.2.

(b) Asymmetric type

Consider a simple asymmetric PMW structure with the following index profile:

$$n(x) = \begin{cases} n_a & x < 0 \\ n_2 & n\Lambda < x < n\Lambda+b \quad (n=0,1,2,\cdots,N-1) \\ n_1 & \text{otherwise} \end{cases} \tag{4.11}$$

with $n_a, n_1 < n_2$. The geometry of the waveguide structure is sketched in Fig. 4.3. The problem will be approached by the procedures illustrated in the same figure. Since every interface can be replaced by a 2 x 2 matrix, the characteristic matrix equation for this case is

$$\begin{pmatrix} 0 \\ b_a \end{pmatrix} = \begin{pmatrix} \cdot & \cdot \\ \cdot & \cdot \end{pmatrix}_{\delta \to 0} \begin{pmatrix} A & B \\ C & D \end{pmatrix}^N \begin{pmatrix} a_N \\ 0 \end{pmatrix} \tag{4.12}$$

where b_a is the field amplitude on the n_a side of the structure, and the matrix $\begin{pmatrix} \cdot & \cdot \\ \cdot & \cdot \end{pmatrix}$ accounts for the imaginary interface at $x = -\delta$ and is given by

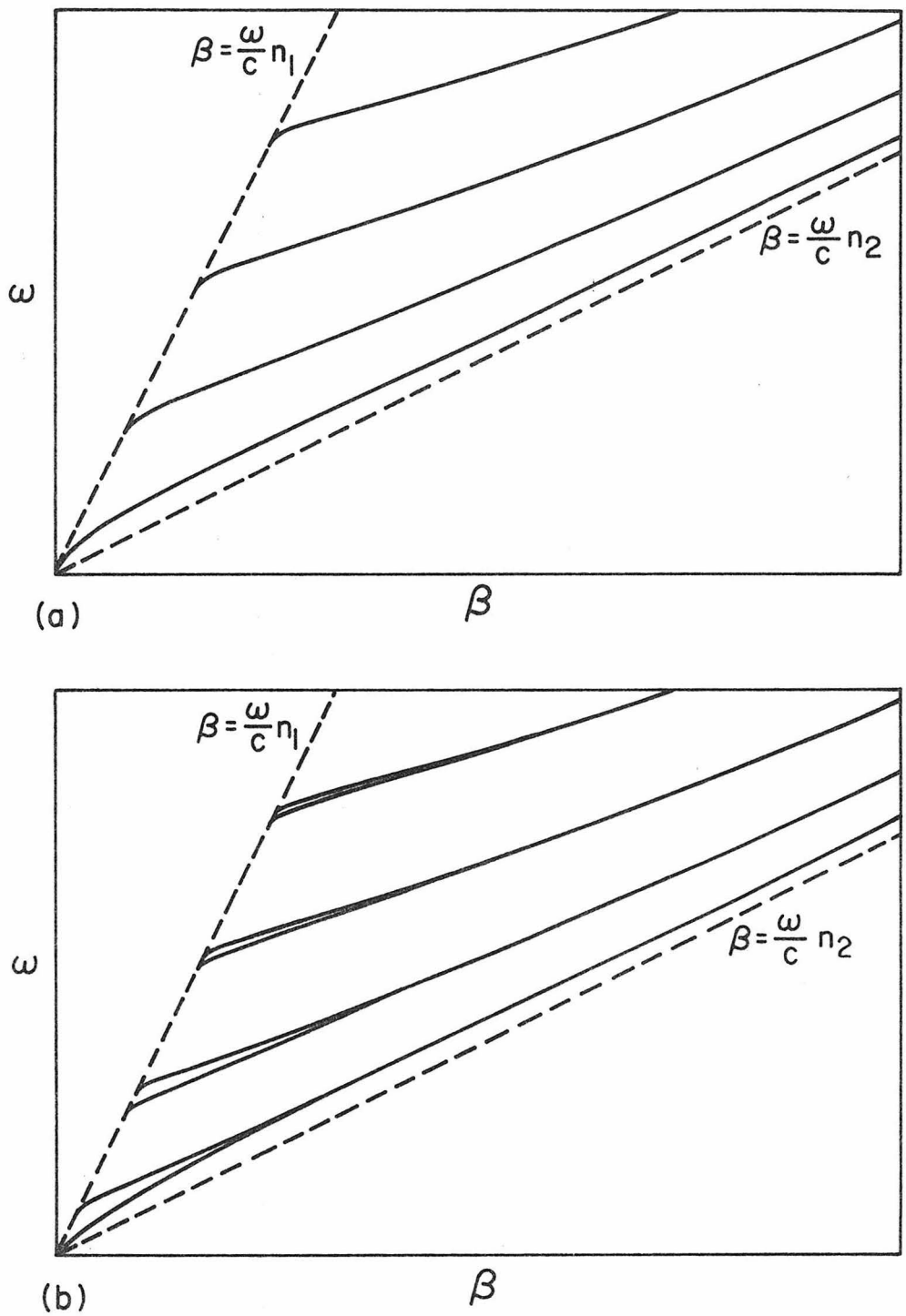

Fig. 4.2 Dispersion curves for the confined modes of symmetric (a) 1-channel, and (b) 2-channel waveguides. Note the splitting of the curves in (b).

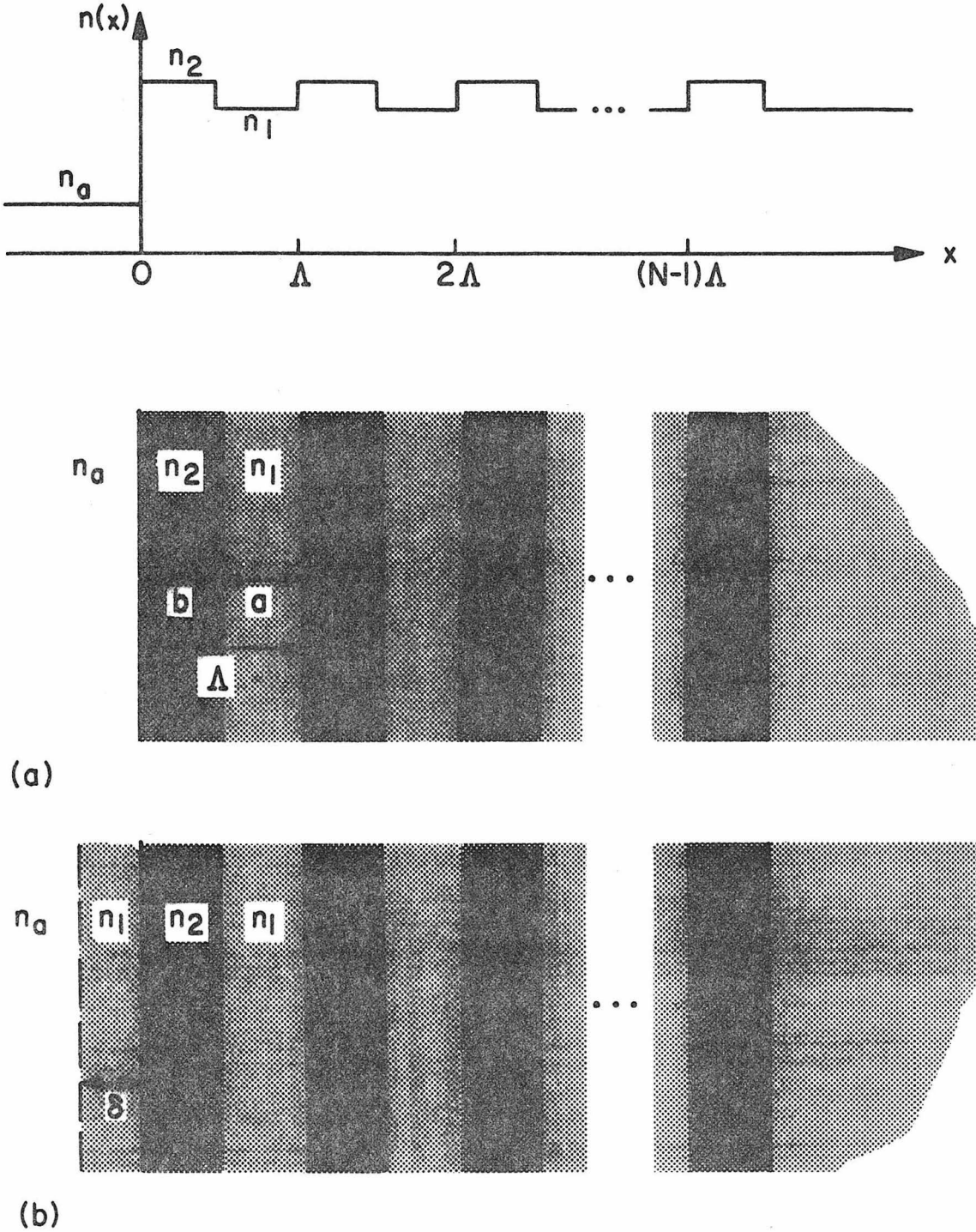

Fig. 4.3 (a) Structure of an asymmetric N-channel waveguide.
(b) Geometry used to approach the problem. The solution is obtained by letting $\delta \to 0$.

$$\begin{pmatrix} \cdot & \cdot \\ \cdot & \cdot \end{pmatrix}_{\delta \to 0} = \frac{1}{2} \begin{pmatrix} 1 + \frac{q}{q_a} & 1 - \frac{q}{q_a} \\ 1 - \frac{q}{q_a} & 1 + \frac{q}{q_a} \end{pmatrix} \tag{4.13}$$

where

$$q_a = \sqrt{\beta^2 - (\frac{\omega}{c} n_a)^2} \tag{4.14}$$

Similarly, the mode dispersion relation is obtained as

$$(A + \frac{q_a - q}{q_a + q} C) \frac{\sin NK\Lambda}{\sin K\Lambda} - \frac{\sin(N-1)K\Lambda}{\sin K\Lambda} = 0 \tag{4.15}$$

The above equation can be reduced to (4.10) by setting $n_a = n_1$.

The eigenvalue β's are determined as in the symmetric case (4.10). Instead of having all eigenvalues in the allowed band, an asymmetric periodic multichannel waveguide can have some eigenvalues in the forbidden gap of the periodic medium. These modes can be traced in terms of perturbation theory to the unperturbed modes of the surface asymmetric channels. Therefore the characteristic of those modes is the localization of energy near the surface. Eigenvalues (β's) of the confined modes as a function of the separation between the neighboring channels are shown in Figs. 4.4 and 4.5. The band edges of the periodic medium are also shown in the same figures. For small separations, all the eigenvalues are in the allowed bands. There are exactly N discrete β-levels in a complete band. At infinite separation the β-levels consist of an (N-1)-fold degenerate level and a nondegenerate level which corresponds to the only surface channel in our structure. The (N-1)-fold degenerate level will split into a band of N-1 levels when the

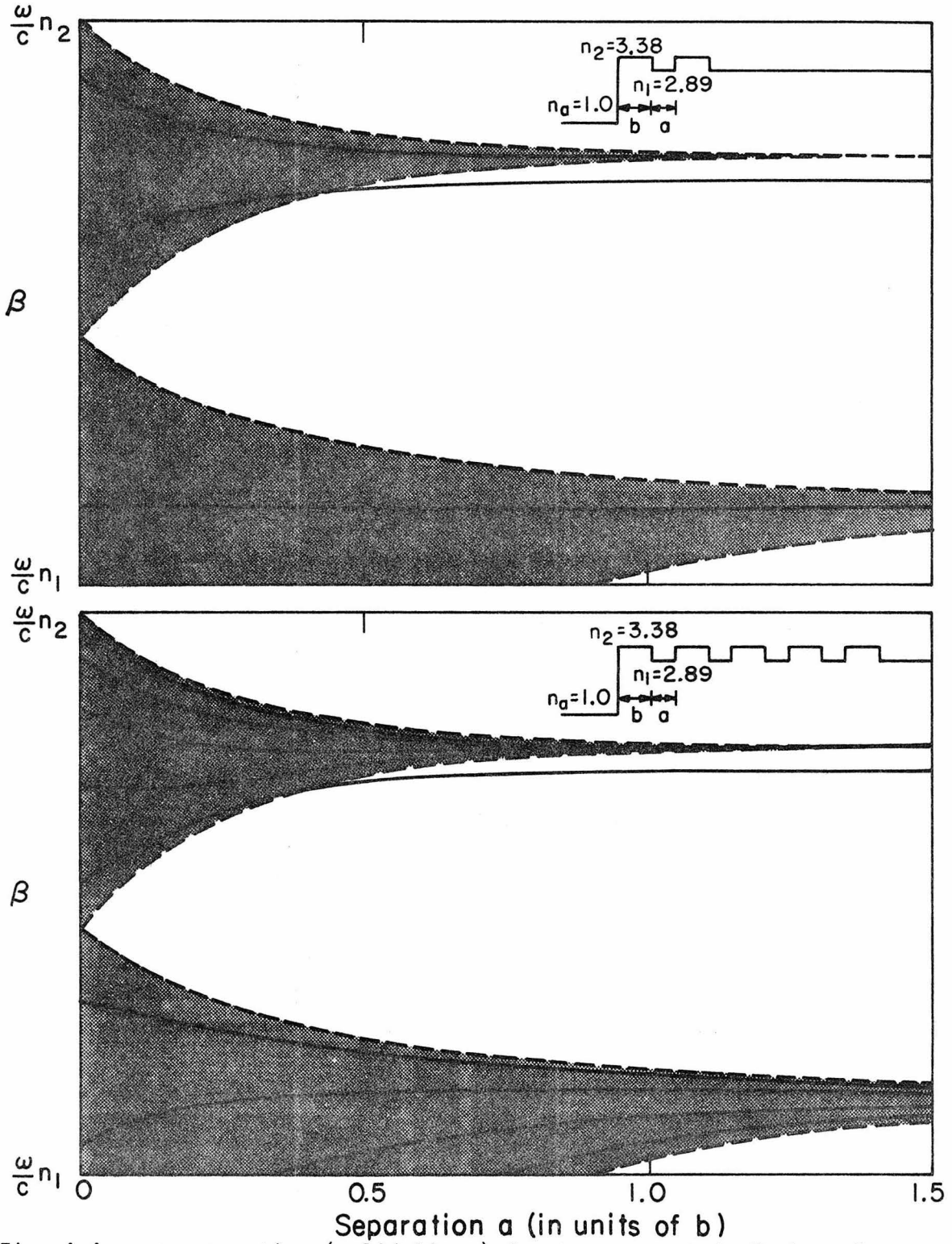

Fig. 4.4 β vs separation (solid lines) for two asymmetric N-channel waveguides with N=2 (upper diagram) and N=5 (lower diagram) at $\omega = \frac{3}{4}\pi\frac{c}{b}$. The dark zones are the allowed bands. Dashed curves are the band edges. The inset shows the refractive index profile.

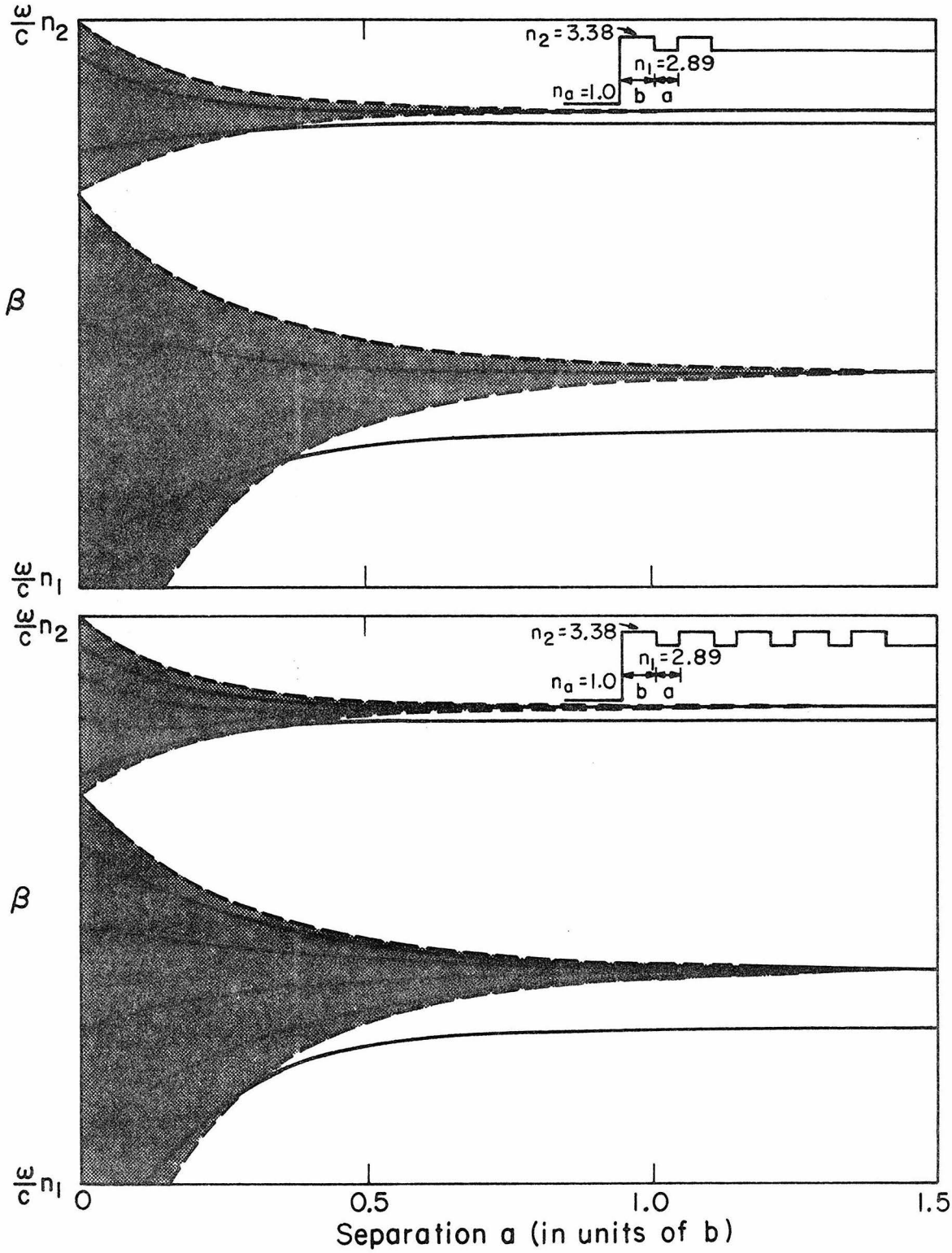

Fig. 4.5 β vs separation (solid lines) for two asymmetric N-channel waveguides with N=2 (upper diagram) and N=5 (lower diagram) at $\omega = \pi \frac{c}{b}$. The dark zones are the allowed bands. Dashed curves are the band edges. The inset shows the refractive index profile.

separation is finite. Those N-1 levels are always in the allowed band regardless of the separation. The crossing between the nondegenerate level and the band edge happens at some critical separation a_c. The surface modes only exist when the separation is larger than a_c.

Typical transverse field distributions are shown in Figs. 4.6 and 4.7 for N = 2 and 5, respectively. Only the confined modes in the first allowed band which is derived from the lowest order modes of the uncoupled individual slab waveguide are shown. As we know, there are exactly N modes in each complete band. The modes will be designated as $TE_{m\ell}$ with ℓ as the band index (ℓ=0,1,2,$\cdots$) and m as the mode index (m=0,1,2,$\cdots$,N-1). There are exactly $m+\ell N$ zero crossings in the transverse field distribution for the $m\ell^{th}$ mode with ℓ zero crossings in each channel layer and m zero crossings in the N-1 separation layers. The field can have at most one zero crossing in each separation layer where the field is evanescent.

The field distribution depends strongly on the index of refraction of the superstrate n_a when n_a is near n_1. The variation of the field distribution of the TE_{00} mode is shown in Figs. 4.8 and 4.9 for N = 2 and 5, respectively. There is a drastic change of the field intensity in the surface channel when n_a is varied slighly from n_1. This phenomenon will become very useful if a superstrate material with an electrooptic property can be found so that n_a can be tuned slightly around n_1 by an applied electric field. The resulting change of the optical energy localization in a dual channel waveguide can thus be used as a switch or modulator.

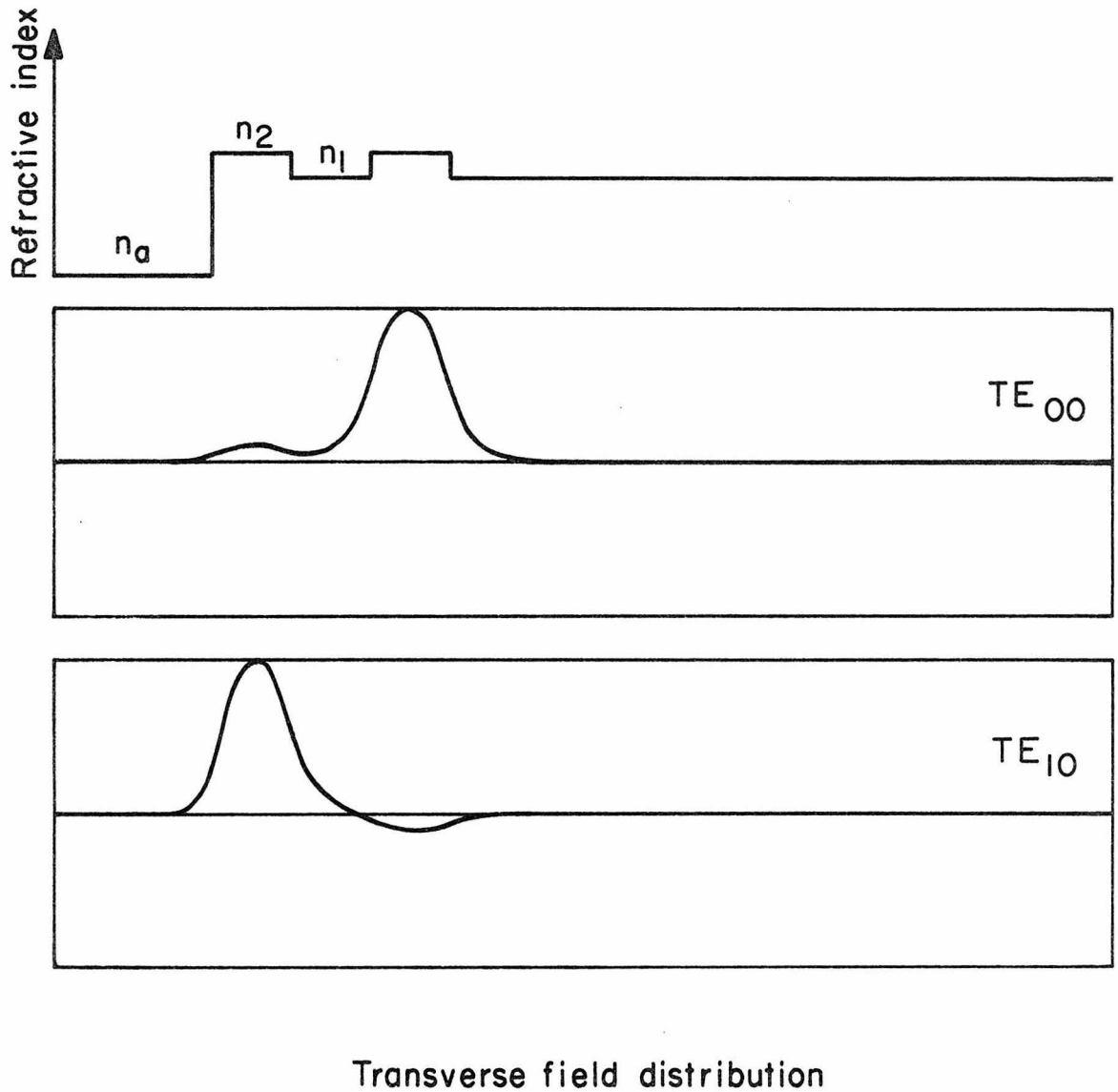

Fig. 4.6 Transverse field distributions for the confined modes in the first band of a 2-channel waveguide.

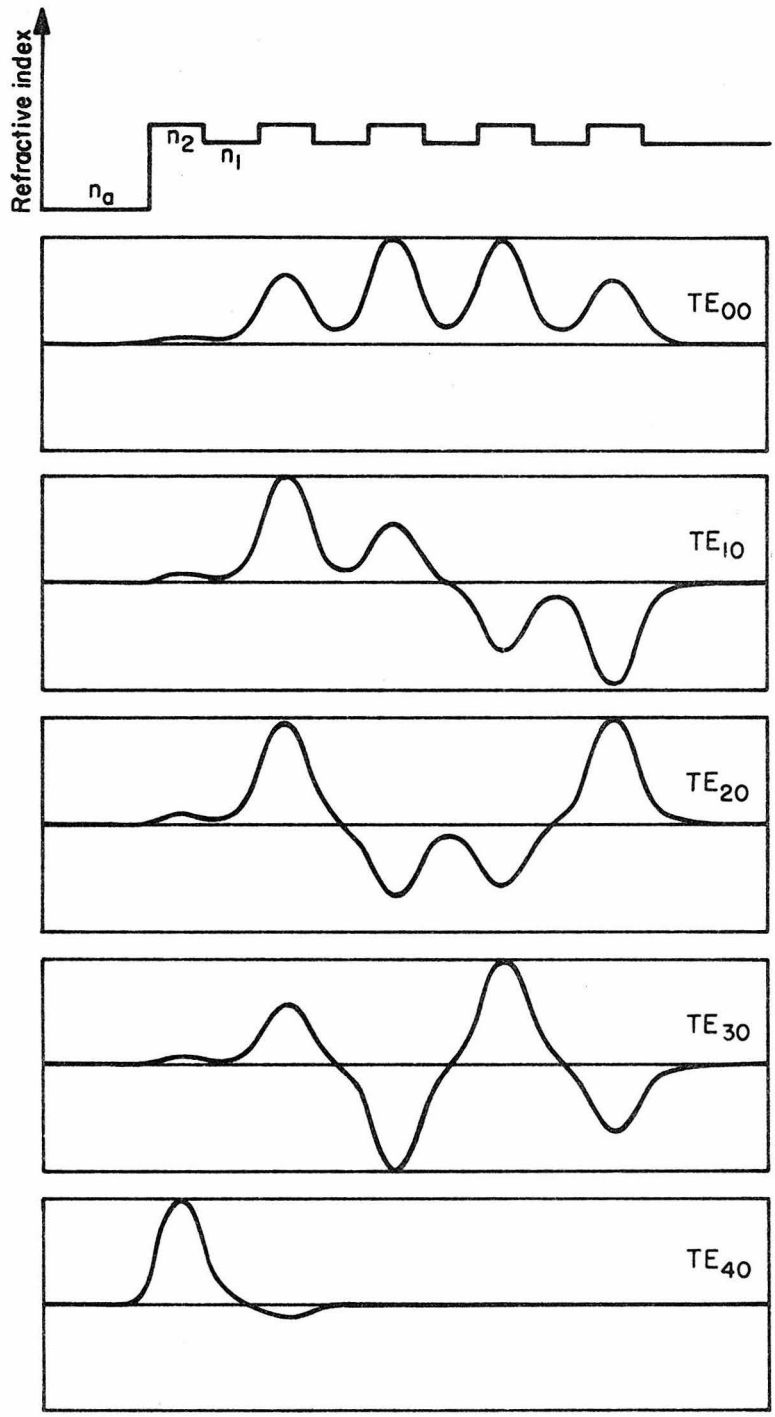

Fig. 4.7 Transverse field distributions for the confined modes in the first band of a 5-channel waveguide.

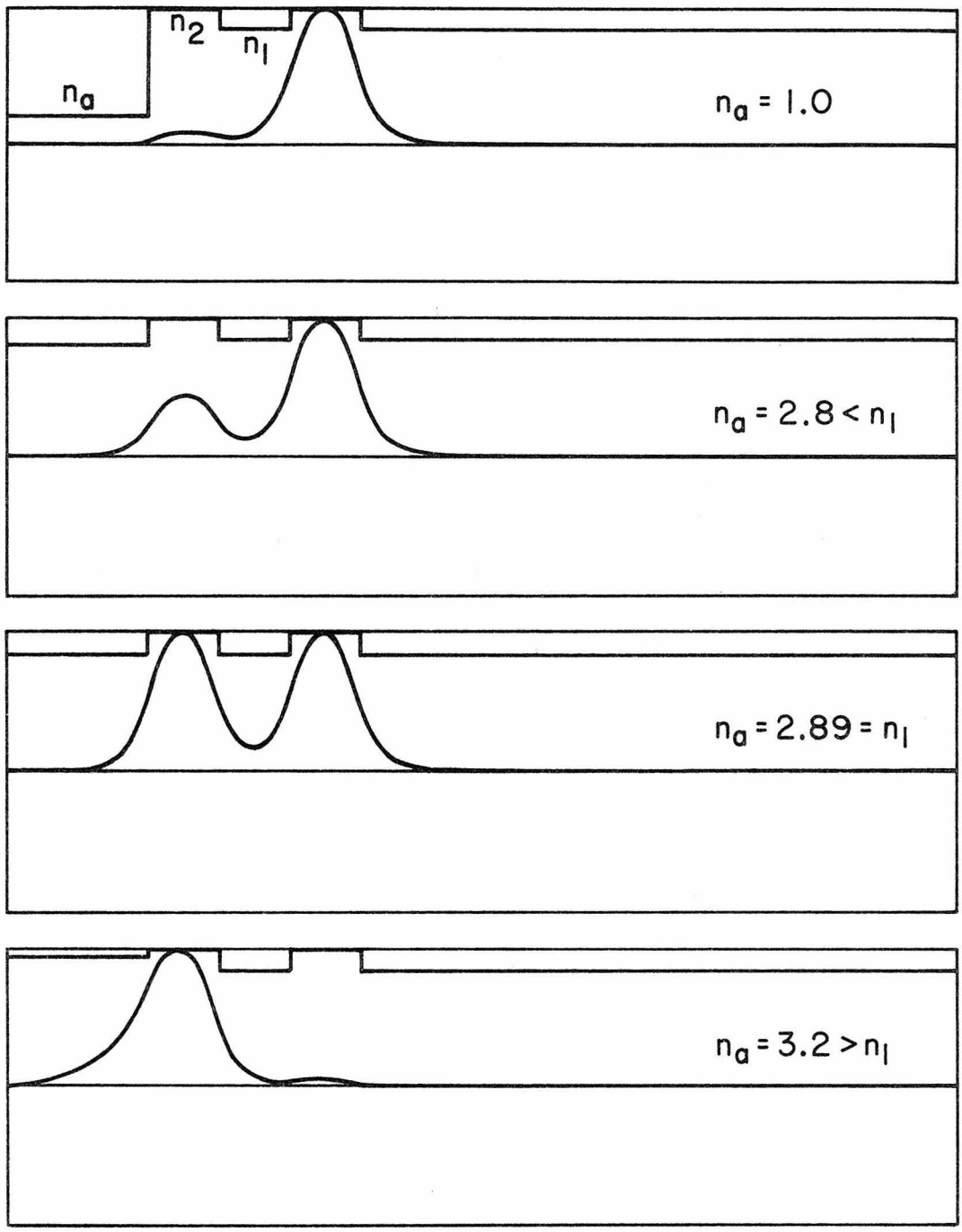

Fig. 4.8 Transverse field distributions for the TE_{00} mode of a 2-channel waveguide at various n_a's.

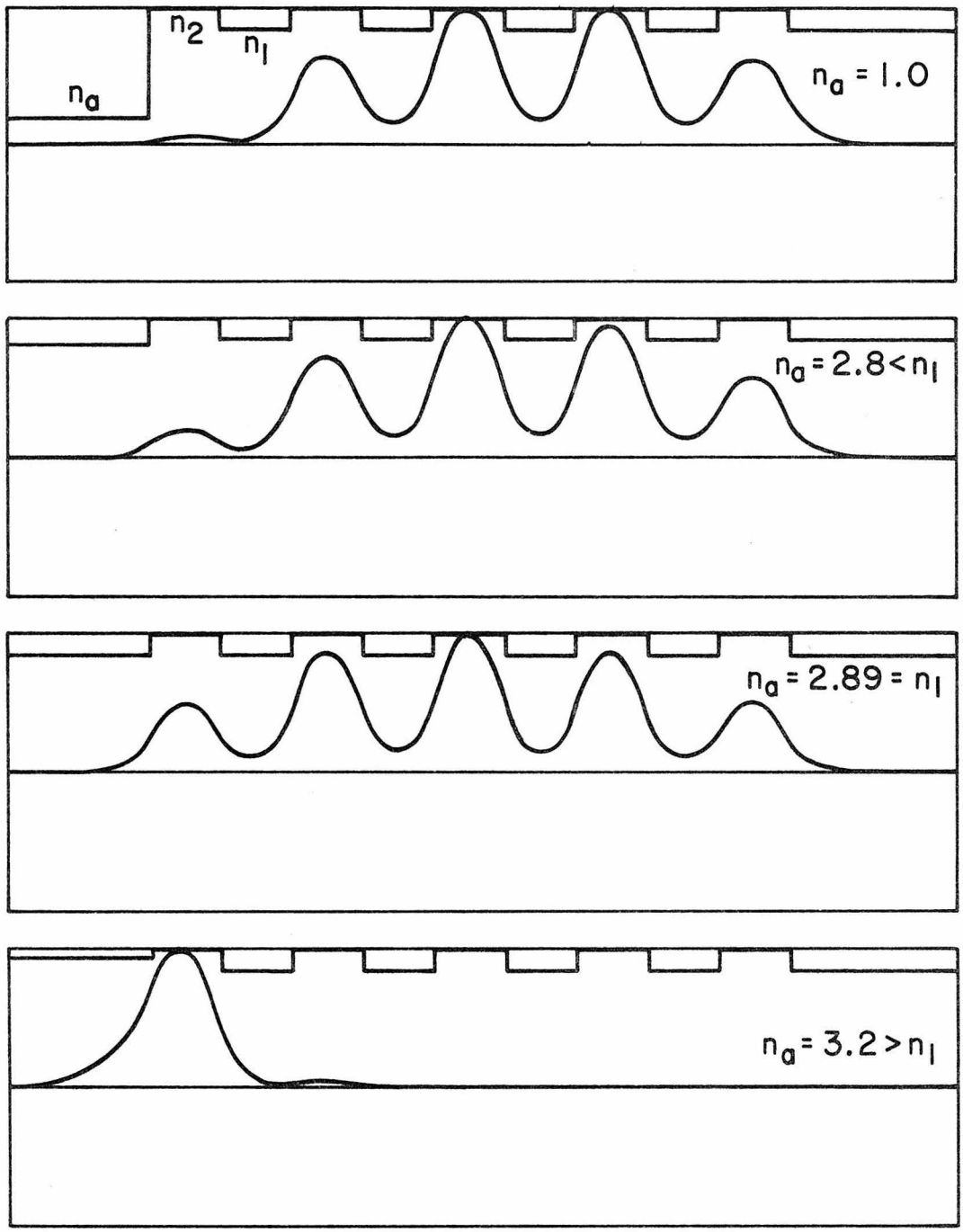

Fig. 4.9 Transverse field distributions for the TE_{00} mode of a 5-channel waveguide at various n_a's.

In the above analysis we assumed that the refractive index of the substrate is the same as n_1 for simplicity of calculation. This is the reason that only one surface mode is found. In general, if $n_s \neq n_1$, two surface modes will exist. This is similar to the electronic surface states in a crystal where the number of surface states is equal to the number of surface atoms. Here the number of surface modes is equal to the number of surface channels. However, as noted above, the electromagnetic surface modes in our structure exist only when the separation between channel layers is large enough. This state of affairs is quite different from that of electronic surface states in crystals where, according to Shockley [2], surface levels appear only when the interatomic distance becomes small enough so that the boundary curves of the allowed energy bands have crossed.

Finally, one thing in Figs. 4.4 and 4.5 has to be mentioned. In those figures we plot β values for the confined modes only. A confined mode has its β value satisfy

$$\beta_{min} < \beta < \beta_{max} \tag{4.16}$$

where

$$\beta_{max} = \frac{\omega}{c} n_2 \tag{4.17}$$

and

$$\beta_{min} = \max\left(\frac{\omega}{c} n_a, \frac{\omega}{c} n_s\right) \tag{4.18}$$

so that the guided wave is transversely standing in the periodic channels and evanescent in the cladding regions. For large enough separation between channels the whole band of β-levels will fall between β_{max} and β_{min} so that there are N confined modes. As the channels are brought

closer together, the β-levels "repel" each other. As a result, some of the modes will find their β value expelled from the confined region in β space. Those modes are transformed into substrate or superstrate modes ($\beta < \beta_{min}$) which are not confined, since the major part of their energy is in those unbounded regions.

4.3 Electromagnetic Surface Waves

Localized surface modes also exist in a semi-infinite periodic medium. They are guided by the interface between two semi-infinite media and will be referred to as electromagnetic surface waves.

The existence of a surface wave can be explained as follows: In Section 2.3 we have shown that, at a given frequency, there are regions of β for which K is a complex number, i.e., $K = \frac{\ell\pi}{\Lambda} + iK_i$. The waves with an exponential intensity variation due to the imaginary part of K cannot exist in an infinite periodic medium, and we refer to these regions as forbidden. However, if the periodic medium is semi-infinite, the exponentially damped solution is a legitimate solution near the surface and the field envelope decays as $\exp(-K_i x)$ where x is the distance from the surface.

The existence of surface waves can also be argued using perturbation theory. According to perturbation theory, our structure can be considered as an array of infinite numbers of interacting slab waveguides. These waveguides are identical to each other except for the one near the surface. When the separation between the neighboring waveguides is infinite, there is no interaction and the guides can be considered as independent of each other. The eigenvalues (β's) thus

fall into two levels: One is an infinitely degenerate level, the other is a nondegenerate level which corresponds to the extreme guide near the surface. As the waveguides are brought together, the interaction between the waveguides causes the eigenlevels to split. As they split, the allowed band is fully occupied by the levels originating from the infinitely degenerate level. As a result, the only place where the nondegenerate level can be accommodated is in the forbidden gap. The field intensity for this wave is localized near the surface because of the fact that in the forbidden gap the corresponding K is complex and the associated field is damped into the periodic medium.

To study the properties of the surface waves, consider a semi-infinite periodic medium as sketched in Fig. 4.10. The distribution of the indices of refraction is

$$n(x) = \begin{cases} n_a & x < 0 \\ n_2 & n\Lambda < x < n\Lambda+b \\ n_1 & n\Lambda+b < x < (n+1)\Lambda, \ (n=0,1,2,\cdots) \end{cases} \tag{4.19}$$

with $n_a, n_1 < n_2$. We look for the surface waves propagating parallel to the surface (say, in the positive z direction). For the sake of definiteness we consider the TE polarization only where the E-vector is in the y direction. The electric field is thus expressed as

$$E(z,x) = E(x)\, e^{i\beta z} \tag{4.20}$$

with E(x) obeying the following equation:

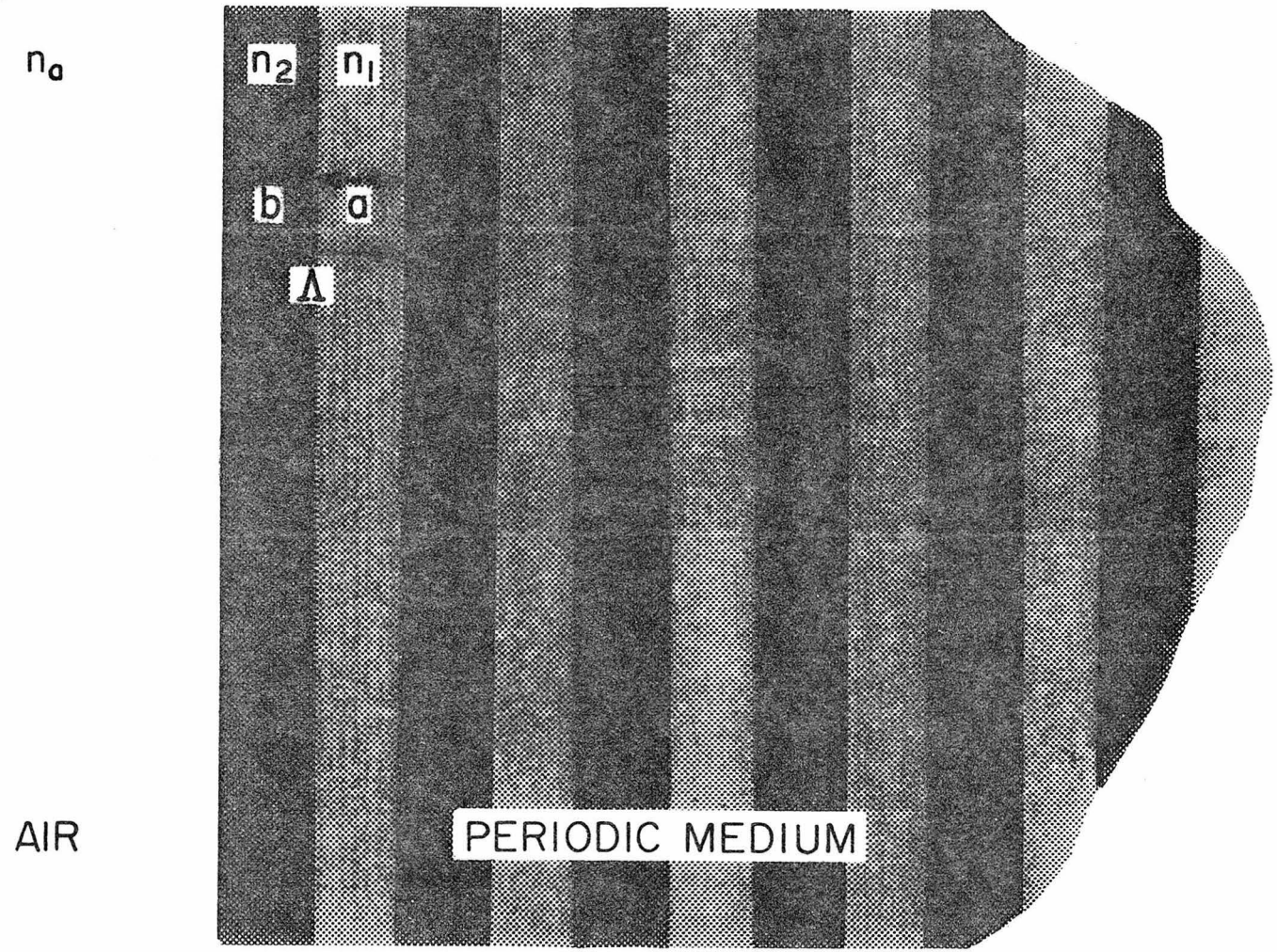

Fig. 4.10 A semi-infinite periodic medium.

$$\frac{d^2}{dx^2} E(x) + [\frac{\omega^2}{c^2} n^2(x) - \beta^2] E(x) = 0 \tag{4.21}$$

We take the solution in the following form:

$$E(x) = \begin{cases} \alpha\, e^{q_a x} & x \leq 0 \\ E_k(x)\, e^{iKx} & x \geq 0 \end{cases} \tag{4.22}$$

where q_a is given by

$$q_a = \sqrt{\beta^2 - (\frac{\omega}{c} n_a)^2} \tag{4.23}$$

and α is a constant. In order to be a surface wave, the Bloch wave number K in (4.22) must be complex so that the field decays as x goes positive. This is possible only when the propagation constant β falls into a forbidden gap of the periodic medium. Another condition is that E(x) and its derivative be continuous at the interface with medium n_a. This immediately gives us the condition for the surface waves:

$$q_a = q \frac{e^{iK\Lambda} - A - B}{e^{-iK\Lambda} - A + B} \tag{4.24}$$

where A, B, and q are given by (4.3), (4.4), and (4.7), respectively. The field distributions of some typical surface waves are shown in Figs. 4.11 and 4.12.

It is evident that the energy is more or less concentrated in the first few periods of the semi-infinite periodic medium. It can be easily

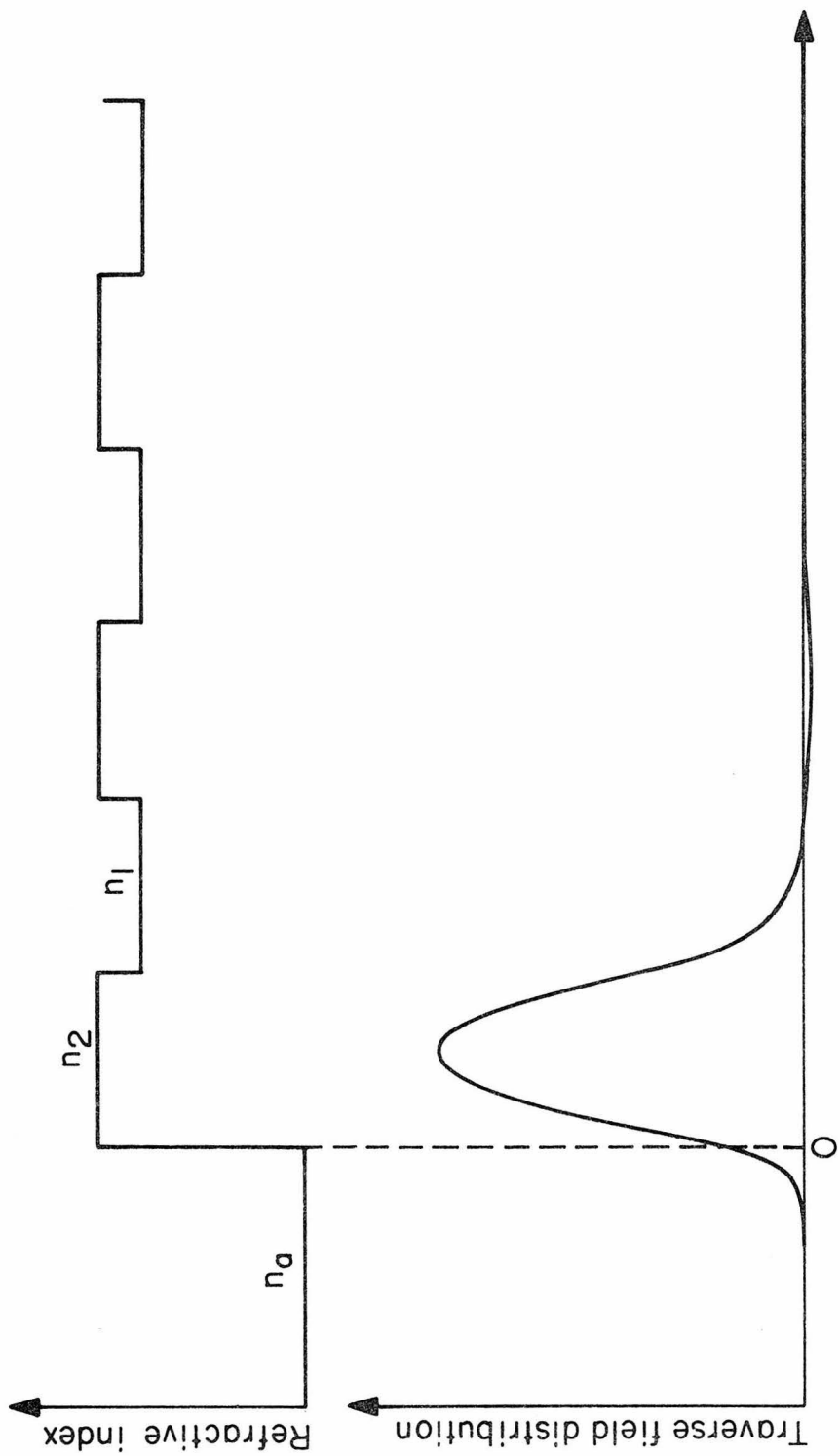

Fig. 4.11 Transverse field distribution for a typical fundamental surface wave guided by a semi-infinite periodic medium.

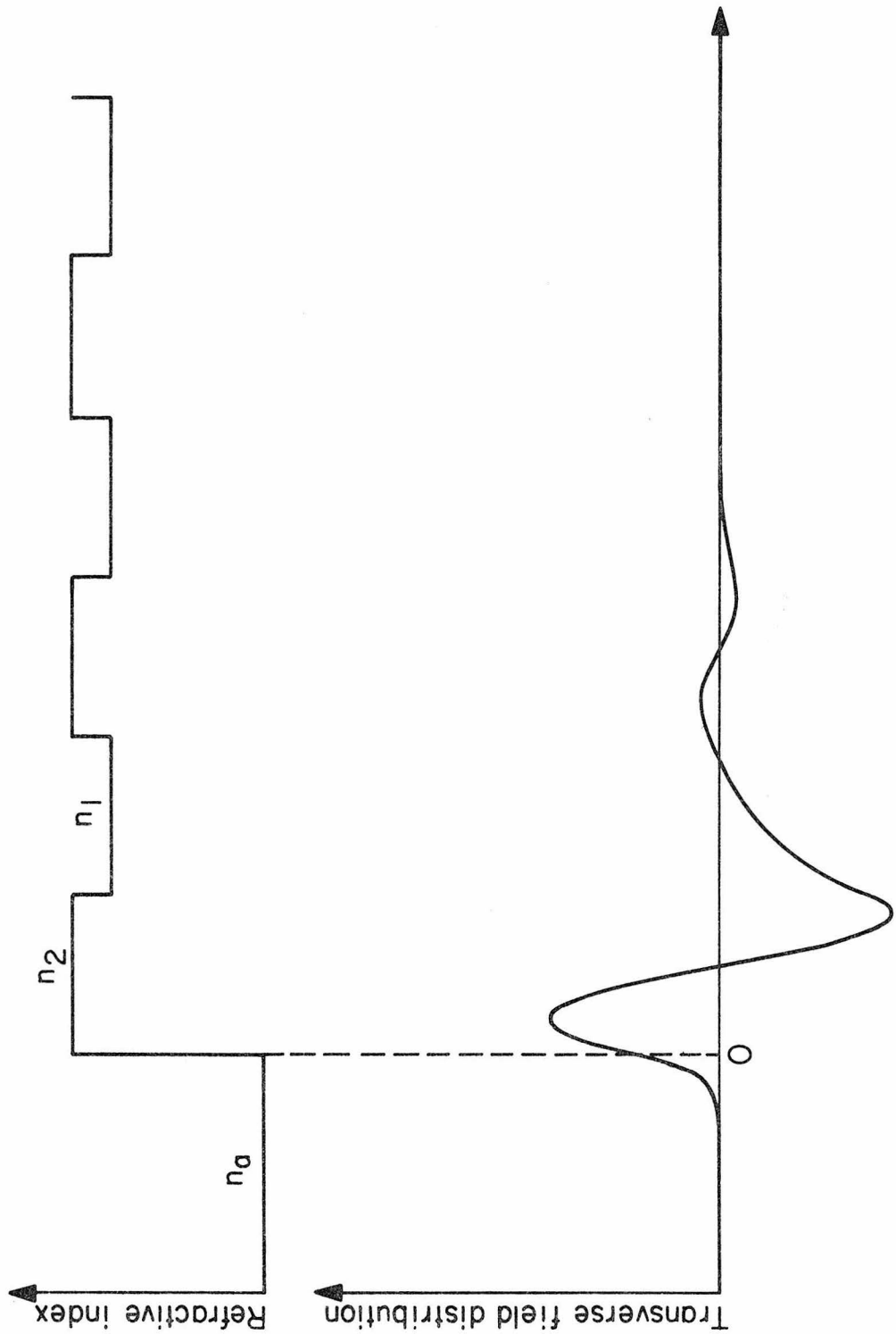

Fig. 4.12 Transverse field distribution for a typical higher order surface wave guided by a semi-infinite periodic medium.

shown that

$$\frac{\text{Energy in the first period}}{\text{Energy in the whole semi-infinite periodic medium}} = 1 - e^{-2K_i\Lambda} \qquad (4.25)$$

where K_i is the imaginary part of K. Generally speaking, the fundamental surface wave has the largest K_i and thus the highest degree of localization. The fundamental surface wave may happen to be in the 0^{th} or the 1^{st} forbidden gap. It depends on the magnitude of the index of refraction n_a. For n_a less than n_1 which is the case of practical interest (say, n_a = index of refraction of air), the fundamental surface wave has its K in the 1^{st} forbidden gap. This is due to the fact that when the individual slab waveguides are separated infinitely from each other, the nondegenerate eigenvalue, which depends on n_a, is lower than that of the degenerate one. The field profile in each period of the medium is similar to that in the preceding period except that the amplitude is reduced by a factor of $(-1)^{\ell} e^{-K_i\Lambda}$, where ℓ is the integer corresponding to the ℓ^{th} forbidden gap. The number of surface wave modes equals the number of the confined modes of the surface channel waveguide.

We have derived the mode condition for the surface wave by matching the boundary condition between an evanescent wave in the homogeneous medium and a decaying Bloch wave in the periodic medium. The existence of the surface wave in a semi-infinite periodic medium is independent of the separation between channel layers, because the allowed band is always fully occupied. However, in a finite structure as discussed in the last section, the allowed band is not fully occupied, and thus the surface wave appears only when the separation is large enough so that the nondegenerate level does not enter into the allowed band.

The surface wave can still be guided when $n_2 < n_1$; however, the local extrema will shift to n_1 layers where the profile becomes sinusoidal. This can be proved as follows. In the region where the field is evanescent $\frac{1}{E}\frac{d^2E}{dx^2}$ is positive. Thus if there is any bending in the profile for $E > 0$ the bending is concave upward, while for $E < 0$ it is concave downward. This definitely excludes the possibility for $E(x)$ to possess any local extremum in the region where the field is evanescent.

In the above calculation we assumed $\frac{\omega}{c} n_1 < \beta < \frac{\omega}{c} n_2$ so that the transverse field is sinusoidal in the n_2 layers while being evanescent in the n_1 layers. However, this condition is not necessary. Surface waves exist also when $\beta < \frac{\omega}{c} n_1$. The transverse confinement, however, is not as tight as that of the former case, since the Bloch waves decay faster whenever there is a region where the wave is evanescent. The surface wave does not exist, however, when $\beta > \frac{\omega}{c} n_2$, since in this case $\frac{1}{E}\frac{d^2E}{dx^2} > 0$ everywhere so that if the field is evanescent in the homogeneous medium n_a, it will blow up without bound in the periodic medium and vice versa.

Chapter 4 - References

1. P. A. Yeh,"Optical Waves in Layered Media", Caltech Ph.D. Thesis, 1978, p. 247.

2. W. Shockley, "On the surface states associated with a periodic potential", Phys. Rev. 56, 317 (1939).